Time-resolved Absorption Spectroscopy Applied to Tropospheric Chemistry

Thomas Robert Lewis

Submitted in accordance with the requirements for the
degree of Doctor of Philosophy

The University of Leeds

School of Chemistry

August 2017

The candidate confirms that the work submitted is his/her/their own, except where work which has formed part of jointly authored publications has been included. The contribution of the candidate and the other authors to this work has been explicitly indicated below. The candidate confirms that appropriate credit has been given within the thesis where reference has been made to the work of others.

Chapters 2 and 6 reference the publication:

Lewis, Thomas R., Mark A. Blitz, Dwayne E. Heard, and Paul W. Seakins. "Direct evidence for a substantive reaction between the Criegee intermediate, CH$_2$OO, and the water vapour dimer." *Physical Chemistry Chemical Physics* **17, no. 7 (2015): 4859-4863.**

For which I designed and built the apparatus used, and carried out all experiments, as well as processing the raw data into time-resolved absorbance.

Chapters 3-6 reference the publication:

Hansen, R. F., Lewis, T. R., Graham, L., Whalley, L. K., Seakins, P. W., Heard, D. E., & Blitz, M. A. (2017). OH production from the photolysis of isoprene-derived peroxy radicals: cross-sections, quantum yields and atmospheric implications. *Physical Chemistry Chemical Physics*, *19*(3), 2332-2345.

My role in this publication was the measurement of the total absorption cross-sections of the isoprene hydroxyperoxy radical using the TRUVAS instrument.

Acknowledgements

Firstly I would like to thank my supervisors Dwayne Heard and Mark Blitz for their support over the last 4 years.

After 5 years of postgraduate study under Professor Heard, I thoroughly appreciate his positive, encouraging attitude towards his students, from which I have learned and benefitted immensely, due in no small part to the ubiquitous and revered red biro.

I would like to thank Dr Blitz for his candour, and his willingness and ability to explain complex problems, drawing from his extensive wealth of instrumental physical chemistry.

I would like to thank Paul Seakins and Daniel Stone for their helpful insights at vital points throughout the project.

I would also like to thank Trevor Ingham for his helpful input in the instrument building on a number of occasions, as well as Chris Empson for his vital knowledge of LabView, and help designing the program used to operate the instrument.

A special thanks to all my co-workers in the Dainton lab, especially Dr Hansen with whom I collaborated on this project.

Outside the sphere of academia I would like to thank my parents Gill and Nev, who have been nothing but supportive my whole life, and to whom I owe everything. Without their encouragement and support, I sincerely doubt I would be in the position I am today.

Finally I would like to thank Tanya for her support and patience throughout the past few years, particularly during the completion of my thesis.

Abstract

A Time-Resolved UV-Vis Absorption Spectrometer (TRUVAS) has been constructed with the ability to record time-resolved absorption spectra between ~250-800 nm, with a maximum time-resolution of 0.78 ms.

The rate of reaction of the C1 Criegee Intermediate (formaldehyde oxide) with water vapour has been studied. The removal rate constant shows a quadratic dependence on $[H_2O]$, implying reaction with the water dimer, $(H_2O)_2$. The removal rate of the Criegee intermediate *via.* reaction with the water dimer $((H_2O)_2)$ was discovered to be $4.0 \pm 1.2 \times 10^{-12}$ cm^3 $molecule^{-1}$ s^{-1}, and sufficiently fast to dominate the species' removal in the troposphere. This result was published in PCCP[3].

The primary motivation for building the TRUVAS instrument was to measure the absorption cross-sections of isoprene-derived peroxy radicals in the actinic region, with a view to calculating the total atmospheric photolysis rates.

The total atmospheric photolysis rates of the isoprene, 2,3-dimethylbutadiene and butadiene hydroxyperoxy (HP) radicals were calculated at noon in Borneo, and were found to be 1.27, 1.81 and 1.01×10^{-3} s^{-1} respectively.

The absorption spectra of ethylene, but-2-ene and 2,3-dimethylbut-2-ene (TetraMethyl Ethylene – TME) HP radicals were measured. The measured absorption spectra show a marked broadening effect, with the Gaussian width increasing 11% from ethylene to but-2-ene HP radical absorption spectrum, and 26% to the TME HP radical, which translate to atmospheric photolysis rates of 0.552, 1.21 and 1.68×10^{-3} s^{-1}.

The absorption spectra of the methyl, tertiary-butyl and cyclohexyl peroxy radicals are presented. The methyl peroxy absorption spectrum measured in this study largely agree with the numerous existing studies. Atmospheric photolysis of methyl peroxy radicals comprises around 1% of the species' removal in the marine boundary layer.

Table of Contents

List of Figures

List of Tables

1   Introduction

1.1   Air quality and climate change

Climate change as a result of human activity is one of the biggest challenges facing society today. A considerable amount of effort goes into trying to elucidate and quantify both the causes of climate change which has already been observed and the role which human activity plays and will continue to play in coming years, decades and centuries. For the purposes of informing the public and the policy makers, the research carried out on many topics is summarised by organisations including the Intergovernmental Panel on Climate Change (IPCC)[33], the National Oceanic and Atmospheric Administration (NOAA) and the National American Space administration (NASA). The IPCC report AR5, which was released in September 2013, is perhaps the most extensive aggregation of research on climate change to date. The effects of climate change are broad and include the effects on the world's Oceans such as sea level rises[34], ocean acidification[35] and ocean warming[36]; effects on the cryosphere such as the decrease in mass of land ice such as glaciers[37] and the Greenland and Antarctic ice sheets[38], as well as the rapidly decreasing extent of Arctic sea ice[39]. These effects on the cryosphere are important when considering the global impact of climate change, however their relevance to this study is limited, and they will not be discussed in any more detail here. Findings and conclusions within the IPCC report are generally expressed in terms of either quantitative probabilistic terms, ranging from virtually certain (99–100% probability) to exceptionally unlikely (0–1%) or qualitative statistical confidence terms ranging from very low to very high confidence, depending on which is the more suitable method of inferring the level of understanding of a certain topic. An example of this method of conveying certainty would be that the fifth Intergovernmental Panel on Climate Change (IPCC) report states with 95% confidence that humans are the main cause of the current global warming.

1.1.1 The effects of climate change on the atmosphere:

Greenhouse gas emissions by humans have led to a change in the composition of the atmosphere most notably an increase in greenhouse gas concentrations in the atmosphere, the most important of which are carbon dioxide (CO_2), methane (CH_4), tropospheric ozone (O_3) and nitrous oxide (N_2O) . It is worth noting that CFCs also play a large part in the increase in overall radiative forcing estimates, however their concentration in the atmosphere has mostly levelled out due to the implementation of sanctions banning their use entirely, as a result of the Montreal Protocol and subsequent amendments. The aim of the Montreal Protocol was primarily to try and prevent further damage to and facilitate the recovery of the ozone layer, however recent research suggests that the cessation of CFC emissions has also contributed to the apparent retardation of radiative forcing increase observed in the period 1998-2012.[40]   Since CFCs were used widely as refrigerants and propellants, various replacements have been used, including HydroFluoroCarbons (HFCs). HFCs are subsequently being phased out due to their contribution to Radiative Forcing (RF), which is the difference between radiant energy received by the earth and energy radiated back to space relative to pre-industrial Earth (pre-1750). RF is affected by various physical processes, as shown in Figure 1.1 which shows the most recent estimates of the effects that anthropogenic activity has had on RF. The consequences of such an increase in RF on the atmosphere are numerous, as shown in Figure 1.2.

The observed changes with the greatest likelihood are the "warmer and/or fewer cold days and nights over most land areas", and the "warmer and/or more frequent hot days and nights over most land areas", and is very likely (90-100%) to have been caused by human activity. Whilst it may be convenient to discuss changes in climate in terms of global change, a description of changes observed at the regional level can be more appropriate, especially when considering the frequency of such phenomena as drought[41-43], heavy precipitation events[44, 45] and intense tropical cyclone activity[46, 47]. An increase in the frequency and severity of these regional effects can pose a substantial threat not only to natural ecosystems such as forested[43] and semi-arid regions[48] but also to human life, both directly[49-51] and indirectly[52].
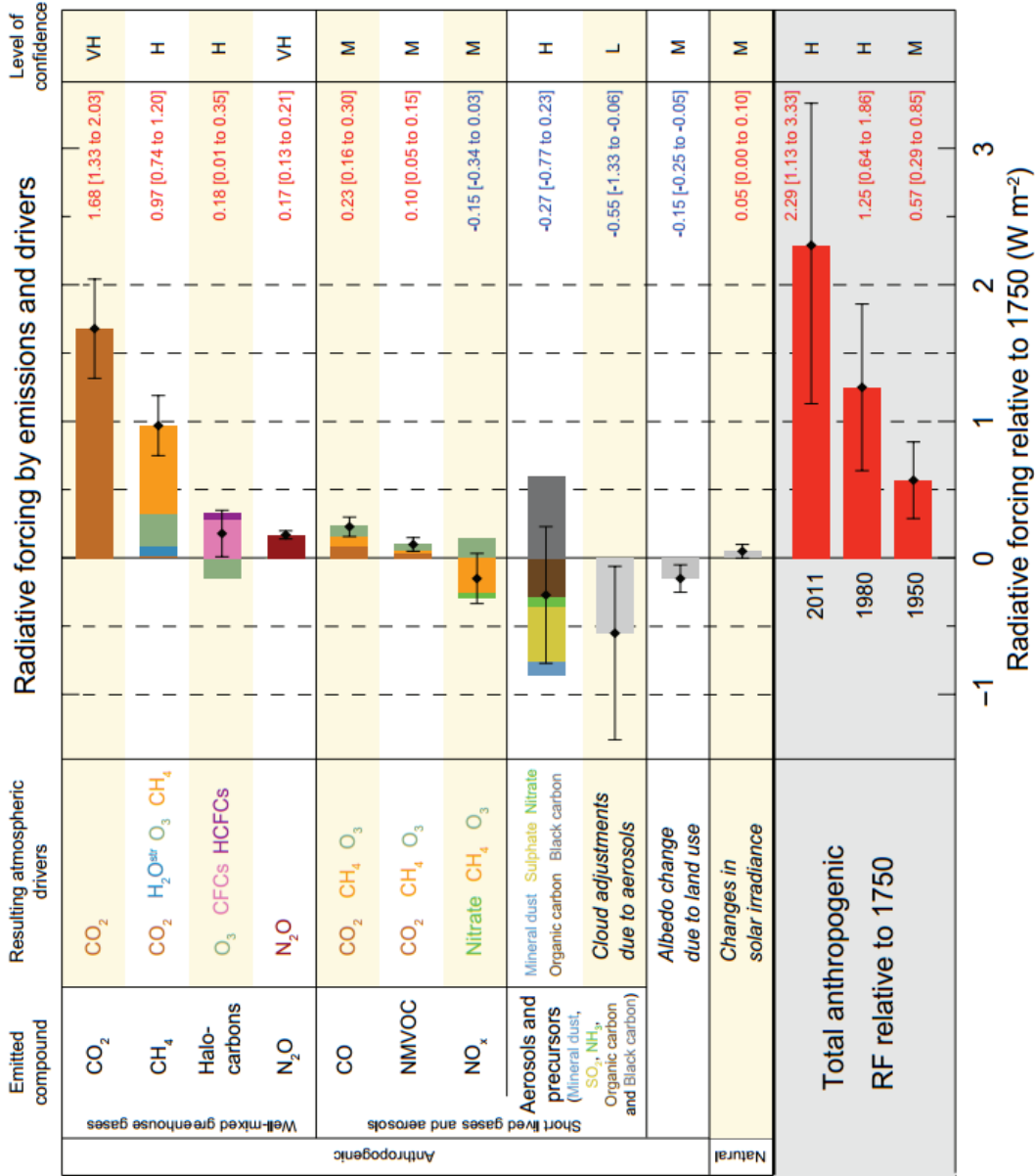
Figure 1.1: Radiative forcing estimates for the main contributors to the total radiative forcing change since pre-industrial times (taken from the IPCC Assessment Report 5)[33].

Figure 1.2: A table outlining the major changes which have been observed in the climate, the level of human contribution to these changes, and the likelihood of further changes (taken from the IPCC Assessment Report 5).

Table SPM.1 | Extreme weather and climate events: Global-scale assessment of recent observed changes, human contribution to the changes, and projected further changes for the early (2016–2035) and late (2081–2100) 21st century. Bold indicates where the AR5 (blue) or AR4 (red) provides a revised* global-scale assessment from the SREX (blue) or AR4 (red). Projections for early 21st century were not provided in previous assessment reports. Projections in the AR5 are relative to the reference period of 1986–2005, and use the new Representative Concentration Pathway (RCP) scenarios (see Box SPM.1) unless otherwise specified. See the Glossary for definitions of extreme weather and climate events.

Phenomenon and direction of trend	Assessment that changes occurred (typically since 1950 unless otherwise indicated)	Assessment of a human contribution to observed changes	Likelihood of further changes	
			Early 21st century	Late 21st century
Warmer and/or fewer cold days and nights over most land areas	*Very likely* {2.6} *Very likely* *Very likely*	*Very likely* {10.6} *Likely* *Likely*	*Likely* {11.3}	*Virtually certain* {12.4} *Virtually certain* *Virtually certain*
Warmer and/or more frequent hot days and nights over most land areas	*Very likely* {2.6} *Very likely* *Very likely*	*Very likely* {10.6} *Likely* *Likely (nights only)*	*Likely* {11.3}	*Virtually certain* {12.4} *Virtually certain* *Virtually certain*
Warm spells/heat waves. Frequency and/or duration increases over most land areas	*Medium confidence* on a global scale {2.6} *Likely* in large parts of Europe, Asia and Australia *Medium confidence* in many (but not all) regions	*Likely*[a] {10.6} *Not formally assessed* *More likely than not*	*Not formally assessed*[b] {11.3}	*Very likely* {12.4} *Very likely* *Very likely*
Heavy precipitation events. Increase in the frequency, intensity, and/or amount of heavy precipitation	*Likely* more land areas with increases than decreases[c] {2.6} *Likely* more land areas with increases than decreases *Likely* over most land areas	*Medium confidence* {7.6, 10.6} *Medium confidence* *More likely than not*	*Likely* over many land areas {11.3}	*Very likely* over most of the mid-latitude land masses and over wet tropical regions {12.4} *Likely* over many areas *Very likely* over most land areas
Increases in intensity and/or duration of drought	*Low confidence* on a global scale {2.6} *Likely* changes in some regions[d] *Medium confidence* in some regions *Likely* in many regions, since 1970[e]	*Low confidence* {10.6} *Medium confidence*[f] *More likely than not*	*Low confidence*[g] {11.3}	*Likely (medium confidence)* on a regional to global scale[h] {12.4} *Medium confidence* in some regions *Likely*[i]
Increases in intense tropical cyclone activity	*Low confidence* in long term (centennial) changes {2.6} *Virtually certain* in North Atlantic since 1970 *Low confidence* *Likely* in some regions, since 1970	*Low confidence*[i] {10.6} *Low confidence* *More likely than not*	*Low confidence* {11.3}	*More likely than not* in the Western North Pacific and North Atlantic[j] {14.6} *More likely than not* in some basins *Likely*
Increased incidence and/or magnitude of extreme high sea level	*Likely* (since 1970) {3.7} *Likely* (late 20th century) *Likely*	*Likely*[k] {3.7} *Likely*[k] *More likely than not*[k]	*Likely*[l] {13.7}	*Very likely*[l] {13.7} *Very likely*[m] *Likely*

1.1.2 Methane lifetime

Of the contributors to increased radiative forcing, methane is second only to CO_2 in its contribution to the trapping of outgoing radiation and warming of the Earth. Methane is a VOC emitted in large quantities annually (~600 Tg yr^{-1})[53] and today exhibits an atmospheric concentration 150% greater than pre industrial times as a result of human activity. The primary removal mechanism of methane is *via.* its reaction with the OH radical, forming the methyl radical (R 1.1), which rapidly reacts with oxygen in the atmosphere to yield methyl peroxy radicals (R 1.2).

$$CH_4 + OH \rightarrow CH_3 + H_2O$$

R 1.1

$$CH_3 + O_2 + M \rightarrow CH_3O_2 + M$$

R 1.2

The global warming potential (the amount that a molecule increases RF relative to CO_2) of methane over a 20 year period is 84 fold greater than that of CO_2, so per unit concentration has a vastly more profound effect on RF. Since reaction with OH is the primary removal mechanism of methane in the atmosphere, it is vital that OH radical concentrations are well known so as to accurately predict the atmospheric lifetime of methane.

1.1.3 Air Quality and emissions

Another challenge which faces modern society is that of deteriorating air quality, and the way in which human activity impacts on the composition of the air we breathe. Studies have shown that there is a link between chronic mortality and exposure to ozone (O_3)[54] and fine particulate matter, which is a mixture of black carbon, metals, sulphates, nitrates, and other direct and indirect by-products of incomplete combustion and high-temperature industrial processes. [55] Another important tropospheric pollutant is NO_x (NO and NO_2), which is formed from fossil fuel combustion. Chronic exposure to NO_2 is linked to airway inflammation, and exacerbation of asthma symptoms in humans.[56-58] NO_x plays an important role in the chemistry of the troposphere, essentially catalysing the oxidation of carbon based emissions, as described in section 1.3.1. Atmospheric radical chemistry plays a vital role in our understanding of both climate change and air quality, as it controls the lifetimes of emissions in the atmosphere.

1.2 Photochemistry

This section will introduce the concept of photochemistry, and the importance of molecular absorption of solar radiation on the composition and chemistry of the atmosphere.

1.2.1 The Beer – Lambert Law

The Beer-Lambert law describes the relationship between the attenuation of light passing through a medium (*A*), the concentration of the attenuating species (*C)*, the distance travelled by the light through the attenuating medium (*l)*, and the probability that each attenuating species will absorb a photon (*σ*) as shown in E 1.1.[59, 60]

$$A = \sigma \cdot C \cdot l \qquad \text{E 1.1}$$

Absorbance is defined as the natural logarithm of ratio of the intensities of light with (*I*) and without (*I$_0$*) the attenuating species present, shown in E 1.2.

$$A = \ln \frac{I_0}{I} \qquad \text{E 1.2}$$

E 1.1 shows that absorbance is linearly dependent on both the concentration of the attenuating species, and the path length of the light through the medium. Attenuation can occur as a result of absorption of the electromagnetic radiation by an atom or molecule, or by scattering due to atoms, molecules and particles.

1.2.2 Absorption of electromagnetic radiation by molecules

Absorption of electromagnetic radiation by molecules involves the interaction between an incident photon and the absorbing molecule leading to a transition between energy levels within the molecule. Broadly speaking, excitations resulting from molecular absorption can be separated into three distinct types: electronic excitation, vibrational excitation and rotational excitation, which most often correspond to the UltraViolet/Visible (UV/Vis), Infra-Red (IR) and microwave regions of the electromagnetic spectrum, respectively. Vibrational and rotational excitation are often coupled, giving rise to ro-vibrational transitions, which exhibit sharp, evenly spaced peaks, centred about a transition energy corresponding to the difference in energy between the two vibrational energy levels. Typically ro-

vibrational transitions occur between low-lying vibrational states, and are not dissociative at 298 K as shown in Figure 1.3
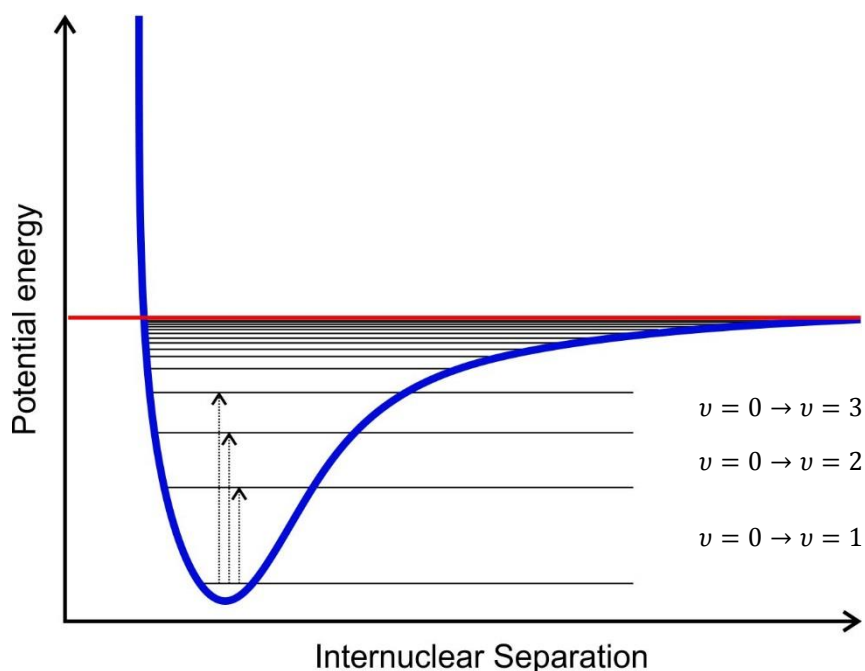
Figure 1.3: A diagram of a morse potential curve, showing the first 3 transitions from the vibrational ground state to the first 3 vibrational energy levels. The number of vibrational energy levels is finite, and energy levels become closer together until they become a continuum at the dissociation limit, shown in red. Note the excited states $v = 1 - 3$ are below the dissociation limit, and will not lead to bond cleavage in this example.

Electronic excitation involves the absorption of a photon leading to the formation of an electronically excited upper state. The fate of the excited state depends on its structure: an electronically excited molecule with a bound upper state will relax down to the ground electronic state *via.* some energy transfer process, whereas an electronically excited molecule with an unbound or repulsive excited state will rapidly traverse the potential energy surface of the excited state and proceeding along the reaction co-ordinate to form new products. Electronic transitions which excite a ground state gas phase molecule to a bound upper state are called ro-vibronic transitions, and involve a simultaneous change in electronic, vibrational and rotational energy states. Ro-vibronic transitions exhibit structure in the form of one or more sharp peaks, the intensities of which are governed by the Franck-Condon principle, whereby the probability of a transition between vibrational levels in the upper and lower state increases with an increase in the degree of overlap of the 2 wavefunctions, as shown in Figure 1.4.
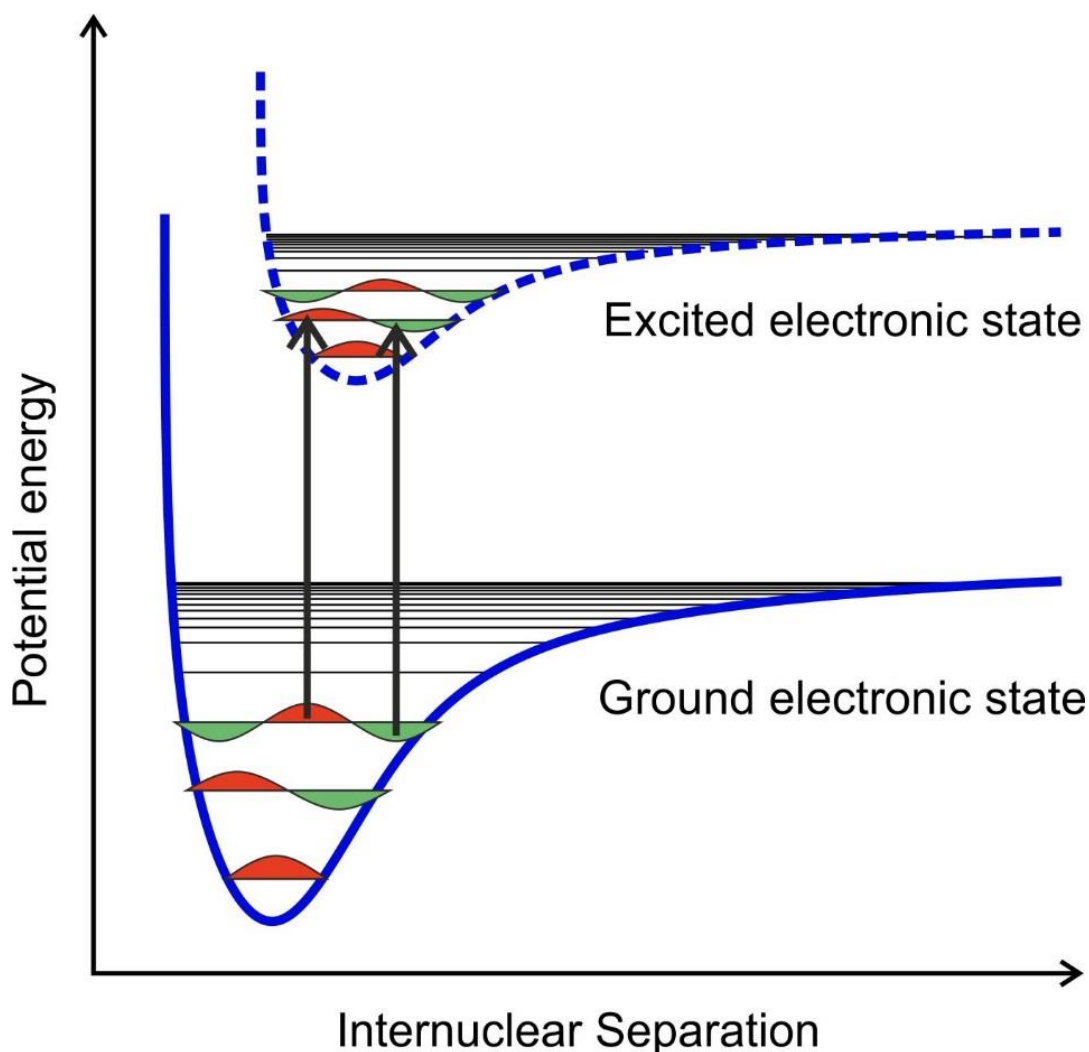
Figure 1.4: Transitions from vibrational levels in the ground state to vibrational levels in the upper state are more likely to happen when the phase of the wavefunctions overlap.

Following excitation to a bound state, the excited state can undergo a variety of different processes to relax back down to the ground state, including intramolecular vibrational relaxation to lower lying vibrational levels of the excited state, internal conversion to a lower lying singlet state, intersystem crossing to a nearby triplet excited state, fluorescence and collisional energy transfer (quenching).

In cases whereby the absorption of photons excites the ground state molecule to unbound or repulsive excited states, smooth and continuous spectra are observed. Following excitation the rapid proceeding of the system along the reaction co-ordinate leads to a change in the structure of the molecule, often resulting in dissociation to 2 or more atoms or molecules. A general schematic of this process is shown in Figure 1.5.
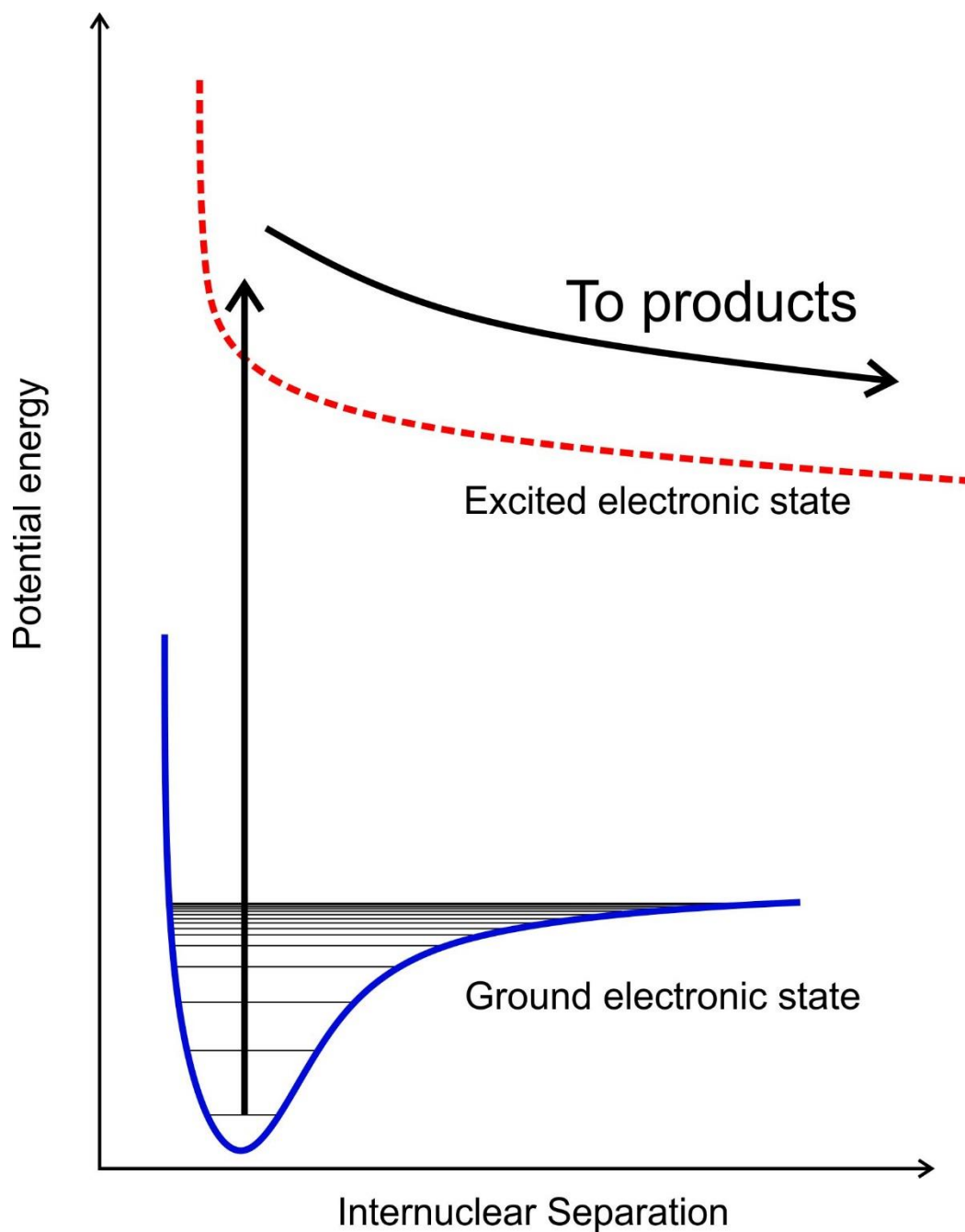
Figure 1.5: Absorption of photons from the ground electronic state to an unbound upper state results in a broad featureless absorption band. Once on the repulsive excited state potential energy surface, the reaction proceeds along the reaction co-ordinate

1.2.3 Fates of electronically excited molecules

For broad, featureless absorption bands such as those observed ubiquitously for the UV absorption band of peroxy radicals[61-69], the molecule is excited to a higher energy electronic state, with a different potential energy surface (PES). Interactions between

nuclei and molecular orbitals on repulsive excited state PES are different to those of the stable ground state PES, in that some of the bonding molecular orbitals which bound the atomic nuclei in the ground state become anti-bonding, causing the nuclei to repel and change configuration. The potential energy, or Correlation Interaction (CI) curve for the O-O bond co-ordinate in the methyl peroxy radical calculated by Jafri et al.[70] is shown in Figure 1.6. From the ground X^2A'' state, several electronically excited states are accessible, the first of which is a low-lying bound state with $1^2A'$ symmetry, followed by the $2^2A''$ and $2^2A'$ states, and the $3^2A''$ and $3^2A'$ states. The broad absorption band in the UV ($\lambda_{max} = 240$ nm) arises from the $2^2A'' \leftarrow X^2A''$ transition.
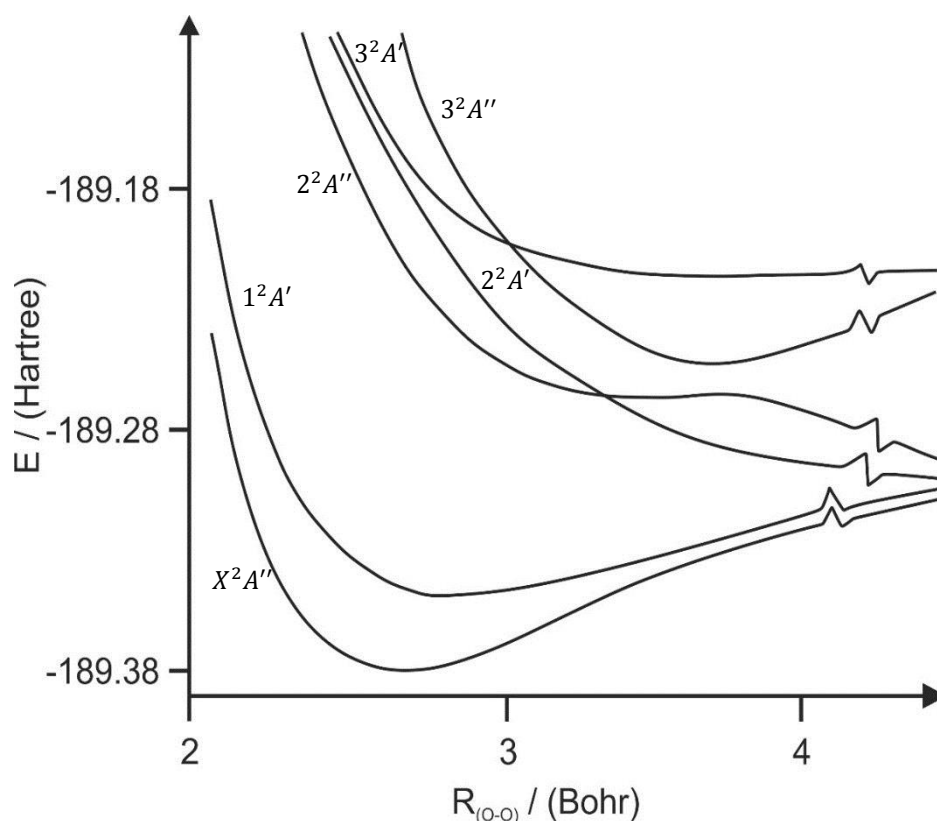
Figure 1.6: Potential energy curves for the ground state, and first three excited states of the O-O bond in the methyl peroxy radical, reproduced from Jafri et al.[70]

The points where the potential energy curves cross are known as conical intersections, whereby the Born-Oppenheimer approximation breaks down, and nuclear motion and electronic motion are coupled, facilitating the possibility of non-adiabatic processes involving the crossing of the system between 2 potential energy surfaces. The energy and correlation diagram for the possible fates of the electronically excited $\tilde{A}^2A'$ and $\tilde{B}^2A''$ ($\tilde{A}$ and $\tilde{B}$ terms are synonymous with states *1* and *2* shown in Figure 1.6) states of the methyl peroxy radical calculated by

Hartmann *et al.*[71] is shown in Figure 1.7. The transition shows the relative energy of the excited peroxy radical upon absorption of a 248 nm photon, and the potential states accessible, including $CH_3O(\tilde{X}^2E) + O(^1D)$ and $CH_3O(\tilde{X}^2E) + O(^3P)$ from adiabatic O-O bond scission.
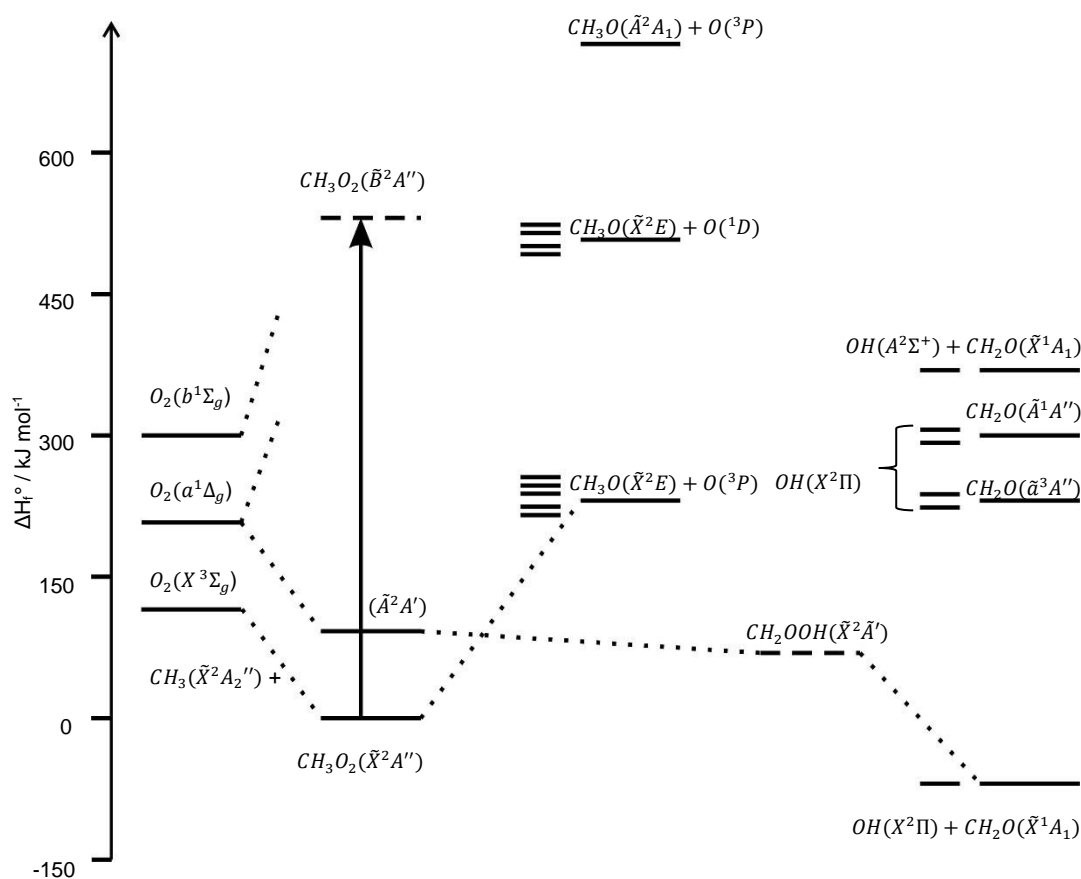
Figure 1.7: Energy and correlation diagram for the electronic excitation of the methyl peroxy radical, and the products of excited methyl peroxy radicals: Products of C-O bond cleavage are shown on the left, and products from O-O bond cleavage are shown on the right. Reproduced from Hartmann *et al.*[71] Note this diagram is duplicated multiple times throughout this work, and is referred to as a base-case for the absorption of photons by peroxy radicals.

The transition $\tilde{A}^2A' \leftarrow \tilde{X}^2A''$, between the ground and low lying first electronically excited state gives rise to a sharp peak at 7383cm^{-1} (1354.46 nm)[72]. The sharp Near IR (NIR) absorption peaks are often used as diagnostic tools for the detection of RO$_2$ species in preference to the broad $\tilde{B}^2A'' \leftarrow \tilde{X}^2A''$ absorption band, despite the fact that the NIR $\tilde{A}^2A' \leftarrow \tilde{X}^2A''$ is forbidden, and has cross sections typically 4-5 orders of magnitude smaller than the UV absorption band.[72, 73] The position of the peaks of the $\tilde{A}^2A' \leftarrow \tilde{X}^2A''$ depends on the R group attached to the peroxy moiety, allowing the resolution of multiple RO$_2$ species.[72, 73] The $\tilde{A}^2A'$ state is not dissociative with

respect to the O-O bond, however Frost *et al.*[74] suggest that at the higher vibrational levels within this state, some molecules may possess sufficient energy (barrier to intramolecular rearrangement ~20 kJ mol⁻¹)[75] to cross the $CH_2OOH(\tilde{X}^2\tilde{A}')$ transition state, rearranging to the unstable CH_2OOH intermediate, which falls apart to formaldehyde and OH. The requirement of vibrational excitation to facilitate this intramolecular rearrangement would suggest that this channel is minor (Boltzmann temperature of 20 kcal mol⁻¹ = 10^5 K) and so the most probable fate of the $CH_3O_2(\tilde{A}^2A')$ state is quenching back down to the ground electronic state. Fluorescence is not observed from the $(\tilde{A}^2A')$ state from any peroxy radical.[72] The energy and correlation diagram shown in Figure 1.7 is reproduced numerous times throughout this thesis to aid the reader, and it is assumed that analogous peroxy radicals have similarly analogous electronic states and correlations.

Another example of an electronic transition to a bound excited state is the OH $A^2\Sigma^+ \leftarrow X^2\Pi$ transition at 308 nm. The excited ($A^2\Sigma^+$,v'=0) state is bound, and has 2 possible fates: quenching or radiative emission (fluorescence). The fluorescence quantum yield, shown in E 1.3, depends on the rate of these processes; k_f is the rate of fluorescence, which for (OH($A^2\Sigma^+$) ,v'=0) is 1.43×10^6 s⁻¹ (fluorescence lifetime ~700 ns[76]) and is independent of pressure and temperature and k_Q is the rate of collisional quenching, which depends on the rate and the efficiency of collisions.

$$\phi = \frac{Photons\ emitted\ through\ fluorescence}{Total\ number\ of\ photons\ absorbed} = \frac{k_f}{k_f + k_Q} \qquad \text{E 1.3}$$

At 760 Torr of air and 298 K, the lifetime of OH($A^2\Sigma^+$) with respect to quenching is ~1 ns[76] ($k_Q = 1 \times 10^6$ s⁻¹).

1.2.4   The Tropospheric Ultraviolet and Visible (TUV) Radiation Model

The Atmospheric Chemistry Observations and Modelling (ACOM) Tropospheric Ultraviolet and Visible (TUV) Radiation Model is used to calculate the tropospheric actinic flux at a given latitude, longitude, date and time.[77] The model calculates the actinic flux at a certain point in the earth's troposphere by considering atmospheric

inputs, including vertical profiles of N_2, O_2, O_3, NO_2, SO_2, clouds, and aerosols, all of which attenuate electromagnetic radiation at certain wavelengths of light *via.* absorption, scattering, or both. The actinic flux at a point in the troposphere is the sum of the direct solar flux, the downward scattered solar flux *via.* Rayleigh and Mie scattering and the upward diffuse flux from reflection and radiation from the earth's surface, as shown in Figure 1.8.
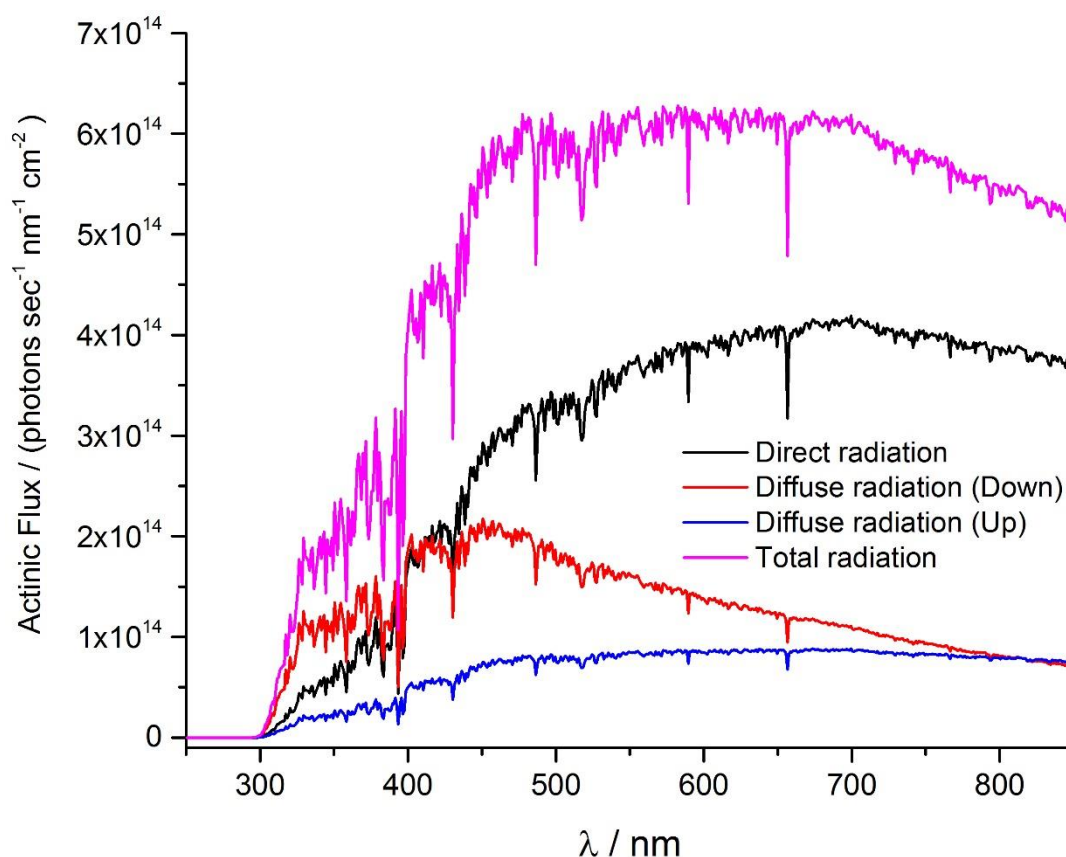
Figure 1.8: The ACOM TUV calculated actinic flux at 12 noon on the 30th of July 2015 at 0° latitude and 0° longitude. The total radiation (pink) is the sum of the direct solar radiation (black), the downward diffuse radiation (red) and the upward diffuse radiation (blue).

The sharp lines which are apparent in the solar flux calculated by TUV are a result of absorption bands of various atoms and molecules in the atmospheres of the Sun and the Earth. The numerous ($>10^3$) sharp absorption lines are called Fraunhofer lines are caused by a variety of molecules, atoms and ions, including but not limited to O_2, Fe, Mg, Na and Ca^+.[78-81] Absorptions from larger molecules such as SO_2, NO_2 and O_3 are included in the TUV model, as their spatial and temporal distributions depend on the time of day, location, and actinic flux levels, the spectra of these molecules in the actinic window are shown in Figure 1.9.
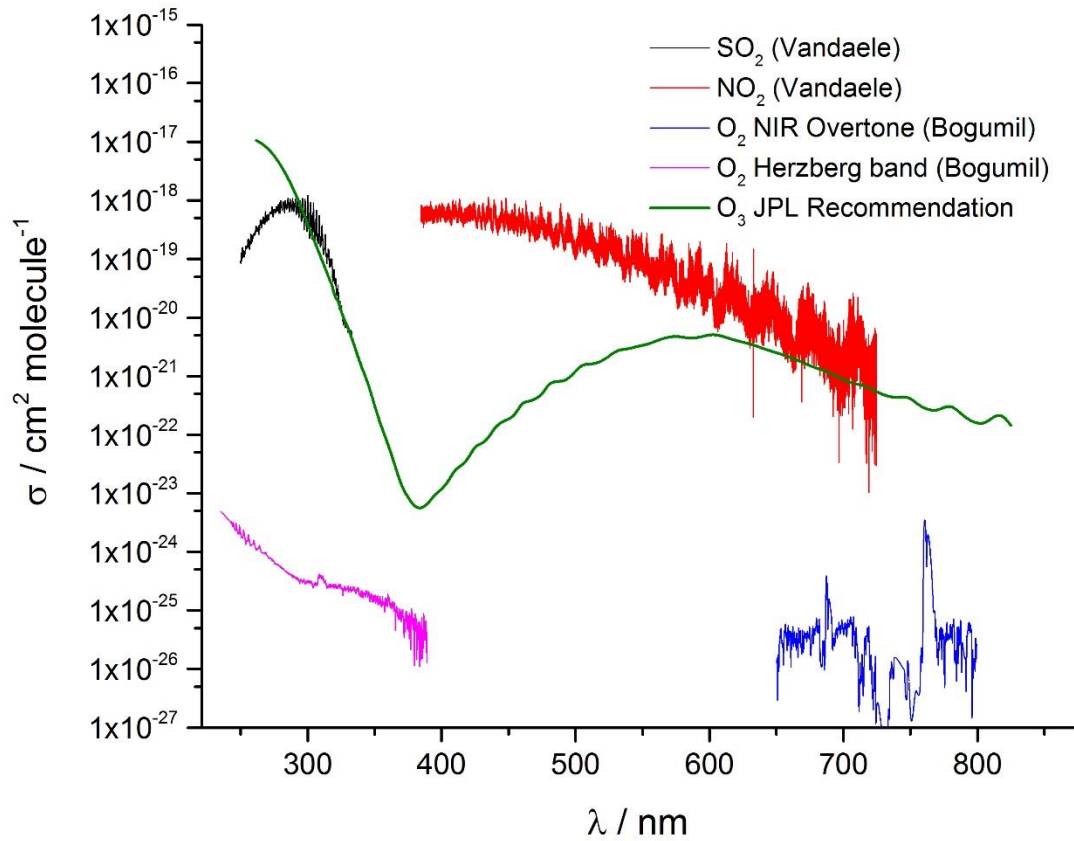
Figure 1.9: UV-Vis / NIR absorption spectra of SO₂ (Vandaele[82] – Black), NO₂ (Vandaele[83] – Red), the O₂ NIR overtone and Herzberg band (Bogumil[84] – Blue and Pink respectively)

The output from TUV is used to calculate atmospheric photolysis rates of molecules which absorb in the actinic window, particularly O_3 and NO_2, as well as trace oxidation products such as aldehydes and ketones.

Absorption of solar radiation by molecules provides the energy required to break bonds, forming radicals and initiating the oxidation of biogenic (natural) and anthropogenic (from humans) emissions in the Earth's atmosphere. In the following section the photolysis products of key photochemical reactions, and their subsequent reactions are outlined.

1.3 Atmospheric Chemistry

1.3.1 Tropospheric radical chemistry

The OH radical is the most important atmospheric oxidant and is responsible for removing many pollutants from the atmosphere. An example of this is NO_2 oxidation to HNO_3 by OH, which is the dominant NO_x sink during the day (R 1.3).

$$NO_2 + OH + M \rightarrow HNO_3 + M \qquad\qquad R\ 1.3$$

HNO_3 is then removed by wet or dry deposition.[85] The primary source of OH in the troposphere is the reaction of excited O atoms (O^1D) from ozone photolysis (R 1.4) ($\lambda < 330$ nm), with water vapour (R 1.5). R 1.5 competes with R 1.6 and R 1.7 which remove O^1D *via.* collisional quenching by O_2 and N_2 respectively.

$$O_3 + h\nu \rightarrow O_2 + O(^1D) \qquad\qquad R\ 1.4$$

$$O(^1D) + H_2O \rightarrow 2OH \qquad\qquad R\ 1.5$$

$$O(^1D) + O_2 \rightarrow O^3P + O_2 \qquad\qquad R\ 1.6$$

$$O(^1D) + N_2 \rightarrow O^3P + N_2 \qquad\qquad R\ 1.7$$

Table 1.1: Rates of the 3 main $O(^1D)$ removal processes, with branching ratios. The rate of R 1.5 depends on [H_2O], which is calculated for 70% relative humidity and 298 K here. Rate coefficients are taken from the Master Chemical Mechanism and rates are calculated at 289 K and 760 Torr.[86]

Reaction	k / cm^3 molecule^{-1} s^{-1}	Rate at 298 K, 760 Torr / s^{-1}	Branching ratio
R 1.5	2.14×10^{-11}	1.03×10^8	0.112
R 1.6	3.53×10^{-11}	2.32×10^8	0.217
R 1.7	2.42×10^{-11}	6.19×10^8	0.671

Since the OH radical is the primary oxidising species in the atmosphere, a comprehensive understanding of its reactivity is the key to understanding the chemistry of the atmosphere as a whole. Figure 1.10 is a schematic of the major HO_x (OH and HO_2) reaction cycles in the troposphere.
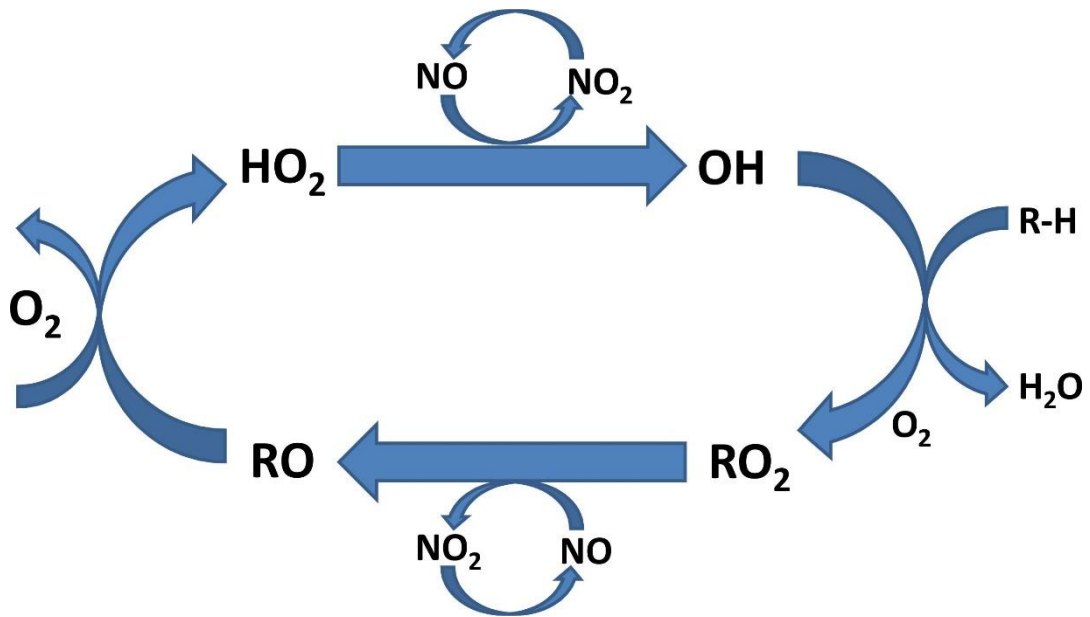
Figure 1.10: The tropospheric HOx cycle. R represents any alkyl group.

$$OH + CO \rightarrow H + CO_2 \qquad \text{R 1.8}$$

$$H + O_2 + M \rightarrow HO_2 + M \qquad \text{R 1.9}$$

Reactions R 1.8 and R 1.9 outline the formation of the hydroperoxy radical (HO_2) in the troposphere.

$$R\text{-}H + OH \rightarrow R + H_2O \qquad \text{R 1.10}$$

$$R + O_2 + M \rightarrow RO_2 + M \qquad \text{R 1.11}$$

Reactions R 1.10 and R 1.11 outline the formation of alkyl peroxy radicals (RO_2) in the troposphere, where R is an alkyl group. The most significant mechanism of OH recycling is represented as the reaction between RO_2 (or HO_2) and NO (R 1.12) producing NO_2. NO_2 can be photolysed by solar radiation to produce $O(^3P)$ (R 1.13), which combines with molecular oxygen to form ozone. This mechanism is significant at NO_x concentrations as low as $NO_x = 55$ ppt and $NO = 20$ ppt.[87]

$$HO_2 + NO \rightarrow OH + NO_2 \qquad \text{R 1.12}$$

$$NO_2 + h\nu \rightarrow NO + O(^3P) \qquad \text{R 1.13}$$

$$O(^3P) + O_2 + M \rightarrow O_3 + M \qquad \text{R 1.14}$$

This reaction scheme represents the major source of O_3 in the troposphere, and it is important to emphasise the role of NO_x (NO and NO_2), which essentially facilitates the formation of O_3. [88, 89] NO_x as previously stated, is formed primarily through industrial processes, specifically processes which involve high temperature combustion in the presence of nitrogen, of which there are four types:

1: Thermal NOx refers to NOx formed through high temperature oxidation of the diatomic nitrogen found in combustion air. Reaction R 1.15 is endothermic, and leads to enhanced NO production at high temperatures.

$$N_2 + O \rightarrow NO + N \qquad \text{R 1.15}$$

$$N + O_2 \rightarrow NO + O \qquad \text{R 1.16}$$

$$N + OH \rightarrow NO + H \qquad \text{R 1.17}$$

2: Fuel NO$_x$ refers to NO_x formed from the liberation of nitrogen from within fuels such as coal and oil, forming radicals which ultimately end up as either NO_x or N_2.

3: Prompt NO$_x$ formation happens *via.* different processes to both thermal and fuel NO_x. Prompt NO_x formation occurs when radical fragments from fuel, e.g. C, CH and CH_2 react with N_2 in air.

4: N$_2$O conversion to NO$_x$ can occur at high pressures and temperatures, R 1.19 leads to the net formation of NO_x, in competition with R 1.20.

$$N_2 + O + M \rightarrow N_2O + M \qquad \text{R 1.18}$$

$$N_2O + O \rightarrow 2\ NO\ (E_{act}\ 97\ kJ\ mol^{-1}) \qquad \text{R 1.19}$$

$$N_2O + O \rightarrow N_2 + O_2 \qquad \text{R 1.20}$$

Areas which burn large amounts of hydrocarbons (e.g. industrial and urban centres) are often subject to high NO_x concentrations (> 10 ppb).[87] Ozone concentrations depend on both NOx and VOC concentrations; a condition best illustrated by 3D contour plots (ozone isopleths), such as the examples in Figure 1.11.
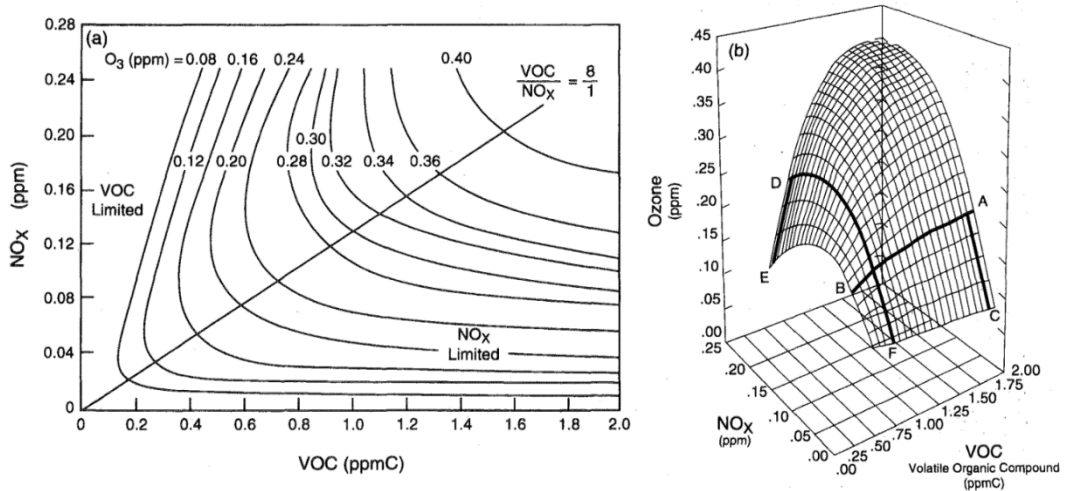
Figure 1.11: . Typical peak ozone isopleths generated from initial mixtures of VOC and NO, in air. (a) Two dimensional depiction generated from the Empirical Kinetic Modeling Approach (EKMA) model (b) three dimensional depiction. The VOC-limited region (e.g., at point D) is found in some highly polluted urban centres while the NO, limited region (e.g., at point A) is typical of downwind suburban and rural areas. Taken from "Atmospheric Chemistry of Tropospheric Ozone Formation: Scientific and Regulatory Implications" by Finlayson-Pitts *et al*.[90]

NO_2 concentrations depend on the rate of conversion of NO to NO_2 by reaction with O_3 or RO_2, highlighting the importance of the peroxy radical in the production of tropospheric ozone. Typically NO_x levels are high in densely populated areas due to processes which involve combustion in air, for example in combustion engine in a car or a HGV. Areas with high populations are particularly important in terms of air quality, as the negative health effects of a specific amount of an emitted pollutant affect a greater number of people in total. NO_x emissions are not the only harmful by-product of high temperature combustion; polycyclic aromatic hydrocarbons (PAHs) are formed during incomplete combustion of fossil fuels[91], biomass[92] and cigarette smoke[93] amongst other things. Certain PAHs have been shown to be highly carcinogenic[94, 95] and are linked to chronic mortality in those subject to high levels of exposure[96] and are thought to contribute to 40,000 to the mortality burden in the UK annually.[97] Whilst NO_x and PAH emissions primarily affect local air quality, transport of these pollutants can be important when considering air quality of surrounding areas. Reaction of the peroxyacetyl radical with NO_2 results in the reversible formation of PeroxyAcetyl Nitrate (PAN), a relatively long-lived species which acts as a reservoir for NO_x and can be transported many miles, and cause an increase in tropospheric ozone in areas which would otherwise be unperturbed.[98]

Understanding these pollutants in terms of their sources, sinks and transport is important for attempting to minimise their effects on the environment.

1.3.2 Atmospheric modelling

Atmospheric modelling involves using complex reaction systems in which chemical mechanisms detailing gas-phase chemical processes are utilised to outline the tropospheric degradation of emitted (biogenic, anthropogenic and natural) compounds. There are 4 main types of atmospheric model:

0-D (Box) models such as the Empirical Kinetic Modeling Approach (EKMA) represent the atmospheric domain as one box, where concentrations of species within the box are uniform, and are a function of time only. Sources of species include emissions and transport into the box. Advection is the transport of a species by the mean horizontal motion of an air packet and entrainment is the vertical movement of air parcels due to turbulent mixing. Species are removed from the box by transport (advection and detrainment), chemical transformations or other removal processes such as uptake by aerosols or wet/dry deposition.

1-D models assume that species concentrations are functions of altitude and time, analogous to a set of box models stacked to form a column or row of boxes (vertical or horizontal) and can be used to model such things as the effect of clouds on radiative transfer[99, 100] and were historically used to model vertical profiles of trace species such as CH_4 and NO_2[101].

2-D models assume that species concentrations are uniform in one dimension and depend on the other two dimensions and time, to model, for example the effect of variations in atmospheric UV flux over time on the middle atmosphere.[102]

3-D or Global models depend on all 3 dimensions as well as time. The chemistry within global models is often greatly simplified due to the computational demands of modelling such a large and complex domain. 3-D models have many applications, for example to assess the impact of the emissions of trace gases (e.g. NO_x) on greenhouse gas concentrations in the troposphere, and the resulting effect on radiative forcing.[103]

The Master Chemical Mechanism (MCM), is a complex reaction model first developed at the University of Leeds by Pilling *et al.* in 1996[104] and was originally developed to provide comprehensive analyses of the degradation of specific organic

compounds and their effect on boundary layer ozone formation to aid air quality policy in Europe. Since then, the MCM has shown its efficacy for calculating how radical and closed-shell intermediates formed during VOC degradation are distributed within the atmosphere. The MCM V3.2 is the most recent version, and draws upon an extensive bank of reaction schemes to describe the degradation processes of 143 primary emitted VOCs, with ~5600 degradation products which undergo ~13500 reactions. Reaction rates used within the MCM are either measured directly, or are defined based on rates of reaction between similar chemical species using structure reactivity correlations.[86]
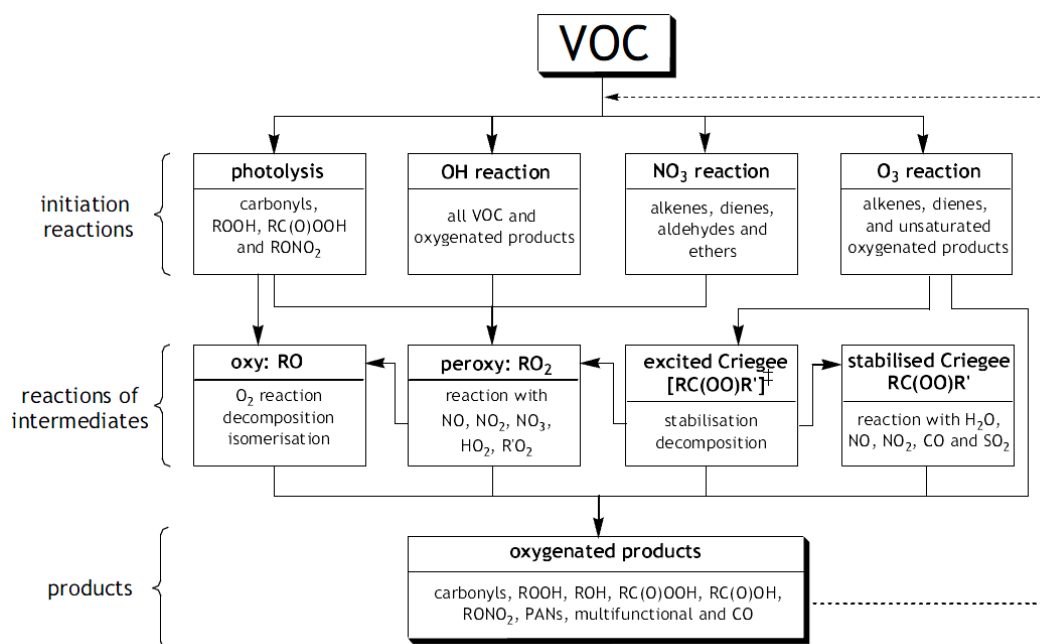
Figure 1.12: A flow chart outlining the 3 major classes and the key reactions of atmospheric species as described in the MCM. Taken from "Protocol for the development of the Master Chemical Mechanism, MCM v3 (Part A): tropospheric degradation of non-aromatic volatile organic compounds" by Pilling *et al*.[86]

Reactions within atmospheric models are represented as a sequence of elementary reactions, each of which may have more than one product. The relative rate of formation of a specific product of a reaction determines the branching ratio, and the absolute rates of formation (in the case of intermediate species) or emission (in the case of primary species) and removal of a species determines the amount of the species in the atmosphere. Formation of reactive species occurs in one of two main ways: solar induced photolysis as deiscussed in 1.2.3; or chemical processes involving the reaction of a molecule with a reactive radical as shown in Figure 1.12. Key removal processes include further chemical transformation of a species and

deposition to a surface, be that uptake by solid or liquid aerosol, to the ocean surface or to solid surfaces on land.[105]

1.3.3 **Atmospheric Field Measurements**

Atmospheric models alone cannot infer the level of understanding of the chemistry governing the composition of the atmosphere; a method of verification is required to test whether the model is accurately calculating concentrations of trace gases within the atmosphere. Comparison between field measurements and atmospheric models is a key method for verifying that the chemical and physical processes are well understood. The OH radical is the most important species when considering the oxidising capacity of the atmosphere, as it reacts with almost all known trace gases, both organic and inorganic, and as a result is a good target species to model. For an atmospheric trace gas X, the lifetime of X is given by E 1.4

$$\tau_X = \frac{1}{k'} = \frac{1}{k[OH]}$$ E 1.4

For removal of trace gas X by OH, a key atmospheric process, the lifetime of X (τ_X) is dependent on the reciprocal of k, the second order rate coefficient of the X + OH reaction, and the OH concentration. It is therefore vital to our understanding of trace gas distributions to quantify both of these terms. The lifetime of OH in the atmosphere is usually around or below 1s and is a good target for indicating the accuracy of models, as OH concentrations are dictated almost entirely by chemical, rather than transport processes. Many species have much longer lifetimes in the atmosphere, for example isoprene (~ 1 hour)[106] and methane (~ 8 years)[107]. Since [OH] defines the oxidative capacity of the atmosphere, the OH lifetime in a region of the atmosphere is indicative of the level of reactive trace species; the greater the concentration of OH sinks (e.g. reaction with VOCs), the shorter the OH lifetime. The total rate of removal of OH is expressed as the summation of the rates of all removal processes (sinks) combined into a single rate coefficient – k_r as defined by E 1.5.

$$k_r = \frac{1}{\tau_{OH}}$$ E 1.5

As mentioned previously [OH] defines the oxidative capacity of the atmosphere in the day time, and therefore the lifetime of trace species such as methane, CO and isoprene, hence it is very important that [OH] is measured accurately in a wide range of environments globally. Three methods for measuring atmospheric [OH] have been

utilised in the field, namely laser induced fluorescence (LIF) including more specifically the Fluorescence Assay by Gas Expansion (FAGE) technique[108, 109]; selected ion-Chemical Ionisation Mass Spectrometry (CIMS)[76] and Differential Optical Absorption Spectroscopy (DOAS)[110]. Note that the DOAS technique is no longer used in the field to measure OH due to the small absorption cross-section of the OH radical, and resulting lack of sensitivity of the method. The method most relevant to this study is the LIF – FAGE technique as it is used most extensively in the field.

1.3.4 Laser Induced Fluorescence spectroscopy

Laser Induced Fluorescence spectroscopy is a method which employs a laser pulse to excite a specific electronic transition of a species to an excited state, which subsequently relaxes back down to the molecule's ground state, *via.* emission of a photon, as discussed in 1.2.3. The intensity of the emission is an indicator of the concentration of the fluorescing molecule at any given time, assuming constant pressure and bath gas constitution. LIF is a technique which shows high sensitivity and selectivity, due to the absence of a background or zero reading, and is useful for measuring low concentrations of small molecules which fluoresce, for example the OH radical. The number of molecules which fluoresce is dependent on the number of excitation events (1.2.2), and the fluorescence quantum yield (1.2.3E 1.3). Lasers emit high numbers of photons with a very narrow range of wavlengths, and are useful for generating high concentrations of excited OH* (E 1.6)

$$OH + h\nu \rightarrow OH*$$
$$\text{E 1.6}$$

$$OH* \rightarrow OH + h\nu$$
$$\text{E 1.7}$$

$$OH* + M \rightarrow OH + M$$
$$\text{E 1.8}$$

Fluorescence (E 1.7) and quenching (E 1.8) are competitive processes, and so to increase the fluorescence quantum yield, the pressure and therefore rate of of collisional quenching must be reduced.

1.3.5 Fluorescence Assay by Gas Expansion – FAGE

The Fluorescence Assay by Gas Expansion (FAGE) technique was established by Hard *et al.* in 1979[111], and in more recent years developed by various groups, including FAGE groups at the University of Leeds[9, 18, 108-110], Penn State[6, 7, 12, 13, 25, 27, 112-114] and Jülich[21, 22, 115] amongst others. FAGE employs the expansion of tropospheric air into a fluorescence cell at low pressure. The low pressure FAGE cell increases the OH fluorescence lifetime so that the on-resonance fluorescence initiated by a probe laser at 308 nm can be separated from the light of the same wavelength which reaches the detector as a result of scattering effects (e.g. light reflected by surfaces within the cell). FAGE can be used to determine OH radical concentrations in ambient air down to concentrations in the order of ~10^5 molecule cm^{-3}, which is well below OH concentrations seen in the majority of tropospheric environments.[109]

1.4 Atmospheric radical chemistry in remote forested locations

The following section contains a brief review of atmospheric radical chemistry in remote forested locations, outlining results of some of the previous field measurements and the unexpected results obtained, as well as proposed explanations for the observed results.

1.4.1 Isoprene

Isoprene (IUPAC - 2-methyl-1,3-butadiene) is an unsaturated VOC, and is emitted into the atmosphere by plants in large quantities (500 - 750 Tg yr^{-1}).[116] Isoprene is emitted by two main plant functional types: broad leaf (evergreen and deciduous) trees and shrubs, which account for 51% and 46% of total emissions respectively. As with all emitted VOCs, their degradation and subsequent removal from the atmosphere is initiated by reaction with radical species or ozone/alkene chemistry, which during the day is dominated by OH. As mentioned previously, it is important that the chemistry of these atmospheric trace species is well understood, to ensure that the chemistry which governs models is as accurate as possible.

Discrepancies between concentrations of species in models and field measurements indicate that the current understanding of the specific chemical and physical processes involved is either incorrect or incomplete.[117-119] An example which supports this statement is the case of [OH] prediction as a result of isoprene oxidation in low NO_x environments.[115, 118-120] The first measurements of OH in an environment with low NO_x and high biogenic VOC concentrations was carried out in 1991 at Fritz peak in Colorado, which employed the use of two methods to measure [OH] : Chemical ionisation mass spectrometry (CIMS) and Long-Path Differential Optical Absorption Spectrometry (LP-DOAS).[121] Using the reaction schemes known at the time, which only contained reaction schemes for the net increase of OH from ozone photolysis followed by the reaction of $O(^1D)$ with water vapour, and net loss of OH by reaction with CO and methane, models predicted [OH] to be a factor of ~4 greater than those observed in the study, a result which highlighted the need for further investigation. The discrepancy between the modelled and measured OH concentration prompted two suggestions to explain this observation: firstly that [OH] was being measured incorrectly, and that the true [OH] was greater (in line with [OH] as predicted by models) or alternatively the suggestion that some other process was taking place; one which involved a radical scavenger which readily reacts with and removes OH. It is important to note that the two measurement techniques employed in this study were carried out separately, and were intrinsically different: LP-DOAS measurements were carried out by Mount *et al.* of the Aeronomy Laboratory and CIMS measurements were carried out by Eisele *et al.* of Georgia Tech. Intercomparison between these two methods yielded the result that the measured OH concentrations were said to be in relatively good agreement, and the majority of disagreements were said to be explained by known interferences with the techniques (for example rain along the path of the LP-DOAS instrument). The intercomparison of the two techniques leads the authors to suggest that the possibility of additional, not yet realised OH removal processes may be a more probable explanation for the discrepancy than erroneously low OH measurements. Attempts were made to reconcile the models with the observed OH concentration by including the presence of 2 ppb of isoprene in the model, which showed great improvement in the agreement with the model; however this purely speculative modification to the model was unsupported by evidence, due to the lack of measurements of biogenic VOCs. Between July-August 1997 the AEROsols formation from BIogenic organic Carbon

(AEROBIC) campaign measured OH and HO_2 radical concentrations using ground based FAGE in a low NO_x, biogenically influenced region of north-western Greece, and was the first of its kind to measure OH in a clean, biogenic emission driven atmosphere in which the first order removal rate of OH by reaction with biogenic VOCs alone is ~10 s^{-1}.[9] An important objective of the AEROBIC campaign was to improve the representation of the oxidation mechanisms of biogenic VOCs in the MCM, containing detailed mechanisms for the degradation of isoprene and α-pinene, another biogenic VOC emitted in large quantities by trees. In contrast to the Fritz Peak study, OH concentrations were found to be elevated well above the levels predicted by the MCM (Figure 1.13, Table 1.2), with the agreement between the modelled and measured OH concentration worsening as NO_x concentrations decrease (Table 1.2).
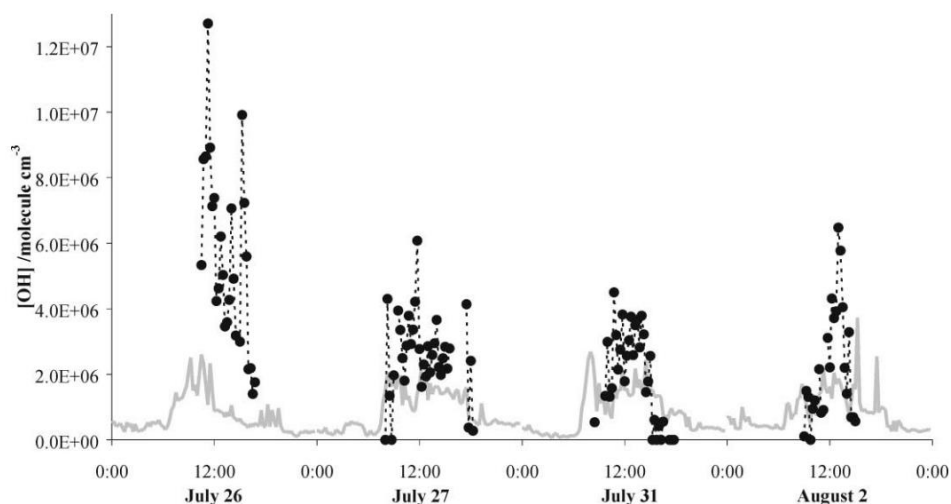
Figure 1.13: Black circles represent [OH] measurements by FAGE in the AEROBIC campaign on the 26, 27, 31 July and 2 August 1997 at a remote forested location in north-western Greece. Solid grey line represents [OH] as predicted by the MCM. [OH] measurements are averaged over 15 minutes and 2σ for the measurements and models are 70% and 30% respectively.

Table 1.2: Average concentrations of measured and modelled OH and HO_2 between 11:00 and 15:00 h on each day. Also shown are measured (meas) and modelled (mod) [HO₂]/[OH] ratios and the NO and NO₂ concentrations. Taken from Heard *et al.*[9].

Dates	[OH]/10⁶ (molecules cm⁻³)		[HO₂]/10⁸ (molecules cm⁻³)		[HO₂]/[OH]		[NO]/ppt	[NO₂]/ppt
	Mod	Meas	Mod	Meas	Mod	Meas		
26-Jul	1	6.4	3.6	6.1	396	109	61	3064
27-Jul	1.5	3	4.4	3.4	295	134	94	1118
31-Jul	1.7	2.8	5.7	0.4	361	17	93	132
02-Aug	1.5	3.1	4.7	0.89	317	45	97	1364

Such observations were again reported during the Program for Research on Oxidants: Photochemistry, Emissions and Transport (PROPHET) campaign carried out in a deciduous forest in North Michigan, where OH levels were again under predicted by as much as a factor of 6 as shown in Figure 1.14 (for [NO] <100 pptv).[114] Attempts to reconcile the models with the field measurements by increasing the levels of NO which reduced the discrepancy, but created additional problems associated with reactions of NO which based on known chemistry would result in O_3 generation.
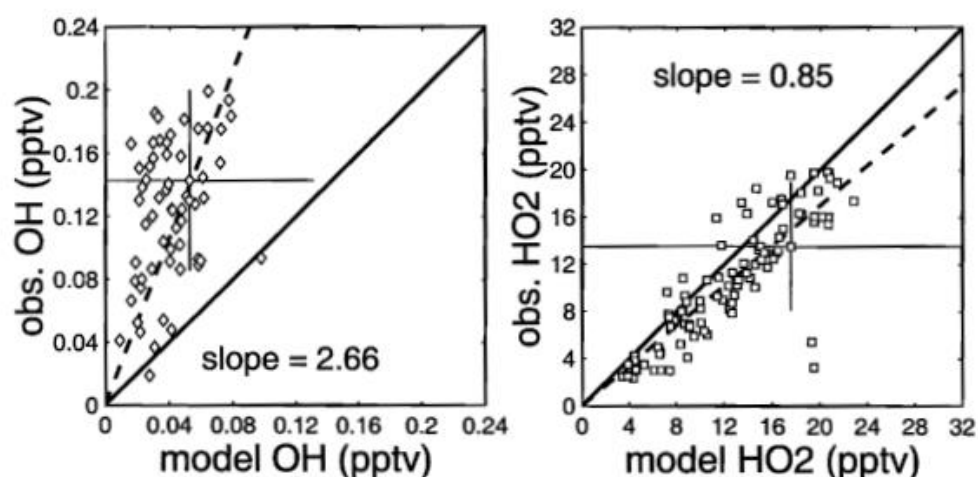
Figure 1.14: Relationship between modelled and measured [OH] from the PROPHET campaign (median [NO] = 68.5 pptv).[114]

The agreement between the AEROBIC and PROPHET campaigns regarding the underprediction of OH radical concentrations in low NO_x, high isoprene atmosphere was substantiated by aircraft measurements made on the INtercontinental Chemical Transport EXperiment-A (INTEX-A)[13] and Guyanas Atmosphere-Biosphere exchange and Radicals Intensive Experiment with the Learjet (GABRIEL)[122], which both found that the ratio of [OH]measured to [OH]modelled increases with increasing isoprene concentration, reaching a factor of 5 increase at isoprene mixing ratio of 1 ppb. The results of these studies serve to provide evidence that the missing source of OH is directly linked to the degradation of isoprene in low NO_x environments.

The OP3 campaign conducted by a number of groups (including the University of Leeds) in Borneo had a number of objectives, of which the most relevant to this literature review are the investigations into emission rates from plants, which in this region is dominated by isoprene (Borneo isoprene emissions account for 2% of the global annual budget)[123]; the oxidative processing of these emissions in the

atmosphere, dominated by OH, and the effects of these observations on the global atmospheric chemistry and climate.
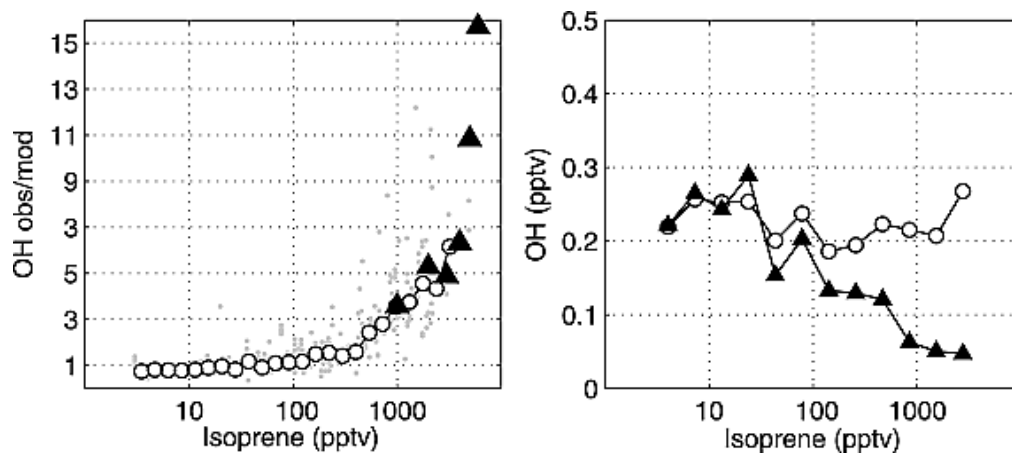
Figure 1.15: [OH]obs/[OH]mod versus isoprene concentration and [OH] versus isoprene concentration from the INTEX-A[13] (circles) and PROPHET[114] campaigns (Triangles). Taken from Ren *et al*. [13]

The campaign sought to address these questions by closely coupling aircraft and ground based measurements of primary emissions and their oxidation products, with modelling studies.[123] The maximum observed OH reactivity was 83.6 ± 26.0 s^{-1} with the diurnally averaged noontime maximum being 29.1 ± 8.5 s^{-1}; significantly higher than the OH reactivity calculated using the observed OH sink concentrations from the campaign which peaks at approximately 18 s^{-1}.[124] Isoprene is the dominant sink in the calculated OH reactivity at noon, accounting for 37% of OH loss and displaying a diurnal profile which follows that of OH reactivity. The discrepancy between observed and calculated OH reactivity highlights a missing sink of OH in this region, and would require an additional source of OH reactivity, which would require a carbon input equivalent to a 50% increase in isoprene concentration.[124] OH concentrations were measured in the field during OP3 using FAGE, with mean peak concentrations of $\sim 2.5 \times 10^6$ molecule cm^{-3}. At noon, when both OH and OH reactivity is at a diurnal maximum, an OH production rate tenfold greater than the total rate from known OH sources is required to maintain these concentrations.

 OH concentrations were significantly under-predicted throughout the campaign by a zero-dimensional box model using known chemistry. Attempts to reconcile measured and modelled [OH] were made by making adjustments to the chemical processes which determine [OH] calculated by the model. The 5 different scenarios

are outlined in Table 1.3, and are displayed graphically in Figure 1.16 and Figure 1.17, ([OH] and [HO$_2$] respectively).

Table 1.3: Description of the 5 different scenarios for OH production, as well as the effect of these processes on the 24 hour mean [OH]$_{calculated}$/[OH]$_{measured}$ for each scenario. f is the fraction of O(^{1}D) which reacts with H$_2$O to form OH, rather than being quenched to O(^{3}P). Taken from Whalley *et al*.[29].

Scenario	$\Sigma_{OH_{sources}}$		Symbol (Fig. 2)	$\frac{[OH]_{calc.}}{[OH]_{meas}}$
(1)	$2j(O^1D)[O_3][H_2O]f$		—	0.05
(2)	$(1)+k_{NO+HO_2}[HO_2][NO]+k_{O_3+HO_2}[O_3][HO_2]+0.26k_{O_3+C_5H_8}[O_3][C_5H_8]+$ $2j(H_2O_2)[H_2O_2]+j(CH_3OOH)[ROOH]$		—	0.15
(3)	$(2)+k_{C_5H_8+OH}[C_5H_8][OH]$		—	0.37
(4)	$(2)+2.7\times k_{C_5H_8+OH}[C_5H_8][OH]$		—	1.0*
(5)	$(2)+k_{X+HO_2}[X][HO_2]$ ([X] = 0.74 ppbv)		—	1.0

* [OH]$_{calc.}$:[OH]$_{meas.}$ = 1 during afternoon and evening hours only (noon–midnight).
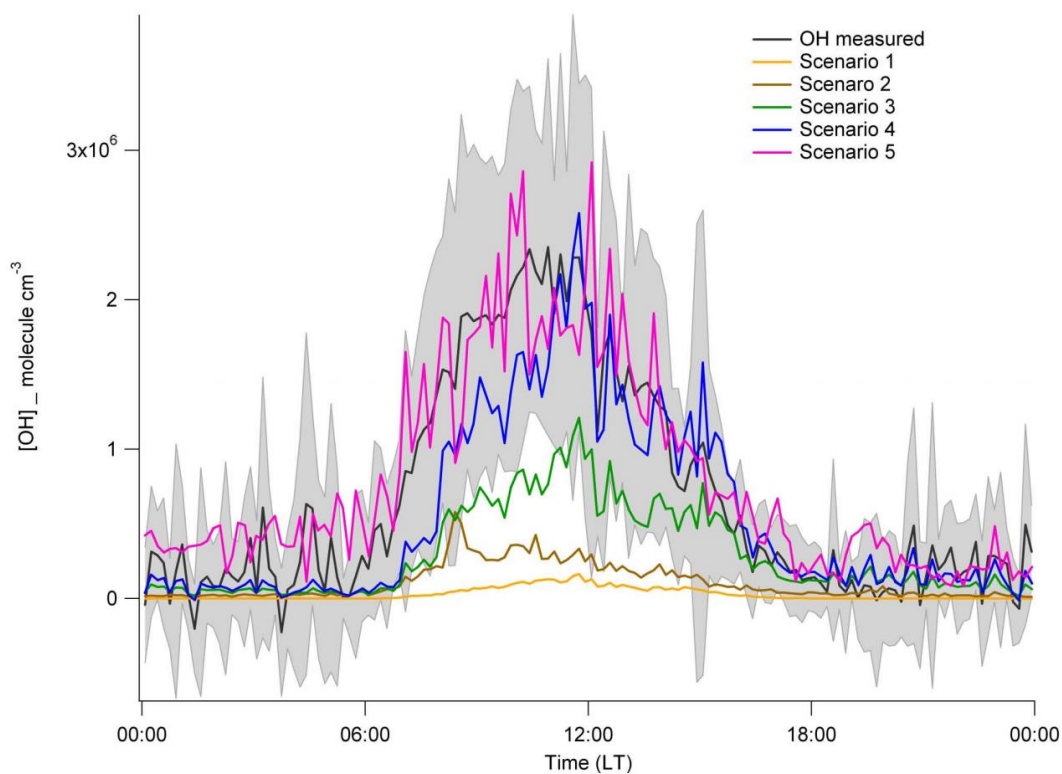
Figure 1.16: A comparison of the measured mean diurnal [OH]$_{measured}$ (black line, grey shading = 1σ standard deviation) with [OH]$_{calculated}$ for the 5 different modelling scenarios. See Table 1.3 for details on the model scenarios.
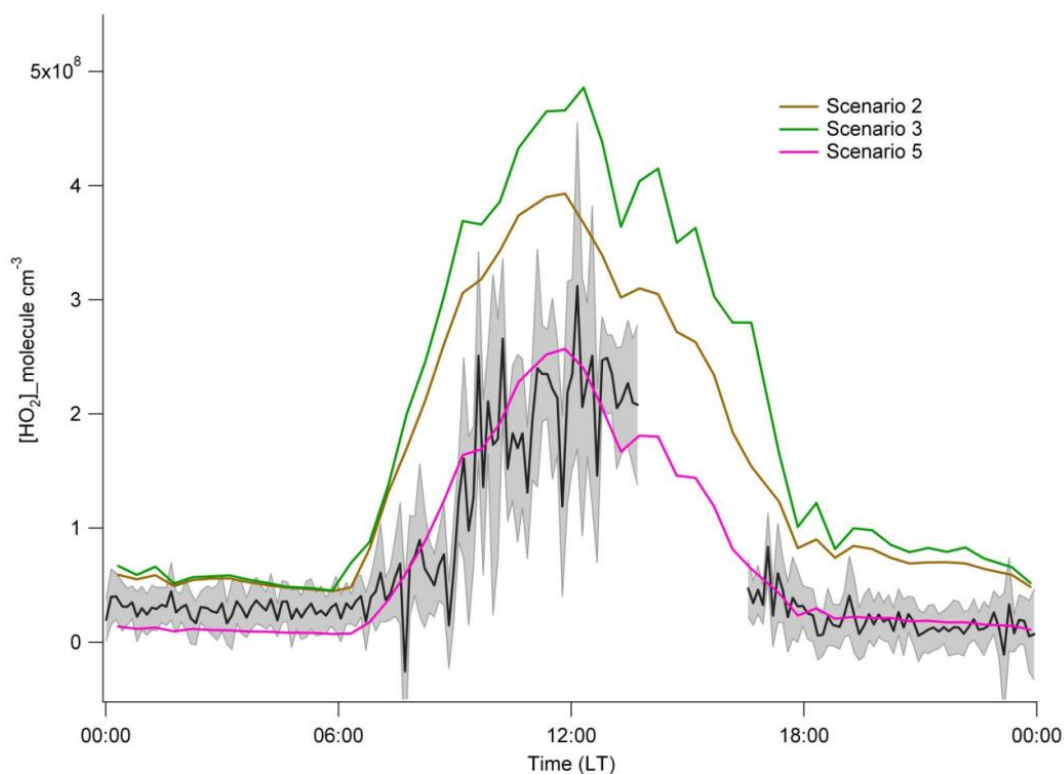
Figure 1.17: A comparison of the measured mean diurnal [HO$_2$]$_{measured}$ (black line, grey shading = 1σ standard deviation) with [HO$_2$]$_{calculated}$ for scenarios 2, 3 and 5. See Table 1.3 for details on the model scenarios.

Whalley *et al.* conclude that additional OH sources are required to reconcile the modelled and measured [OH] in this remote, low NO$_x$ environment. Furthermore, based on known chemistry, an increase in isoprene alone is insufficient to adequately reconcile models, as this would worsen the HO$_2$ measurement/model agreement, so any OH production process must also include a HO$_2$ sink.

When considering the effect of biogenic emissions on a larger scale, Global models are subject to a conflicting argument concerning the amounts of BVOCs emitted, and the concentration of [OH]: Isoprene emissions in models have been reduced by half or more relative to predicted emission rates[116], so that the depletion of [OH] and isoprene resulting from the reaction between the two species falls more in-line with the observed concentrations of both these species. Various hypotheses have been suggested to try and explain the discrepancy between measured and modelled OH. In the following section, a brief review of the suggested explanations is accompanied by reasons why each hypothesis may or may not serve to explain the observed discrepancies in OH measurement.

Table 1.4: Previous field campaigns measuring OH concentrations in clean or semi-polluted, biogenically influenced environments, reproduced with permission from "New Insights into the Tropospheric Oxidation of Isoprene: Combining Field Measurements, Laboratory Studies, Chemical Modelling and Quantum Theory"[2]

Campaign	Year	Dates	Location	Platform	Technique	OH measured	HO₂ measured	Comments	References
Fritz Peak	1991	Summer	Fritz Peak Observatory, Colorado	Ground	CIMS, LP-DOAS, FAGE (for HO2)	0.1 – 0.2 pptv range	-	Model OH over-prediction unless >2 ppbv isoprene included. (NO generally below 100 pptv)	4, 5
TOHPE	1993	Aug - Oct	Fritz Peak Observatory, Colorado	Ground	CIMS	2×10^6 (mean)	$\sim 1.2 \times 10^8$ (case studies)	Model over predicts OH by 50% and HO₂ up to a factor of 4 under low NOₓ (50 pptv) conditions	6-8
AEROBIC	1997	July-August	Indigenous forest, North West Greece	Ground	FAGE	$4\text{-}12 \times 10^6$ (noon)	$0.4 - 9 \times 10^8$ (noon)	Model under prediction of OH by ~50%. Modelled HO₂ was typically higher than obs. But obs. showed high variability	9, 10
PROPHET-98	1998	Summer	Deciduous forest, North Michigan	Ground	FAGE	0.1 – 0.2 pptv (noon)	10 -25 pptv (noon)	OH obs ~ 2.7 times greater than modelled; HO₂ obs and mod in good agreement	11, 12
PROPHET-2000	2000	Summer	Deciduous forest, North Michigan	Ground	FAGE	HOₓ similar to that measured during PROPHET-1	HOₓ similar to that measured during PROPHET-1	HOₓ similar to that measured during PROPHET1 OH reactivity measured	25
PMTACS-NY	2002	Summer	Whiteface mountain, New York	Ground	FAGE	2.6×10^6 (noon)	20 pptv (noon)	Semi-polluted – reasonable agreement between model and measurements – only low isoprene concentrations	26

				Ground flux measurements					
ECHO	2003	July	Julich, Germany		FAGE eddy covariance	Not reported	Not reported	Downward OH fluxes and upward HO$_2$	
INTEX-A	2004			aircraft	FAGE	$\sim$0.25 pptv (median near surface)	$\sim$ 30 pptv (median near surface)	Obs. To mod. Up to 5 at high isoprene ($>$2 ppb). Good mod. Obs. Agreement for HO$_2$ near surface	13
HOxComp	2005	July	Julich, Germany	Ground	FAGE, CIMS	$5\text{-}15 \times 10^6$ (noon)	$\sim 2\text{-}10 \times 10^8$ (noon)	Good agreement between mod and obs OH under high isoprene low NO$_x$ (fresh isoprene emissions)	15
GABRIEL	2005	October	Suriname	Aircraft	FAGE	0.25 pptv (mean over forest)	$\sim 50 - 55$ pptv (mean over forest)	Obs:mod = 12.2 for OH and 4.1 for HO$_2$	16-19
PRIDE-PRD	2006	July	Rural, Southern China	Ground	FAGE	$\sim 1.5 \times 10^7$ (noon)	$\sim 1.5 \times 10^8$ (noon)	Observed OH $\sim$ factor of 3 -5 times greater than mod. At NO levels $<$ 1 ppb	20-22
AMMA	2006	July-August	Niamey, Niger, Africa	Aircraft	FAGE	Potentially unstable measurements		Mid-level NO$_x$, isoprene influenced	23, 24
BEARPEX-2007	2007	August - October	Blodgett forest, California	Ground	FAGE	$\sim 7 \times 10^6$ (noon)	$\sim 28 \times 10^8$ (noon)	Model underpredicts OH by a factor of 6 and HO$_2$ by 25% at noon	27
OP3	2008	April & July	Sabah, Borneo	Ground & Aircraft	FAGE	2.5 $\times 10^6$ (noon)	$\sim 2 \times 10^8$ (noon)	Factor of 10 under prediction in OH when model constrained to OH reactivity. HO$_2$ overpredicted at ground level	28-31
BEARPEX-2009	2009	June - July	Blodgett forest, California	Ground	FAGE	4×10^6 (noon) (wave)1.5×10^6 (chem)(noon)	~ 22 pptv (noon)	Reasonable agreement between modelled OH and OH measured using chemical removal to determine OH background. HO$_2$ overpredicted by $\sim$ 30	32

1.4.2 HO$_2$ + RO$_2$ → OH reactions

As a result of the Southern Oxidant Study (SOS), it was suggested that errors in the modelled OH concentrations could be the result of a misrepresentation of the formation *via.* the RO$_2$ + HO$_2$ reaction and subsequent reaction of the organic peroxides formed. Evidence to support this hypothesis includes the observed dependence on NO concentration: In environments with significant NO concentrations, reactions between NO and HO$_2$ and RO$_2$ dominate and limit peroxide formation. The absence of processes which limit the production of organic peroxides would result in greater amounts of these species being produced, so any misrepresentation of their chemistry would result in an amplified miscalculation of model predictions in a high VOC low NO environment. It was proposed that OH regeneration from the RO$_2$ + HO$_2$ reaction, where RO$_2$ is the peroxy radical formed from isoprene oxidation (ISOPO$_2$), could provide the missing source of OH required to reconcile observed and modelled OH concentrations. Evidence contrary to this theory consists of laboratory measurements which suggest that the branching ratio of this reaction is much slower than would be required to achieve such reconciliation, as OH yields from RO$_2$ + HO$_2$ reactions have only been seen to be significant for acyl, α-alkoxy, α-carbonyl and α-hydroxy functionalised organic peroxy radicals, whereas isoprene derived peroxy radicals are thought to have much lower yields of OH upon reaction with HO$_2$ (6%) by structure-reactivity correlations with similar molecules.[2]

1.4.3 Incomplete mixing (Air mass segregation)

Thus far, only chemical processes have been proposed to explain the observed elevated [OH] versus models as seen in high isoprene atmospheres, however the rates of these chemical processes assume that the system is fully mixed. Boundary layer dynamic effects were incorporated into modelling studies by Butler *et al.*[122]. and Pugh *et al.*[28] where it was found that a reduction in the rate of the reaction between OH and isoprene by 50% as a result of mass segregation of packets of air containing elevated concentrations of each species (as opposed to complete mixing), could somewhat improve agreement between models and field measurements. As a result of these findings, as well as a study by Orlando *et al.*[125] which investigated the effects

of boundary layer dynamics on the reactivity of OH and isoprene, it was concluded that the OH/isoprene model discrepancy could in equal parts due to physical dynamic processes as chemical mechanistic effects. These findings are in contrast to those of other groups[119, 126, 127], which emphasise the importance of an unknown OH source in the oxidation of isoprene. Further studies by Dlugi et al.[1] suggest that an upper limit of 15% for the reduction of the rate of the OH + Isoprene reaction by air mass segregation effects is appropriate, a finding which was later supported by Pugh et al. as a result of a model analysis[128] carried out based on highly spatially resolved isoprene measurements to quantify the small scale fluctuations in BVOC concentrations. Further evidence to suggest that the observed model discrepancies are mechanistic in nature rather than due to the aforementioned physical processes is the dependence of the magnitude of the measured to modelled OH discrepancy on the concentration of NO, which would not be expected to be observed if air mass segregation was a dominant process.[128]

1.4.4 OH regeneration *via.* isomerisation of Isoprene peroxy radicals: The Leuven Isoprene Mechanism (LIM)

The unimolecular decomposition of isoprene to yield OH as part of the isoprene oxidation process was investigated by Peeters et al.[127] using *ab initio* and density functional theory (DFT) at the University of Leuven, resulting in the comprehensive Leuven Isoprene Mechanism (LIM). The first iteration of the LIM (LIM0) proposed two reaction channels subsequent to this initial OH oxidation and O_2 addition which could result in recycling of OH: 1,5-H shift followed by unimolecular decomposition and 1,6-H shift to form photolabile hydroperoxy-methylbutenals (HPALDs), which it was thought would photolyse to OH. A more recent study by Wolfe et al. on the photolysis of the C6 HPALD, found the quantum yield for photolysis to be 1.0 ± 0.4 and a quantum yield for photolysis to OH of 1 ± 0.8, concluding that the C5 HPALD formed from isoprene oxidation would likely exhibit similar photolytic behaviour.[129] Peeters et al. suggested that these processes could improve the representation of isoprene oxidation in models by up to 50%.[127, 130] The LIM0 is shown in Figure 1.18. Note that the addition of O_2 to the OH-isoprene adduct is a reversible process, with ISOPO$_2$ isomers resulting from 1 and 4 OH addition interchanging under near pristine, low NO_x conditions such as the Borneo rainforest.
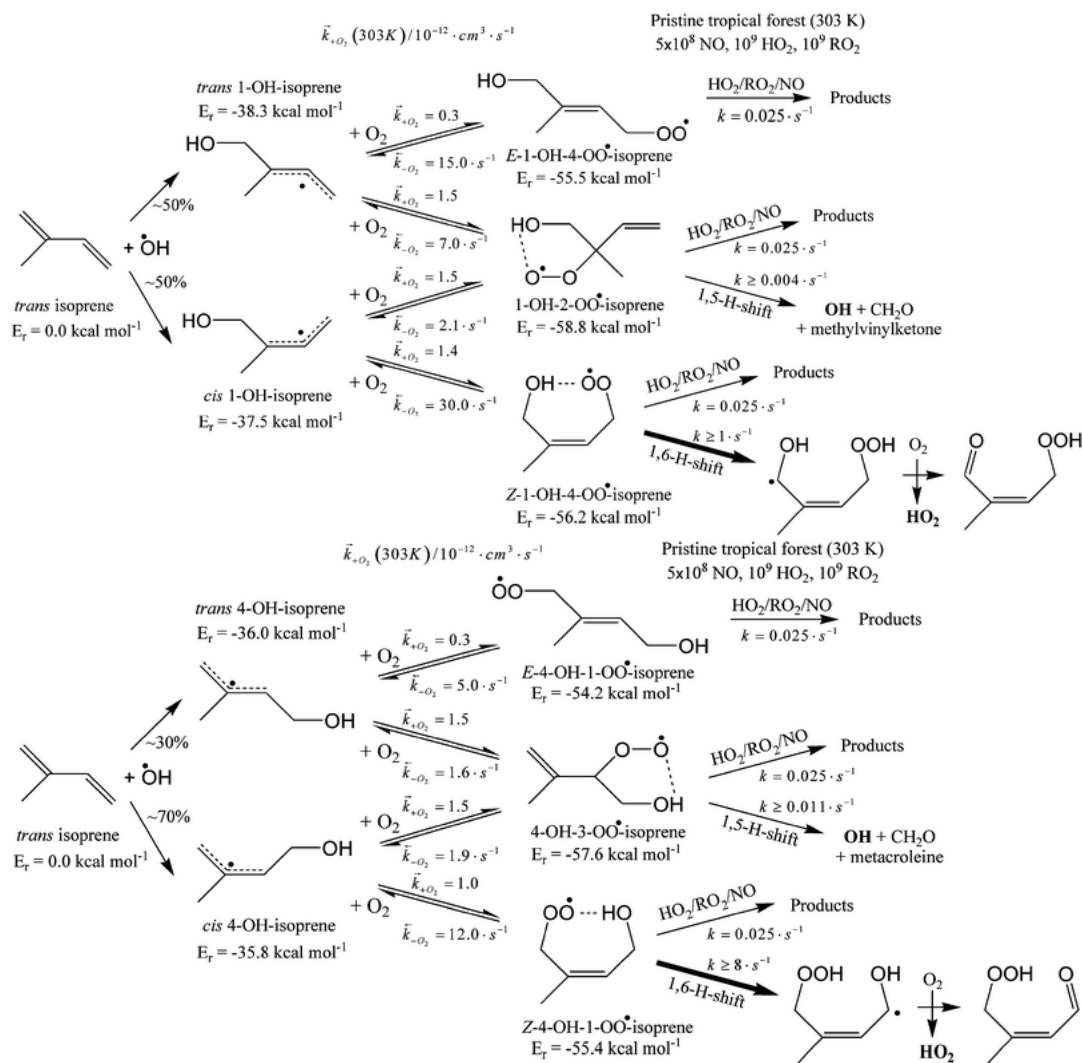
Figure 1.18: The LIM0 reaction scheme for isoprene oxidation following 1-OH (top, 60%) and 4-OH (bottom, 40%) addition to isoprene, at 303 K calculated by Peeters *et al*.. HPALD formation occurs as the result of 1,6-H-shift from the Z-4-OH-1-OO and Z-1-OH-4-OO isomers.

Bulk rates of the unimolecular 1,5 and 1,6-H shift reactions depend on both the isomerisation rate from the corresponding ISOPO$_2$ isomer, and the population of the ISOPO$_2$ isomer. The rate of the 1,5-H shift followed by unimolecular decomposition was calculated by both Peeters *et al*.[127, 130] and da Silva *et al*.[131] with the rate calculated by Peeters *et al*. exceeding that of da Silva by a factor of ~8. Both da Silva *et al*. and Peeters *et al*. predict the same products of the 1,5-H shift channel, forming OH, formaldehyde and methyl vinyl ketone (MVK) or methacrolein (MACR) as shown in Figure 1.18. A study by Paulot *et al*.[126] observed a yield of MVK and MACR of 12 $\pm$ 12 %, leading Peeters and Muller[130] to further increase the rate of the 1,5-H shift by a factor of 5. Paulot *et al*. however, assign the observed yield of MVK and MACR to a radical channel in the ISOPO$_2$ + HO$_2$ reaction, rather than the unimolecular 1,5-H shift channel.

A chamber study carried out at the California Institute of Technology by Crounse *et al.* provided experimental evidence of HPALD formation from the 1,6-H-shift isomerisation in the OH initiated oxidation of Isoprene. The rate of isomerisation ($k_{1.21}$) was calculated relative to the rate of reaction of the isoprene hydroxyperoxy radical with HO_2 (R 1.22, $k_{1.22} = 2.06 \times 10^{-13}e^{(1300/T)}$) recommended by the MCM[86] in agreement with experiments by Boyd *et al.*[132].

$$ISOPO_2 \rightarrow HO_x + HPALD \hspace{3cm} \text{R } 1.21$$

$$ISOPO_2 + HO_2 \rightarrow ISOPOOH + O_2 \hspace{2cm} \text{R } 1.22$$
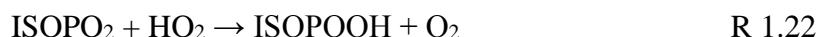
The rate of HPALD formation observed during these experiments was substantially slower (~50 × slower) than the bulk isomerisation rate predicted by Peeters *et al.* Hofzumahaus *et al.*[133] noted that whilst the inclusion of the aforementioned HO_x regeneration pathways improves the agreement between $[OH]_{measured}$ and $[OH]_{modelled}$, previously well-characterised $[HO_2]$ agreement worsens, a finding supported by modelling studies by Stone *et al.*[119] More recent chamber studies by Fuchs *et al.*[115] at Julich assess the impact of RO_2 isomerisation on OH recycling using various iterations of the Leuven Isoprene Mechanism (LIM), as well as the MCM and a generic OH recycling mechanism, whereby a species X which reacts with RO_2 and HO_2 to regenerate OH in a similar way to NO.[115] Fuchs concludes that the overall OH recycling by processes outlined in the LIM0 is exaggerated beyond the experimental evidence, however the author remarks that agreement between $[OH]_{modelled}$ from the various models used, and the observed $[OH]_{obs}$ worsens over the duration of the experiment, implying that the missing OH recycling mechanism is linked to reaction products which build up over time.

Peeters *et al.* subsequently acknowledged the shortcomings of their original LIM0 model, in particular the overestimation of 1,5 and 1,6-H shift isomerisation rates, attributed to the fact that LIM0 was based on quantum chemical data calculated at too low levels of theory[134]. The upgraded LIM1 mechanism has much slower bulk rates of 1,5 and 1,6-H shift isomerisation, and predicts HPALD formation rates much closer to the study by Crounse *et al.*, exceeding the experimental HPALD formation rate by a near constant factor of 1.8.

Figure 1.19: The upgraded LIM1 mechanism of the OH initiated oxidation of isoprene. Rate constants shown are at 298K.

Furthermore, the LIM1 mechanism accurately predicts the strong temperature dependence of the rate of HPALD formation seen by Crounse *et al.,* resulting from the enhanced dissociation and interconversion rates of the $ISOPO_2$ radical isomers. Another feature of the LIM1 is the more detailed analysis of the products of 1,6-H shift, with introduction of a second channel from the "Z,Z'-OH-allyl" adduct leading to the formation of dihydroperoxy-carbonyl peroxy radicals (di-HPCARP) shown in Figure 1.19, which the authors assign a yield of 50%.

Whilst the LIM1 is a comprehensive mechanism of the OH initiated oxidation of Isoprene, comprising multiple isomerisation reactions which efficiently recycle OH, it falls short of reconciling the discrepancy between measured and modelled [OH] in near-pristine, high-BVOC environments.

1.4.5 Possible instrumental interferences

It has been suggested that concentrations of OH and HO_2 detected by LIF at low pressures using FAGE may experience an interference in some environments, specifically environments subject to high BVOC emissions such as isoprene or methyl-butenol, initiating discussion as to whether such interferences could explain the observed difference between measured and modelled OH.[112, 135] Mao *et al.* propose that the decomposition of Criegee intermediates formed from ozonolysis of BVOCs in the sample gas could yield OH, and provide an explanation for the elevated OH radical concentration observed by LIF studies. It is suggested by this group that atmospheric trace gas concentrations specific to certain atmospheres may influence the magnitude of the interference, for example ozone concentration in the case of ozonolysis. It is also suggested that the 30-40% smaller [OH] measured by CIMS compared to LIF in the BEARPEX field campaign which the study is based on, may be due to interference from BVOCs and that the BVOC concentration in the atmosphere of their measurements is lower than many of the previous field campaigns, which they offer as a potential explanation for the elevated [OH] seen previously.

 The recent SAPHIR chamber study conducted at Jülich by Fuchs *et al.* provides evidence contrary to the suggestion that the elevated OH levels seen are an artefact of the FAGE technique, by using a combination of inherently different techniques:

FAGE and DOAS.[115] Conditions in the simulation conducted at Jülich were intended to replicate those seen on the PRIDE-PRD field campaign in China, which showed elevated [OH] concentrations seemingly characteristic of low NO_x, high isoprene environments. Comparison between OH measurements by FAGE and DOAS gave a slope of 1.02 ± 0.01 and an intercept of $(1.0 \pm 0.3) \times 10^5$ molecule cm^{-3}, implying good agreement between the two fundamentally different methods, and reducing the likelihood of the elevated [OH] concentrations being a result of instrumental interference inherent to the FAGE technique. Further evidence to suggest that [OH] has not been erroneously over measured lies in the results of modelling studies using data obtained in the OP3 field campaign, in which glyoxal and formaldehyde were monitored by DOAS[136]. The constraints on the atmospheric model require elevated [OH], (close to the measured [OH]) to reproduce the glyoxal and formaldehyde concentrations which were observed.[120, 136]

Summary

The introductory chapter to this work begins by outlining the "big picture" with respect to the effects that human activity has on the Earth's atmosphere, and the importance of understanding of the processes which contribute to the changes in climate observed since pre-industrial times. To effectively reduce the negative impacts associated with the unprecedented rate of greenhouse gas emission, climate modelling and meta-analysis of primary research is required to inform policy at the national and international level.

Understanding reaction mechanisms which affect the oxidation capacity of the atmosphere is important for accurately calculating the atmospheric lifetime and therefore global warming potential of anthropogenic emissions such as methane, as well as other hydrocarbons and VOCs.

Discrepancies between measured and modelled OH concentrations in near-pristine, high-BVOC, particularly high [isoprene] environments have been observed in numerous field campaigns, as described in section 1.4.1. Various OH recycling mechanisms have been suggested, all of which fall short of reconciling the underprediction of [OH] in models.

The Leuven Isoprene Mechanism (LIM) is a detailed mechanism based on sophisticated quantum chemical data. Importantly, the LIM highlights the complex OH-initiated oxidation mechanism of isoprene in near-pristine environments: when NO_x levels are low, rates of removal of certain isoprene peroxy radicals *via*. bimolecular reaction becomes comparable with various isomerisation reactions, as outlined in section 1.4.4.

Products of the aforementioned isomerisation reactions include the photolabile hydroperoxy-methylbutenals (HPALD), which photolyse at wavelengths within the actinic window to form OH. Whilst photolysis of HPALDs to OH is efficient, the rate of their formation is insufficient to reconcile measured and modelled [OH] in remote, near-pristine environments.

The work contained within this thesis outlines the measurement of total absorption spectra of peroxy radicals, with a view to investigating the role that photolysis of these species plays in remote, high BVOC, low NO_x environments. The TRUVAS instrument measures total absorption cross-sections, which are used in conjunction with absorption cross-sections for the formation of OH measured using LIF spectroscopy.

Chapter 2 outlines experimental details of the newly built TRUVAS instrument, including a summary of previous time-resolved absorption spectrometric methods. The TRUVAS instrument has a number of advantages over previous time-resolved absorption experiments, particularly the ability to measure time resolved absorption over a broad range of wavelengths (~600 nm range). Various experimental results obtained with the TRUVAS instrument are presented to demonstrate the ability of the instrument for measuring spectroscopic and kinetic parameters. Results discussed in this section include the rate of reaction of the simplest Criegee intermediate (formaldehyde oxide) with H_2O dimer, which was published in Physical Chemistry Chemical Physics (PCCP)[3].

Chapter 3 is the first of 3 results chapters, all of which focus on absorption spectra of various peroxy radicals. The absorption spectra of hydroxyperoxy (HP) radicals derived from ethylene, but-2-ene and 2,3-dimethylbut-2-ene (TME) are presented in this chapter. The main focus of these results is on the effect that the increasing molecule size and number of electron pushing groups bonded directly to the peroxy radical centre has on the absorption spectra of these peroxy radicals. Unlike the

spectra of the isoprene, butadiene and 2,3 dimethylbutadiene HP radicals, the suite of peroxy radicals studied in this section only have a single isomer per peroxy radical, allowing the effect of increased substiution of the peroxy radical centre to be investigated on wholly separate systems. A broadening effect on the absorption spectra was observed, increasing from the ethylene HP to but-2-ene HP and again to the TME HP radical spectra. The atmospheric photolysis rates are presented in this chapter, increasing greatly with the aforementioned broadening effect from 0.552 to 1.21 and $1.68 \times 10^{-3} \, s^{-1}$ for the ethylene, but-2-ene and TME HP radicals respectively. Finally in this chapter, the absorption cross-sections for OH formation for the ethylene and TME HP radicals measured by Dr. Hansen are presented alongside the total absorption cross-sections and used to generate wavelength dependent OH quantum yields for photolysis of these HP radicals.

Chapter 4 focuses on the absorption spectra of the isoprene HP radical ensemble, which comprises 8 isomers. Alongside the isoprene HP radical spectum, the spectra of butadiene and 2,3-dimethylbutadiene are presented, the isomeric HP radicals of which mimic 3 of the isoprene HP radicals each respectively. The broadening effect observed for the single isomeric HP radicals outlined in chapter 3 is again observed in the absorption spectra of the dienes measured here, increasing from butadiene, to isoprene, to 2,3-dimethylbutadiene, due to the increasing fraction of tertiary HP radicals. Absorption cross-sections for OH formation are again presented, and used to generate the quantum yield for OH formation from the isoprene HP radical.

Chapter 5 contains the absorption spectra of the methyl, tertiary-butyl (*t*-butyl) and cyclohexyl peroxy radicals. The methyl and *t*-butyl peroxy radicals are generated by photolysing *t*-butyl peroxide in the presence of oxygen, in a manner not currently employed in any existing studies. The quantum yield for OH production from the methyl peroxy radical is shown to be much larger than for the previous HP radicals, appearing to have a near-unit quantum yield at wavelengths longer than 305 nm. Despite the high quantum yield for OH formation, the rate of photolysis of methyl peroxy radicals at noon in Cape Verde to OH does not contribute significnatly to the rate of OH formation in this region.

2 Experimental

2.1 Absorption spectroscopy

Absorption spectroscopy is widely used as a method of detecting molecules, atoms and radical species in gas, liquid and solid phase media. A common application of absorption spectroscopy is for Gas-Phase kinetics and spectroscopic measurements, since the technique allows concentrations of species to be followed in time, particularly in the infra-red and UV/Vis regions. Most UV-Vis absorption systems currently in use are single-pass, such that the probe light travels directly from the source into the detector, without being directed through the sample more than once. The advantage of a single pass absorption system is that the intensity of the light that reaches the detector is high, as only a small fraction of the incident light passing through the sample is lost; useful for probing systems with high optical densities. Absorption systems of this type often utilise monochromators to select very narrow wavelength ranges (~1 nm) in order to follow changes in absorption over time for a given wavelength. Multiplexing absorption systems exist in the literature, typically restricted to a range roughly ~100-200 nm wide.[137-139] The Beer-Lambert law (E 2.1) describes the linear relationship between absorbance (*A*) and concentration (*c*) of an absorbing species as a function of wavelength. Since cross sections are fixed, and concentrations are determined by experimental factors (excimer energy, precursor cross sections, probe light stability etc.), then it is desirable to extend the path length when probing molecular absorptions, so as to increase to magnitude of the absorbance. Multipassing the probe light through the sample is a commonly employed technique to increase the absorbance measured in absorption experiments.

$$A = -\ln\frac{I}{I_0} = \sigma_\lambda \cdot c \cdot l$$

E 2.1

The White[114, 140-143] and Herriott[140, 144-149] designs represent the two most often used optical arrangements utilised for the multipassing of probe light through a sample.

2.1.1 The White cell

First described in 1942 by John U. White[141], the White optical arrangement involves three spherical mirrors of identical radius of curvature, arranged such that the

incoming light is reflected between the mirrors and finally out of the cell. The number of passes through the cell medium must be a multiple of 4, and can be adjusted by changing the angle of the two smaller mirrors. White cells have proven very useful for certain applications[114, 142, 143], however the sensitivity of the technique for transient absorption spectroscopy is hindered by the requirement of an acute angle of overlap with the photolysis light source. A simplified schematic of the White optical arrangement is shown in Figure 2.1, with an example of how a photolysis laser may be aligned to overlap with the detection region of the probe beam in the optical arrangement. Note that whilst the probe beam used with a White optical arrangement does not necessarily need to be highly collimated (unlike the Herriott optical arrangement discussed below), divergence of the probe beam becomes increasingly problematic as the distance between the 2 identical mirrors and the large mirror is increased.
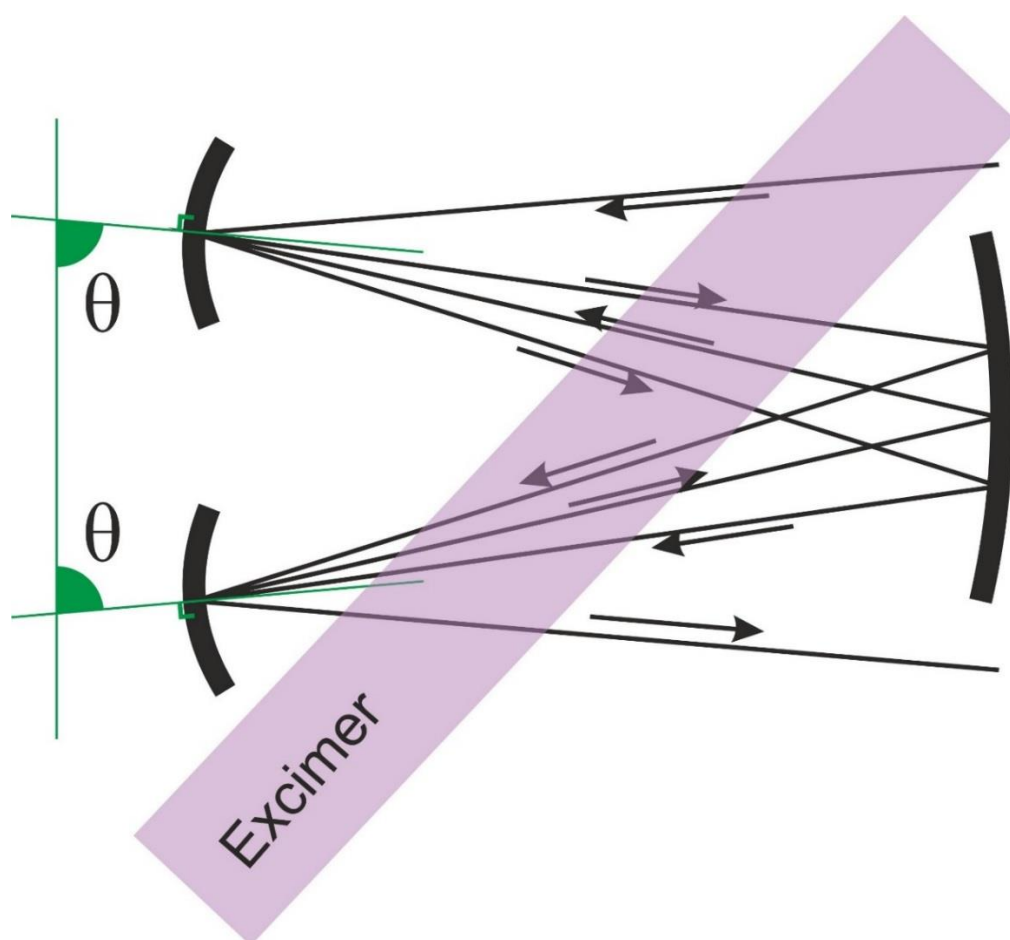
Figure 2.1: A simple schematic of the White optical arrangement, with an example of a typical geometry used to overlap a photolysis beam, typically an excimer laser. The number of passes can be altered by increasing the distance between the mirrors, as well as the angle (θ) of the 2 smaller mirrors.

If one were to attempt to achieve a long overlap of photolysis and probe beams (greater than a few metres), the length, width and therefore total volume of the reaction cell would necessarily have to increase substantially, causing significant issues with reagent flow and cell evacuation.

2.1.2   The Herriott cell

The Herriott cell, first outlined by Donald R. Herriott in 1965[144] employs two identical spherical mirrors, one of which contains an entrance/exit hole for the probe beam. The number of passes is determined by the separation of the two mirrors and the angle of attack of the probe beam. Herriott cells are used extensively in absorption spectroscopy[145-149], owed to their simplicity of operation, resistance to mechanical disturbance and their stability.[140] A simple schematic of a spherical Herriott cell is shown in Figure 2.2, coupled with an excimer beam coaxial to the absorption cell, similar to the setup used by Pilgrim *et al*.[148] Astigmatic Herriott cells operate on the same principle as spherical Herriott cells, except the 2 multipassing mirrors are not equivalent in their radius of curvature. [150-154] The resulting circulating optical beam of the astigmatic optical arrangement more fully fills the whole volume of the cell, with a pattern of spots on the cell mirrors that more evenly fills their area, allowing a greater number of passer per unit volume of the cell.

The astigmatic Herriott cell is often used when a smaller, lighter cell is beneficial, for example in aircraft mounted systems, however this arrangement would be unsuitable for photolysis experiments, as coaxial excimer alignment is precluded by the spread of the beam path into the centre of the mirrors. Of the common types of absorption experiment, the multipass arrangement in the TRUVAS instrument most closely resembles the Herriott cell, but with the added feature of fully translatable mirrors. The ability to translate each mirror is a vital feature of the TRUVAS instrument, as it allows each pass to cut through the path of the excimer optimally, unlike the spherical Herriott cell, which is constrained by the required geometry shown in Figure 2.2
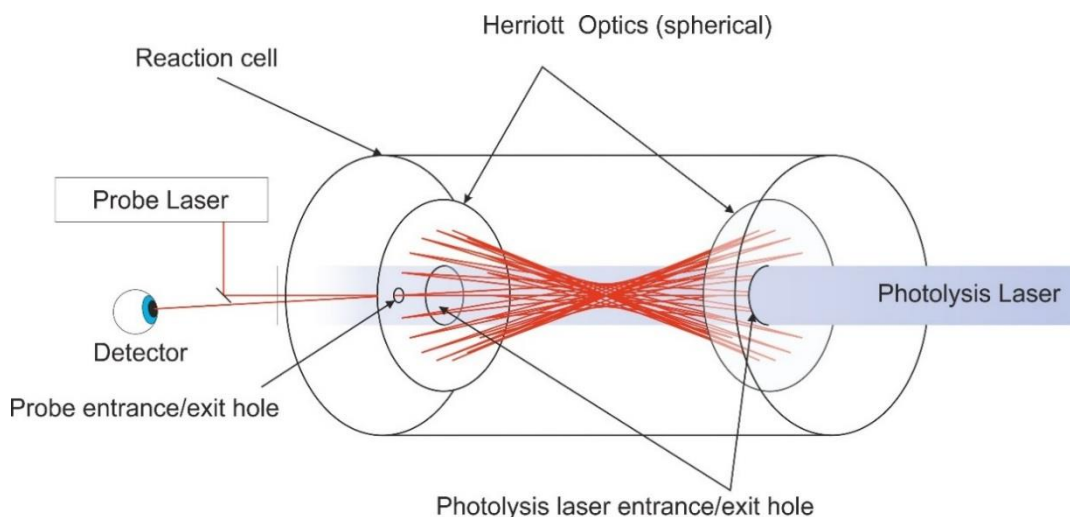
Figure 2.2: A simple schematic of a typical spherical Herriott optical arrangement. An excimer beam is shown running coaxial along the cell, overlapping with the probe beam. The probe beam in a Herriott optical arrangement must be highly collimated in order to follow the specified beam path. Multiple beam path geometries are achievable by altering the angle with which the probe beam enters the cell, however the possible beam paths are constrained by the requirement of the probe to exit the cell through the same hole through which it entered, and must be aligned accordingly.

The most salient drawback of this technique is the requirement of a highly collimated laser light source to probe absorption, limiting the technique to single-wavelength absorption experiments, and is as such unsuitable for the multiplexed, broad-band absorption spectroscopy achieved by the TRUVAS instrument.

2.1.3 Cavity Ring-Down Spectroscopy

Cavity ring-down spectroscopy (CRDS) is a technique which has enjoyed great success in measuring absorption for a variety of applications, including: probing the weak $\tilde{A}^2A' \leftarrow \tilde{X}^2A''$ NIR transition of peroxy radicals[72, 73, 155-165], kinetic measurements of OH and HO_2 [158, 166] and direct measurement of atmospheric trace species[155]. CRDS operates by introducing light into an optical cavity through the rear of a set of highly reflective optics and measuring the rate at which the light intensity exiting through the far side of the optical cavity decreases (the "ring down time"); a simple schematic is shown in Figure 2.3. E 2.2 links the concentration of the absorbing species, to the measurable properties τ and τ_0.

$$\alpha = [A] \times \sigma = \frac{R_L}{c}\left(\frac{1}{\tau} - \frac{1}{\tau_0}\right)$$

E 2.2

where c is the speed of light, σ is the absorption cross section of the species A, τ and τ_0 are the ring-down times (time taken for the light intensity to fall to 1/e of its initial intensity) in the presence and absence of the absorbing species, and R_L is the ratio

between the cavity length (*L*, distance between the two mirrors) and the absorption path length.
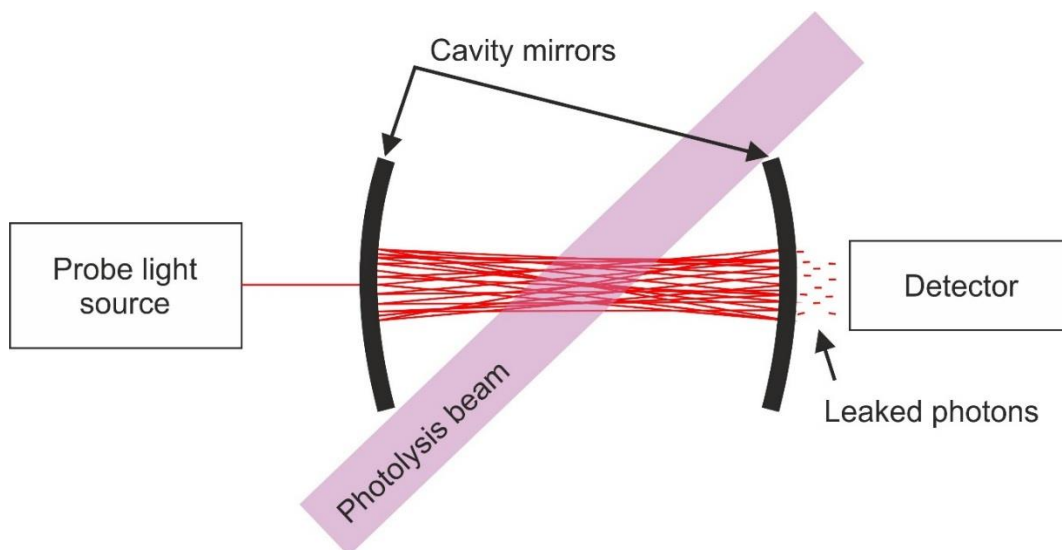
Figure 2.3: A simple schematic of an optical cavity. Probe light is introduced from the back side of one of the cavity mirrors and is reflected many times (often >1000 reflections) inside the cavity. A small fraction (typically <10^{-5} % per reflection, depending on the specification of the mirrors) of the light "leaks" out of the far side of the cavity, and is measured by a photodetector. An example of a possible geometry for coupling a photolysis beam is shown.

Conventional CRDS optics are highly reflective (>99.99%) over a small range of wavelengths (~50 nm); however the reflectivity of the optics outside the specified range is too low to perform broad-band, multiplexed absorption spectroscopy, and is as such unsuitable for applications where multiplexed absorption over a wide range of wavelengths is desirable.

2.1.4 Incoherent Broad Band Cavity Enhanced Absorption Spectroscopy

First developed by Fiedler *et al.* in 2003[167], Incoherent Broad Band Cavity Enhanced Absorption Spectroscopy (IBB-CEAS) is a technique which uses broad-band optical cavity mirrors and an incoherent broad band light source such as a Xenon arc lamp[167, 168], or a super continuum laser[169, 170] to probe the absorption of molecules within an optical cavity. Similarly to CRDS, probe light is directed at the back of one cavity mirror, through which a small fraction of light enters the cavity. Unlike the dichroic mirrors used in CRDS, IBB-CEAS uses broad-band reflective mirrors to trap and multipass the probe radiation through the sample to enhance the effective path length of the absorption.

Recent instrumental developments by Chandler and Sheps[168] have resulted in a system which can measure time resolved, multiplexed absorption of transient radical species, a technique termed Time-Resolved Broad Band Cavity-Enhanced Absorption Spectroscopy (TR-BB-CEAS). This technique uses a novel time-resolved absorption spectrometer, which uses a rotating mirror, synchronised with the excimer pulse to "sweep" the outgoing light from the optical cavity across a 1024 x 1024 pixel Charge Coupled Device (discussed in the subsequent section 2.1.5) array to give a time-resolved spectrum.
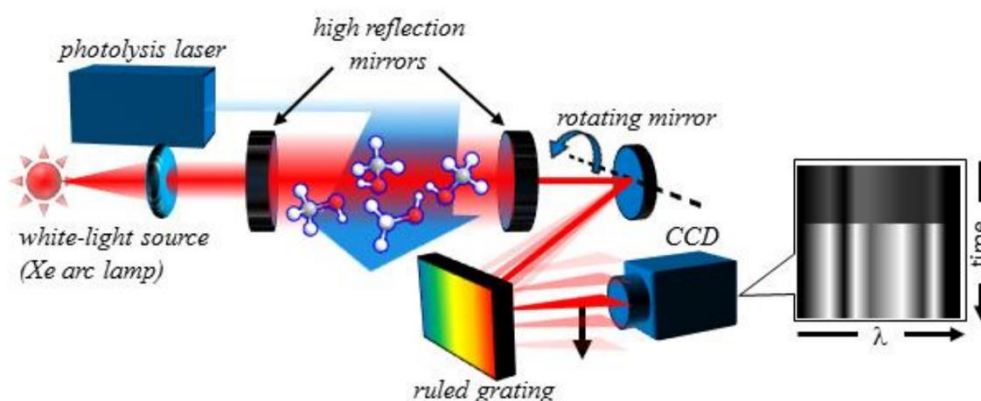
Figure 2.4: A schematic of the TR-BB-CEAS setup designed by Sheps *et al*. , taken from "Time-Resolved Broadband Cavity-Enhanced Absorption Spectroscopy for Chemical Kinetics".[168] Radical generation is achieved by an excimer laser perpendicular to the axis of the cavity.

The effective path length of this setup is wavelength-dependent, due to the dependence of the number of passes on the reflectivity of the cavity mirrors and varies between 56-160 m. The system must be calibrated against a "molecular absorption standard", which in this case is NO_2.

The TRUVAS instrument can measure absorption cross sections down to wavelengths of around 260 nm for the multipass optical arrangement, and ~ 190 nm for the single pass arrangement. The wavelength range 280-450 nm an important spectral region as many molecules (including peroxy radicals) absorb strongly in the U.V. The TR-BB-CEAS is limited in its ability to measure absorption at wavelengths lower than 300 nm as the cavity mirrors are not sufficiently reflective below this wavelength to facilitate the cavity-enhancement effect. Cavity enhanced absorption techniques greatly increase the path length of the probe light, however the sensitivity of these techniques is impeded by the fact that the probe intensity which reaches the

detector is low. This effect can be exemplified by considering the probe intensity required to detect an absorbance of 10^{-5}.

$$e^{-A} = \frac{I}{I_0} \qquad \text{E 2.3}$$

$$\frac{I - I_0}{I_0} = 1 - \frac{I}{I_0} = 1 - e^{-A} \qquad \text{E 2.4}$$

$$1 - e^{10^{-5}} \approx 10^{-5} \qquad \text{E 2.5}$$

Equation E 2.4 shows the fraction of I_0 absorbed as a function of I and I_0, substituting E 2.3 gives the fraction of light absorbed for absorbance A. E 2.5 shows that $\approx 10^{-5}$ of the probe intensity is absorbed, and therefore I and I_0 must exceed 10^5 counts to detect an absorption of 10^{-5}. This illustrates that whilst it is beneficial to extend the path length of absorption, sufficient probe intensity is required to detect small changes in absorbance.

2.1.5   Charge Coupled Device (CCD)

In order to measure multiplexed absorption, a detector with multiple channels is required, of which the Charge Coupled Device is the most common. First used for spectroscopic and kinetics applications by Rowley *et al.*[171], CCDs comprise an array of metal oxide semiconductor pixels which accumulate charge upon absorption of electromagnetic radiation. The amount of charge accumulated by each pixel is proportional to the number of photons which are incident on the pixel within a given exposure time. Broadband probe light is separated into a frequency spectrum using a spectrograph, which projects a narrow (~0.1-1 nm) range of wavelengths onto each pixel. Traditionally, 2D CCDs are used for time-resolved absorption applications by shifting the charge obtained by each row of pixels in the detection region, to the adjacent row in the 2D array, as shown in Figure 2.5.[171, 172] Once all the rows in the 2D array have been exposed, the array is transferred to the readout register, before being amplified and read by a computer. An alternative method for achieving temporally resolved absorption spectra is *via.* "sweeping" the probe light across the CCD chip, a method more recently developed by Chandler and Sheps[168] as part of their time resolved TR-BB-CEAS setup shown in

Figure 2.4. A spinning mirror sweeps the entire output spectrum onto ruled optical grating, which disperses the probe cavity output in wavelength horizontally and projects it vertically across the CCD detector. Both aforementioned techniques essentially involve mapping spectral and temporal information onto a CCD, creating a two-dimensional "transient absorption image" of a chemical reaction.
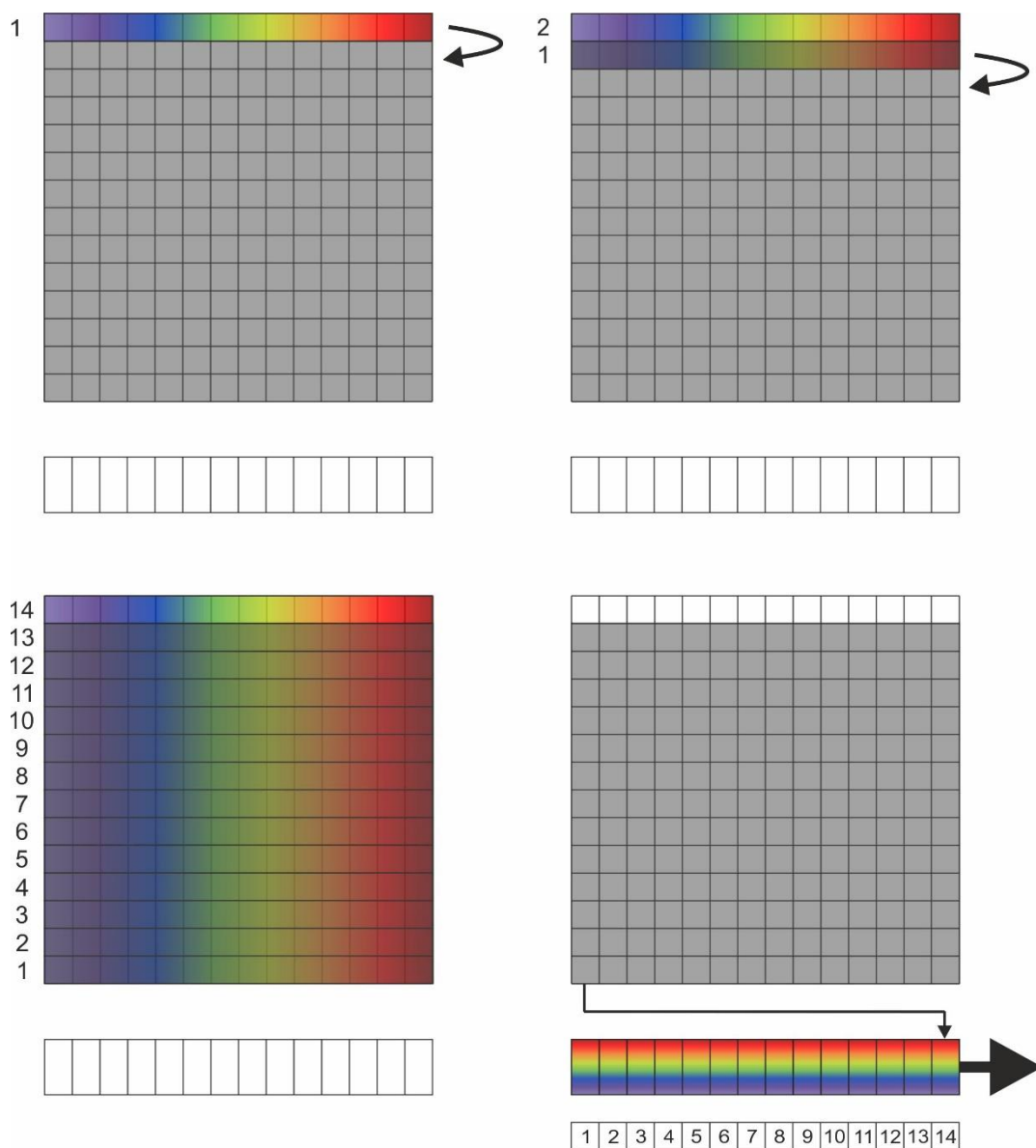
Figure 2.5: A simple schematic of the charge transfer process of a 2D CCD absorption experiment. The first row is the active region of the CCD, where incoming photons are converted into charge, which accumulates on each pixel (top left). Parallel electrodes are phased such that charge accumulated by a row of pixels is shifted to the adjacent row and stored (top right) in the storage region (shown in grey). Once the storage region is full (bottom left) the 2D array is transferred into the readout register, before being amplified and transferred to a computer for analysis.

A drawback common to both 2D CCD techniques is the requirement of cooling: the long exposure times (>ms) necessary for each technique results in substantial "dark

current", whereby charge accumulates in the potential wells of the CCD pixels due to thermally generated electron-hole pairs. To account for dark current, the contribution to the overall intensity from dark current must be measured, and subtracted from the probe intensity measured by the CCD.

Each CCD will have a specification dark current at a particular temperature, however in reality, dark current fluctuates randomly. Random fluctuations in dark current is termed dark current noise, and contributes to the overall noise on the absorbance signals measured by a CCD absorption experiment. To reduce the level of thermally generated dark current, and therefore dark current noise, various cooling systems are employed, including liquid nitrogen and most commonly electronic Peltier cooling systems[171-174].

2.2   Instrumental

A schematic of the setup is shown in Figure 2.6. The instrument outlined in this paper features 14 individually translatable mirrors, adjusted to direct the probe beam in such a way that overlap with the excimer beam, which is directed coaxial to the centre of the cell , is maximised. The reaction cell is a 1.5 m long glass tube, 54 mm OD, with ½" OD inlet and outlet ports, manufactured by York Glassware, sealed with 3 mm thick, 60 mm diameter fused silica windows at both ends. Additional to the multipass optical arrangement is a single-pass optical arrangement, which intersects the reaction volume only once. The probe beams in this setup are produced by a Laser Driven Light Source (LDLS – Energetiq EQ-99X purchased from Elliott scientific). The LDLS is more suitable for this application than a standard Xe short arc lamp because temperature of the spectral output is much higher (~11000 K vs 3000 K), producing more UV radiation. The output of the LDLS is more stable, affording improved signal-to-noise and shorter required averaging/integration times. The ionisation source is from a much smaller point (100-200 µm vs ~2-3 mm long for a standard Xenon arc lamp), making the beam much easier to collimate over the long distances (up to ~20 m) required for this application.
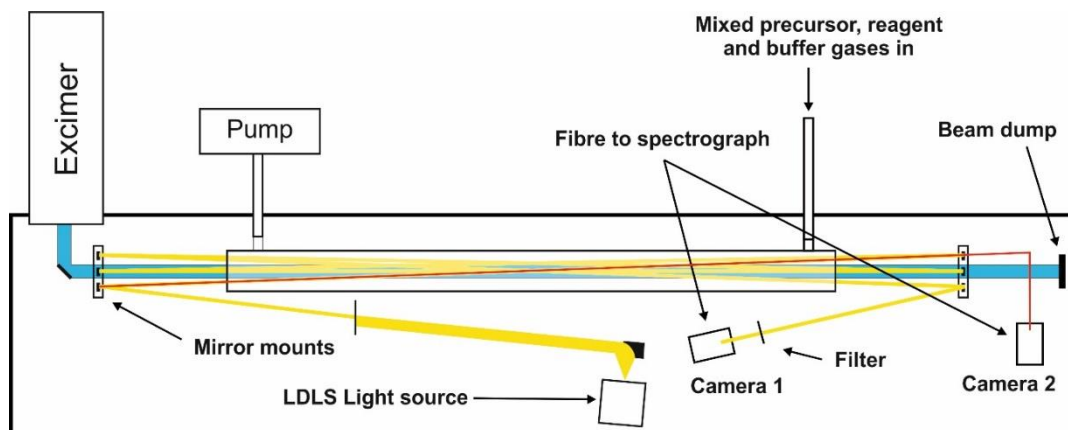
Figure 2.6: A schematic of the experimental setup. The yellow beam shows the path of the multipass optical arrangement, and the red beam shows the path of the single pass optical arrangement.
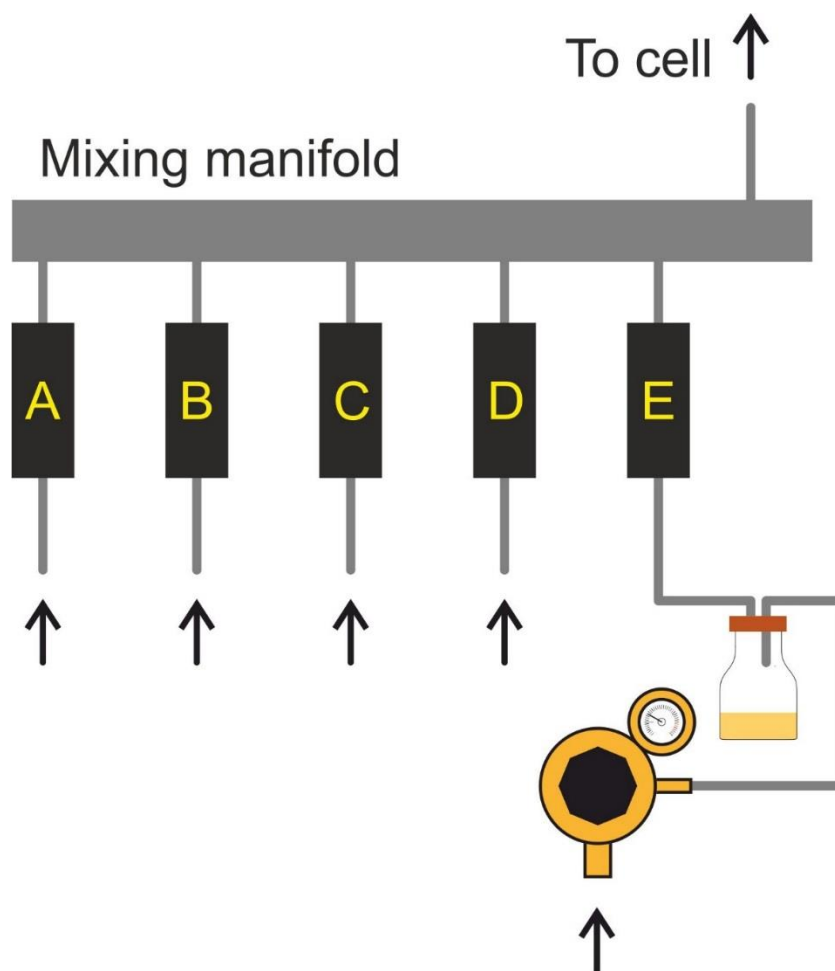
Figure 2.7: The mixing manifold setup used to mix reagent and buffer gases in known ratios. A-E represent mass flow controllers A – Tylan FC260-SA 10 slm; MKS flow controllers Type 1179A: 1 slm (B), 500 sccm (C), 50 sccm (D) and 20 sccm (E). The pre-manifold bubbler can be attached to any of the flow controllers. The backing pressure of the bubbler is regulated using a BOC line regulator. Typically residence times in the mixing manifold are 0.1-1 s, depending on the total flow rate.

Gases are introduced to a mixing manifold via. 5 separate mass flow controllers (MFCs - Figure 2.7), the largest, Tylan (FC260-SA 10 slm) delivers the buffer gas (N2 / Departmental), and a range of MKS flow controllers (Type 1179A, 1 slm, 500 sccm, 50 sccm and 20 sccm) for the O2 and other reagents. If hydrogen peroxide is used for an experiment, the mixture of buffer and reagent gases can be passed through a bubbler containing hydrogen peroxide solution (50% - Sigma-Aldrich). Gas is evacuated from the cell by an Edwards (EM2) 2-stage rotary pump, holding the cell at a typical pressure of ~50-100 Torr (cell pressure can be readily altered in the range 10-760 Torr)

Probe intensity is recorded between 250 and 850 nm for the multipass arrangement and 185-600 nm for the single pass arrangement using a high throughput spectrograph and a fast-read (1 kHz) line-array CCD, which is significantly populated (10-100% of 65535 counts, depending on wavelength) per millisecond, to produce 2D time-resolved absorption spectra. A KrF excimer laser (Lambda-Physik CompEx 210 – 248 nm) is directed along the cell using a dichroic turning mirror to initiate chemistry. The duty cycle of the excimer is selected to allow sufficient time for the processed reaction mixture to be pumped out of the cell, to be replaced by unprocessed reagents avoiding secondary photolysis of reaction products.

2.2.1 Optical Arrangement

The multipass optical arrangement is one previously unreported in the literature, featuring up to fourteen 12 mm diameter mirrors. The number of mirrors can be altered for different applications and desired path lengths – typically 8 passes is optimal for measuring cross sections in the UV (250-400 nm), however up to 13 passes can be used if small cross sections in the visible region are to be measured. Each of the mirrors is adjustable, allowing for translation in the x and y planes (vertical and lateral), so that the overlap between the probe beam and the excimer beam can be maximised. The 12 mm diameter mirrors are spherically curved with a 2.4 m radius of curvature and are UV enhanced such that their reflectivity is ~85% in the UV (custom made by Knight Optical). The mounts were designed in SolidWorks 2013 and consist of 2 aluminium back plates and 8 individual threaded

mounting disks, onto which the mirrors are mounted. M3 screws hold the disks in place and silicone O-rings separate the threaded disks and mounting plate, which allows the angle of each mirror to be adjusted so that the probe beam can be arranged in the configuration outlined in Figure 2.6, which maximises overlap with the excimer beam along the axis of the cell. The final design of the mirror mount assembly, uses small O-rings to give the <1 mm adjustability required, as shown in Figure 2.8.
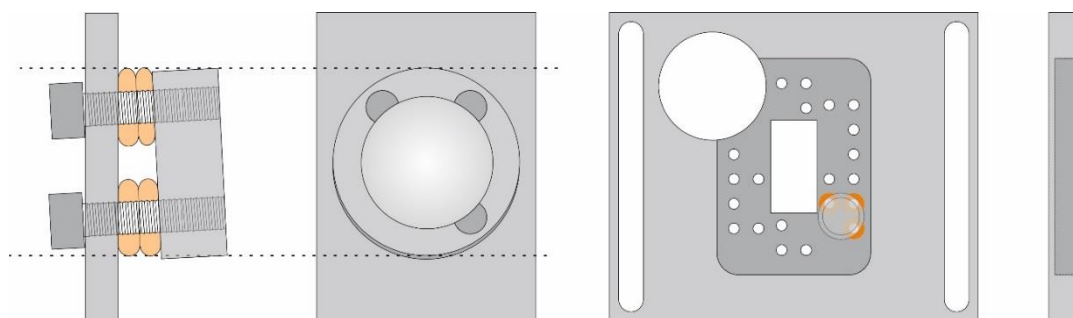
Figure 2.8: A schematic of the mirror mount design. The M3 screws are fed through the back plate, through the orange silicone O-rings, and screwed into the threaded mounting plate. Mirrors are adhered to the mounting plate with superglue.

The mounting plates and threaded disks were milled from aluminium in-house and the optical mounts are fixed in place with custom made L-shaped brackets, which are slotted to allow vertical and horizontal translation of the mount assembly. To remove as much scattered excimer light as possible, whilst retaining probe intensity at short wavelengths (250-290 nm), a sharp cut-on filter (248 nm RazorEdge® ultrasteep long-pass edge filter – Semrock) is placed in the path of the beam, before the fibre-launcher for the multi-pass arrangement. For the single pass arrangement, light enters the spectrograph directly for optimum throughput of UV light (down to ~180 nm)

2.2.2 The Camera / Spectrograph

The spectrographs (Horiba CP140 - Imaging Spectrograph) used in this experimental setup have a range of 650 nm. A schematic of the spectrograph is shown in Figure 2.9. The camera which collects the multipassed light is set to record 250-800 nm, and the single pass camera ~185-600 nm (the lower wavelength limit is dictated by the geometry of the spectrograph). The F number of the spectrograph, which is a measure

of the light throughput, is relatively low (2.5), resulting in lower resolution than many spectrographs (resolution 1.5 nm FWHM), but total light throughput is high. High throughput is desirable as exposures are typically less than 1 ms. With such short exposure times, more light is required to accumulate sufficient charge on the CCD pixels to see adequate signal for measuring absorption.
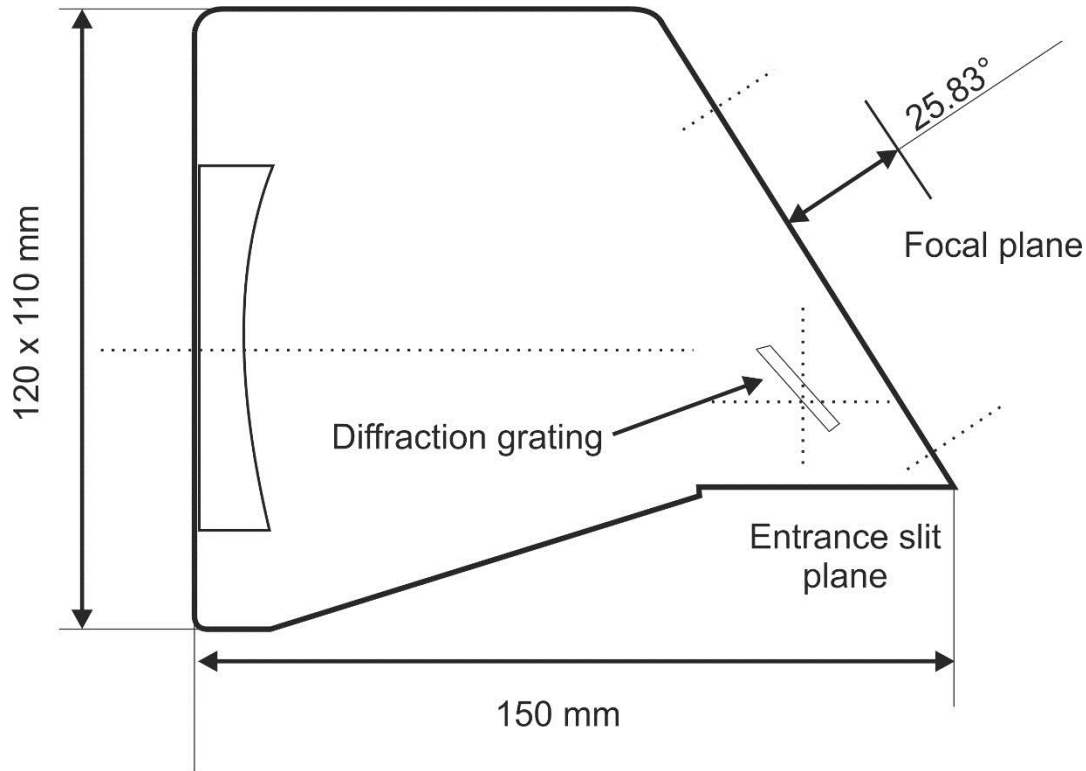
Figure 2.9: A schematic of the Horiba CP140 spectrograph used in this experiment. Light enters the spectrograph through a narrow (~0.1 mm) slit, illuminating the diffraction grating, which wavelength disperses the light. The divergent wavelength dispersed light is focussed onto the 1D line array CCD by 70 mm off-axis parabolic mirror.

The cameras used here are 16 bit line CCD detectors (Hamamatsu S7030-1006 FFT) which comprise an array of 1030 by 64 pixels, aligned with the dispersive axis of the spectrograph (average dispersion = 24.2 nm/mm). Charge which accumulates on pixels is binned and summed by the 64 vertical clocks (FFT – Full Frame Transfer) into the horizontal sum register. An important feature of this CCD chip is that the data are read off at a speed > 1000 Hz (780 μs minimum read time), meaning time resolved absorption data are acquired at a time resolution of 1 ms. Such high data acquisition read rates are most commonly achieved by using a 2D CCD array, and shifting each time slice into masked areas of the array, and then reading the 2D array at the end of each shot.[174, 175]
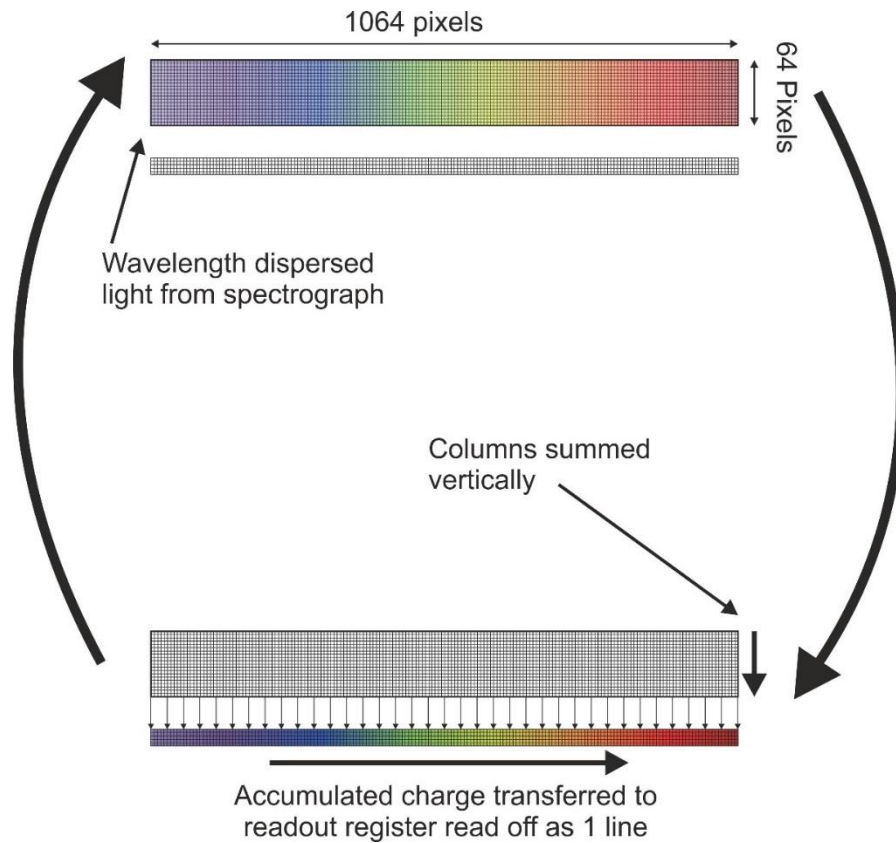
Figure 2.10: The acquisition process of the 1D line-array CCD. The wavelength dispersed light illuminates the line CCD array during the exposure (typically ~0.7 ms for a 1 ms cycle). After the exposure, the charge accumulated in each row of the 64 pixel CCD array is summed, and transferred to the readout register, before being transferred to the computer.

Masking and shifting CCD signals in this way introduces the possibility of "dark noise"; charge accumulation due to processes within the CCD itself, however the fast expose-bin-read cycle of the line-CCD avoids this effect without the need for expensive cooling systems. Faster "1D" CCDs do exist, however they tend to be less efficient at collecting light and faster read rates necessarily result in shorter exposure times and therefore less charge accumulation, which would negatively impact the instrument sensitivity.[176] The wavelength is calibrated using the emission from a Hg pen-ray lamp, the emission lines of which are well-known. The light from the pen-ray lamp is directed into the spectrograph, with each of the peaks being assigned to a Hg atomic emission line, as shown in Figure 1.9.

$$Wavelength = m \times pixel\ number + c$$ E 2.6

For this reason the single pass absorption arrangement is useful for retaining The CCD in the second camera used in this experiment is positioned in the spectrograph

so that it can measure light <180 – 600 nm. When broadband light is passed through fused silica windows and reflected off aluminium mirrors, ~15% of the light is lost.

Short wavelengths are attenuated the most strongly, meaning the UV light which reaches the detector in the multipass system is much less intense (~80% relative to 550 nm) than in the broadband light from the LDLS light source directly. high intensity of UV probe intensity for probing absorption at wavelengths shorter than 250 nm, simultaneous to the multipass absorption system.
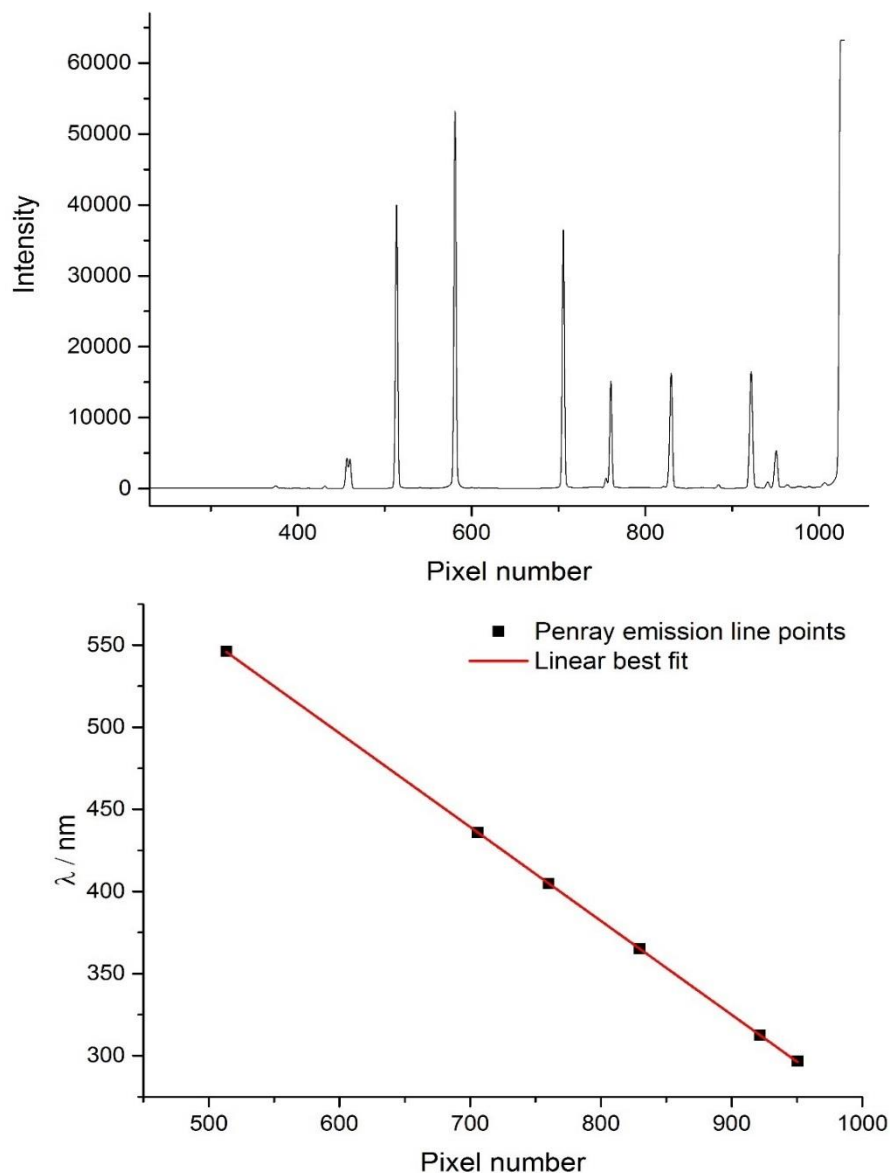
Figure 2.11: Hg pen-ray lamp emission lines are shown as they are measured by the spectrograph/CCD of the multipass camera in the top graph. Each peak corresponds to an emission line and a pixel number on the CCD, and is plotted on a graph of λ/nm vs Pixel number to construct a linear plot (bottom). The gradient and intercept of the points describes the relationship between the pixel number and the corresponding wavelength, which for the multipass camera were calculated to be m = 0.571 and c = 846.3.

2.2.3 Stray light contamination

The camera/spectrograph was found to experience scattering of long-wavelength light onto regions of the CCD. To investigate this effect, filters were used to block out the desirable wavelengths of light, to reveal the intensity of the stray light (referred to henceforth as "false photons"). Between 250-280 nm the UV light intensity collected by the CCD is low (~100-2000 counts), and so even small intensities of non-UV light collected by the CCD in these regions will affect the absorbance calculated using Beer-Lambert's Law (E 2.1). This effect can be described mathematically using equations E 2.7-E 2.9.

$$A_{t,obs} = \ln\frac{I_{0,obs}}{I_{t,obs}} = \ln\frac{I_{0,real} + I_{false}}{I_{t,real} + I_{false}} \qquad \text{E 2.7}$$

where $A_{t,obs}$ is the

$$A_{t,real} = \ln\frac{I_{0,real}}{I_{t,real}} = \ln\frac{I_{0,obs} - I_{false}}{I_{t,obs} - I_{false}} \qquad \text{E 2.8}$$

$$if\ A_{t,real} > 0, then\ I_{0,real} > I_{t,real}\ \therefore \left|A_{t,real}\right| > \left|A_{t,obs}\right| \qquad \text{E 2.9}$$

absorbance is measured by the instrument at time t. $I_{0,obs}$ and $I_{t,obs}$ are the intensities measured by the instrument at a particular wavelength pre-trigger and at time t respectively. $I_{0,real}$ and $I_{t,real}$ are the intensities of real (i.e. the wavelength assigned to that region of the CCD based on the Hg lamp calibration) probe light measured by the instrument at a particular wavelength pre-trigger and at time t respectively. I_{false} is the intensity of the scattered light, assumed to be due to light between 850-1100 nm, as this range corresponds to the wavelength region beyond the maximum wavelength incident on the CCD chip, and the maximum wavelength detectable by the CCD. Since none of the molecules studied in these experiments are believed to absorb strongly in this region, I_{false} is assumed to be constant before and after the excimer. The observed intensities comprise the sum of the real and false photons, and so to calculate the real intensities (and therefore real absorbances), I_{false} is subtracted from the observed intensities. When $I_{real} \gg I_{false}$, $A_{t,real} \cong A_{t,obs}$, however at short wavelengths (250-280 nm) where real intensities are low, I_{false} becomes comparable to I_{real} and leads to underestimation of the absorbance change. To characterise and attempt to correct for this effect, real wavelengths of light were filtered from the probe beam using long-pass filters, in order to observe the residual

I_{false} signal. Figure 2.12 shows the intensity measured by the CCD as a function of wavelength with the various filters in place.
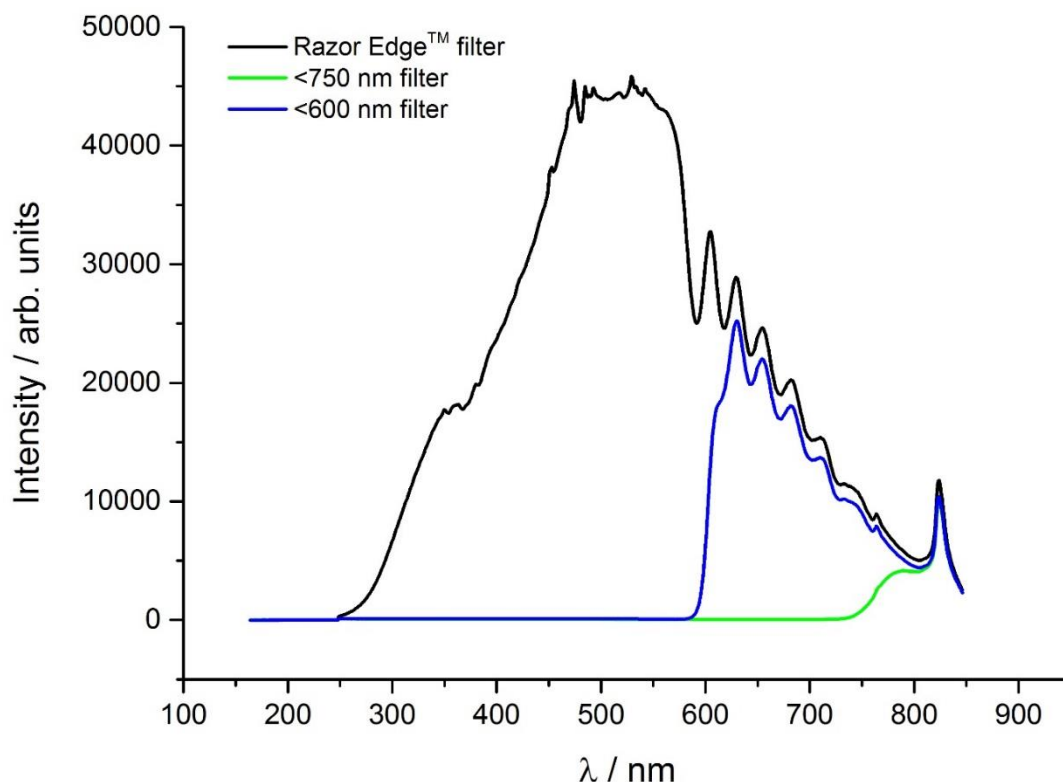
Figure 2.12: Intensity measured by the CCD/spectrograph of the LDLS lamp output with a variety of filters in-line. The razoredge filter is used to block excess scattered excimer light from entering the spectrograph and damaging the CCD, and cuts on sharply at 248 nm (Transmission$_{248 \text{ nm}}$ = 2.7 × 10^{-5}), whilst transmitting UV light >250 nm (Transmission$_{260 \text{ nm}}$ = 0.841, Transmission$_{280 \text{ nm}}$ = 0.923). Intensities were also recorded using the razoredge filter (black line) and 2 coloured Perspex filters, which cut on at 750 nm (green line) and 600 nm (blue line). Note the Razoredge filter was in place for all 3 of the plots shown.

Figure 2.13 shows the false and observed intensities in the region of interest. The number of false photons stays approximately constant across the region pictured, and as such, it was deemed reasonable to subtract a single, constant number from each intensity profile obtained by the TRUVAS instrument. The magnitude of this constant was determined using a process outlined in the following section (precursor concentration measurement). Figure 2.14 shows the ratio of I_{false} to I_{obs} from the measurements shown in Figure 2.12, which declines from ~25% at 250 nm to ~1% at 310 nm, highlighting the enhancement of this effect at the shorter wavelengths.

Whilst the issue of scattered light within the spectrograph is a solved with relative ease for the multipass setup, the same is not true for the single pass setup, which

experiences unpredictable levels of stray light, and as such is not used to make quantitative time resolved absorption measurements.
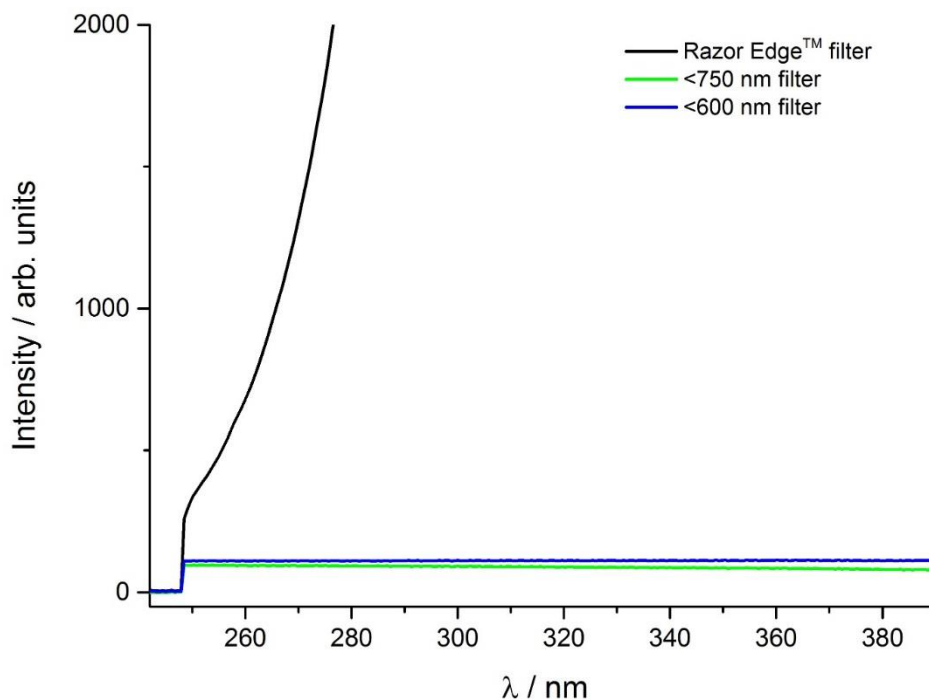
Figure 2.13: An expanded version of the plot shown in Figure 2.12. Note the observed intensity at ~250 nm with both the <600 and <750 nm filters is significant compared to the observed intensity with the Razoredge filter, comprising ~40% of the total signal. The intensity of the false signal remains almost constant at around 112 counts between 250-390 nm for the <600 nm filter. The false light from the <750 nm filter appears to deviate slightly, most likely due to the extinction of some of the wavelengths of light responsible for the false signal.
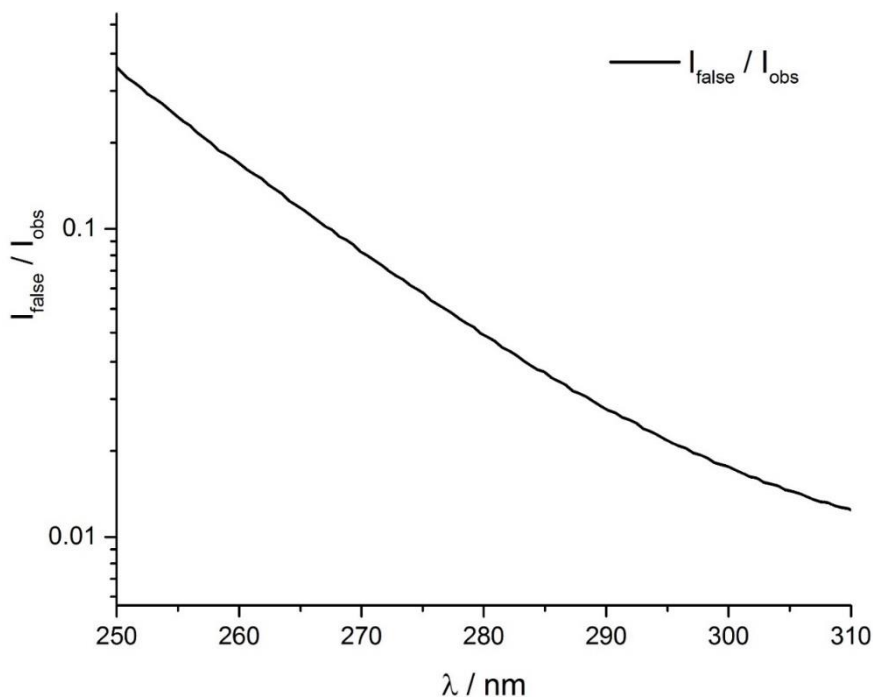
Figure 2.14: The ratio of I_{false} to I_{obs} from the measurements shown in Figure 2.12. The ratio falls from ~25% at 250 nm to ~1% at 310 nm.

2.2.4 Precursor concentration measurement

In order to accurately calculate the radical density at t_0, it is imperative that the precursor cross section is well-known (E 2.10).

$$[Radical]_0 = n_{248\ nm} \times [Precursor] \times \sigma_{precursor,248\ nm} \qquad \text{E 2.10}$$

The TRUVAS instrument can be used for non-time resolved absorption spectroscopy, whereby the absorption of stable molecules can be measured. This is achieved by measuring light intensity in the presence and absence of the precursor, using the same camera for both I and I_o. The bubbler shown in Figure 2.15, is designed such that the down pipe carrying the main flow into the bubbler chamber is not submerged in the precursor liquid, so as to avoid creating aerosol particles in the flow which attenuate the probe light (as discussed in 1.2.1). The absorbance measured is then used to determine the concentration of the absorbing species, by multiplying a literature spectrum by *M*, where *M* is the product of *[Precursor]* and *l*, the path length. Since the probe beam in these experiments is not required to overlap with a photolysis laser, the path length is simply the length of the cell, multiplied by the number of times the probe beam is passed through the cell, which for the 7 pass arrangement is 1050 cm (7×150 cm). As explained in the previous section, scattered light of undesirable wavelengths is incident on the CCD at short wavelengths. The measurement of the absorption due to a precursor such as H_2O_2, which has a well characterised absorption spectrum[177-180] , can be used as a template to estimate the number of counts to subtract from the observed intensities (I_{false}) measured by the CCD detector, as shown in Figure 2.16.
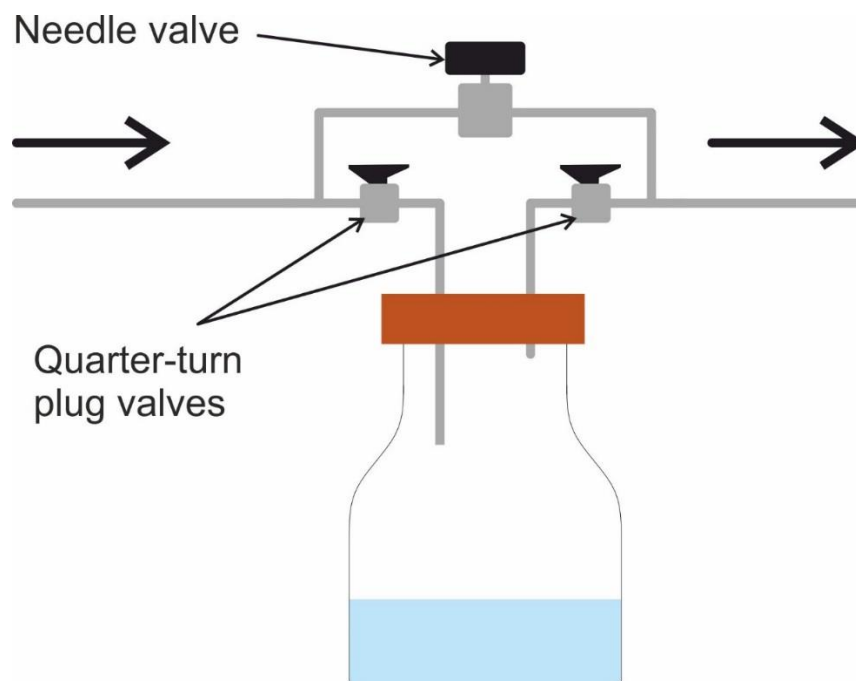
Figure 2.15: A schematic of the bubbler positioned beyond the mixing manifold, used to introduce H₂O₂ (amongst other low vapour pressure liquids) into the reaction cell. To measure I_0, both quarter turn plug valves are turned to the off position and the needle valve is opened. Turning the quarter turn plug valves to the on position allows some of the main gas flow to pass through the bubbler, carrying the H₂O₂ into the reaction cell. The needle valve position can be adjusted to allow more or less of the main flow to bypass the bubbler; the more open the needle valve, the smaller the H₂O₂ concentration measured in the reaction cell. When it is desirable to obtain the highest possible H₂O₂ concentration, the needle valve is fully closed.
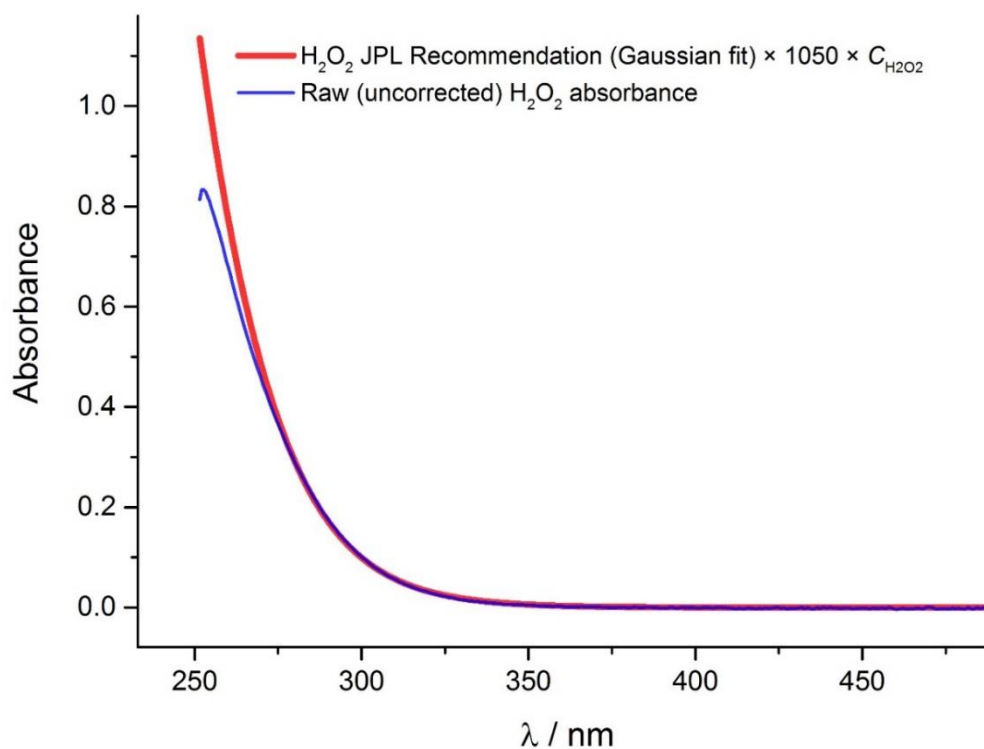
Figure 2.16: The JPL recommendation for the H₂O₂ absorption spectrum is multiplied by *M*. The value of *M* is varied until the spectrum approximately matches the measured absorbance at wavelengths longer than 320 nm.

Figure 2.17 shows the real absorbance due to H_2O_2, obtained by increasing I_{false} and M until the 2 spectra are in agreement. Typically the number of counts which require subtraction from the intensities measured by the camera due to stray light is around 90-120. The subtraction calculated *via.* this method is then applied to the corresponding time resolved absorption trace; typically I_{false} remains relatively constant throughout a day of experiments.
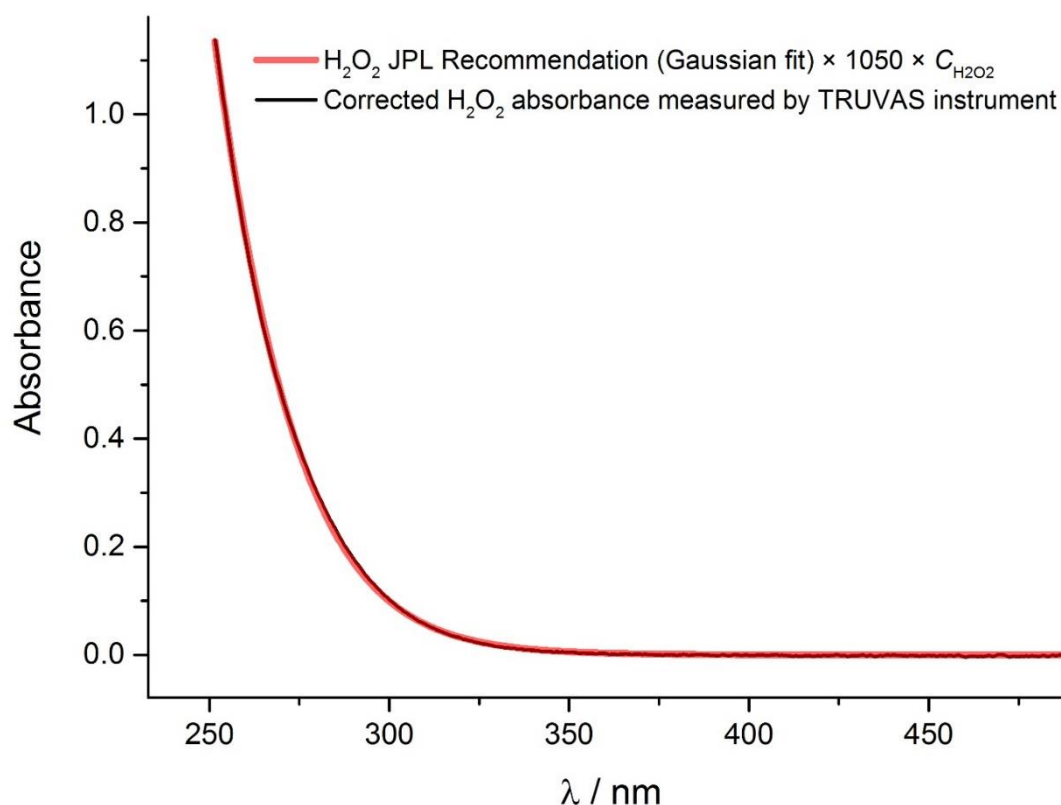
Figure 2.17: An example of the absorbance measured due to H₂O₂ in the reaction cell with a suitable number of counts (I_{false}) subtracted from I_{obs} for the absorbance to match the up scaled literature spectrum.

2.2.5 Data processing

Data are transferred from the camera to the computer *via.* the dedicated Peripheral Component Interconnect (PCI) board supplied with the camera. The transfer rate of the PCI board is sufficiently fast to read the data in real time, and the data are fed into a LabVIEW program written in-house, which converts the raw 2D array, which is in the form of Pixel number vs. time, into wavelength vs. time, where in both cases the magnitude of the number is effectively the Z axis, representing the amount of charge accumulated by each pixel during the exposure. The intensity of the light prior

to t_0 is averaged and represents I_0, and the intensity of the light subsequent to t_0 represents I_t (Figure 2.18). A cut through the 2D array can be taken through the wavelength axis to view the spectrum at a given time delay, which have x and y assignments of wavelength and absorbance respectively. Alternatively, for kinetic applications, cuts through the time axis gives the time evolution of the total absorbance change for any given wavelength.
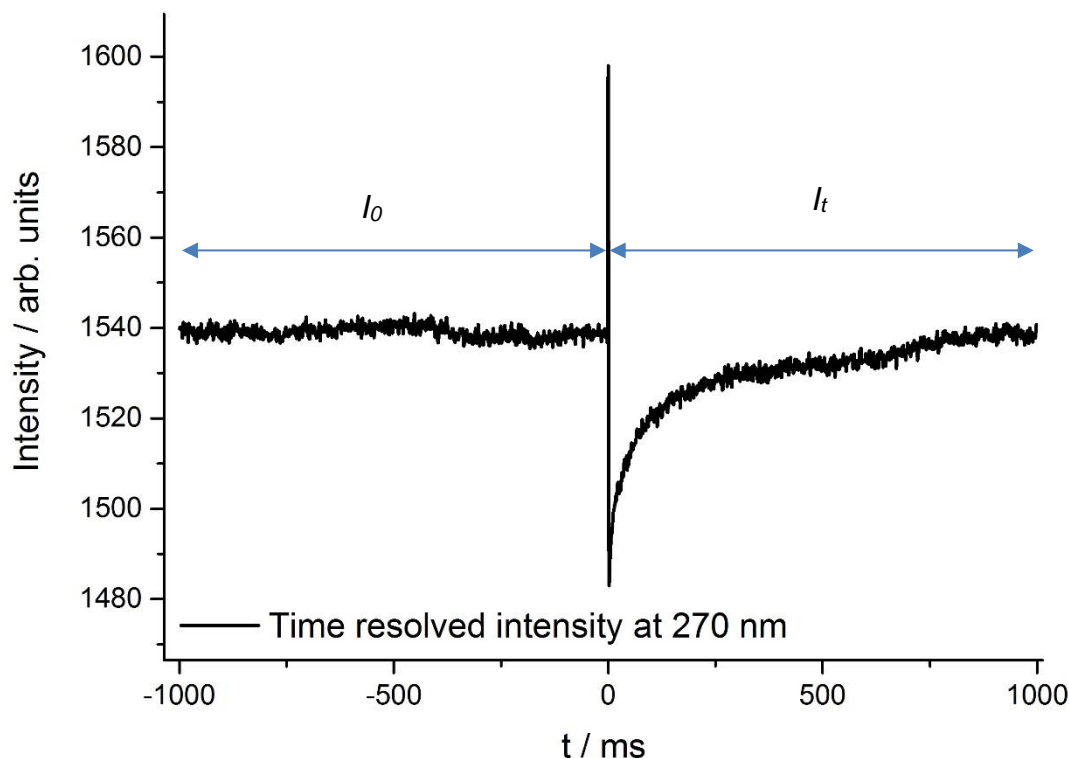
Figure 2.18: An example of a time resolved intensity trace from the generation of Isoprene hydroxyperoxy radicals *via*. H_2O_2 photolysis at 248 nm. I_o is the average of 1000 points prior to t_0, I_t is the intensity at time t. The spike in intensity at $t = 0$ is due to residual excimer pickup at 248 nm.

To account for fluctuations in lamp intensity, a wavelength region where no absorption occurs (typically 500-600 nm) is fixed to 0 (referred to as "pinning" hereafter). Fixing A to 0 where no absorption is seen in this way reduces the noise due to lamp fluctuations (Figure 2.19), and reduces the number of excimer shots required to obtain a satisfactory signal and therefore increases the number of experiments which can be performed in a given time period. Signals are deemed satisfactory by the user inspection, since analysis is carried out prior to data
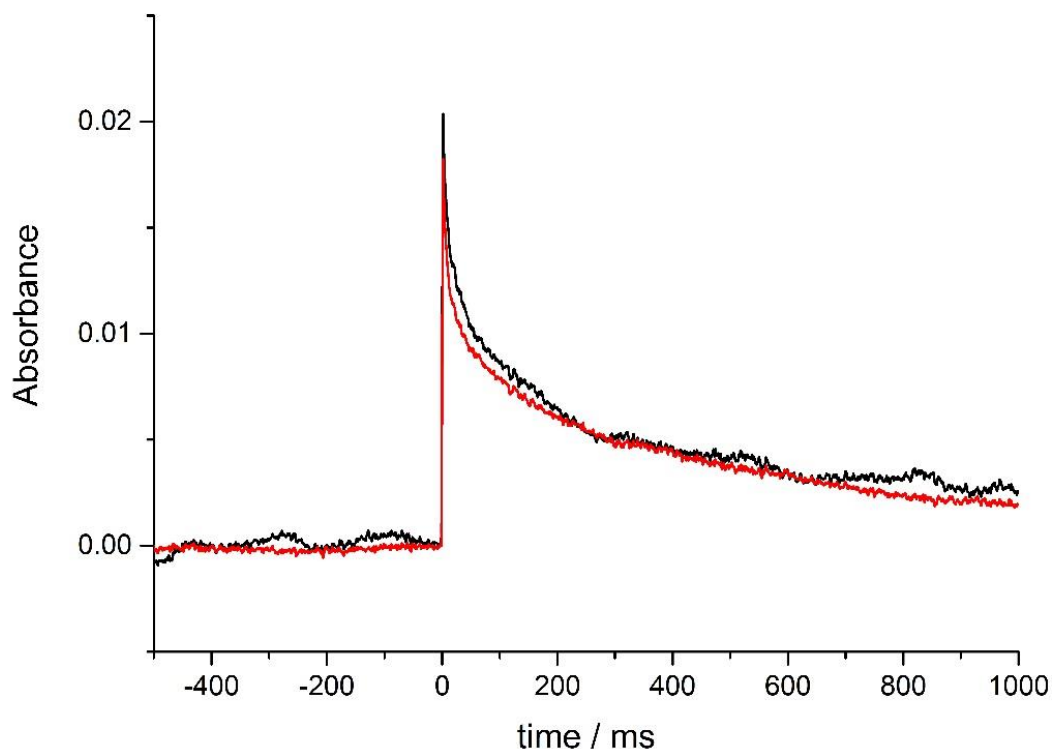
Figure 2.19: An example of the effect of pinning on a time resolved absorption trace (1 ms time resolution). The black trace is unpinned, raw data and the red trace is pinned at 600 nm, where the absorbing species (isoprene hydroxyperoxy radical)[134] has negligible absorption cross section, reducing the noise due to fluctuations in lamp intensity. The red trace displays less random fluctuation due to fluctuations in lamp intensity, and is therefore more useful for kinetic analysis.

2.2.6 Effective path length

Whilst this setup is optimised to maximise the overlap between the probe beam and the excimer beam, complete overlap inside the cell is not possible, such that the path length for photolytic experiments is not equal to the length of the cell multiplied by the number of passes (Figure 2.20).
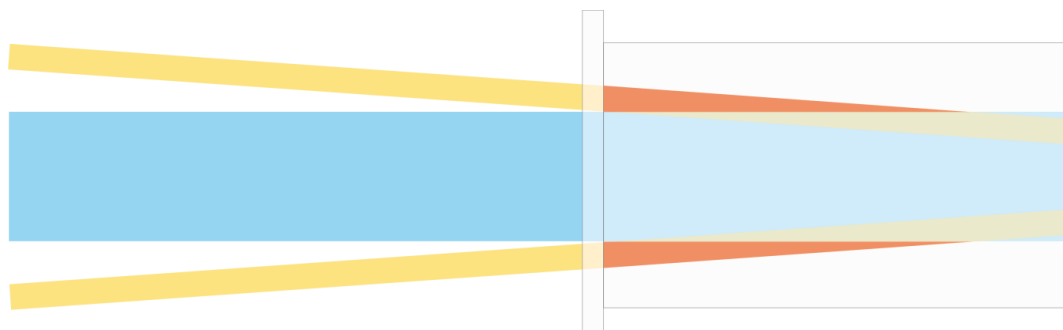
Figure 2.20: A diagram illustrating incomplete overlap of probe and excimer beams within the cell. The blue beam represents the KrF excimer laser volume; the volume of the probe beam (yellow) which does not overlap with the excimer inside the cell is shown in red and the volume of the probe beam which does overlap the excimer beam is shown in yellow behind the transparent cell.

For this reason it is necessary to measure the extent of the overlap between the excimer and the probe, which is achieved by photolysing isopropyl nitrate at 248 nm ($^{i}PrNO_3 = (CH_3)_2CHONO_2$) to yield NO_2 with a quantum yield of near unity (R 2.1).[138]

$$^{i}PrNO_3 + h\nu \rightarrow {}^{i}PrO + NO_2$$

R 2.1
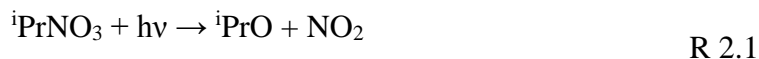
The magnitude of the NO_2 absorption is measured using the multipass arrangement, and in a single pass coaxial along the excimer beam simultaneously, as illustrated in Figure 2.21.

$$\frac{A_{coaxial}}{l_{coaxial}} = \frac{A_{Multipass}}{l_{multipass}}$$

E 2.11

$$l_{multipass} = l_{coaxial} \cdot \frac{A_{Multipass}}{A_{coaxial}}$$

E 2.12

The measurement of the absorbance coaxial to the excimer beam has a well constrained path length equal to the length of the cell (150 cm), making it possible to then calculate the effective path length - $l_{multiapass}$ (E 2.11, E 2.12).

Figure 2.21: Multipass (top, black beam trace) and coaxial (bottom, red beam trace). Note, the coaxial beam overlaps with the excimer beam for the entirety of the length of the cell, and as a result, is constrained to 150 cm.

In practice, the high resolution NO_2 spectrum measured by Vandaele *et al.* [83] was degraded using the *rectangular smooth* adjacent averaging technique, whereby each point is replaced by the average of *n* adjacent points, in order to visually match the resolution of the TRUVAS instrument (1.5 nm FWHM). The degraded NO_2 spectrum was then multiplied by a number *M* (E 2.13 and E 2.14), until it matched the absorbance measured by each camera. The ratio of the value of $M_{multipass}$ and $M_{coaxial}$ is multiplied (E 2.15-E 2.17) by the coaxial path length ($l_{coaxial}$ = 150 cm) to yield the effective multipass path length $l_{multipass}$ (E 2.18).

$$M_{coaxial} = C_{NO_2} \times l_{coaxial} \qquad \text{E 2.13}$$

$$M_{multipass} = C_{NO_2} \times l_{multipass} \qquad \text{E 2.14}$$

$$A_{coaxial,NO_2} = M_{coaxial} \times (NO_2 \; spectrum) \qquad \text{E 2.15}$$

$$A_{Multipass,NO_2} = M_{multipass} \times (NO_2 \; spectrum) \qquad \text{E 2.16}$$

$$\frac{A_{Multipass,NO_2}}{A_{coaxial,NO_2}} = \frac{M_{multipass} \times \cancel{(NO_2 \; spectrum)}}{M_{coaxial} \times \cancel{(NO_2 \; spectrum)}} \qquad \text{E 2.17}$$

$$\frac{A_{Multipass,NO_2}}{A_{coaxial,NO_2}} \times l_{coaxial} = \frac{M_{multipass}}{M_{coaxial}} \times l_{coaxial} = l_{multipass} \qquad \text{E 2.18}$$

^{i}PrNO$_3$ photolysis to NO$_2$ is the ideal method for this application due to the strong, structured, well characterised absorption spectrum of NO$_2$ in the visible region. A photolytic species which absorbs in the visible region is necessary due to the requirement of the coaxial beam passing through the dichroic 248nm turning mirror, which absorbs very strongly below ~350 nm.

The effective path length is essentially $M_{multipass}$ divided by $M_{coaxial}$ multiplied by 150 cm (the coaxial path length), which in the example shown in Figure 2.21 returns a value of 430 cm. The average value of 10 experiments was found to be 442±21 cm for the configuration comprising 7 passes. The error on the path length is given as the standard deviation of the results from the 10 runs. 7 passes were chosen as a trade-off between total effective path length, and retention of suitable levels of UV light (250-350 nm), since UV light is scattered (and therefore lost) more efficiently by surfaces, particles and dust along the beam path. The maximum number of passes with the current configuration is 13, yielding a path length of 1040 ± 78 cm. Changing the number of passes can be achieved readily by simply directing the probe beam from the mirror corresponding to the desired number of passes +1, into the detector.
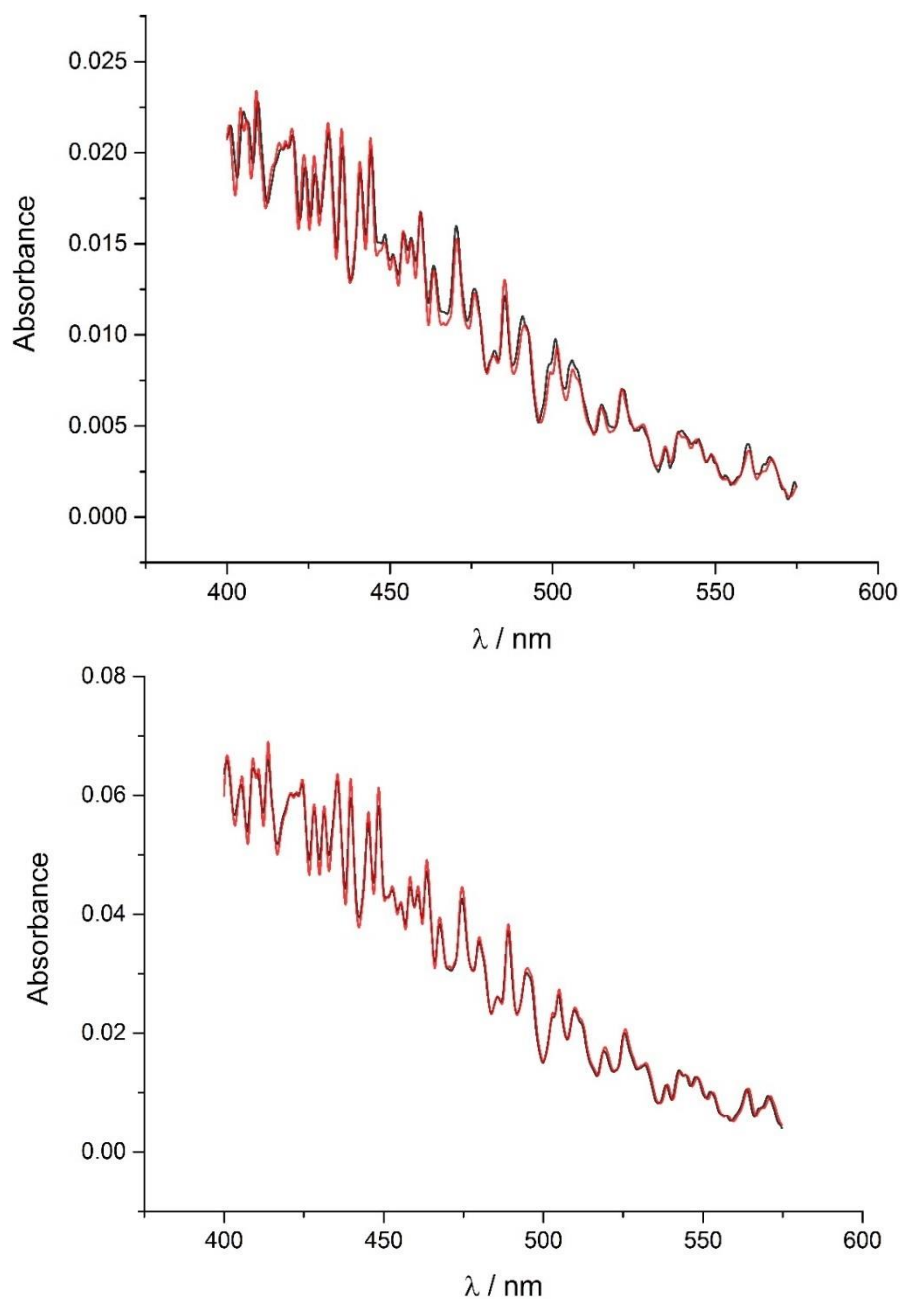
Figure 2.22: The degraded Vandaele *et al*. NO₂ spectrum[83] (red) is multiplied by *M* until it overlaps with the absorbance measured from ${}^{i}PrNO_3$ photolysis from NO₂ (black). The coaxial absorbance is shown in the top graph, and the multipassed absorbance is shown in the bottom graph. The traces shown here were obtained simultaneously, using the optical arrangement shown in Figure 2.21.

2.2.7 Absorption Cross-section Calculation

The Beer-Lambert law (1.2.1, E 1.1), states that the absorption cross section at a given wavelength is equal to the ratio of the observed absorbance signal, to the sum of the number density of molecules per cm³ and the path length in cm. To calculate

the radical density, the precursor concentration and the number of photolytic absorption events must be measured.

The precursor concentration is measured using the aforementioned stable molecule mode and the excimer energy is measured using a calibrated energy meter (Molectron JMAX 11). The excimer beam is approximately 12 mm wide, and 30 mm high, overfilling the 1 cm diameter energy meter sensor, allowing an accurate representation of the excimer beam energy to be measured.

For each experiment, the excimer energy is measured before and after the cell, with the excimer energy taken as the average of the 2 values; measuring the excimer energy in this way allows the measurements to be carried out without moving the reaction cell. The accuracy of this method of measuring the excimer energy was verified by comparing the value to the value of the excimer energy measured with the energy meter in a position half way between the mirror mounts, with a quartz window placed in the position of the first window of the cell in order to mimic the level of scatter and divergence experienced by the excimer beam within the cell. The values obtained for the excimer energy using both methods agreed to ~5%.

Figure 2.23: The energy meter (red rectangle) was placed in front of the cell (top) and after the cell (middle) with the average of the values measured in each position taken as the excimer energy in the middle of the cell. The bottom arrangement was used to verify the agreement between the aforementioned method and the real excimer energy in the middle of the cell; a quartz window is placed in the same position as the cell window, and the excimer energy is measured half way between the mirror mounts.

The energy from the energy meter is converted into fluence ($n_{photons}$) of 248 nm photons and is used to calculate the radical density, using the precursor concentration and precursor cross section at 248 nm (E 2.19).

$$n_{photons,248\,nm} \times \sigma_{248} \times \phi_{radical} \times [Precursor] = [Radical] \qquad \text{E 2.19}$$

The radical concentration calculated using E 2.19 represents the radical generated from the 248 photolysis of a radical precursor. The excimer beam diverges by approximately 15% over the detection region. Often the molecule being probed is made *via.* reaction of this radical with a reagent, to form the target radical species, a peroxy radical for example. To extract cross sections, it is assumed that [Radical] is equal to the concentration of the target radical (i.e. 100% of radicals formed from precursor photolysis react to form the target species) at t_0 – the moment the excimer fires. If the target radical is removed *via.* reaction, it is necessary to extrapolate the absorption signal back to t_0, to give A_0 the absorption signal at the moment the excimer fires. The absorption signal observed by the instrument at t_0 is unusable, due to contamination by the intense 248 nm excimer pulse, some of which is reflected along the path of the probe beam, entering the spectrograph.
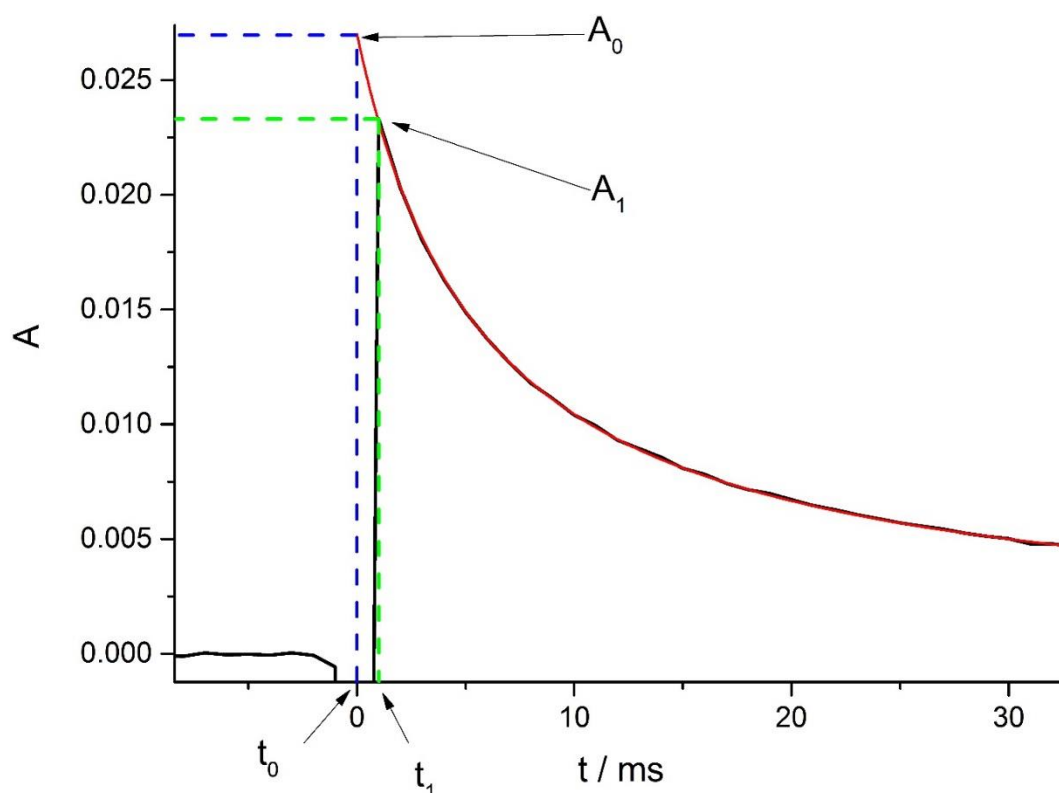
Figure 2.24: A time resolved absorption trace for the ethylene HP radical self-reaction at 280 nm. A second-order fitting function is used to extrapolate the absorbance signal back to t0. A0 is the absorbance at t0, prior to any removal of absorbing species by self-reaction or diffusion.

The equation E 2.20 describes a second order loss consistent with the time self-reaction (k_{self}), coupled with a first order diffusion loss, to account for loss of the

analyte *via.* diffusion (k_{diff}) out of the beam, as well as "pump out" (reactants pumped out of the reaction cell and replaced with fresh reactant and buffer mixture).

$$A_t = \frac{k_{diff}N_0}{k_{diff}e^{k_{diff}t}} - 2k_{self}N_0 + 2k_{self}N_0 e^{k_{diff}t} \times l \times \sigma_\lambda \qquad \text{E 2.20}$$

2.3   Instrument Performance and Results

2.3.1   RO$_2$ absorption spectra

The UV-vis time resolved absorption spectrometer described here has been constructed to measure cross sections of organic peroxy radicals as part of the National Earth and Research Council (NERC) funded Peroxy Radical Photolysis and its Impact on Atmospheric Chemistry (PRIPiAC) project.[181] Peroxy radicals are measured in this system by photolysing an OH precursor (H$_2$O$_2$) at 248 nm in the presence of a co-reagent (for example alkene) and oxygen; the OH adds to one side of the double bond (R 2.2) followed by the addition of oxygen to the other side of the double bond (R 2.3).

$$\text{C}_2\text{H}_4 + \text{OH} \xrightarrow{M} \text{HOCH}_2\text{CH}_2 \qquad \text{R 2.2}$$

$$\text{HOCH}_2\text{CH}_2 + \text{O}_2 \xrightarrow{M} \text{HOCH}_2\text{CH}_2\text{O}_2 \qquad \text{R 2.3}$$

Figure 2.25 shows an example 2D time resolved absorption spectrum of the ethylene hydroxyperoxy radical.

The ability to measure small ($<1 \times 10^{-19}$ cm^2 molecule^{-1}) cross sections at wavelengths longer than 280 nm is important when considering the photolysis rates of atmospheric radicals and molecules. Figure 2.26 shows the absorption cross-sections for the ethylene hydroxyperoxy radical measured by the TRUVAS instrument, compared to the IUPAC recommendation by Lightfoot *et al.*, which are shown to have a similar shape and magnitude, providing some verification as to the accuracy of the cross section measurements made by the TRUVAS instrument, and highlighting the improved sensitivity and smaller limit of detection compared to existing systems.[67]
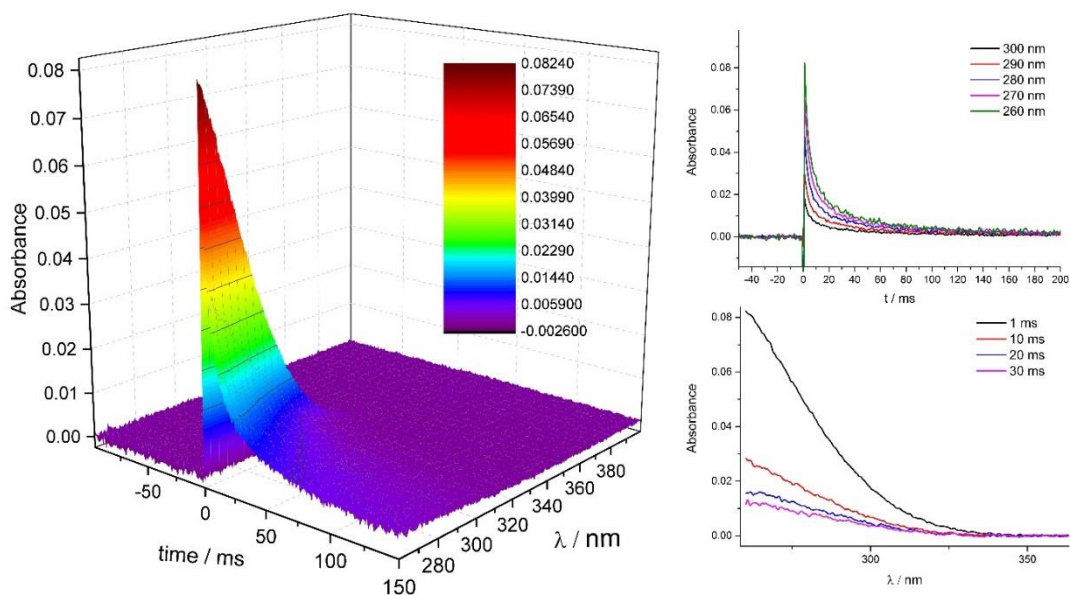
Figure 2.25: A 2D time and wavelength-resolved absorption spectrum (left) of the HOCH₂CH₂O₂ radical. Absorbance decay traces (top right) for the removal of the HOCH₂CH₂O₂ radical by self-reaction at a range of wavelengths, and absorbance as a function of wavelength at a range of time delays (bottom right).
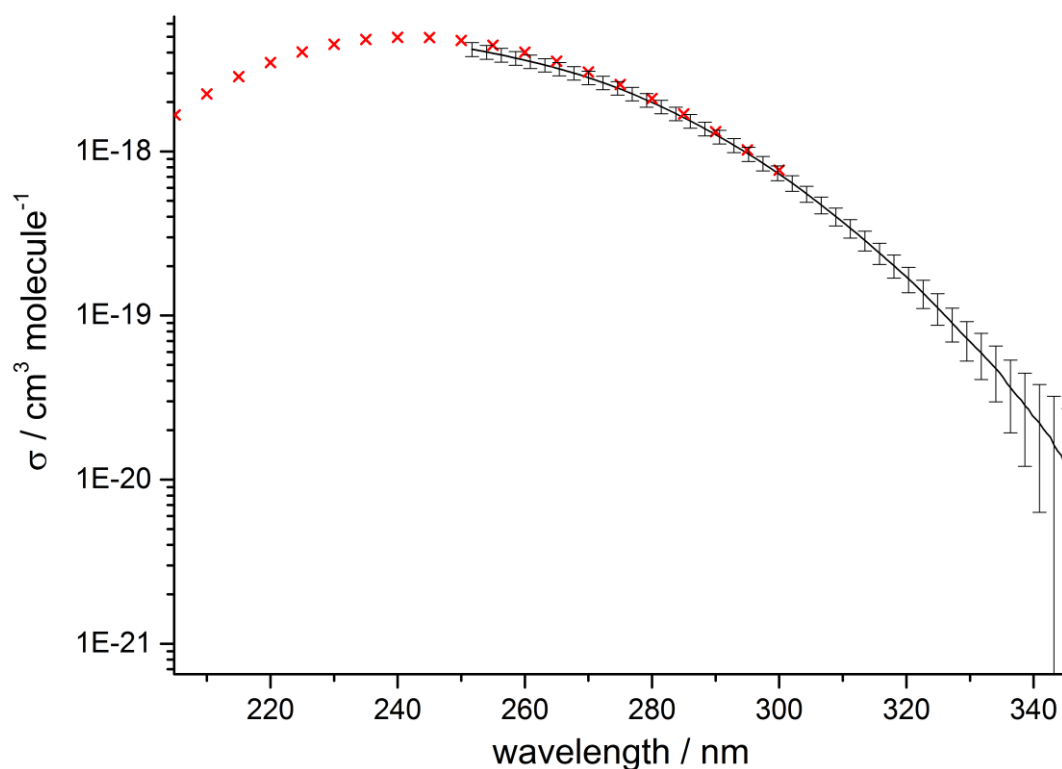
Figure 2.26: HOCH₂CH₂O₂ absorption cross sections. The solid black line represents the cross sections measured using the TRUVAS instrument. The red crosses represent cross sections measured by Lightfoot _et al._[67] Currently the smallest measured cross sections in the literature are around 7.7 × 10⁻¹⁹ cm² molecule⁻¹ at 300 nm. The experimental data obtained using this instrument measure the HOCH₂CH₂O₂ cross section down to ~2.2 × 10⁻²⁰ at ~340 nm, which represents in excess of an order of magnitude greater sensitivity compared to previous measurements.

2.3.2 Limit of Detection

The Limit Of Detection (LOD) of the system is determined by the level of noise relative to the signal or Signal to Noise Ratio (SNR). To see a signal-to-noise ratio of 1 for example, the signal must be at least as big as the random noise experienced by the system, therefore the LOD is equal to the level of noise on the absorption signal. In the absence of any reagents or photolysis pulse, I and I_0 are equivalent, and should produce a plot with absorbance values of 0. Deviation of the absorption away from 0 in this case is due exclusively to the noise experienced by the system. The standard deviation of (indicative of noise level) of the absorbance signal in the experiment at 300 and 500 nm was probed, and found to be 2.3×10^{-5} and 5.5×10^{-5} respectively after 2000 camera shots. Figure **2.27** shows how the standard deviation of the absorption baseline decreases as a function of the number of averages.
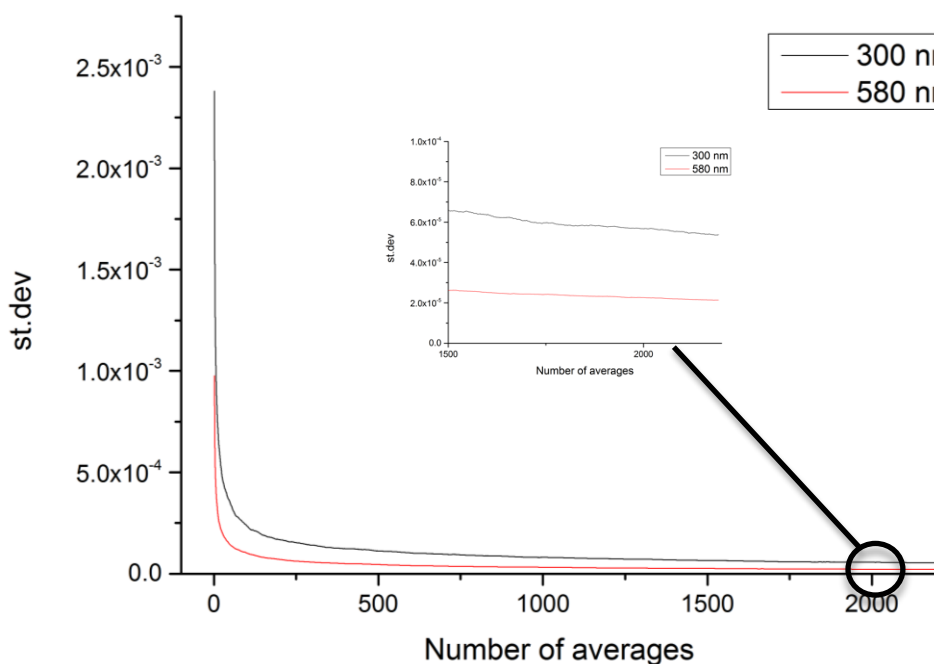
Figure 2.27: The standard deviation of the absorption signal as a function of the number of averaged shots at 300 nm (black) and 580 nm (red). A close up of the graph is shown, note the standard deviation has fallen to roughly 5.5×10^{-5} (300nm) and 2.2×10^{-5} (580 nm) after ~2000 shots .

 If the SNR is to be equal to 1, then the observed absorption must be greater than or equal to the noise (E 2.21). Using equations E 2.21 and E 2.22, the minimum cross section detectable at 300 nm by the system at a typical radical concentration of 5×10^{13} molecules cm^{-3} (typically radical concentrations in this experiment are in the range 3-9 $\times 10^{13}$ molecules cm^{-3}) and a path length of 442 cm, is 2.4×10^{-21} cm^2 molecule^{-1}.

$$\sigma_{min} \cdot c \cdot l \geq 5.5 \times 10^{-5}$$

E 2.21

$$\sigma_{min} \geq \frac{5.5 \times 10^{-5}}{c \cdot l} = \frac{5.5 \times 10^{-5}}{5 \times 10^{13} \times 442}$$
$$= 2.4 \times 10^{-21} \; cm^2 \; molecule^{-1} \qquad \text{E 2.22}$$

In reality, for broad, featureless absorption bands, such as the $\tilde{B}$-$\tilde{X}$ transition common to all peroxy radicals[61-69], noise can be reduced using a digital filter such as the Savitzky-Golay[182] (SG) smoothing filter. In short, the SG filter essentially fits a low order polynomial through successive subsets of n points adjacent to each point, and replaces the point with the value of the polynomial at the central point of each subset. The SG filter in this way can improve the signal-to-noise ratio of a dataset without greatly distorting the signal.
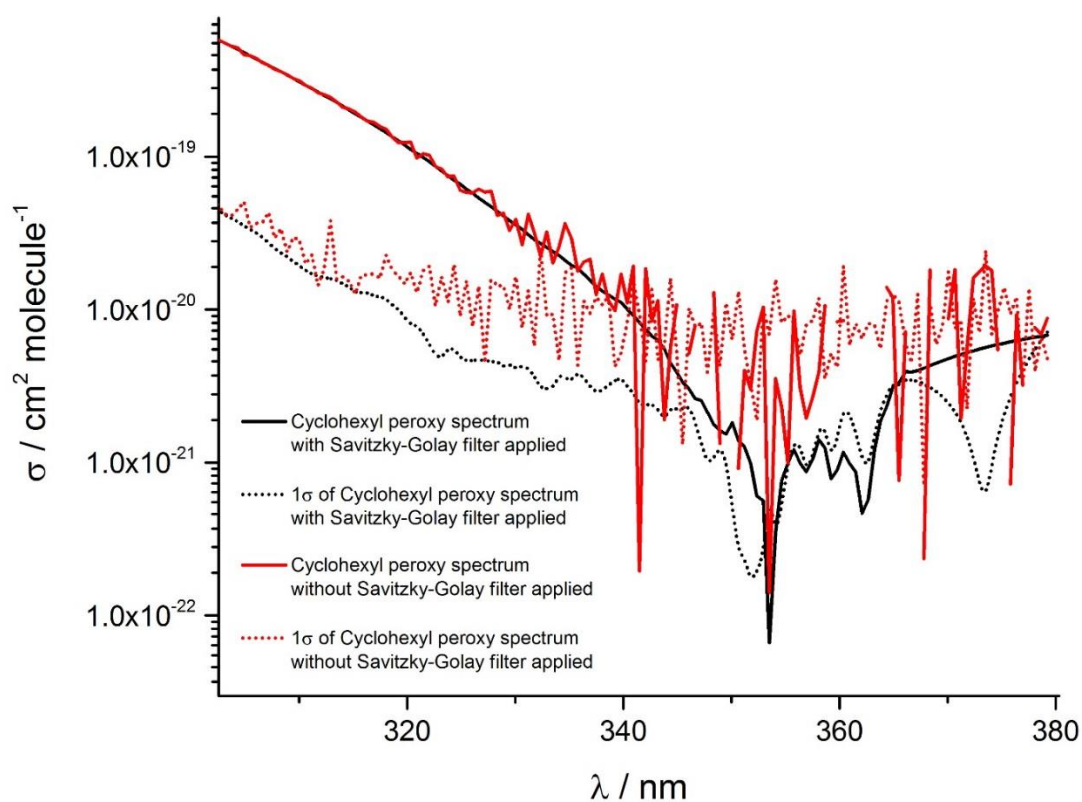
Figure 2.28: The cyclohexane spectrum measured by the TRUVAS instrument with and without the SG filter applied are shown as red and black solid lines respectively. The value of the 1σ error of the dataset with and without the SG filter applied are shown as red and black dotted lines respectively. The point at which the value of the cross section and the 1σ error of the cross section cross is given as the detection limit for a particular set of experiments, and is much larger for the unfiltered dataset (~1 × 10⁻²⁰ at ~340 nm) compared to the dataset with the SG filter applied (3.21 × 10⁻²² cm² molecule⁻¹ at 353.1 nm).

As shown in Figure 2.28, the application of the SG filter to a dataset can improve the signal-to-noise ratio by more than an order of magnitude. The SG filter is applicable to the data generated using the TRUVAS instrument, due to the fact that the data

points are close together and evenly spaced (0.57 points nm^{-1}), in contrast to most other studies of peroxy radical spectra (typically points spaced 5 nm apart).

2.3.3 Kinetic application example – The reaction of the Criegee intermediate with water dimer

The first set of experiments carried out using this apparatus investigated the simplest stabilised Criegee Intermediate (CI − formaldehyde oxide, CH_2OO) which has been the subject of significant interest in recent times.[3, 14, 183] CIs are important atmospheric species as they are the major product of alkene ozonolysis[184]. The simplest Criegee intermediate (CH_2OO) is the product of the ozonolysis of ethylene[184, 185], which is emitted by anthropogenic and biogenic sources in large amounts worldwide.[186] Experimentally, CH_2OO is made *via.* diiodoalkane photolysis (R 2.4), in this case CH_2I_2 in the presence of oxygen, which yields the stabilised CI: CH_2OO (R 2.5).[187]

$$CH_2I_2 + h\nu \rightarrow CH_2I + I \qquad\qquad \text{R 2.4}$$

$$CH_2I + O_2 \rightarrow CH_2O_2 + I \qquad\qquad \text{R 2.5}$$

The system showed great efficacy in investigating reactions of CH_2OO, owed to its high sensitivity in the region of the broad CH_2OO absorption band centred around 340 nm (Figure 2.29). The rate constant for CH_2OO with water dimer (R 2.7) was found to be $4.0 \pm 1.2 \times 10^{-12}$ cm^3 molecule^{-1} s^{-1}.[3]

$$CH_2OO + (H_2O)_2 \rightarrow HO\text{–}CH_2OOH + H_2O \qquad\qquad \text{R 2.7}$$

Previous studies of the reaction of the CI suggested that reaction with H_2O in the atmosphere would be a minor sink for the CI[187] ($k_{H2O} = 4 \times 10^{-15}$ cm^3 molecule^{-1} s^{-1}), however these experiments were conducted at relatively low pressures and [H_2O], and focussed on the removal by monomeric H_2O vapour (R 2.6). Typically experiments studying the reactions of CIs require the concentration of the CI to be

$$CH_2OO + H_2O \rightarrow HO\text{–}CH_2OOH \qquad\qquad \text{R 2.6}$$

in excess of 10^{13} molecule cm^{-3}, whereas this system can detect CH_2OO down to around 10^{11} molecule cm^{-3}, which is important when considering the rapid self-reaction of the CIs, which dominate their removal when their concentration is high.

The ability of the system to detect low CI concentrations and therefore minimise the self-reaction rate allows the reaction of CIs with other species to be probed within the timescale of this experiment. The ability of the TRUVAS instrument to operate under a range of pressures facilitated the investigation of the pseudo first-order loss of CI in the presence of H_2O at pressures where $[H_2O]_2 > 10^{12}$ molecule cm^{-3} (increasing pressure and $[H_2O]$ results in a higher concentration of the H_2O dimer[188]), in contrast to previous experiments carried out at lower pressures.

Removal rate constants up to 600 s^{-1} were measured for removal of CI by $(H_2O)_2$.
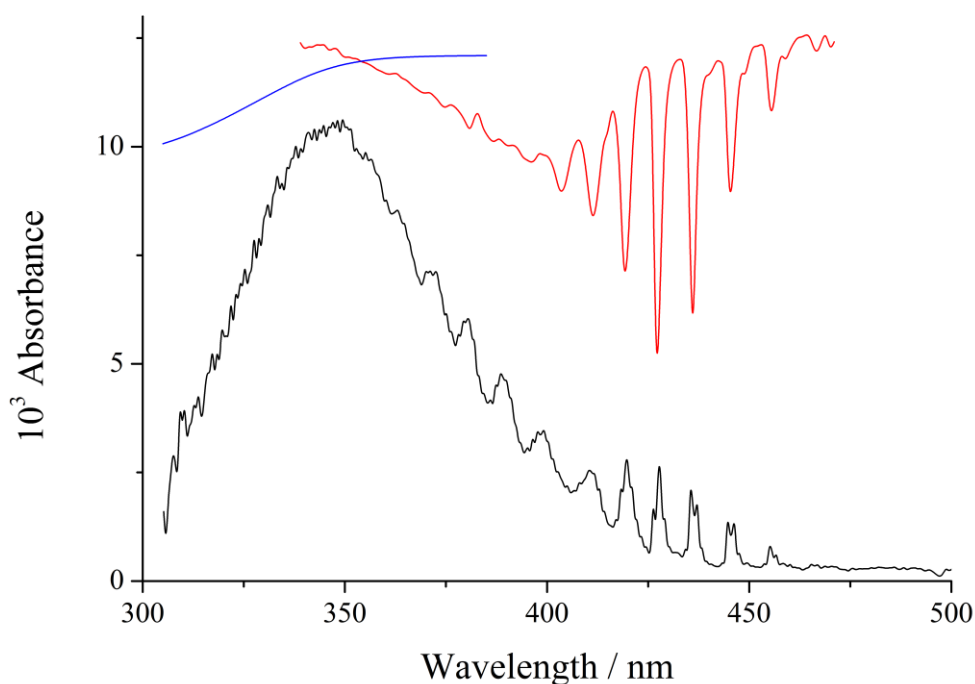
Figure 2.29. -ln(I/I_0) spectrum of the system at early-times over the wavelength range 300 – 800. CH_2I_2 was photolysed at 248 nm (energy ~ 50 mJ pulse^{-1} cm^{-2}) in the presence of O_2: total pressure (N2), O_2, CH_2I_2 and H_2O equal 1.52×10^{18}, 1.77×10^{17}, ~3×1013 and 2.2×10^{16} molecule cm^{-3}, respectively. The spectrum is recorded 1 milli-second after the photolysis laser. The sharp peaks in the spectrum above 400 nm are due to IO, while the spectrum between 300 – 460 nm is the Criegee intermediate, CH_2OO. In red and blue the literature spectra of IO and CH_2I_2 (inverted to aid clarity) have been added to guide the eye.

Kinetic parameters were obtained using the modified exponential decay function E 2.23:

$$[CH_2OO] = [CH_2OO]_0 \exp(-k_{obs}t) + [B]_0 \exp(-k_b t) + C \qquad \text{E 2.23}$$

which includes a first order loss term due to CH_2OO removal, a first order expression to account for the contribution to the observed absorbance from IO and a constant C to account for the step-change decrease in absorbance due to precursor removal *via.* photolysis of the diiodomethane precursor.

Despite the observation of second order CH_2OO loss in some studies[189, 190] at high (~10^{13} molecule cm^{-3}) [CH_2OO], first order removal kinetics were observed under all conditions, consistent with experiments carried out by Sheps *et al.*. The first-order removal kinetics of CH_2OO are most likely due to removal *via.* unimolecular dissociation.[191-193]

$$CH_2OO \rightarrow Products \qquad\qquad \text{R 2.8}$$

The observed rate coefficient k_{obs} comprises the sum of the rates of the unimolecular first order loss (k_1, R 2.8) and k_2': the rate of removal by water ($k_2' = k_2[H_2O]$), as shown in E 2.24.

$$k_{obs} = k_1 + k_2' \qquad\qquad \text{E 2.24}$$

Bimolecular rate coefficients were calculated based on the rate of removal of CH_2OO in the presence and absence of H_2O, whereby subtraction of k_{obs} in the absence of water (whereby $k_{obs} = k_1$) from k_{obs} in the presence of water yields the contribution to the removal rate from reaction with water k_2'.

$$k_2' = k_{obs} - k_1 \qquad\qquad \text{E 2.25}$$

Time-resolved absorbance data at 353, 350, 346, 344 and 341 nm were analysed using global fitting, whereby k_{obs} was treated as a global parameter and all other parameters were local.
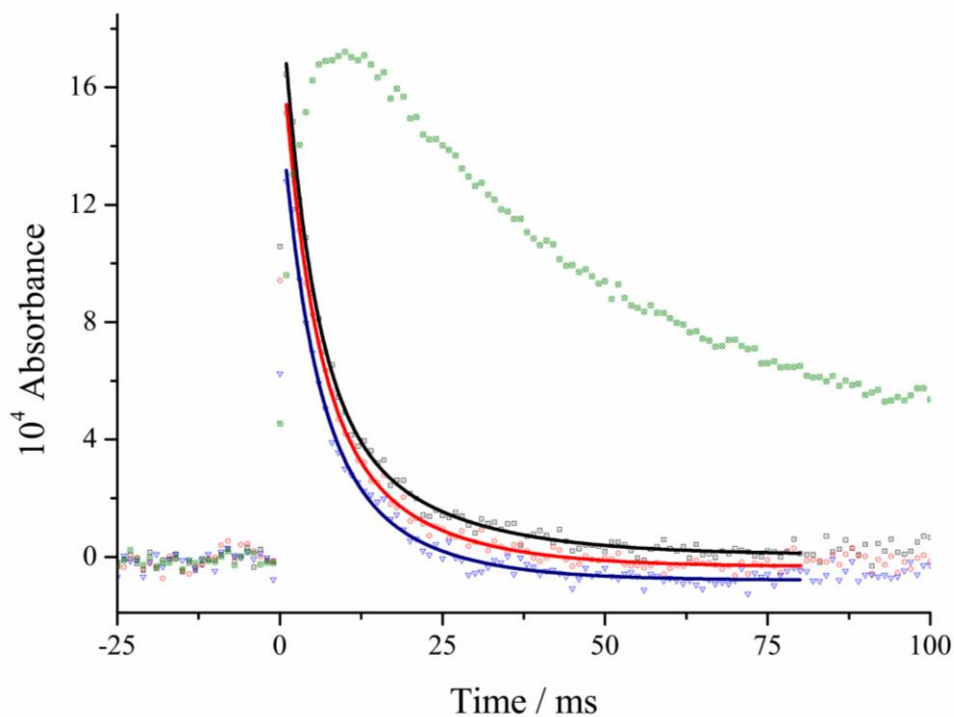
Figure 2.30. ln(I$_0$/I) versus time traces for wavelengths that correspond predominantly to the Criegee intermediate (black- 353 nm, red – 350 nm and blue – 344 nm) and IO (green 436 nm). Traces at 341 and 346 nm have been omitted for clarity. The Criegee intermediate removal under all conditions is much faster than IO removal. The above data returns k$_{obs}$ = 221 ± 17 s^{-1}.
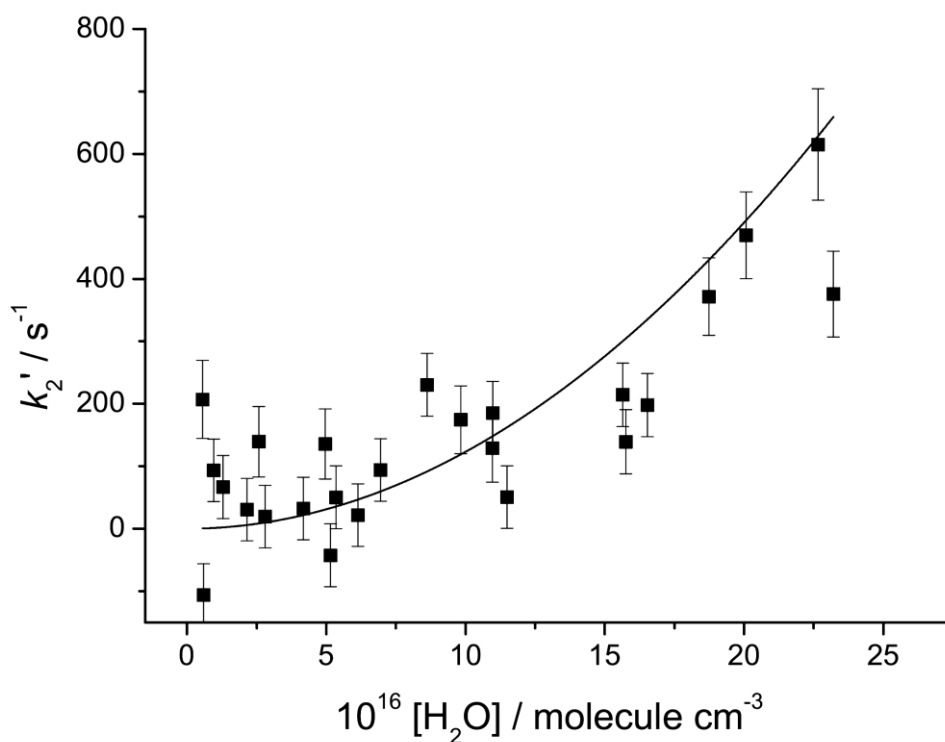
Figure 2.31. Bimolecular plot of the removal rate constant, $k2'$, in the presence of H$_2$O vapour, which exhibits distinct upward curvature. The solid line is the least squares fit of a quadratic function to the data.

2.4 Experimental chapter - Conclusion

A novel TRUVAS experiment has been designed, which can measure absorption between ~260 – 600 nm simultaneously, with a maximum time resolution of 780 µs. The path length of the instrument is increased by a factor of 8-13 by the novel multipass optical arrangement. If the cross sections of the absorbing species is known, time resolved concentrations, and therefore kinetic parameters can be measured; similarly if the concentration of the absorbing species is known, cross sections of absorbing species can be measured. The TRUVAS experiment outlined in this paper has shown a greater than 10 fold increase in sensitivity compared to other time resolved UV-Vis absorption instruments, particularly in the actinic region (λ >300 nm), where solar flux is high. The broad range of wavelengths able to be probed by this instrument is an important feature, facilitating the kinetic measurement of multiple species simultaneously. The TRUVAS experiment outlined here has proven to be a powerful tool for measuring absorption cross sections of transient species, as well as kinetic parameters for important atmospheric reactions.[3, 194]

3   Measurements of the absorption spectra of the Ethylene, But-2-ene and TME hydroxyperoxy radicals

3.1   Introduction

Ethylene, systematic name ethene, is the simplest alkene and a biogenic VOC emitted in large quantities by plants, soil and the oceans (~4, ~3 and ~1 Tg yr^{-1} respectively) [186]. Biogenic sources account for 74% of global emissions, the remaining 26% of the total budget is anthropogenic, with the majority of anthropogenic ethylene emitted from biomass burning resulting from terrestrial land clearing (77%) and to a lesser extent fossil fuel combustion (21%).[195] Removal by OH is the main (~89%) sink for ethylene in the atmosphere, (OH + C$_2$H$_4$ $k = 8.2 \times 10^{-12}$ cm^3 molecule^{-1} s^{-1}) initiating a series of oxidation reactions which breaks the molecule down[86].

The principal aim of the work outlined in this section is to measure total absorption cross-sections for hydroxyperoxy (HP) radicals above 260 nm, particularly those above 300 nm, in order to calculate the total photolysis rate, as well as quantum yields for OH generation from the photolysis of these species in the actinic region, in an attempt to find a pathway which reconciles discrepancies between measured and modelled [OH] in remote, low NO$_x$, high VOC environments. The ethylene HP radical is the most atmospherically relevant of the 3 HP radicals discussed in this section, however the but-2-ene and 2,3 dimethylbut-2-ene (TME) HP radicals are investigated to probe the effect of alkyl substitution of the peroxy radical carbon centre on the spectra of the HP radical.

The transition which gives rise to the broad, featureless absorptions of HP radicals is the $\tilde{B} - \tilde{X}$ transition, from the electronic ground state, to the unbound $\tilde{B}$ state. Previous works show that most HP and alkyl peroxy radicals have similar UV absorption spectra, displaying absorption maxima between 240-250 nm[63, 66, 67, 196]. Miller *et al.*[72, 73] describe a shift in the position (λ_{max}) of the near IR $\tilde{A} - \tilde{X}$ electronic absorption band of alkyl peroxy radicals, observing red shifting as the number of carbons in the alkyl chain increases. Miller *et al*. attribute the red shifting of the IR absorption band to the destabilisation of the ground electronic $\tilde{X}$ state due to inductive effects from the additional alkyl groups attached to the α peroxy carbon centre. In this chapter, absorption spectra of a series of the 3 symmetrical HP radicals

of ethylene, but-2-ene and TME are presented, illustrating the effect that increasing the number of electron donating constituents and size of the molecule has on the shape and intensity of the $\tilde{B} - \tilde{X}$ absorption band. It has also been shown that functional groups attached to the peroxy radical carbon centre have an effect on the position and width of the broad $\tilde{B} - \tilde{X}$ transition; electron withdrawing groups shifting the maximum to shorter wavelengths[66]. Electron withdrawing groups more than one carbon away from the peroxy radical centre are thought to have little effect on the spectra.[67]

Whilst the ethylene HP radical is of atmospheric relevance, but-2-ene and TME are not thought to be present in large concentrations in the atmosphere. The motivation for studying the absorption cross-sections of these radicals is their analogy to the different isoprene HP radical isomers, of which there are 6: 1 tertiary HP radical, 2 secondary HP radicals, and 3 primary HP radicals, as shown in Figure 3.1. When measuring the OH initiated isoprene HP radical absorption spectrum, the HP radical isomers are necessarily formed as a mixture, with yields described by computational investigations in the Leuven Isoprene Mechanism (LIM)[127, 130, 134], as well as a recent experimental study.[197] As such, spectra measured in this way are "ensemble" cross-sections, such that the sum of the absorption cross-sections of each isomer ($\sigma_{\lambda,n}$), multiplied by the fractional concentration of that isomer (χ_n).

$$\sigma_{\lambda,ensemble} = \sum (\sigma_{\lambda,a} \cdot \chi_a) + (\sigma_{\lambda,b} \cdot \chi_b) + (\sigma_{\lambda,c} \cdot \chi_c) \ldots (\sigma_{\lambda,n} \cdot \chi_n) \qquad \text{E 3.1}$$

The ethylene, but-2-ene and TME HP radicals are all formed as a single isomer, owed to the fact that they are symmetrical molecules and both OH attack sites are degenerate, forming exclusively primary, secondary and tertiary HP radicals respectively. Investigation of the absorption spectra separately then allows the effect of the degree of substitution of the peroxy radical carbon centre to be investigated, with a view to applying and comparing the findings to the more complex isoprene system.
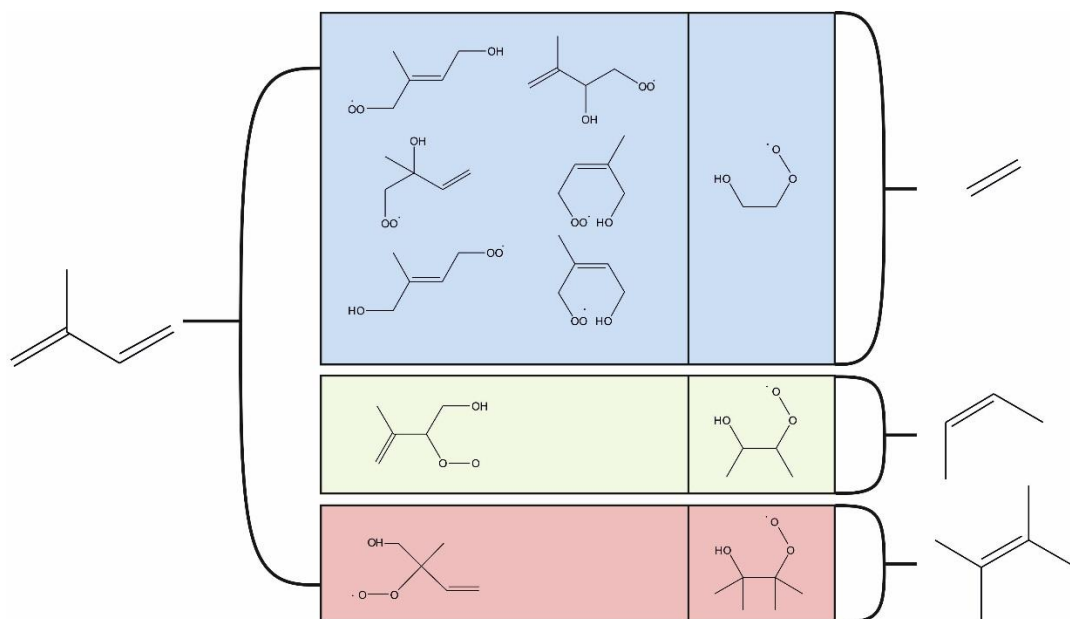
Figure 3.1: The 6 HP radical isomers generated from the OH initiated Isoprene HP radical scheme. The 3 primary HP radical isomers are shown in the blue box, alongside the somewhat analogous ethylene HP radical. The green box shows the 2 possible secondary isoprene HP radical isomers, alongside the but-2-ene HP radical. The red box shows the sole tertiary isoprene HP radical isomer, (thought to be the most abundant) and the analogous TME HP radical.

3.2 Experimental

The absorption cross-sections of the HP radicals of ethene, but-2-ene and 2,3-dimethylbutene (TME) were measured using the TRUVAS instrument outlined in section 2.2. HP radicals were generated *via.* reaction of alkenes with OH from H_2O_2 photolysis at 248 nm using a KrF excimer laser (R 3.1). The OH-alkene adduct reacts rapidly with O_2 to form the corresponding HP radical (R 3.1-R 3.7).
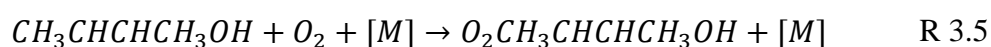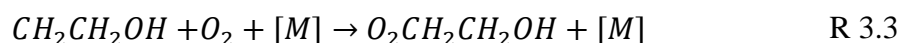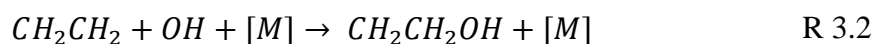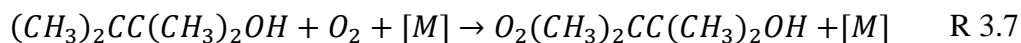
$$HOOH \xrightarrow{248\ nm} 2OH$$ R 3.1

$$CH_2CH_2 + OH + [M] \rightarrow CH_2CH_2OH + [M]$$ R 3.2

$$CH_2CH_2OH + O_2 + [M] \rightarrow O_2CH_2CH_2OH + [M]$$ R 3.3

$$CH_3CHCHCH_3 + OH + [M] \rightarrow H_3CHCHCH_3OH + [M]$$ R 3.4

$$CH_3CHCHCH_3OH + O_2 + [M] \rightarrow O_2CH_3CHCHCH_3OH + [M]$$ R 3.5

$$(CH_3)_2CC(CH_3)_2 + OH + [M] \rightarrow (CH_3)_2CC(CH_3)_2OH + [M]$$ R 3.6

$$(CH_3)_2CC(CH_3)_2OH + O_2 + [M] \rightarrow O_2(CH_3)_2CC(CH_3)_2OH + [M] \qquad \text{R 3.7}$$

The H_2O_2 concentration and the 248 nm photon flux produced by the excimer laser are measured, in order to calculate [OH] at t_0 (typically ~3-6 $\times 10^{13}$ cm^{-3}). OH then rapidly reacts with an excess of alkene, to form the corresponding hydroxyalkene radical, which then adds O_2 and is stabilised by [M] to form the HP radical. Under the regime whereby the alkene is in excess, the vast majority (>99%) of the OH reacts with the alkene (R 3.2,R 3.4 and R 3.6) rather than with the H_2O_2, (R 3.8) meaning [OH]$_0 \approx$[HP radical]$_0$.

$$\text{HOOH} + \text{OH} \rightarrow \text{HO}_2 + \text{H}_2\text{O} \qquad \text{R 3.8}$$

None of the 3 alkenes studied in this chapter have significant absorption cross-sections (<10^{-21}) at 248 nm, negating the need for consideration of radical production *via.* alkene photolysis.

Table 3.1: experimental conditions for the results shown in Figure 3.2-Figure 3.4.

	$[\text{H}_2\text{O}_2]$ / 10^{-15} molecule cm^{-3}	[OH]/ 10^{-13} cm^{-3}	P_{total} / Torr	Excimer energy / mJ pulse^{-1}
Ethylene run 1	4.28	6.79	128	70.0
Ethylene run 2	2.24	3.55	128	70.0
Ethylene run 3	4.34	6.72	237	68.2
Ethylene run 4	4.67	7.23	239	68.2
Ethylene run 5	4.67	6.92	244	65.3
Ethylene run 6	4.67	6.48	244	61.2
Ethylene run 7	4.66	5.69	244	53.8
Ethylene run 8	4.67	7.94	244	75.0
Ethylene run 9	5.68	9.67	128	75.0
Ethylene run 10	2.72	4.62	128	75.0
Ethylene run 11	2.56	4.36	237	75.0
Ethylene run 12	2.18	3.71	127	75.0
Ethylene run 13	2.75	4.68	239.5	75.0
But-2-ene run 1	4.04	5.1	47	55.6
But-2-ene run 2	1.90	2.4	417	55.6
But-2-ene run 3	2.70	3.4	182	55.6

But-2-ene run 4	4.28	5.4	98	55.6
But-2-ene run 5	5.87	7.4	98	55.6
TME HP 1	2.06	2.5	182	53.5
TME HP 2	4.45	5.4	112	53.5
TME HP 3	6.67	8.1	98	53.5
TME HP 4	3.46	4.2	98	53.5

3.3   Results

The absorption cross-sections of the ethylene, but-2-ene and TME HP radicals were measured using the TRUVAS instrument over a range of pressures and radical densities. The hydrogen peroxide concentration is measured for each experiment in the method described in section 2.2.4, and used in conjunction with the excimer power to calculate the radical density.

Figure 3.2 shows the individual absorption cross-sections of the ethylene HP radical measured from 13 separate runs carried out under a range of conditions. No pressure dependence was observed for the total absorption cross-sections measured for the ethylene HP radical. 1 σ confidence limits were constructed by considering both the 5% error in the path length (443 ± 21 cm) and the standard deviation of the absorption cross-sections calculated for each run at each wavelength, and summing these 2 values. Since the absorption spectrum measurements for the ethylene HP radical displayed no pressure dependence, and good reproducibility, fewer runs were carried out for but-2-ene (Figure 3.3) and TME (Figure 3.4).
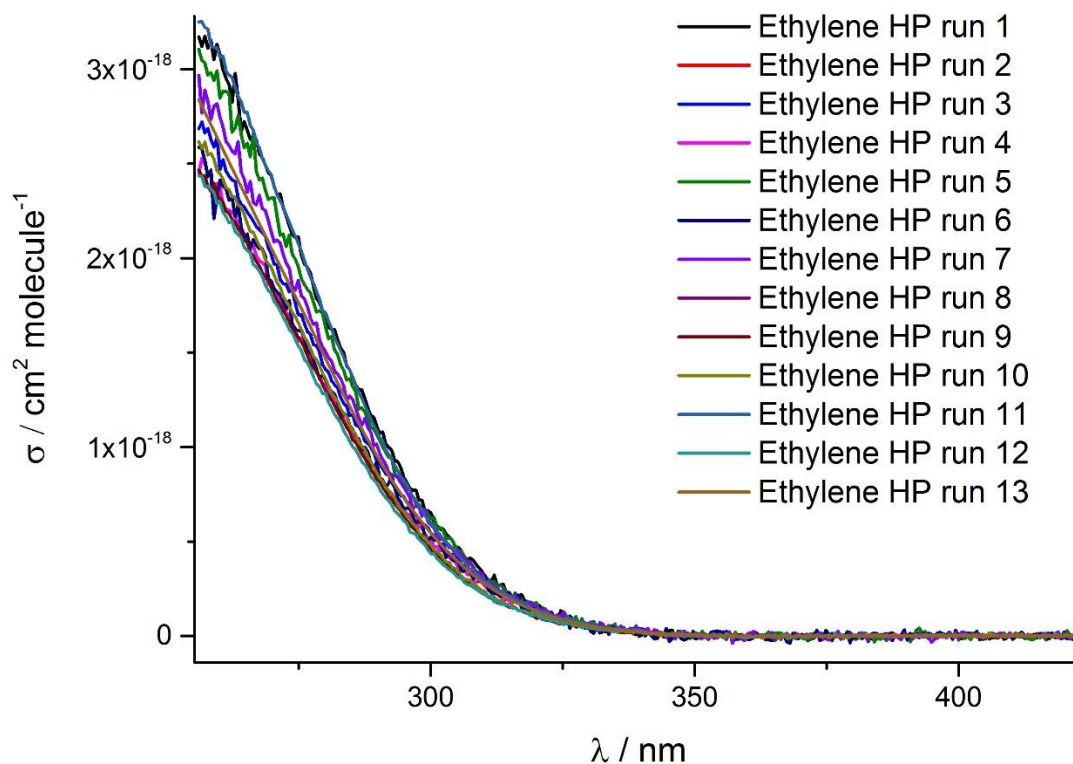
Figure 3.2: Runs 1-13 of the ethylene HP radical absorption cross-sections. Transient absorption profiles are recorded at 0.57 nm intervals (resolution 1.5 nm) following the pulsed excimer photolysis of H_2O_2-Ethylene-O_2-N_2 mixtures at 248 nm.
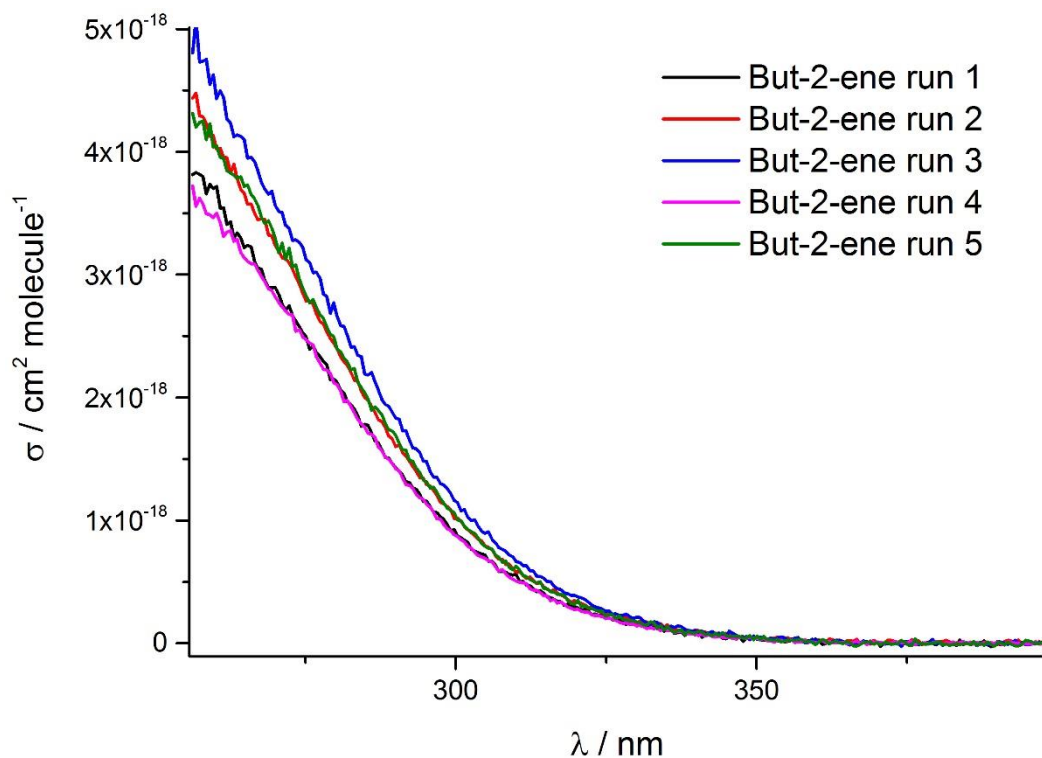
Figure 3.3: Runs 1-5 of the but-2-ene HP radical absorption cross-sections. Transient absorption profiles are recorded at 0.57 nm intervals (resolution 1.5 nm) following the pulsed excimer photolysis of H_2O_2-but-2-ene-O_2-N_2 mixtures at 248 nm.
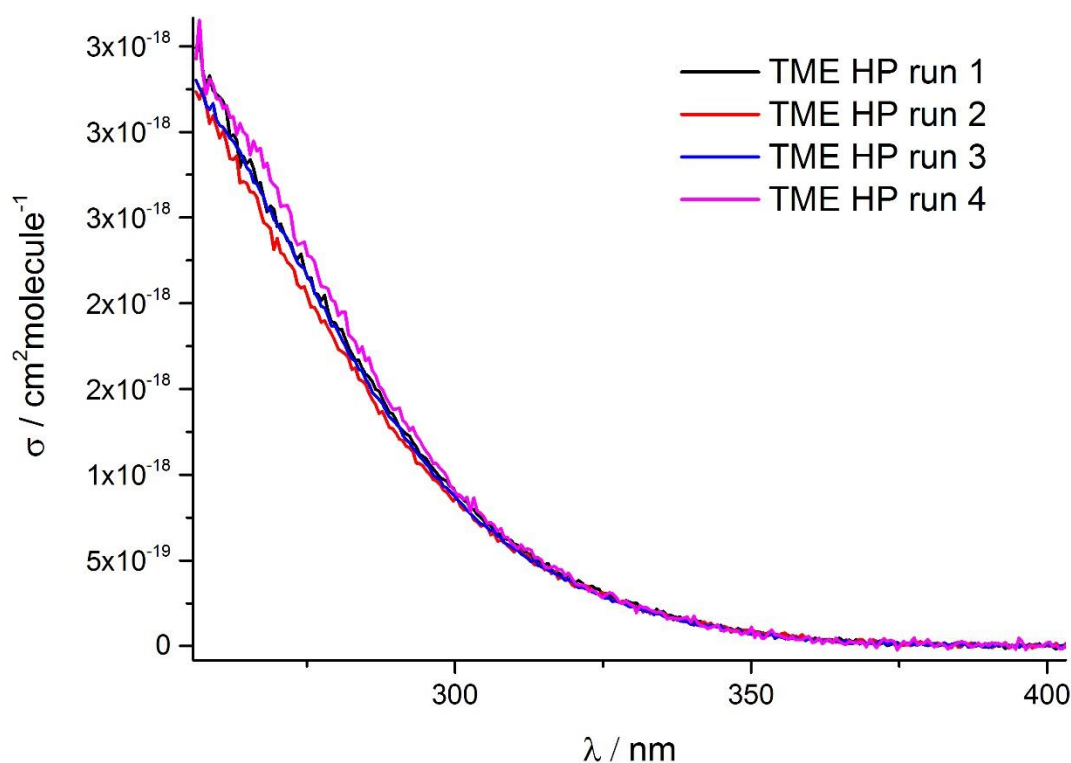
Figure 3.4: Runs 1-4 of the TME HP radical absorption cross-sections. Transient absorption profiles are recorded at 0.57 nm intervals (resolution 1.5 nm) following the pulsed excimer photolysis of H_2O_2-TME-O_2-N_2 mixtures at 248 nm.

Since the upper $\tilde{B}^2A''$ state is unbound, the UV absorption band of the HP radicals are broad and featureless. To improve the data, a Savitzky-Golay[182] smoothing filter is applied to the absorption spectra, as outlined in section 2.3.2. An example of the effect of a Savitzky-Golay filter on an absorption spectrum measurement is shown in Figure 3.5. A second order function (E 2.20) is used to simulate the early time removal of the absorbing species *via.* self-reaction. The value of A_0 is calculated using E 2.20 for a single wavelength, and scaling the whole absorption spectrum by the ratio of the calculated A_0/A_1, correcting for the inability to use the data at t_0 as outlined in section 2.2.7.
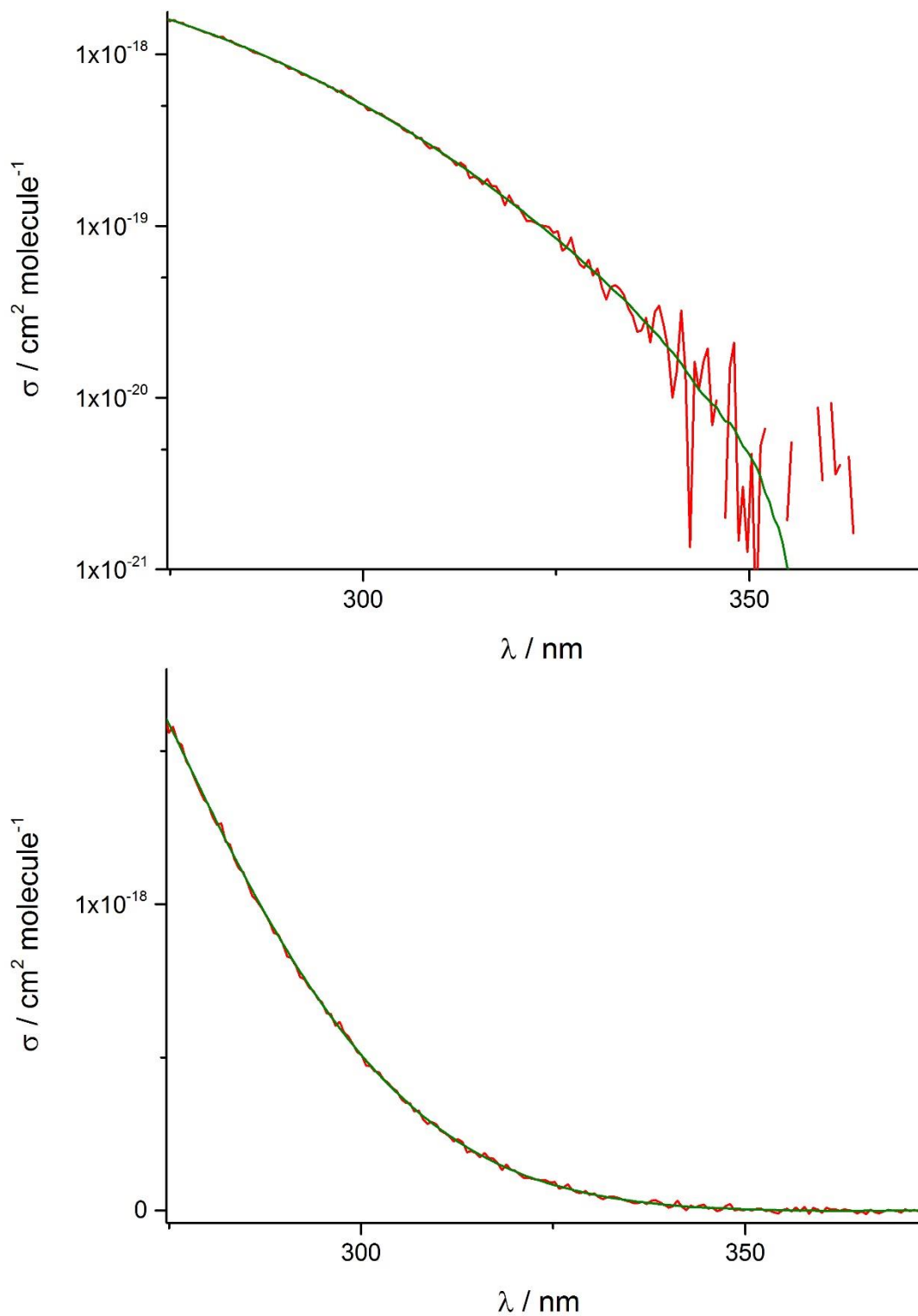
Figure 3.5: An example of the effect of smoothing on a single run of the ethylene HP radical. A second-order Savitzky-Golay[182] filter is applied with 60 points in the window. The plot is shown on both log (top) and linear (bottom) axes.
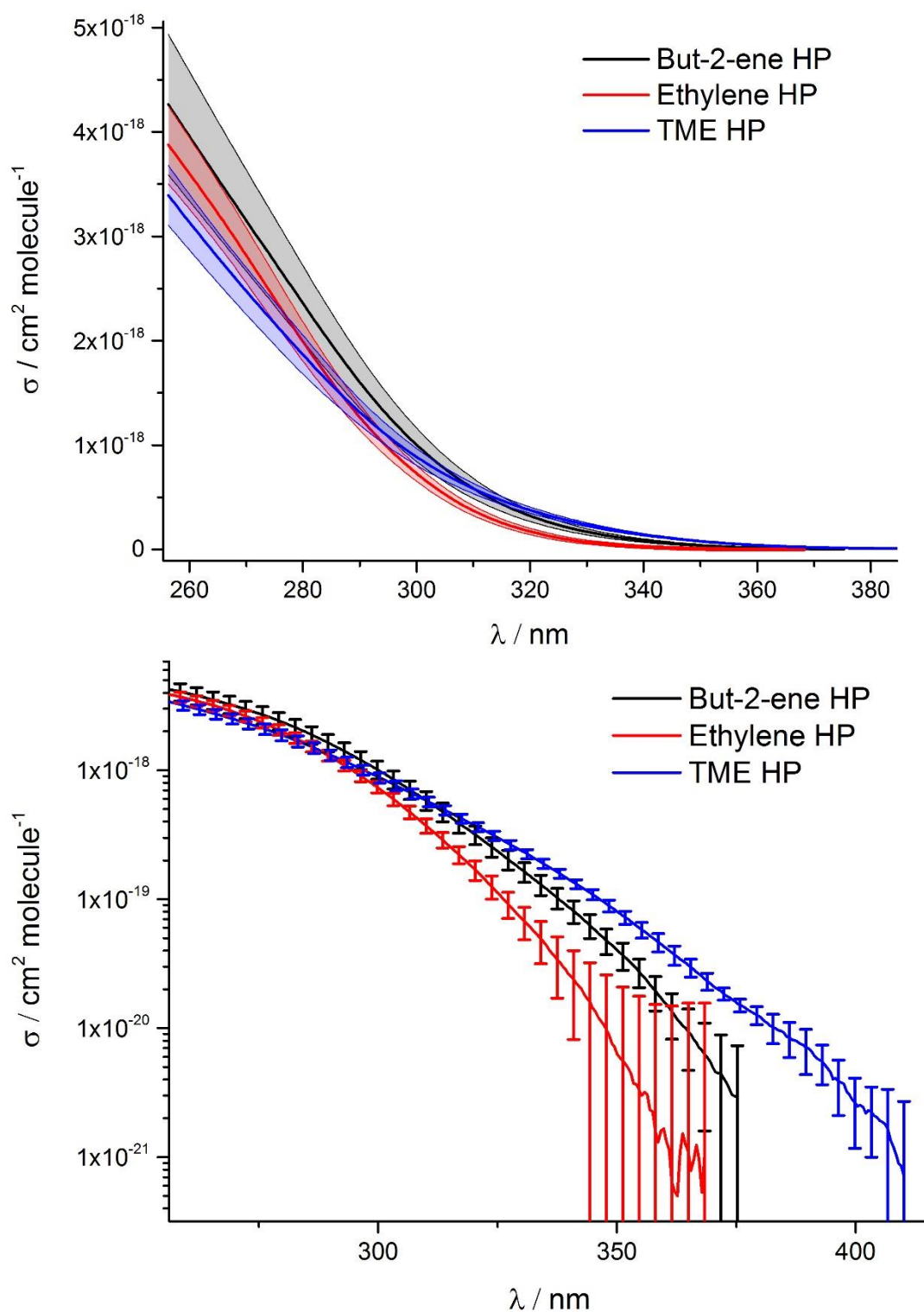
Figure 3.6: Average values for the absorption spectra for the ethylene, but-2-ene and TME HP radicals, with 1σ error bars, shown on linear (top) and logarithmic (bottom) axes. Averages are constructed from the plots shown in Figure 3.2 (ethylene), Figure 3.3 (but-2-ene) and Figure 3.4 (TME) and error bars are constructed from the sum of the standard deviation of the points used in the averaging, and the error in the path length (~5%).

Figure 3.6 shows the ethylene HP, but-2-ene HP and the TME HP on the same axis. It can be seen that the greater the degree of substitution of the peroxy radical centre, the more red-shifted the absorption spectrum, i.e. the absorption spectrum of the tertiary TME HP radical extends further into the visible region than the But-2-ene HP radical absorption spectrum, followed by the ethylene HP. This effect is shown on a logarithmic scale in Figure 3.6, showing the TME HP radical spectrum extending the furthest into the visible region.

The smallest reliable absorption cross-sections are presented here as the point where the 1σ confidence interval value is equal to the calculated absorption cross-section which is 1.6×10^{-20} at 344 nm , 4.4×10^{-21} at 372 nm and 1.65×10^{-21} at 408 nm for the ethylene HP, the but-2-ene HP and TME HP respectively, as shown in Figure 3.7.
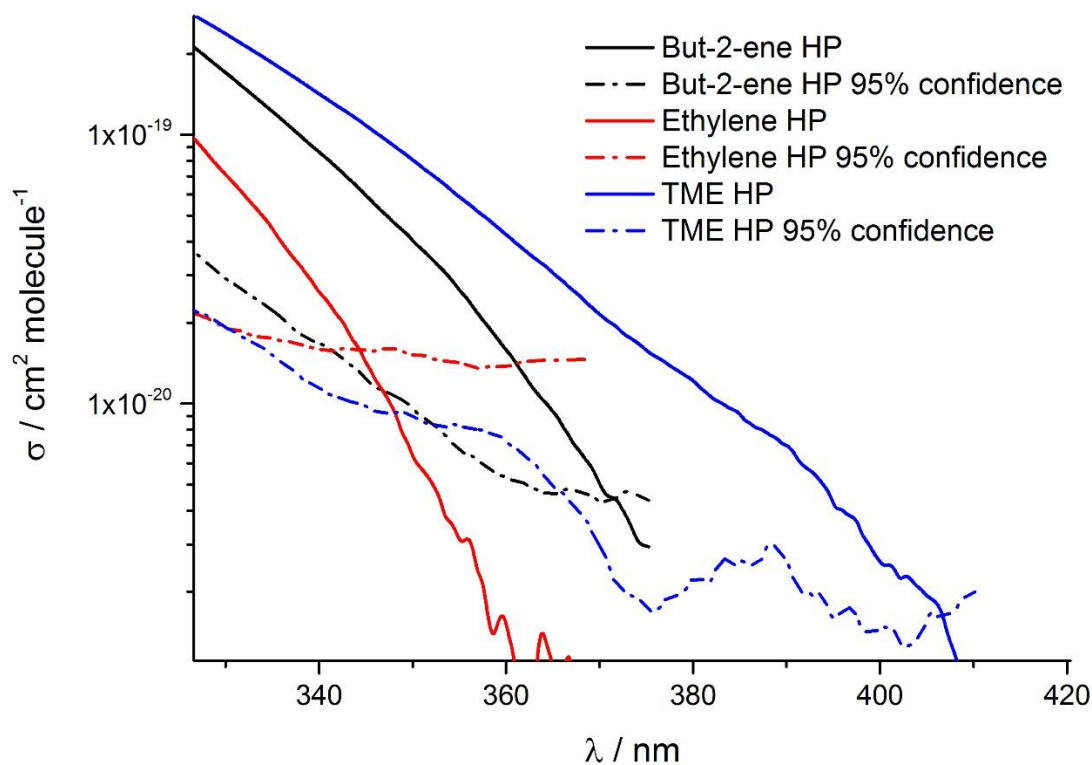
Figure 3.7: A plot showing the absorption cross-sections and the corresponding 1σ error value. The point at which the 2 values are equivalent is given as the lower limit of the absorption cross-sections that have been measured, which are 1.6×10^{-20} at 344 nm , 4.4×10^{-21} at 372 nm and 1.7×10^{-21} at 408 nm for the ethylene HP, the but-2-ene HP and TME HP respectively.

3.4 Existing studies on the absorption spectra of ethylene, but-2-ene and TME hydroxyperoxy radicals

The ethylene HP radical has been studied previously by Cox *et al.*[198], Murrells *et al.*[199] and Anastasi *et al.*[200], disagreeing somewhat on the magnitude and shape of the absorption spectrum. An exhaustive list of previous studies of the ethylene HP radical absorption spectra is shown in Figure 3.8. The spectrum measured in this study most closely resembling the recommended absorption cross-sections in an extensive review of peroxy radical kinetics, spectra and atmospheric chemistry by Lightfoot *et al.*[67]. The recommendation by Lightfoot comprises an average of absorption cross-sections measured in the studies by Murrells *et al.* and Cox *et al.* , excluding the points measured by Cox *et al.* at 270, 280 and 290 nm, deemed subject to considerable uncertainty by the authors). The experiments carried out previously in all 3 of the studies named are significantly different; Anastasi *et al.* generate the ethylene HP radical *via.* pulsed radiolysis of SF_6-H_2-C_2H_4-O_2 mixtures using 2-MeV electrons from a field emission accelerator. The spectrum measured by Anastasi *et al.* exhibits significant absorption cross-sections below 210 nm, and absorption cross-sections above 210 nm smaller than the studies by Jenkin *et al.* and Murrells *et al.* indicating prompt formation of HO_2 unaccounted for in their analysis. Another drawback of the method used by Anastasi *et al.* is the high concentration of the ethylene HP ($\sim 10^{15}$ cm^{-3}) and inefficient conversion of F to ethylene HP necessitating of the use of estimated rate coefficients to calculate the concentration of the analyte.

Murrells *et al.* employ the reactions R 3.1-R 3.4 to generate the ethylene, but-2-ene and TME HP radicals, in both flash photolysis and molecular modulation experiments. Both methods give the same result within the error limits of each method, suggesting the model used by Murrels *et al.* to calculate [RO_2] are accurate.
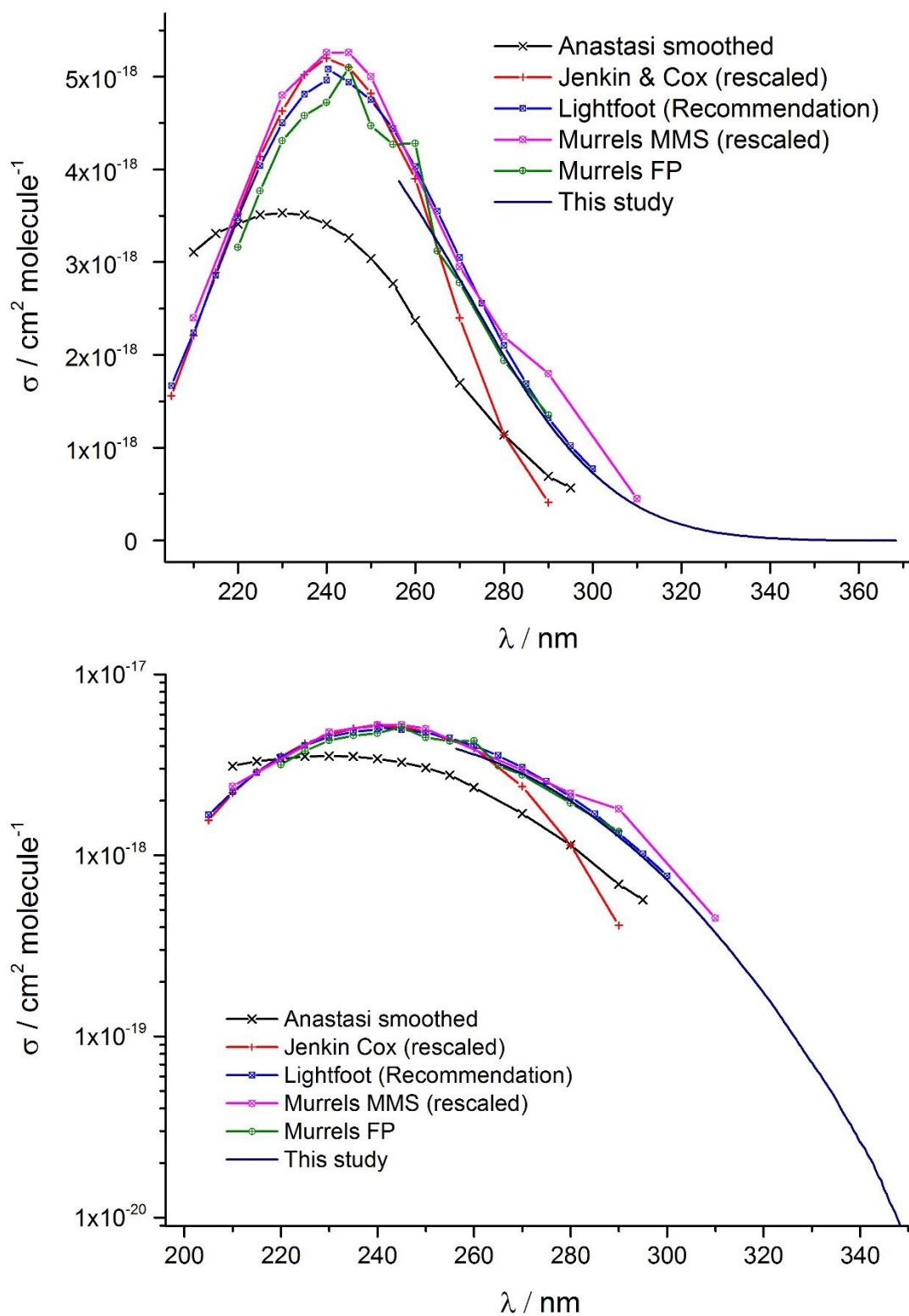
Figure 3.8: Previous studies on the absorption spectrum of the ethylene HP radical by Anastasi *et al.*[200], Cox *et al.*[198] and Murrells *et al.*[199] as well as recommendations from Lightfoot[67], alongside the absorption cross-sections measured in this study. The recommended absorption cross-sections by Lightfoot *et al.* are given to 7.7×10^{-19} at 300 nm and represent the smallest reliable literature absorption cross-sections available.

The spectra of but-2-ene HP and TME HP have previously been studied by Murrells *et al.*[201], representing the only published work on the absorption spectra of these radicals. Whilst the substituted ethylene HP radicals (but-2-ene and TME HP) are of less atmospheric importance than the ethylene HP radical, they are useful for illustrating the effect of substituent groups on the peroxy radical centre. The spectra recorded in this study are in good agreement with the spectra measured by Jenkin *et al.*, exhibiting similar shape and magnitude and agreeing within the error of each set of measurements (Figure 3.9 and Figure 3.10).
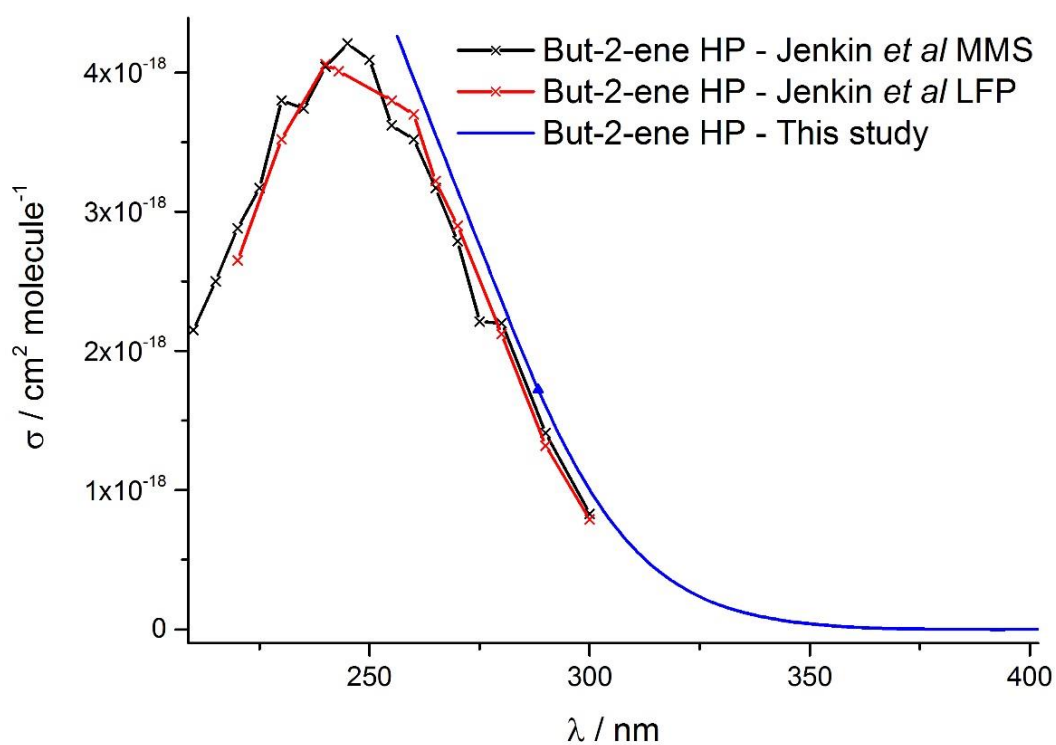
Figure 3.9: previous absorption cross-sections measured for the but-2-ene HP radical by Jenkin *et al.*[201] using Molecular Modulation Spectroscopy MMS and Laser Flash Photolysis (LFP) methods. The smallest absorption cross-sections measured by Jenkin *et al.* are 8.3 and 7.9 $\times$ 10^{-19} cm^2 molecule^{-1} at 300 nm for MMS and LFP methods respectively. The absorption cross-sections measured in this study are shown in blue.
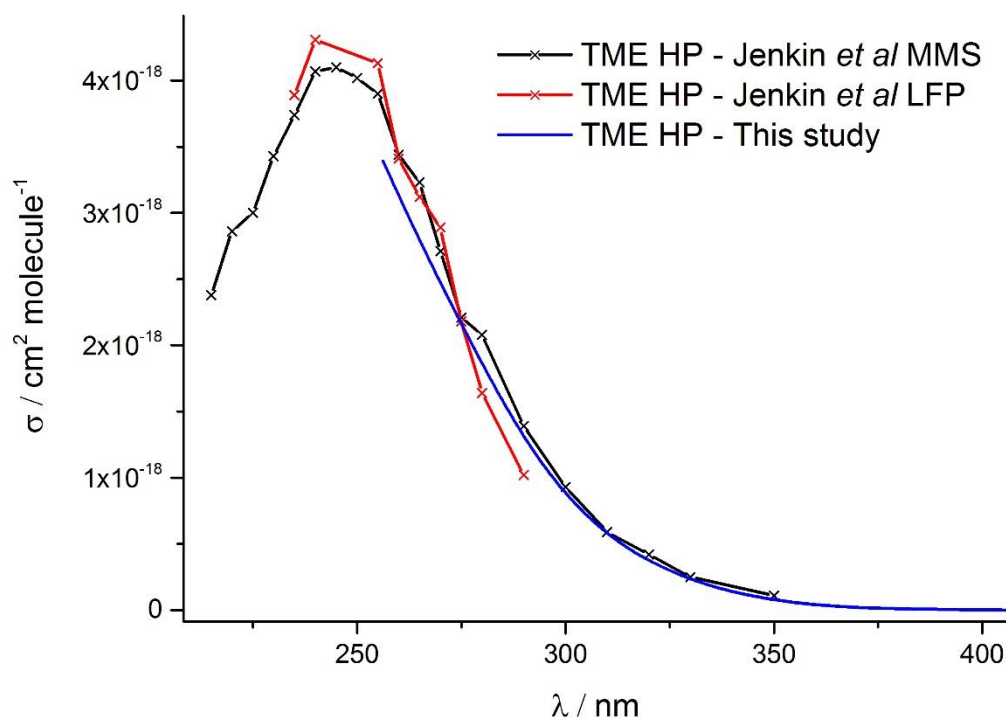
Figure 3.10: previous absorption cross-sections measured for the TME HP radical by Jenkin *et al*.[201] using MMS and LFP methods. The smallest absorption cross-sections measured by Jenkin *et al*. are 1.1×10^{-19} at 350 nm and 1.02×10^{-18} cm^2 molecule^{-1} at 290 nm for MMS and LFP methods respectively. The absorption cross-sections measured in this study are shown in blue.

3.5   Atmospheric photolysis rates:

The absorption cross-sections of the ethylene, but-2-ene and TME HP have been measured beyond 280 nm, where solar flux increases sharply. The excitation of HP radicals *via*. absorption of a photon results in photolysis of the molecule *via*. the unbound upper $\tilde{B}$ state, as described in section 1.2.3. Calculating the rate of the photolysis of these species in the atmosphere is important, as currently it is not included as a loss process of HP radicals in models, and could be a significant sink for RO$_2$ in the atmosphere. Calculating total photolysis rates requires both the absorption cross-sections of the molecule, as well as the total solar flux at a certain date, time and place. The Tropospheric Ultraviolet and Visible radiation model[77] (TUV) calculates solar flux as a function of wavelength, in this case at intervals of 1 nm, giving Actinic flux / (quanta s^{-1} cm^{-2} nm^{-1}) vs wavelength / (nm). The data generated by the instrument in this study has wavelength intervals of .57 nm, and must be fitted with a suitable function, so that absorption cross-sections can be aligned with the output from TUV. A simple Gaussian function is used to fit the experimental data, as shown in Figure 3.11. A Gaussian function (E 3.2) was used to

fit to the experimental data, as shown in Figure 3.11, with parameters given in Table 3.2.

$$y = \frac{a}{w\sqrt{\pi/2}} e^{-2\left(\frac{x-x_c}{w}\right)^2} \qquad \text{E 3.2}$$

Table 3.2: Parameters from Gaussian function shown in E 3.2, where x_c is the wavelength at which the Gaussian function is at a maximum, w is the Gaussian width at one tenth the height of the maximum and a is the height of the curve's peak.

	Ethylene HP	**But-2-ene HP**	**TME HP**
x_c	241	247	252
w	67.1 nm	74.6 nm	84.6 nm
a	2.43×10^{-16}	2.83×10^{-16}	2.21×10^{-16}
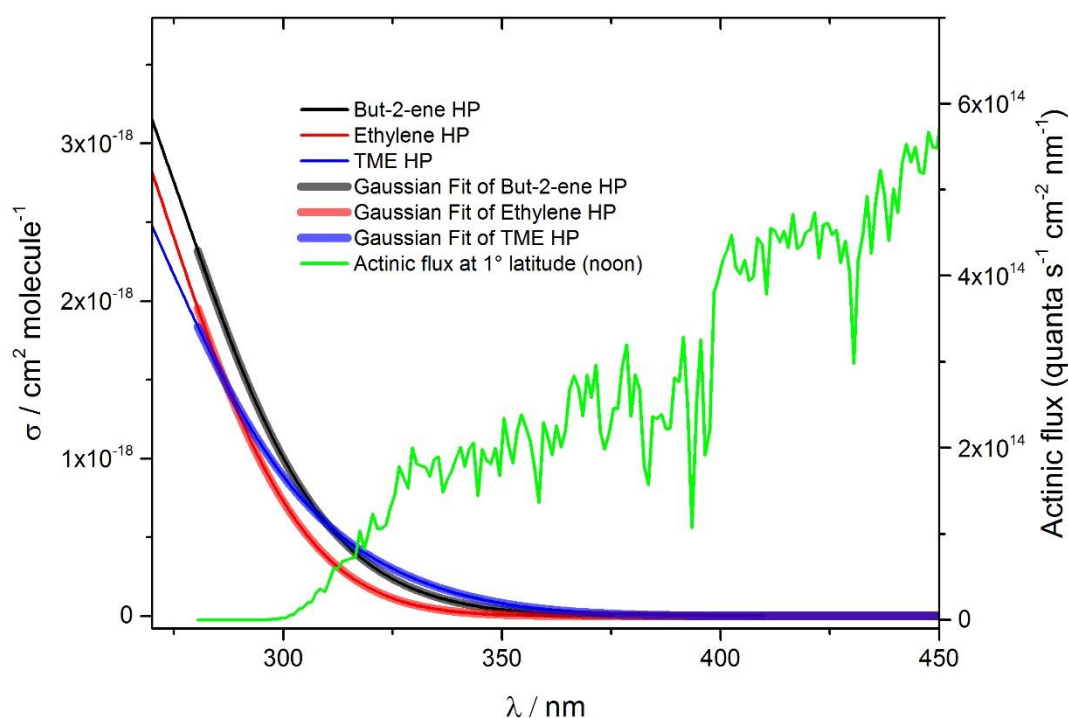
Figure 3.11: Gaussian fits to the experimental data, necessary for calculating photolysis rates (Left Y axis). Actinic flux at 1° latitude at 12 noon calculated by TUV is shown in green (right Y axis).

To calculate the total photolysis frequency (the rate of loss of the HP radical due to photolysis, regardless of the products), J_{total} the photolysis frequency at each wavelength $J_{\lambda,\text{total}}$ is calculated for each of the ethylene, but-2-ene and TME HP radicals. To calculate $J_{\lambda,\text{total}}$ the total photolysis frequency at a particular wavelength, the absorption cross-section is multiplied by the radiant (actinic) flux ($S_{e,\lambda}$) at

wavelength λ (E 3.3). . Figure 3.12 shows $J_{\lambda,total}$ as a function of λ for each HP radical; the photolysis rates for the 3 HP radicals increase at all wavelengths in the order TME HP > but-2-ene HP > ethylene HP. To quantify the total photolysis rate in the atmosphere, J_{total} must be calculated (E 3.4) by integrating the $J_{\lambda,total}$ vs λ function, to find the total area underneath the plot. The broad, featureless UV absorption band common to all peroxy radicals is due to excitation to the repulsive $\tilde{B}$ state, and so the quantum yield for dissociation from the excited state ($\phi_{dissociation}$) is assumed to be 1. To calculate $J_{\lambda,total}$, the absorption cross-section is multiplied by radiant (actinic) flux ($S_{e,\lambda}$) at wavelength λ. Total photolysis rates for each HP radical calculated at noon and 1° latitude are given in Figure 3.12. TME HP has the fastest rate of photolysis in the atmosphere, with a rate of 1.68×10^{-3} s^{-1} , followed by but-2-ene HP with a rate of 1.21×10^{-3} s^{-1} and ethylene with a rate of 0.552×10^{-3} s^{-1}. Actinic flux at 1° latitude is used in this example as it corresponds to the latitude of Borneo in Southeast Asia's Malay Archipelago, which was subject to an extensive field campaign Oxidant and Particle Photochemical Processes above a Southeast Asian tropical rainforest (OP3)[119, 123, 124].

$$\sigma_\lambda \cdot S_{e,\lambda} = J_{\lambda,total} \qquad\qquad \text{E 3.3}$$

$$J_{total} = \Sigma(\sigma_\lambda \cdot S_{e,\lambda}) \qquad\qquad \text{E 3.4}$$

Large amounts of of biogenic VOCs are emitted by plants in rainforest environments, the primary sink of which is *via.* reaction with OH. Unsaturated compounds undergo OH addition, and subsequently O_2 addition in the atmosphere (for example the reactions R 3.2-R 3.4) to form HP radicals. The most dominant removal processes for these HP radicals is *via.* reaction with NO (R 3.9) and HO_2 (R 3.10).

$$HOCH_2CH_2OO + NO \rightarrow HOCH_2CH_2O + NO_2 \qquad\qquad \text{R 3.9}$$

$$HOCH_2CH_2OO + HO_2 \rightarrow HOCH_2CH_2OOH + O_2 \qquad\qquad \text{R 3.10}$$

The rate coefficients of these reactions are included in the MCM, and at 300 K are equal to 9.0×10^{-12} and 1.2×10^{-11} cm^3 molecule^{-1} s^{-1} for R 3.9 and R 3.10 respectively.
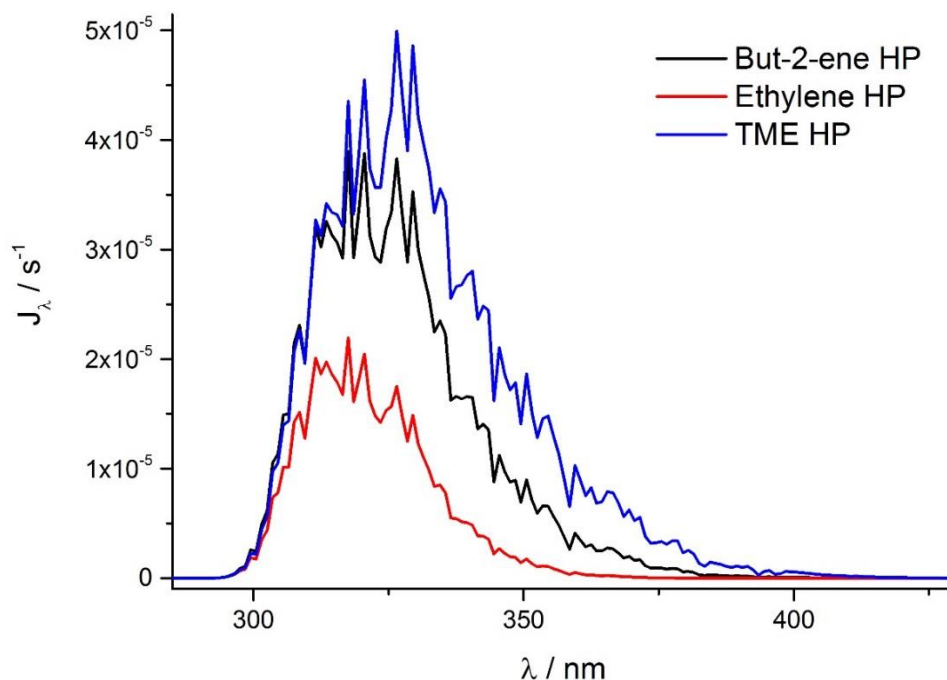
Figure 3.12: J_λ **values for the ethylene, but-2-ene and TME HP radicals calculated from the actinic flux at noon and 1° latitude calculated by ACOM TUV[77]. The total photolysis rates (J) of these HP radicals is calculated by integrating each function.**

Table 3.3: removal rates of the ethylene, but-2-ene and TME HP radicals *via.* photolysis

	Ethylene HP radical	But-2-ene HP radical	TME HP radical
J_{total} / 10^{-3} s^{-1}	0.552	1.21	1.68

NO and HO$_2$ concentrations of 1×10^9 and 2×10^8 molecule cm^{-3} were used based on average noon values measured during the OP3 campaign in Borneo[2, 29, 120, 123, 124], yielding removal rates of the ethylene HP radical of 8.9×10^{-3} and 2.3×10^{-3} s^{-1}, corresponding to lifetimes of 1.9 and 7.2 minutes respectively (Table 3.4. Removal of ethylene HP by photolysis has a rate of 0.552×10^{-3} s^{-1} which represents 5 % of the rate of removal *via.* reaction with NO and HO$_2$, as shown in Figure 3.13 and a lifetime of 30.2 minutes. Removal of ethylene HP radicals *via.* Photolysis is a process which should be included when considering the fate of the ethylene HP radical in near-pristine environments.

Table 3.4: The lifetime of the ethylene HP radical with respect to the 3 removal processes outlined here, based on [NO] = 1.0×10^9 molecule cm^{-3}, [HO$_2$] = 2.2×10^8 molecule cm^{-3}.

Removal process	τ_{RO2} / minutes
NO	1.9
HO$_2$	7.2
Photolysis	30.2
Total	1.4
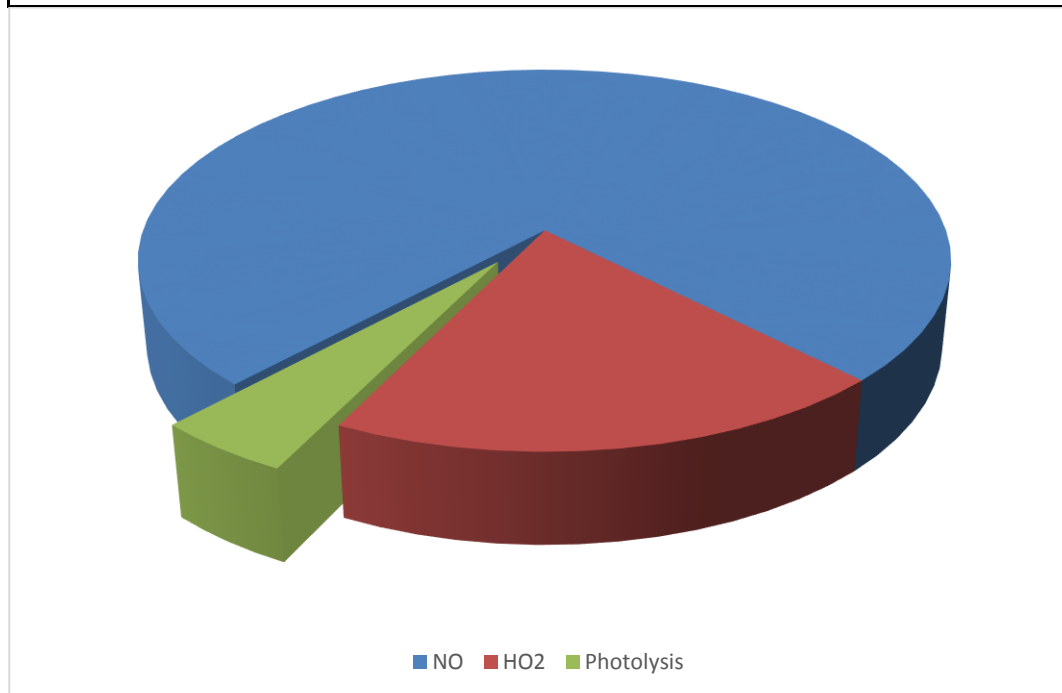
Figure 3.13: Removal rates of the ethylene HP radical. Removal *via.* reaction with NO and HO$_2$ comprise 75.7 and 19.6% of the total removal rate at noon in Borneo respectively. Photolysis of the ethylene HP radical comprises 4.7% of the total removal rate under these conditions.

If the rate of photolysis of the ethylene HP radical is important for its budget, it follows that the products of the photolysis should be considered. The principal aim of this investigation, in conjunction with the work carried out by Dr Hansen into the absorption cross-sections of HP radicals, was to test the propensity of these radicals to photolyse to OH, in an attempt to reconcile measured and modelled OH concentrations in remote, low NO$_x$, high VOC environments such as the Borneo rainforest studied in the OP3 campaign[119, 123, 124]. Whilst the instrument in this work is effective for measuring absorption cross-sections of peroxy radicals, determination of the products of the photolysis is precluded by the absence of products with strong absorption features. Alongside the work carried out with the TRUVAS instrument, a 3-laser photolysis experiment was employed by Dr. Robert Hansen to measure the

absorption cross-section for OH production of various peroxy radicals[194], including the ethylene and TME HP radicals between 310 and 362.5 nm (Figure 3.14). In short, a radical precursor is photolysed within a LIF cell at 248 nm, to yield radicals; in the case of the ethylene and TME HP radicals, hydrogen peroxide is photolysed to yield 2 OH radicals, as per R 3.1. OH radicals react with ethylene or TME *via.* R 3.2 or R 3.6 and subsequently with O_2 *via.* R 3.3 or R 3.7 to form the corresponding HP radical. The reaction mixture is then photolysed a second time using a high energy, tuneable YAG pumped dye laser to photolyse the HP radicals, followed by a 308 nm OH probe laser, at a delay of typically 1-2 µs. OH is detected *via.* LIF at 308 nm before and after the tuneable photolysis laser, with the increase in OH observed immediately prior to the 248 nm photolysis assigned as OH from RO_2 photolysis. The absorption cross-section for OH formation from an RO_2 radical $(\sigma_{RO_2,OH})$ is equal to the total absorption cross-section $(\sigma_{RO_2,\lambda})$ multiplied by the quantum yield for OH production $(\phi_{RO_2,\lambda})$. The OH absorption cross-section at a particular wavelength in the experiments by Dr Hansen, is dependent on the absorption cross-section of the radical precursor at that wavelength, as illustrated in E 3.5 and E 3.6.

$$
\begin{aligned}
\frac{OH_{RO_2}}{OH_{H_2O_2}} &= \frac{[RO_2]_0 \times [h\nu]_\lambda \sigma_{RO_2,\lambda}\phi_{RO_2,\lambda}}{[H_2O_2] \times [h\nu]_\lambda \sigma_{H_2O_2,\lambda}\phi_{H_2O_2,\lambda}} \\
&= \frac{[h\nu]_{248\,nm}[H_2O_2]\sigma_{H_2O_2,248\,nm}\phi_{H_2O_2,248\,nm} \times [h\nu]_\lambda \sigma_{RO_2,\lambda}\phi_{RO_2,\lambda}}{[H_2O_2] \times [h\nu]_\lambda \sigma_{H_2O_2,\lambda}\phi_{H_2O_2,\lambda}} \quad \text{E 3.5} \\
&= \frac{[h\nu]_{248\,nm}\sigma_{H_2O_2,248\,nm}\sigma_{RO_2,\lambda}\phi_{RO_2,\lambda}}{\sigma_{H_2O_2,\lambda}}
\end{aligned}
$$

$$
\sigma_{RO_2,\lambda}\,\phi_{RO_2,\lambda} = \frac{\sigma_{H_2O_2,\lambda}}{[h\nu]_{248\,nm}\sigma_{H_2O_2,248\,nm}} \quad \text{E 3.6}
$$

where OH_{RO_2} and $OH_{H_2O_2}$ represent the OH generated from 248 nm photolysis of the corresponding peroxy radical and hydrogen peroxide respectively; $[RO_2]_0$ is the concentration of RO_2 radicals at t_0; $[h\nu]_\lambda$ is the number of photons of wavelength λ; $\sigma_{RO_2,\lambda}$ and $\phi_{RO_2,\lambda}$ are the absorption cross-sections and OH quantum yields of the peroxy radical at wavelength λ; $[H_2O_2], \sigma_{H_2O_2,\lambda}$ and $\phi_{H_2O_2,\lambda}$ are the concentration, absorption cross-section and OH quantum yield for hydrogen peroxide at wavelength λ respectively.
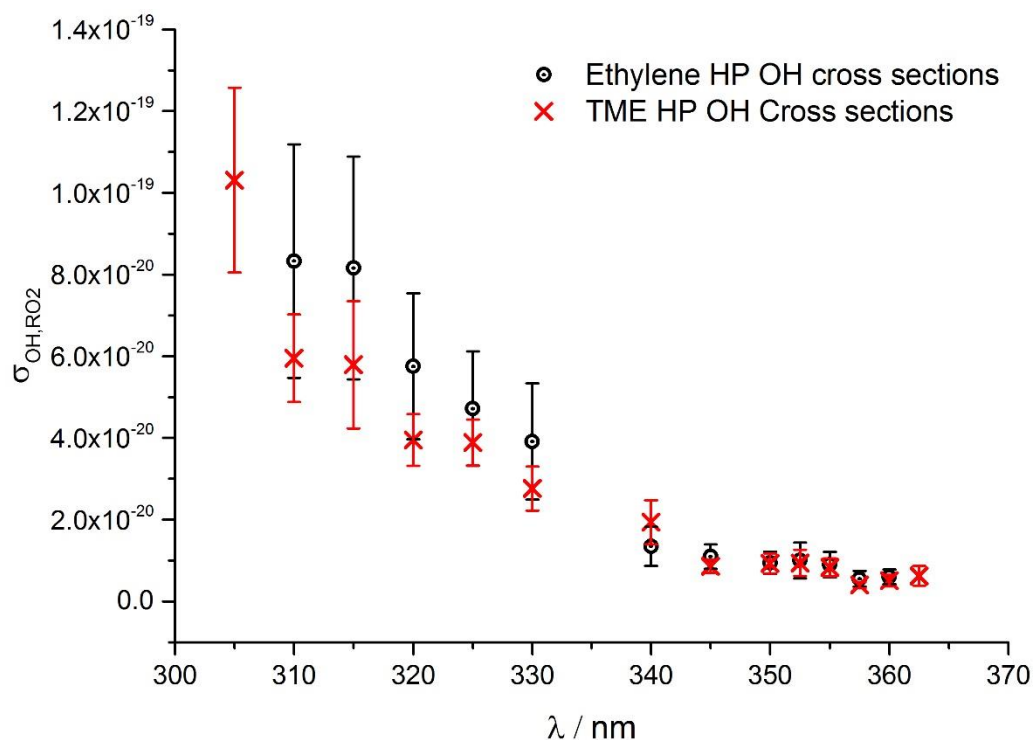
Figure 3.14: The absorption cross-section for OH production of the ethylene and TME HP radicals as measured by Dr. Robert Hansen using the 3 laser experiment. Values are given as averages of a number of runs, and errors are propagated from the standard deviation of the results.
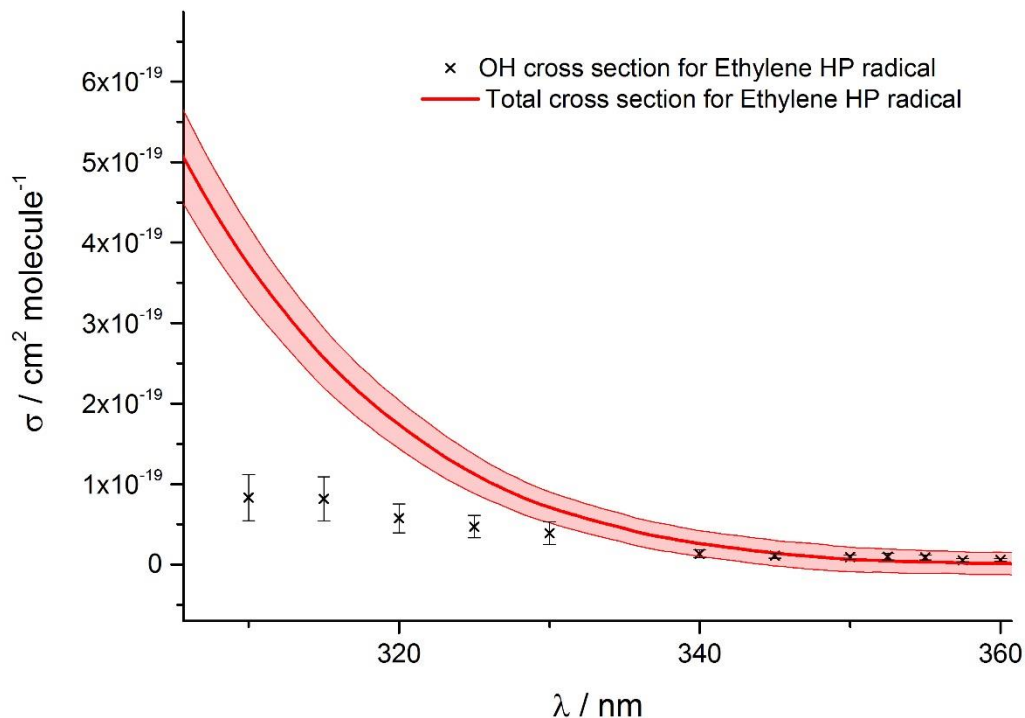
Figure 3.15: Total absorption cross-sections of the ethylene HP radical as measured by the TRUVAS instrument, with the 1σ confidence band (red). The absorption cross-sections for OH generation are shown (black crosses) with confidence limits. As shown in Figure 3.7, the smallest reliable absorption cross-sections measured by the TRUVAS instrument for the ethylene HP radical are around 344 nm.
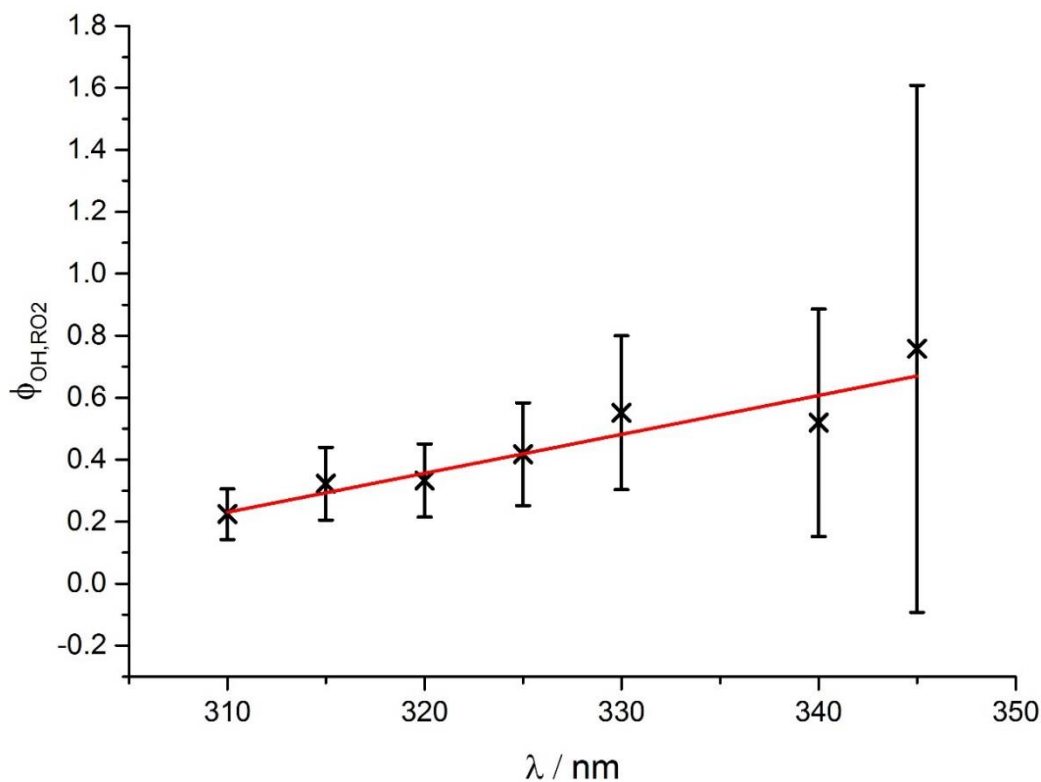
Figure 3.16: The OH quantum yield ($\phi_{OH,RO2}$) for the ethylene HP radical, from the ratio of $\sigma_{OH,\lambda}/ \sigma_{total,\lambda}$ between 310 – 345 nm. The quantum yield appears to increase as a function of wavelength, a linear fit yields a gradient of 0.0126 ± 0.0017.
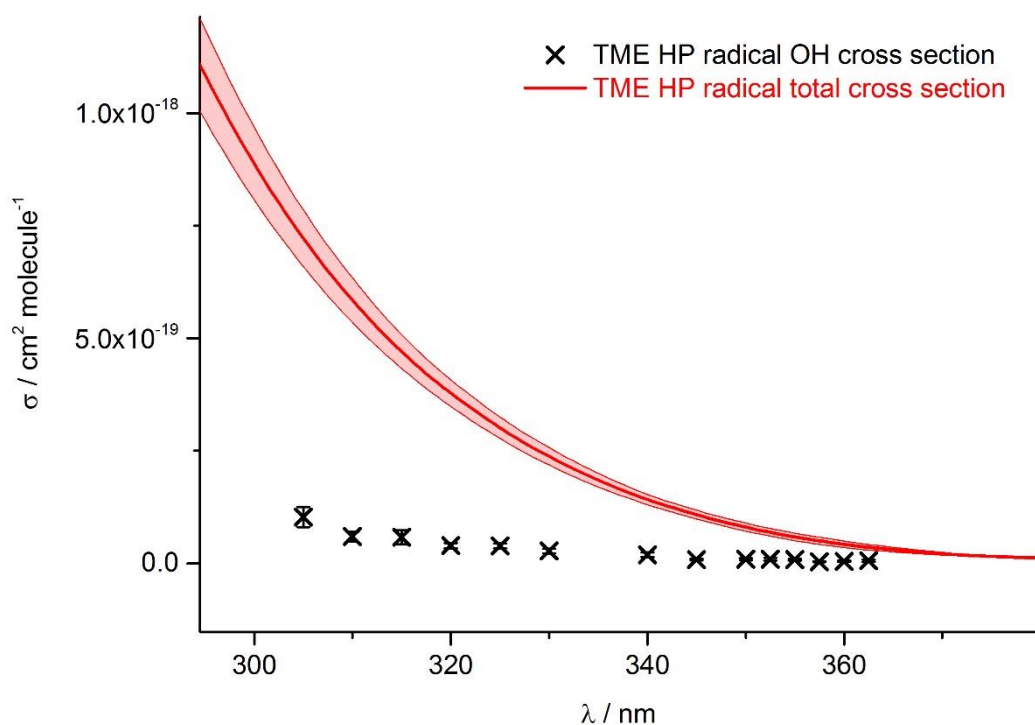
Figure 3.17: Total absorption cross-sections of the TME HP radical as measured by the TRUVAS instrument, with confidence limits (red). The absorption cross-sections for OH generation are shown (black crosses) with confidence limits. As shown in Figure 3.7, the smallest reliable absorption cross-sections measured by the TRUVAS instrument for the TME HP radical are around 408 nm.
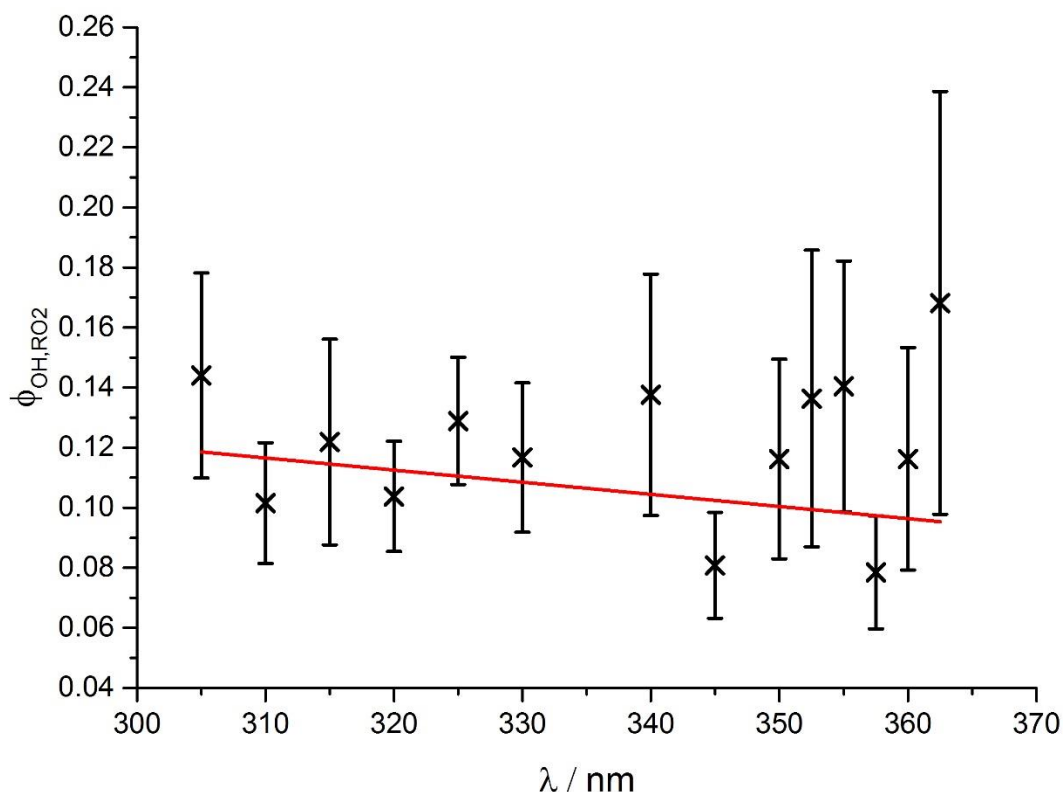
Figure 3.18: The OH quantum yield ($\phi_{OH,RO2}$) for the TME HP radical, from the ratio of $\sigma_{OH,\lambda}$/ $\sigma_{total,\lambda}$ between 305 – 363 nm. The quantum yield appears to decrease as a function of wavelength, a linear fit yields a gradient of -0.0004±0.0003.

3.6   Discussion

The measurements of the 3 HP radical total absorption cross-sections outlined here show a clear trend; the more substituted the peroxy radical carbon centre, the more red-shifted the absorption cross-section into the actinic window. Although the extent of the enhanced absorption cross-sections in the actinic window appear small, actinic flux rises sharply beyond 280 nm, amplifying the increase in the photolysis rates disproportionately, as shown in Figure 3.12, whereby the overall photolysis rate (at noon in Borneo) of the secondary but-2-ene HP radical (1.21×10^{-3} s^{-1}) is more than double that of the ethylene HP radical (0.552×10^{-3} s^{-1}), and the TME HP radical photolysis rate is faster still (1.68×10^{-3} s^{-1}). Whilst the ethylene HP radical is the most atmospherically relevant of the 3 HP radicals outlined in this chapter, the comparison between their absorption spectra is important when considering structure

activity relationships. Previous studies have shown that electron withdrawing groups attached to the peroxy radical carbon centre have the propensity to shift the absorption spectra towards shorter wavelengths[66]. In this study, it has been demonstrated that the electron pushing alkyl groups attached to the peroxy radical centre has the opposite effect; red-shifting absorption spectra to extend to longer wavelengths, dramatically increasing the photolysis rates of HP radicals in the atmosphere, as shown in Figure 3.12. OH production absorption cross-sections of the ethylene and TME HP radicals are of similar magnitude over the range $305 - 360$ nm. OH quantum yields from the photolysis of ethylene and TME HP radicals in the atmosphere are around 35% (Figure 3.15, Figure 3.16) and 12% (Figure 3.17, Figure 3.18) respectively.

Clear red shifting and broadening of the $\tilde{B} - \tilde{X}$ absorption band observed for the 3 alkene HP radicals is observed. The electronic ground and excited states of all HP radicals discussed here are assumed to be analogous to those of methyl peroxy (CH_3O_2), which is the most well characterised peroxy radical.[61, 62, 70-72, 198, 202] Miller *et al*. describe a shift in the position (λ_{max}) of the near IR $\tilde{A} - \tilde{X}$ electronic absorption band of alkyl peroxy radicals, observing red shifting as the number of carbons in the alkyl chain increases. Miller *et al*. attribute the red shifting of the IR absorption band to the destabilisation of the ground electronic $\tilde{X}$ state due to inductive effects from the additional alkyl groups attached to the α peroxy carbon centre. Destabilisation of the ground electronic state of the peroxy radical is thought to coincide with an increase in energy the electronically excited states, and so for a change in the transition energy to be observed, the destabilisation of the ground state must exceed that of the excited state giving rise to the transition. The alkyl groups effectively donate electron density toward the electronegative O atom bonded directly to the α carbon, which serves to decrease the polarisation, and therefore electrostatic restoring force of the O-O bond.

Figure 3.19: Suggested explanation for the broadening observed due to inductive effects from alkyl substitution of the α peroxy carbon. The blue potential curve represents the O-O bond adjacent to the least substituted (primary) α carbon, and has the narrowest and deepest potential energy well. The green curve represents the secondary peroxy radical, and the red curve represents the tertiary potential energy well. Note this diagram is both speculative and qualitative.

Figure 3.19 shows a qualitative illustration of the proposed effect of the induction of electron density from alkyl groups toward the peroxy moiety; increased substitution destabilises the O-O bond stretch for the ground state, resulting in a broader, shallower well. Miller *et al.*[72] calculated an increase in the energy of the ground state for the alkyl peroxy series methyl , ethyl, propyl and butyl peroxy. A destabilisation of ~10 kJ mol^{-1} per additional carbon in the alkyl chain attached to the peroxy radical carbon centre was observed between methyl and ethyl peroxy, with the effect diminishing with increasing total chain length to ~3 kJ mol^{-1} for the change in the ground state energy between n-propyl and n-butyl peroxy radicals. A broader and shallower well would be expected to have more population in higher vibrational states, facilitating excitation to the upper state at longer wavelengths.

The electronically excited states of the methyl peroxy radical have been calculated by Jafri *et al.*, who provides potential energy surface information with respect to the O-O and C-O bond stretch, as shown in Figure 3.20. Dissociation about the C-O bond would give rise to an alkyl radical and molecular oxygen (R 3.12-R 3.14).
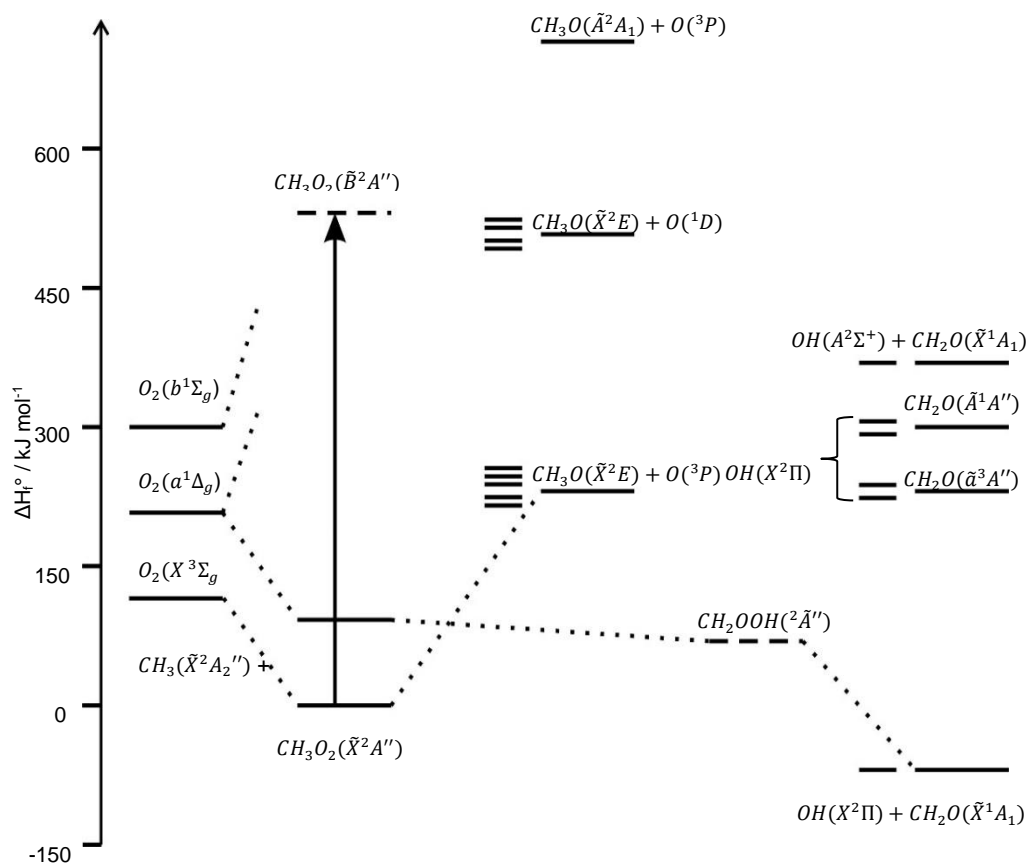
Figure 3.20: Energy and correlation diagram for the electronic excitation of methyl peroxy, and the products of excited methyl peroxy: Products of C-O bond cleavage are shown on the left, and products from O-O bond cleavage are shown on the right. Reproduced from Hartmann *et al.*[71]

Hartmann *et al.* propose a mechanism for OH formation from electronic excitation of CH_3O_2 *via.* a non-adiabatic process (i.e. one which involves a crossing between 2 excited state potential energy surfaces) involving isomerisation of excited $CH_3O_2(\tilde{B}^2A'')$ to excited $CH_2OOH(^2\tilde{A}'')$ and then subsequent dissociation to $CH_2O(\tilde{X}^1A_1)$ plus rotationally hot $OH(A^2\Sigma^+)$.[71] Hartmann *et al.* also note that excitation of CH_3O_2 at 248 nm could produce $O(^1D)$, which would react rapidly to

form the observed OH($A^2\Sigma^+$), however the experiments carried out by Dr Hansen at the University of Leeds show OH production from the excitation of CH$_3$O$_2$ at wavelengths longer than the threshold wavelength for O(^{1}D) (273 nm - Table 3.5).

Table 3.5: Potential reaction pathways resulting from electronic excitation of ground state CH$_3$O$_2$ ($\widetilde{X}^2A''$). $\varDelta H_R$ /kJ mol^{-1} represents the change in potential energy between the ground state CH$_3$O$_2$ and the corresponding intermediate or product. Threshold wavelength is the longest λ able to excite ground state CH$_3$O$_2$ to its corresponding state in a 1-photon absorption process. Symmetries are taken from Hartmann *et al*.[71]

Reaction	$\varDelta H_R$ /kJ mol^{-1}	Threshold Wavelength / nm	
$CH_3O_2(\widetilde{X}^2A'') + h\nu \rightarrow CH_3O_2(\widetilde{B}^2A'')$	-	-	R 3.11
$\rightarrow CH_3(\widetilde{X}^2A_2'') + O_2(X^3\Sigma_g)$	129.0	927	R 3.12
$\rightarrow CH_3(\widetilde{X}^2A_2'') + O_2(a^1\varDelta_g)$	223	836	R 3.13
$\rightarrow CH_3(\widetilde{X}^2A_2'') + O_2(b^1\Sigma_g)$	286	418	R 3.14
$\rightarrow CH_3O(\widetilde{X}^2E) + O(^1D)$	438	273	R 3.15
$\rightarrow CH_3O(\widetilde{X}^2E) + O(^3P)$	248	482	R 3.16
$\rightarrow CH_2OOH(^2\widetilde{A}'')$	293	408	R 3.17
$CH_2OOH(^2\widetilde{A}'') \rightarrow OH(A^2\Sigma^+) + CH_2O(\widetilde{X}^1A_1)$	299	400	R 3.18
$\rightarrow OH(X^2\Pi) + CH_2O(\widetilde{X}^1A_1)$	-88	-	R 3.19
$\rightarrow OH(X^2\Pi) + CH_2O(\widetilde{A}^1A'')$	243	493	R 3.20

Ethylene HP radical photolysis experiments were carried out in a Helium-H$_2$ buffer mixture by Dr Hansen in order to confirm or deny the production of O(^{1}D) by detection of OH($A^2\Sigma^+$), which would be formed *via.* reaction R 3.21. Indeed no OH($A^2\Sigma^+$) was detected, suggesting the route to OH formation from ethylene and TME HP radical photolysis is not occurring *via.* O(^{1}D), but *via.* the isomerisation route similar to that suggested by Hartmann *et al*. for CH$_3$O$_2$.

$$O(^1D) + H_2 \rightarrow OH(X^2\Pi) + H \qquad\qquad \text{R 3.21}$$

Zhu *et al*. have more recently calculated the possible fates of excited CH_3O_2, proposing a concerted H-migration/OH-elimination mechanism from the excited $CH_2OOH(^2\tilde{A}'')$ transition state, which lies 288 kJ mol^{-1} above the $OH(X^2\Pi) + CH_2O(\tilde{X}^1A_1)$ products.[75] The transition state $CH_2OOH(^2\tilde{A}'')$ lies 293 kJ mol^{-1} above the $CH_3O_2(\tilde{X}^2A'')$ ground state, corresponding to a threshold frequency of 408 nm. Upon excitation to the electronically excited state, the reaction proceeds *via.* the repulsive $\tilde{B}$ state, before either continuing along the O-O bond stretch to yield the alkoxy radical and O(^{3}P) or crossing *via.* the $^2\tilde{A}''$ transition state resulting in concerted H-migration/OH-elimination.

A similar reaction pathway from the excited $\tilde{B}$ state of ethylene and TME HP radicals is the most likely route to the photolytic formation of OH observed by Dr Hansen. The mechanism for H-migration/OH-elimination proposed by Zhu *et al*. occurs *via.* a 4 membered transition state in the methyl peroxy radical.
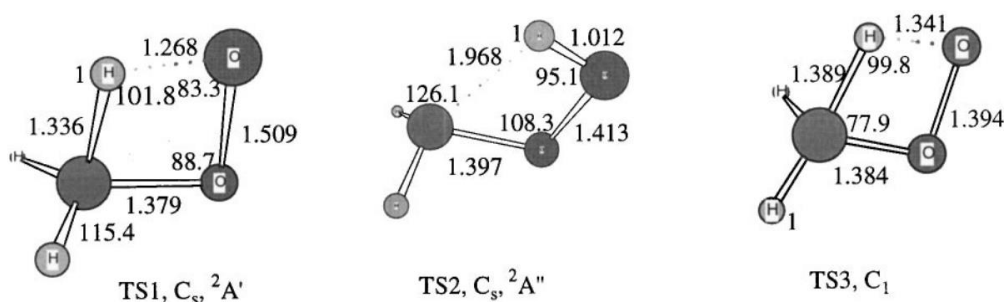
Figure 3.21: The configurations of the 3 transition states leading to H-migration/OH-elimination calculated by Zhu *et al*.[75]

Zádor *et al*. calculated the stationary points on the ethylene HP electronic ground state potential energy surface[203], shown in Figure 3.22. Of the reaction pathways in Figure 3.22, 3 result in the formation of OH *via.* H-shift: R 3.22 is a concerted 1,4-H-migration/OH-elimination reaction, yielding OH and glycolaldehyde, R 3.23 is a concerted 1,5-H-migration/OH-elimination reaction yielding OH and 2-oxiranol, R 3.24 outlines 1,6-H-migration/CH$_2$O-elimination, yielding CH$_2$O and the unstable CH$_2$OOH radical, which decomposes unimolecularly to CH$_2$O and OH.
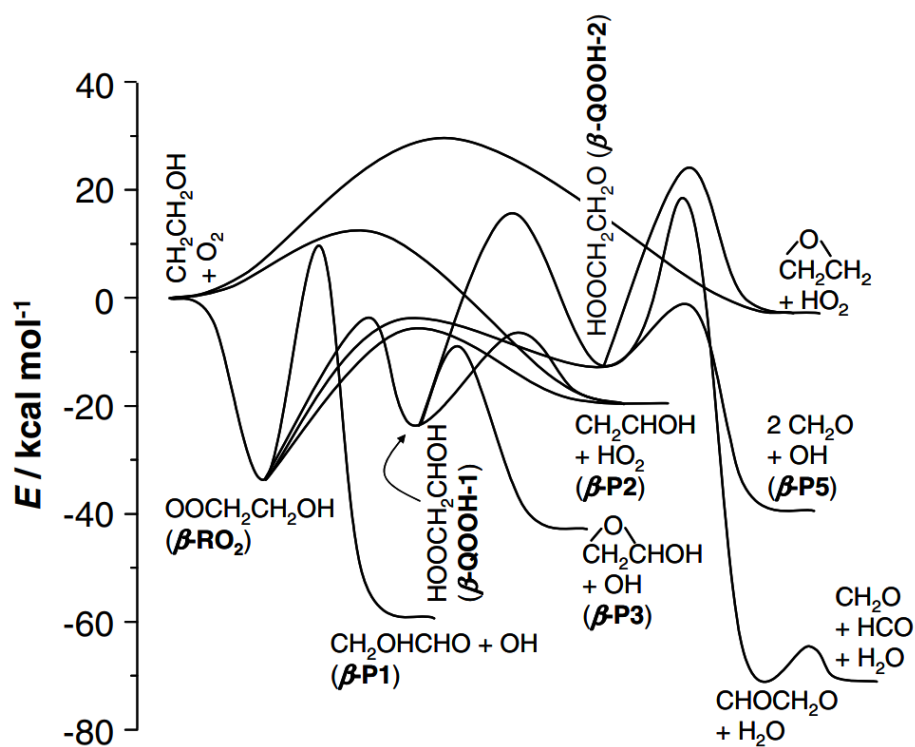
Figure 3.22: Stationary points on the CH₂CH₂OH + O₂ potential energy surface calculated by Zádor *et al.*[203].
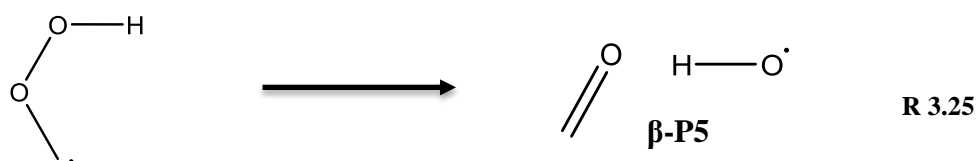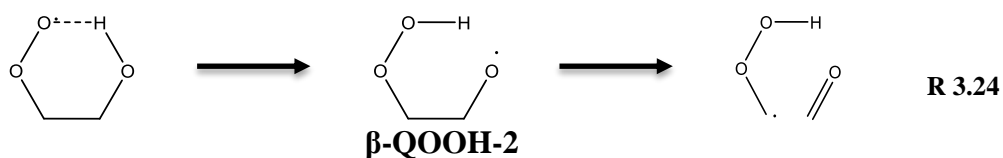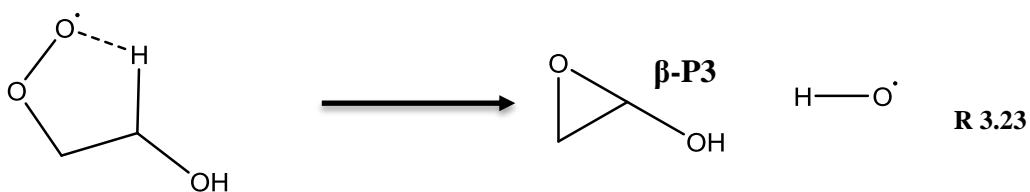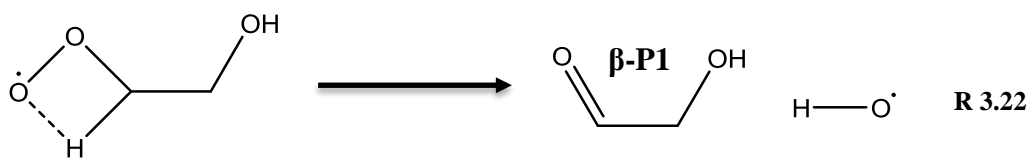
No potential energy surfaces have been calculated for the TME HP radical, however potential reaction pathways to OH are presented here based on the analogous reactions of the ethlene HP radical. R 3.26 shows 1,6-H-migration/OH-elimination resulting in the formation of 2,2,3-trimethyl-3-oxetanol, R 3.27 shows 1,5-H-migration/OH-elimination resulting in the formation of 2,3-dimethyl-3-buten-2-ol oxide and R 3.28 shows the 1,6-H-migration/Acetone-elimination reaction leading to the unstable hydroperoxy isopropyl radical, which decomposes unimolecularly *via.* R 3.29 to acetone and OH.

R 3.26

R 3.27

R 3.28

R 3.29
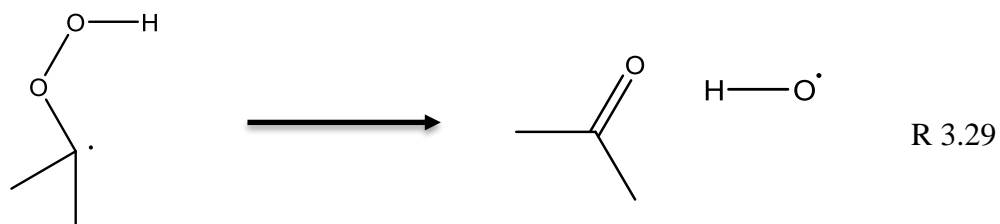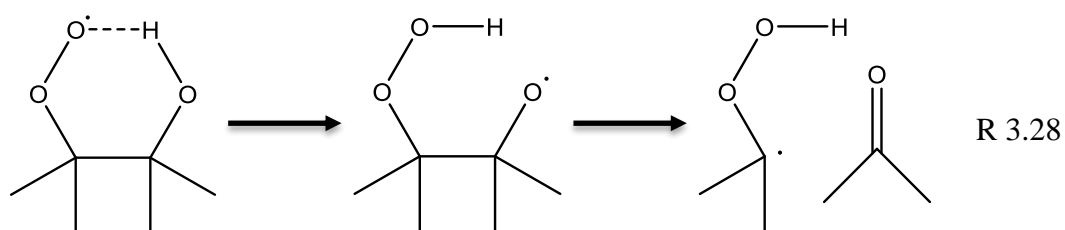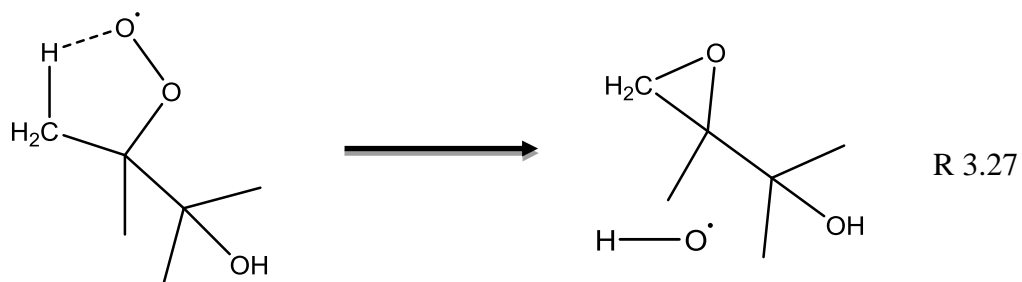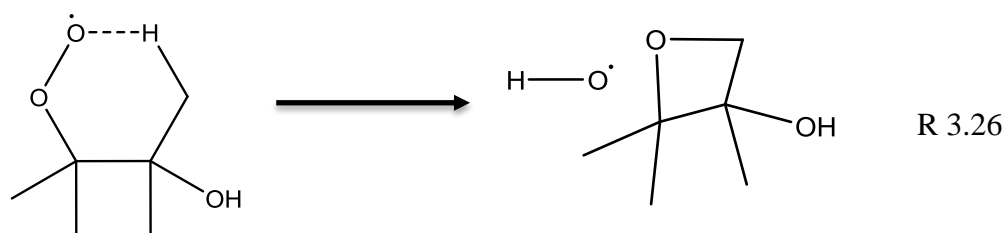
The OH yields from the electronic excitation of the ethylene and TME HP radicals depend on the branching ratios of all adiabatic and non-adiabatic reaction pathways from the excited state. An explanation for the decreased OH yield from TME to ethylene HP radical photolysis could be that the difference in stability of the co-products of the OH elimination pathways. For the ethylene HP radical, OH elimination co-products are the stable glycolaldehyde molecule, 2-oxiranol and formaldehyde, for the TME HP radical, the co-products of OH elimination are 2,2,3-trimethyl-3-oxetanol: a strained 4 membered cyclic ether, 2,3-dimethyl-3-buten-2-ol oxide: a strained 3 membered cyclic ether and acetone.

3.7   Conclusion

In summary, the novel TRUVAS instrument has been employed to measure total absorption cross-sections of HP radicals resulting from the addition of OH and subsequently O_2 to alkenes ethylene, but-2-ene and TME. A red shifting and broadening effect has been observed, increasing in the series ethylene > but-2-ene > TME HP radicals. The broadening and red shifting effect is attributed here to the change in the ground state potential energy surface; specifically the O-O peroxy bond, which is weakened by inductive effects (shown by Miller et $al.$[72]), facilitating electronic excitation from higher rovibrational levels of the ground $\tilde{X}^2A''$ state to the upper $\tilde{B}^2A''$ state.

Atmospheric photolysis rates (J_{total}) at noon in Borneo were calculated using TUV, $J_{total} = 0.552 \times 10^{-3}$ s^{-1} , 1.21×10^{-3} s^{-1} and 1.68×10^{-3} s^{-1} for the ethylene, but-2-ene and TME HP radicals respectively. As the number of alkyl groups bonded directly to the peroxy radical carbon centre increases, the peroxy radical becomes increasingly photolabile: an effect which could be important for other substituted atmospheric peroxy radicals.

OH absorption cross-sections for the ethylene and TME HP radicals were measured by Dr Hansen at the University of Leeds, and were used in conjunction with the total absorption cross-sections measured by the TRUVAS instrument to calculate $\phi_{OH,RO2}$ - the quantum yield for OH formation upon excitation of the HP radicals to the upper $\tilde{B}$ state. $\phi_{OH,RO2}$ for the ethylene HP radical increases steadily from around $21 \pm 8\%$ at 310 nm to around $64 \pm 70\%$ at 345 nm. $\phi_{OH,RO2}$ for the TME HP radical remains relatively constant at around 13 ± 4 between 305-365 nm, deacreasing slightly at

longer wavelengths. The decrease in the OH quantum yield from the excited states of the ethylene and TME HP radicals is due to the rates of the non-adiabatic H-migration/OH-elimination reactions, relative to other non-adiabatic processes, such as adiabatic O-O bond cleavage.

Further work is required to determine the products of ethylene and TME HP radical photolysis. R 3.25 yields 2 molecules of formaldehyde per reaction, which can be detected using the sensitive Laser Induced Fluorescence spectroscopy method outlined in section 1.3.4.

4 Measurements of the absorption spectra of the Isoprene, Butadiene and 1,3-Butadiene Hydroxyperoxy radicals

4.1 Introduction

2-methyl-1,3-butadiene, more commonly known as isoprene, is a diene emitted largely by deciduous trees, and is the single largest non-methane hydrocarbon emission globally (~500 Tg yr^{-1}), comprising roughly half of the biogenic VOC budget.[116, 204] In remote forested regions such as the Borneo rainforest, concentrations of isoprene are usually in the range 100-1000 pptv.[205] Significant effort has been made by the atmospheric chemistry community to understand the oxidation of isoprene, not only because of its relative abundance, but also its role in HO$_x$ levels observed in low (<50 ppt) NO$_x$, high (~3-4 ppb) VOC (particularly high isoprene) environments. Large discrepancies currently exist between measured levels of OH and those predicted by models; OH levels are expected to be low in these high-VOC environments, due to the short lifetime of OH as a result of removal *via.* reaction with VOCs. [21, 22, 119, 123, 124] In polluted urban environments, OH is recycled by NO$_x$ subsequent to reaction with VOCs. Various OH recycling mechanisms have been proposed for reconciling measured and modelled [OH] in near-pristine, high [isoprene] , low [NO$_x$] (<50 ppt NO) environments, outlined in section 1.4.

The oxidation of isoprene in the atmosphere is initiated, as with most atmospheric trace species, by the OH radical. Isoprene is a diene with 2 olefinic groups, to which addition of OH occurs with a rate coefficient close to the kinetic limit[206] (~1 × 10^{-10} cm^3 molecule^{-1} s^{-1}). Upon addition of OH to the isoprene molecule, 8 potential hydroxyperoxy (HP) radical isomers are formed, as shown in

Figure 4.1, with relative abundances given in Table 4.1. The HP radical isomers HP R1 and HP R6 are minor adducts (~4.2 and 2.0 % respectively), decomposing under atmospheric conditions to yield the corresponding carbonyl species and HO$_2$. These reactions are included in the Master Chemical Mechanism (MCM) as 1-step processes (R 4.1,R 4.2).[86]

The OH initiated oxidation of 1,3-butadiene (BD) and 2,3-dimethyl-1,3-butadiene (DMBD) forms 2 sets of HP radicals (see Figure 4.2), each of which essentially

mimics (meaning is structurally similar, differing only by 1 methyl group) 4 of the 8 HP radical isomers present for the isoprene HP radical ensemble.

Table 4.1: Relative abundances of the 8 HP radical products of OH initiated isoprene oxidation based on branching ratios calculated by Peeters *et al*.are given, as well as those determined experimentally by Wennberg *et al*.[134, 197] 1,3-butadiene and 1,3-butadiene are also included and branching ratios are assumed to be identical to those of their analogous isoprene carbon centred radical and are similar to those given by Jenkin *et al*.[61]

Isomer	isoprene (Peeters)	isoprene (Wennber	2,3-dimethyl 1,3-butadiene	1,3-butadiene
HP R1	~3.5%	~3.5 %	6.7 %	-
HP	4.42 %	3.7 ± 2 %	3.5 %	-
HP	16.7 %	8.4 ± 3 %	23.7 %	-
HP R3	40.8 %	46.5 ± 4 %	66 %	-
HP	1.2%	4.7 ± 2 %	-	3.2 %
HP	21.9%	5.6 ± 1.5	-	22.0 %
HP R5	21.9%	24.2 ± 3 %	-	61.3 %
HP R6	~3.5 %	~3.5 %	-	13.4 %

HP radicals HP R1-HP R2C are mimicked by the 4 HP radical isomers formed from

$$\text{isoprene} + OH \xrightarrow{O_2} HP\ R1 \xrightarrow{O_2} HO_2 + \text{product} \quad \text{R 4.1}$$

$$\text{isoprene} + OH \xrightarrow{O_2} HP\ R6 \xrightarrow{O_2} HO_2 + \text{product} \quad \text{R 4.2}$$
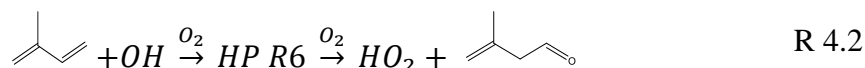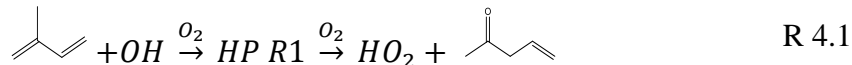
DMBD and HP radical isomers HP R4T - HP R6 are mimicked by the HP radical isomers formed from BD as shown in Figure 4.2. The differences between the isoprene HP radical isomers and their analogues are simply the extra methyl group on the 3 position for DMBD, and the lack of methyl group on the 2 position for BD; neither difference affects the degree of substitution of the peroxy radical carbon centre, and should have negligible effects on the absorption cross-section of the peroxy chromophore ($\tilde{B} - \tilde{X}$ transition).[72]
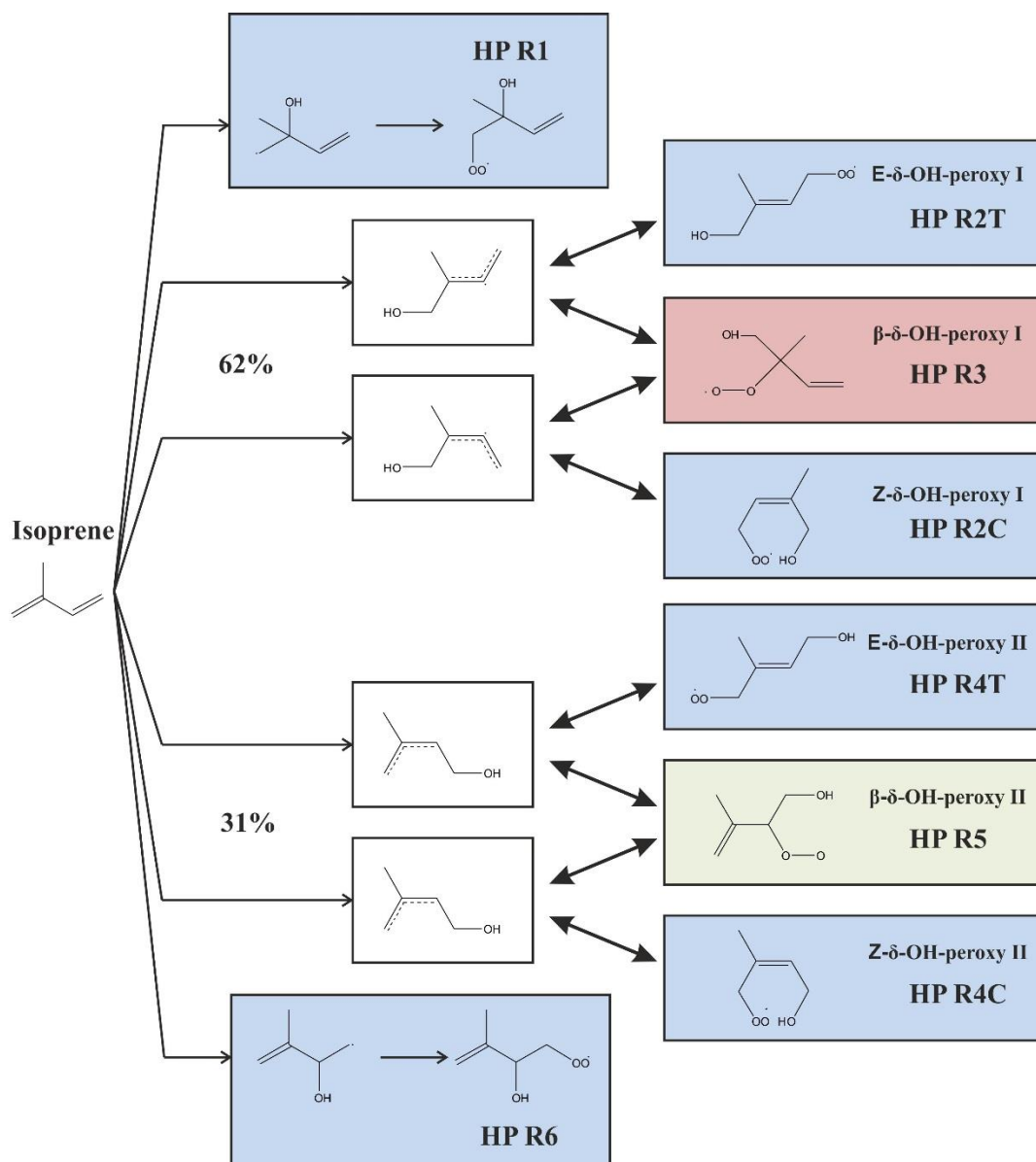
Figure 4.1: All 8 HP radical isomers formed subsequent to OH addition to isoprene. The minor HP radical isomers shown at the top and bottom account for ~8% of the total HP radical yield and are not considered in the Leuven isoprene Mechanism. [127, 130, 134] The HP radicals shown in the coloured boxes are the major products of the OH and subsequent O_2 addition; the HP radicals shown in the blue, green and red boxes are primary, secondary and tertiary HP radicals respectively. Note the species labelled HP R2T and HP R2C are Trans and Cis isomers respectively, as are HP R4T and HP R4C.
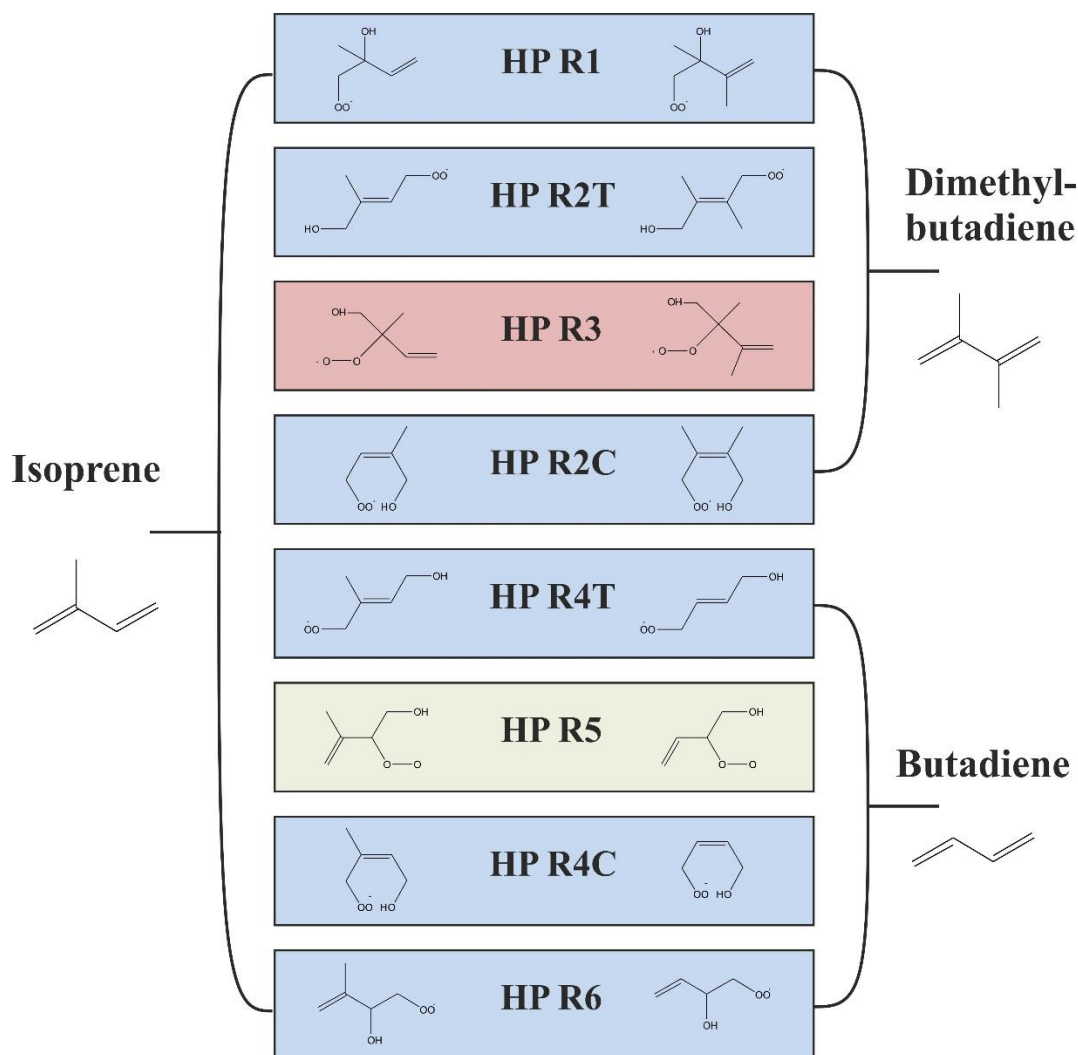
Figure 4.2: Isoprene HP radical isomers shown alongside the analogous HP radical isomers formed from OH initiated oxidation of DMBD (HP R1-HP R2C) and BD (HP R4T - HP R6).

This study aims to investigate the propensity of isoprene HP radical photolysis to reconcile measured and modelled OH discrepancies observed in remote forested locations.[2, 28, 29, 123, 124, 136] The TRUVAS instrument was used to measure total absorption cross-sections for the isoprene, DMBD and BD HP radical isomer ensembles. DMBD and BD HP radical isomer absorption cross-sections were investigated to further probe the effect that the degree of substitution of the peroxy radical carbon centre has on the shape and intensity of the broad, featureless $\tilde{B} - \tilde{X}$ transition common to all peroxy radicals.[67] The total ensemble absorption cross-sections measured by the TRUVAS instrument were used with experimental work carried out by Dr. Robert Hansen, in which absorption cross-sections for photolysis to OH were measured, to calculate the OH photolysis quantum yield.[194]

Isoprene photolysis to OH accounts for around 1% of the observed OH measured/modelled discrepancy in the Borneo rainforest. The quantum yield to OH from photolysis is around 11 ± 2 % from $310 - 345$ nm.[194] At 345 nm it appears that the quantum yield for OH production resulting from electronic excitation increases sharply to around 30 ± 20 %, indicating a switching in the dominant reaction pathway of the excited $\tilde{B}$ state. The remaining 90% of HP radical photolysis most likely leads to $O(^3P)$. Isoprene HP absorption cross-sections have previously been studied by Jenkin *et al.*, who estimated absorption cross-sections of the isoprene HP radical ensemble at 280 and 290 nm to be 2.8 and 2.1×10^{-18} cm^2 molecule^{-1} respectively, based on existing allyl and β-hydroxy peroxy spectra.[61, 199, 207, 208] The absorption cross-sections used for the isoprene HP ensemble by Jenkin *et al.* were used to determine the radical density of the HP radicals in the system, and were found to agree well with the calibrated OH radical concentration in the study, implying that the absorption cross-sections used were appropriate.

4.2 Experimental

The absorption cross-sections of the HP radicals of isoprene, DMBD and BD measured using the TRUVAS instrument. Each of the molecules was reacted with OH, generated from H_2O_2 photolysis at 248 nm using a KrF excimer laser (R 3.1). The OH-alkene adduct reacts rapidly with O_2 to form the corresponding HP radical (R 3.2-R 3.7).

$$HOOH \xrightarrow{248\ nm} 2OH \qquad\qquad \text{R 4.3}$$

$$Isop + OH \rightarrow \cdot IsopOH \qquad\qquad \text{R 4.4}$$

$$\cdot IsopOH + O_2 \rightarrow O_2IsopOH \qquad\qquad \text{R 4.5}$$

$$DMBD + OH \rightarrow DMBDOH \qquad\qquad \text{R 4.6}$$

$$DMBDOH + O_2 \rightarrow O_2DMBDOH \qquad\qquad \text{R 4.7}$$

$$BD + OH \rightarrow BDOH \qquad\qquad \text{R 4.8}$$

$$BDOH + O_2 \rightarrow O_2BDOH \qquad\qquad \text{R 4.9}$$

The H_2O_2 concentration and the 248 nm photon flux produced by the excimer laser are measured *via.* the methods outlined in sections 2.2.4 and 2.2.7 respectively, in order to calculate [OH] at t_0 (typically ~3-6 × 10^{13} cm^{-3}). OH then rapidly reacts with an excess of alkene (typical [Alkene] ~ 2 × 10^{15} molecule cm^{-3}), to form the corresponding hydroxyalkene radical, which then rapidly adds O_2 to form the HP radical. Concentrations of the dienes used in these experiments must be controlled to ensure that >95% of the OH reacts with the alkene (R 3.2, R 3.4, and R 3.6 , rates given in Table 4.2) rather than with the H_2O_2, (R 3.8 – k_{10} = 1.7 × 10^{-12} cm^3 molecule^{-1} s^{-1}) such that [OH]$_0 \approx$ [HP radical]$_0$ (Table 4.2). All of the alkenes studied in this chapter are thought to have significant absorption cross-sections (>10^{-21} cm^2 molecule^{-1}) at 248 nm, and so the alkene concentration must be optimised, so as to limit photolysis of the diene, but ensure complete conversion of OH to RO_2.

$$HOOH + OH \rightarrow HO_2 + H_2O \qquad\qquad R\ 4.10$$

Diene concentrations are estimated using equation E 4.1, whereby the vapour pressure of the diene at room temperature, divided by the regulated carrier gas pressure, gives the partial pressure of the diene/carrier gas mixture which flows through one of the flow controllers, allowing the concentration of the diene in the main flow to be estimated.

$$\frac{P_{Vapour, 298\ K}}{P_{Total}} = \rho_{diene} \qquad\qquad E\ 4.1$$

The concentration of isoprene was measured using the stable molecule concentration measurement technique outlined in the section 2.2.4, to test the accuracy of the estimation method, agreeing well: [isoprene] estimated = 2.17 × 10^{15} molecule cm-3, [isoprene]measured= 2.0 × 10^{15} molecule cm^{-3} as shown in Figure 4.3.

Table 4.2: The rate of reaction of OH with isoprene, DMBD and BD are used to calculate the ratio of [diene]/[H$_2$O$_2$] required to ensure >95% of OH reacts with the diene.[209]

Molecule	$k_{diene + OH}$ (×10^{10})	$k_{H2O2 + OH}$/ $k_{diene + OH}$	[diene]/[H$_2$O$_2$]for > 95% conversion
Isoprene	1.0	0.017	0.34
DMBD	1.2	0.014	0.28
BD	0.67	0.025	0.51
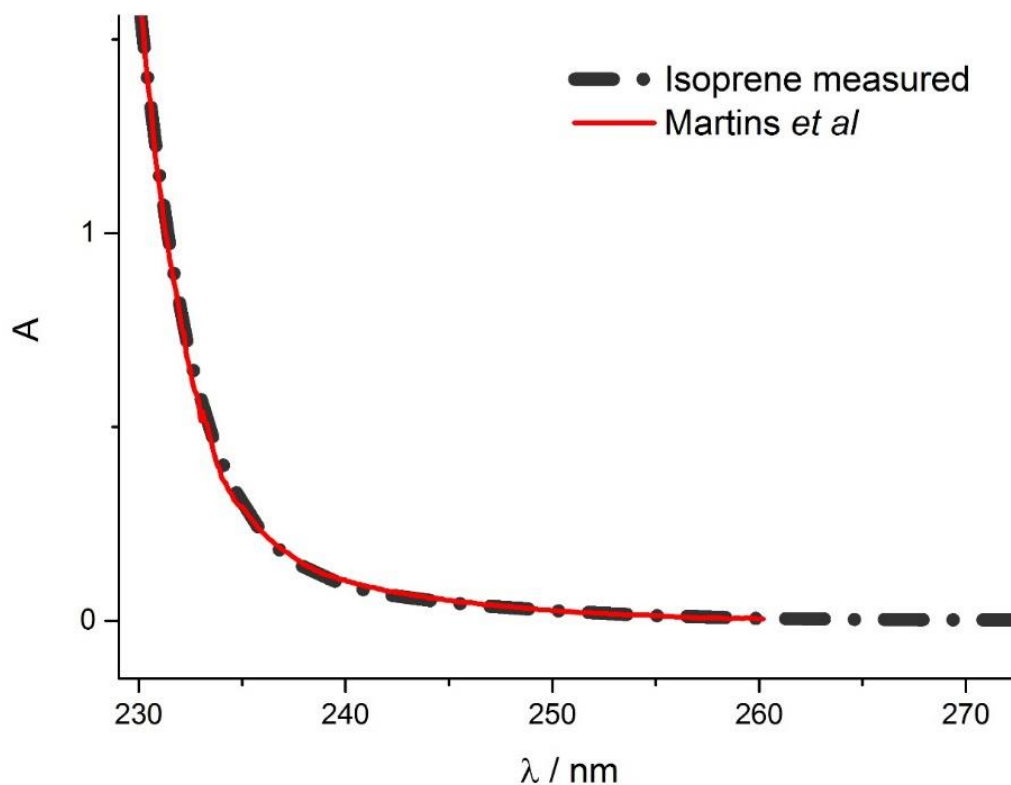
Figure 4.3: Isoprene absorbance measured with the single-pass arrangement (Black dot-dash) compared to the spectra measured by Martins *et al*.[210] The literature spectrum is multiplied by the path length (*l* = 150 cm) and [Isoprene] was varied until the resulting curve matched the recorded isoprene absorbance, in manner described in section 2.2.4. [Isoprene] for the trace shown was found to be 2×10^{15} molecule cm^{-3}.
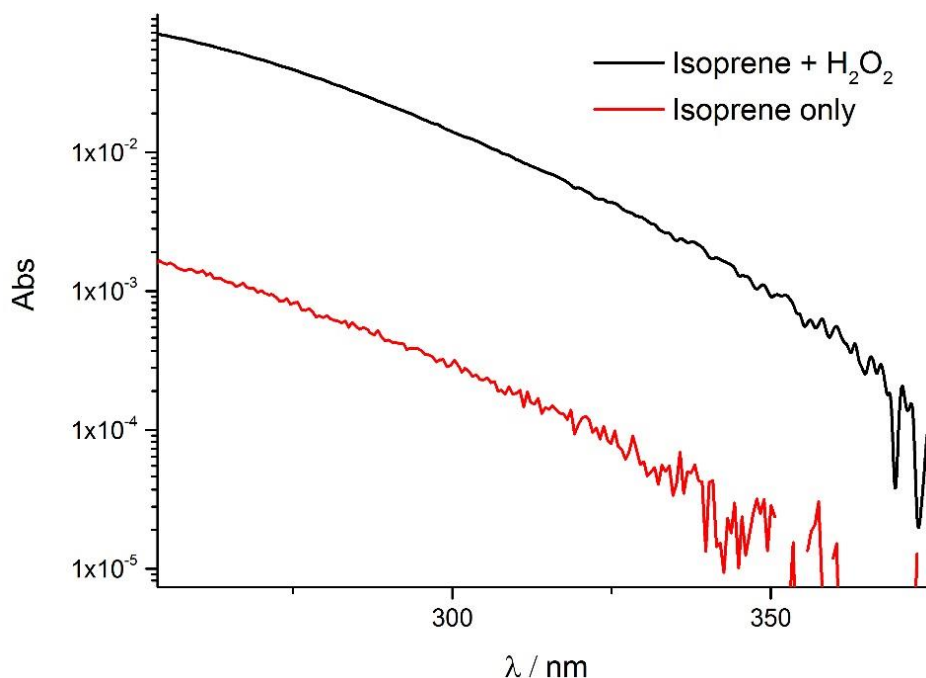
Figure 4.4: An example of the absorption signal observed due to isoprene photolysis at the concentration shown in Figure 4.3 (red line). Absorption due to isoprene photolysis products accounts for roughly 2% of the absorbance seen when hydrogen peroxide is present (black line), and as such, is a minor source of error.

Table 4.3: Conditions for the experimental data shown in Figure 4.5, Figure 4.6 and

	[H$_2$O$_2$] / 10^{-15} molecule cm^{-3}	[OH]/ 10^{-13} cm^{-3}	P$_{total}$ / Torr	Excimer energy / mJ pulse^{-1}
Isoprene run 1	6.4	7.6	82	52.3
Isoprene run 2	3.1	3.7	82	52.3
Isoprene run 3	5.8	6.5	82	49.3
Isoprene run 4	4.8	5.3	82	48.6
DMBD run 1	3.2	3.8	82	52.3
DMBD run 2	6.7	7.9	82	52.3
DMBD run 3	8.4	9.4	82	49.2
DMBD run 4	4.3	4.8	135	49.2
BD run 1	6.7	7.9	82	52.3
BD run 2	3.3	3.9	82	52.3
BD run 3	8.2	9.1	82	48.9

4.3 Results

The absorption cross-sections of the isoprene, DMBD and BD HP radical ensembles were measured using the TRUVAS instrument over a range of pressures and radical densities. The hydrogen peroxide concentration is measured for each experiment in the method described in section 2.2.4, and used in conjunction with the excimer power to calculate the radical density 2.2.7). A Savitzky-Golay smoothing filter[182] is applied to the data, details of this process are given in section 2.3.2.

Figure 4.5, Figure 4.6 and show the individual absorption cross-sections calculated separate absorption experiments for the isoprene, DMBD and BD HP radical ensembles, carried out over a range of initial peroxy radical densities ($3.7 - 7.6 \times 10^{13}$ cm^{-3}). 1σ confidence limits were constructed by summing the 5% error in the path length (443 ± 21 cm) and the standard deviation of the absorption cross-sections calculated for each run at each wavelength.

Average absorption cross-sections with 1σ error bars are shown in Figure 4.8 and Figure 4.9. It can be seen that the DMBD ensemble absorption cross-sections exhibit spectral red shifting, and extend further out into the visible region than both the isoprene and BD radical ensembles. An explanation for this is the relative abundance of HP radicals with substituted, electron-rich peroxy radical carbon centres, shown in the previous chapter to broaden and red-shift the broad UV absorption band. Based on computational studies[61], around 66% (Table 4.1) of the HP radicals formed from OH initiated oxidation of DMBD are expected to be the tertiary HP R3 isomer as shown in Figure 4.2. The absorption cross-sections of the isoprene HP radical ensemble, which has a mixture of 8 distinct HP radical isomers, lie between the DMBD and BD HP, showing a greater degree of red shifting than BD, but a lesser degree of red shifting than DMBD. Of the 8 potential HP radical isomers of isoprene, 2 have substituted peroxy radical carbon centres : HP R3 (tertiary) and HP R5 (secondary), which comprise 40.8% and 21.9% respectively, based on computational studies by Peeters *et al.* [134] or 46.5 ± 4 % and 24.2 ± 3 % respectively based on recent experimental results by Wennberg *et al.*[197] as shown in Table 4.1.
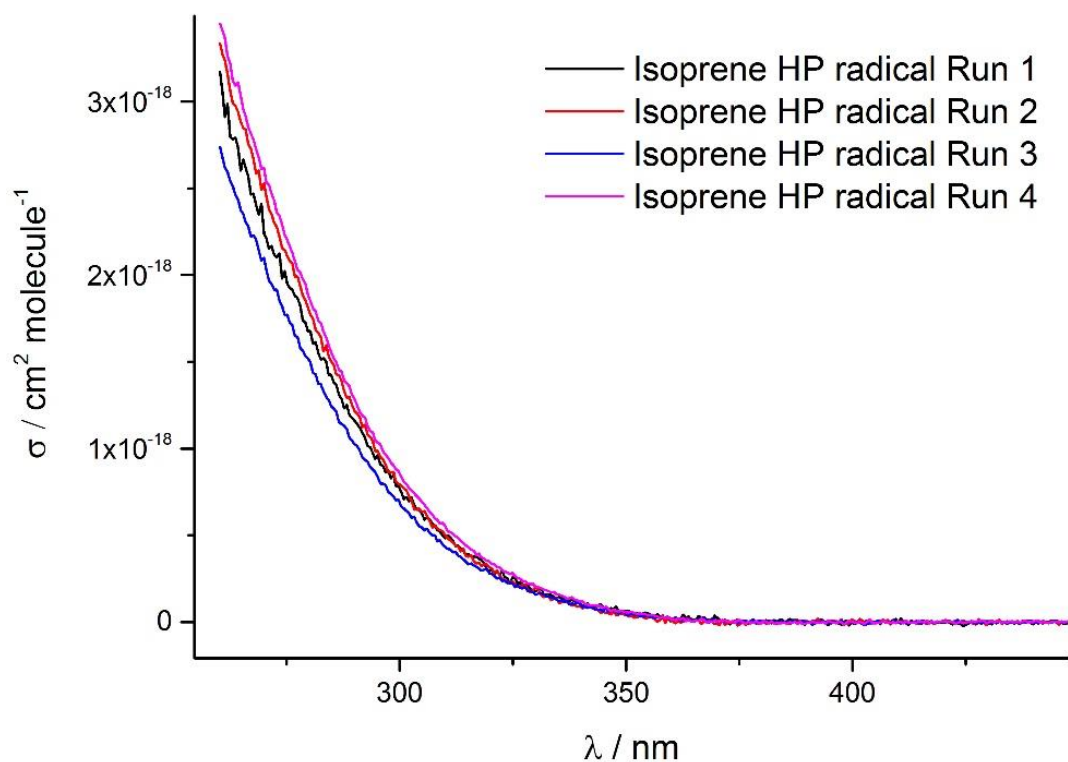
Figure 4.5: Runs 1-4 of the isoprene HP radical absorption cross-sections (1 – black, 2 – red, 3 – blue, 4 – pink. Conditions given in Table 4.3). Transient absorption profiles are recorded at 0.57 nm intervals (resolution 1.5 nm) following the pulsed excimer photolysis of H_2O_2-isoprene-O_2-N_2 mixtures at 248 nm.
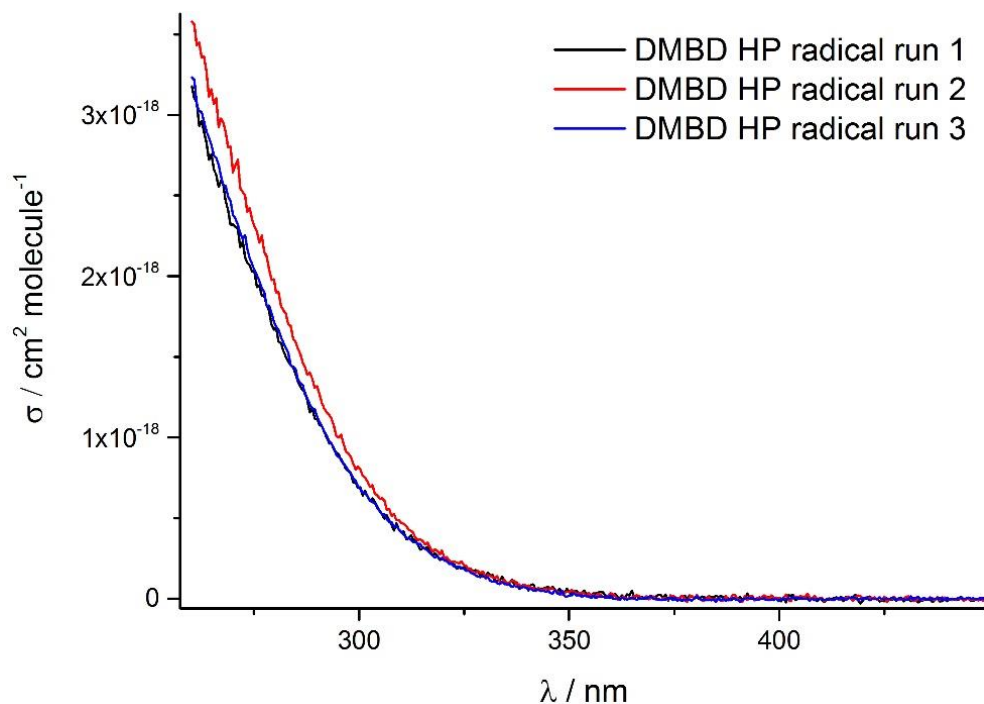
Figure 4.6: Runs 1-3 of the DMBD HP radical absorption cross-sections (1 – black, 2 – red, 3 – blue, 4 – pink. Conditions given in Table 4.3). Transient absorption profiles are recorded at 0.57 nm intervals (resolution 1.5 nm) following the pulsed excimer photolysis of H_2O_2-DMBD-O_2-N_2 mixtures at 248 nm.
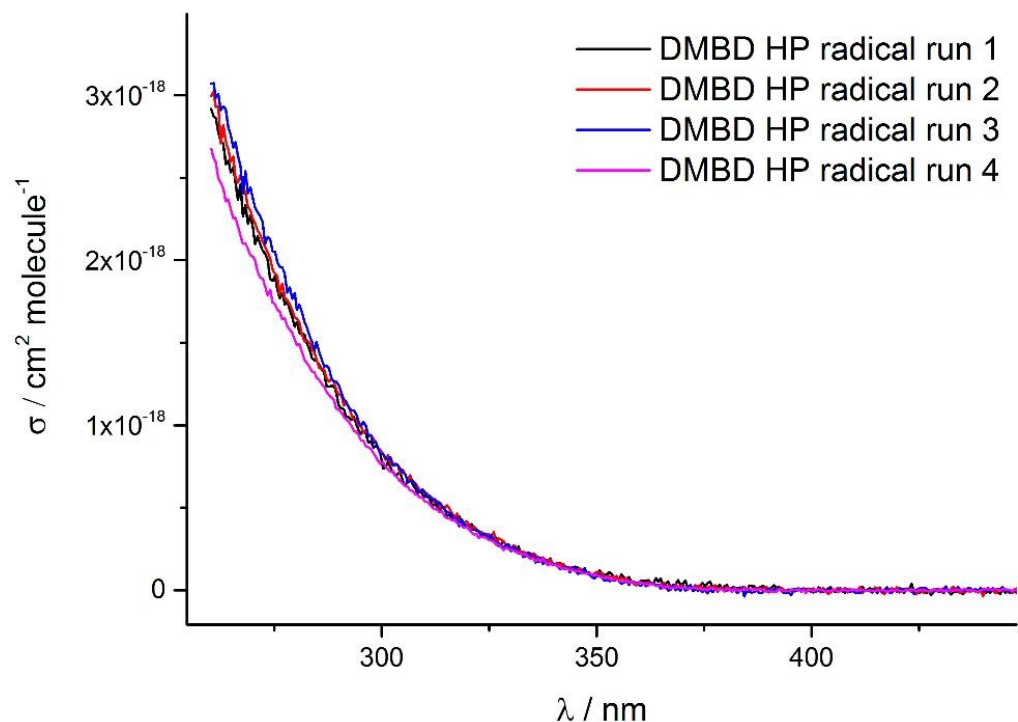
Figure 4.7: Runs 1-3 of the BD HP radical absorption cross-section (1 – black, 2 – red, 3 – blue. Conditions given in Table 4.3). Transient absorption profiles are recorded at 0.57 nm intervals (resolution 1.5 nm) following the pulsed excimer photolysis of H_2O_2-BD-O_2-N_2 mixtures at 248 nm.
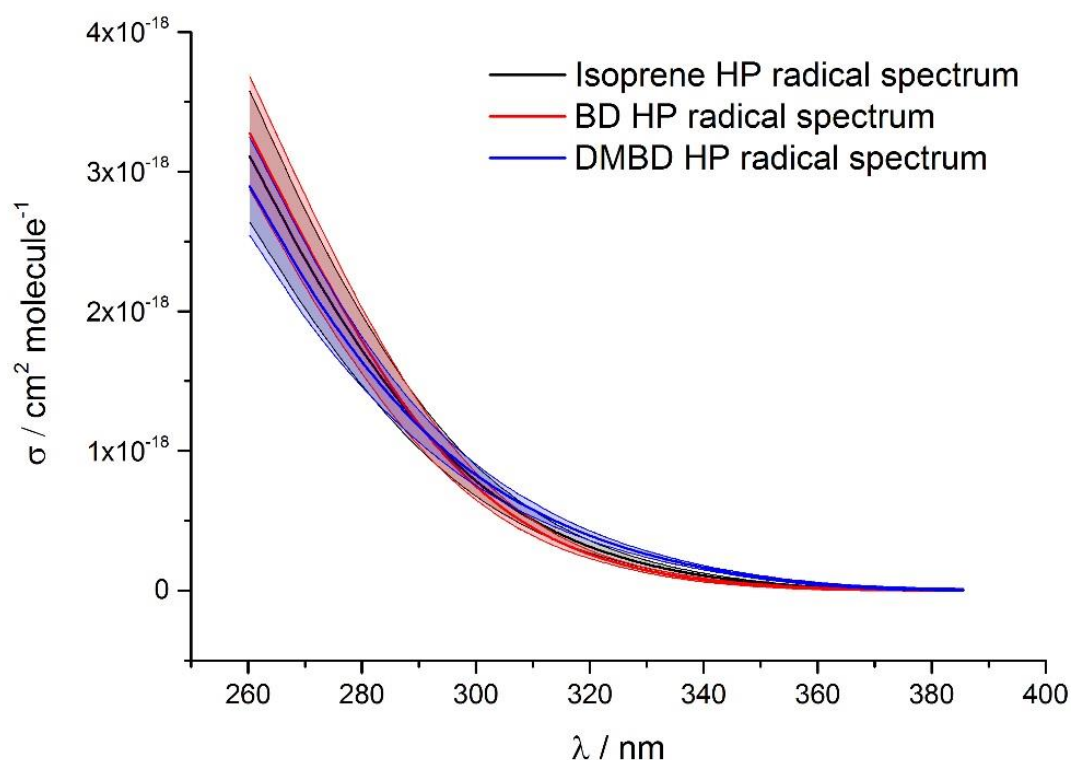
Figure 4.8: Average values for the absorption spectra for the isoprene, BD and DMBD HP radical ensembles, presented on a linear scale with 1σ confidence bands. Averages are constructed from the plots shown in Figure 4.5 (isoprene), Figure 4.6 (DMBD) and (BD) and confidence bands are constructed from the sum of the standard deviation of the points used in the averaging, and the error in the path length (~5%).
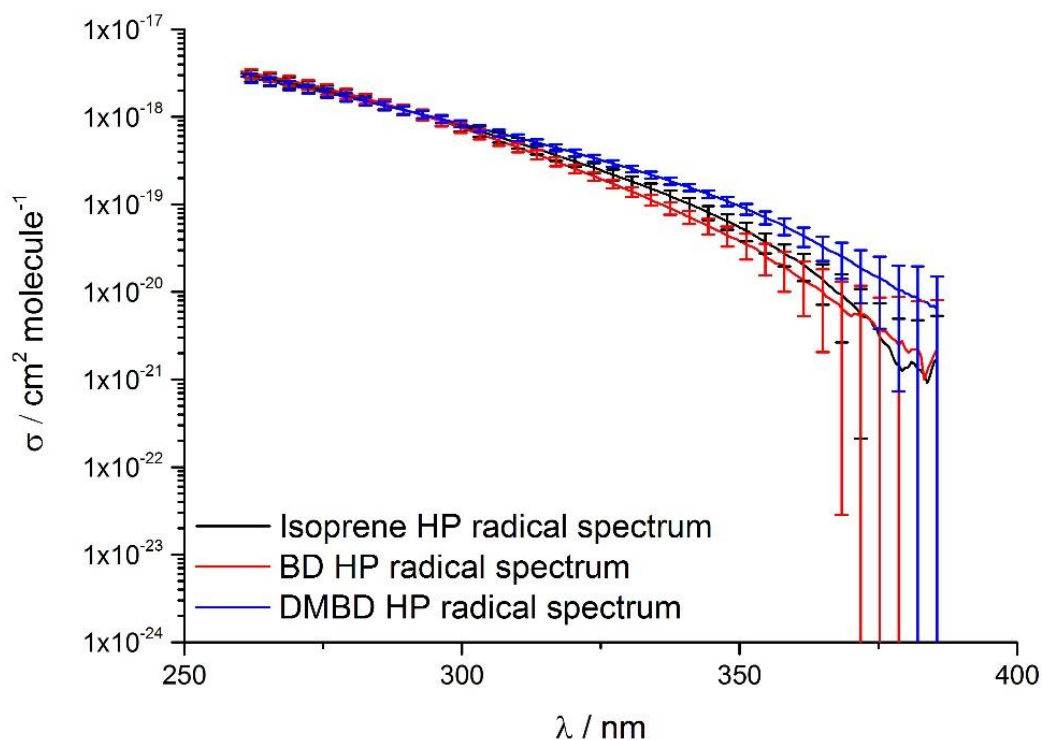
Figure 4.9: Average values for the absorption spectra for the isoprene, BD and DMBD HP radical ensembles, presented on a log scale with 1σ error bars. Averages are constructed from the plots shown in Figure 4.5 (isoprene), Figure 4.6 (DMBD) and (BD) and error bars are constructed from the sum of the standard deviation of the points used in the averaging, and the error in the path length (~5%).
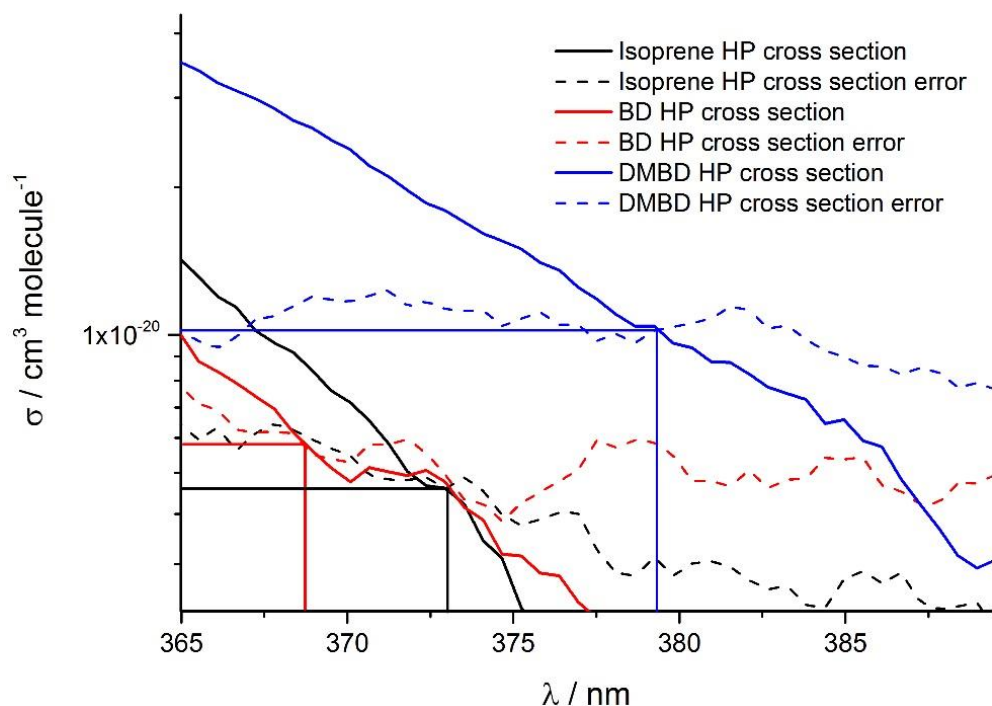
Figure 4.10: Absorption cross-sections and the corresponding 1σ error value. The point at which the 2 values are equivalent is given as the lower limit of the absorption cross-sections that have been measured, which are 4.1×10^{-21} cm² molecule⁻¹ at 373 nm , 5.2×10^{-21} cm² molecule⁻¹ at 368 nm and 1.0×10^{-20} cm² molecule⁻¹ at 379 nm for the isoprene HP, the BD HP and DMBD HP respectively.

The absorption cross-sections measured for the BD HP radical ensemble exhibit the smallest absorption cross-sections beyond 291 nm, most likely owed to the fact that there are no tertiary HP radical isomers formed from the OH initiated oxidation of BD. The Secondary HP R5 HP radical isomer shown in

Figure 4.1, is the most abundant HP radical formed from BD, at 61.3% as shown in Table 4.1, all other HP radical isomers formed from BD are primary. The values for the absorption cross-sections of the isoprene, DMBD and BD HP radical ensembles are almost equivalent at 291 nm. At shorter wavelengths, the BD HP radical ensemble has largest absorption cross-sections, followed by isoprene, with the DMBD exhibiting the smallest absorption cross-sections at short wavelengths. The smallest reliable absorption cross-sections are given as the point where the 1σ confidence interval value is equal to the calculated absorption cross-section which are 4.1×10^{-21} cm^2 molecule^{-1} at 373 nm , 5.2×10^{-21} cm^2 molecule^{-1} at 368 nm and 1.0×10^{-20} cm^2 molecule^{-1} at 379 nm for the isoprene HP, the BD HP and DMBD HP respectively (Figure 4.10).

The following section covers previous work carried out on the absorption cross-sections of isoprene, DMBD and BD HP radicals for comparison.

4.4   Existing studies on the absorption spectra of Isoprene, butadiene and 2,3-dimethylbutadiene hydroxyperoxy radicals

Previous work on the absorption cross-sections of the HP radical ensembles of isoprene, DMBD and BD are limited to a kinetic study by Jenkin *et al.*, in which values for the absorption cross-sections of each diene are assigned based on experimentally determined[61, 199, 207, 208, 211, 212] absorption cross-sections of peroxy radicals with allyl and β-hydroxy functionality, which have similar absorption cross-sections at the wavelengths studied. Absorption cross-sections of 2.8×10^{-18} cm^2 molecule^{-1} at 270 nm and 2.1×10^{-18} cm^2 molecule^{-1} at 280 nm were assigned to each of the isoprene, DMBD and BD HP radical ensembles, and were found to agree well with the radical calibration method used in the study, which involved using the HO$_2$ (formed *via.* reaction R 3.8) self-reaction rate and literature absorption cross-sections, to quantify the number of radicals generated.
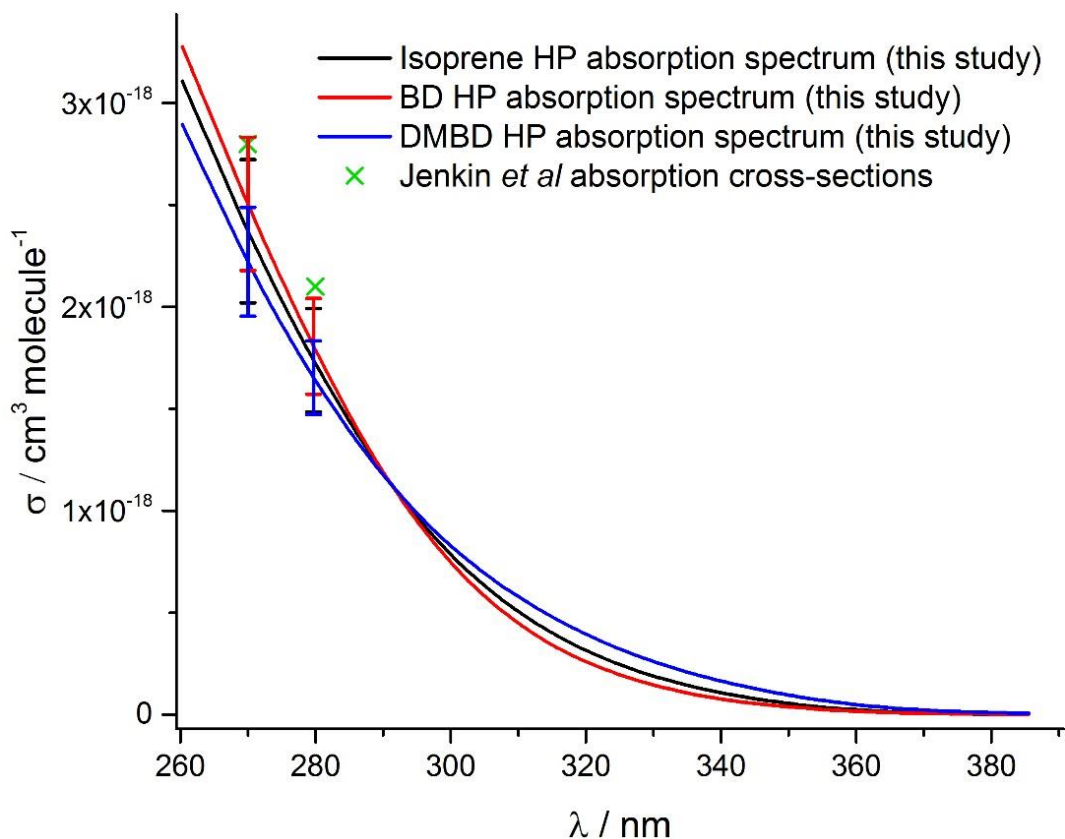
Figure 4.11: Absorption cross-sections of the isoprene, BD and DMBD HP radical ensembles (black, red and blue lines respectively), compared to the absorption cross-sections assigned to the 3 radical ensembles by Jenkin *et al*..[61] Jenkin *et al*. assumed that σ_{270} and σ_{280} of the isoprene, BD and DMBD HP radical ensembles were equivalent, however slight differences between the absorption cross-sections are observed in this study.

Figure 4.11 shows the absorption cross-sections of the isoprene, BD and DMBD HP radical ensembles (black, red and blue lines respectively), compared to the absorption cross-sections assigned to the 3 radical ensembles by Jenkin *et al.*[61] Overall the absorption cross-sections measured in this experiment are smaller in magnitude than those assigned by Jenkin *et al*. and differ in magnitude between each HP radical ensemble, from ~11% for the BD HP radical absorption cross-section at 270 nm, to ~27% for the DMBD HP radical absorption cross-section at 280 nm. The source of this error is most likely the calibration method used by Jenkin *et al*., which is dependent on both the absorption cross-section of HO_2 at 270 nm. The absorption cross-section of HO_2 at 270 nm was estimated by Jenkin *et al*. using the Lightfoot recommendation[67] which extends only to 1.8×10^{-19} cm^2 $molecule^{-1}$ at 260 nm. Direct measurements at 270 nm by Maricq *et al*.[213] and Sander *et al*.[214] are both approximately 1.1×10^{-19} cm^2 $molecule^{-1}$ at 270 nm in contrast to the value used by Jenkin *et al*. of 6.0×10^{-20} cm^2 $molecule^{-1}$ at 270 nm. Any error in the HO_2 cross section used to calibrate the system used by Jenkin *et al*. would translate directly into

an equivalent error in the cross sections used in the experiments, and substantial error margins on the presented absorption cross-section values.

In the following section, the results and implications of these experiments are discussed, in particular the potential products formed consequently to the electronic excitation of the HP radicals to the repulsive $\tilde{B}$ state – the transition which gives rise to the broad, featureless UV absorption spectra common to all peroxy radicals.

4.5   Atmospheric photolysis rates

The absorption cross-sections of the isoprene, DMBD and BD HP radical ensembles have been measured beyond 280 nm, where solar flux increases sharply. The excitation of HP radicals by UV-vis photons corresponds to the $\tilde{B} - \tilde{X}$ transition, a broad, featureless transition to the unbound $\tilde{B}$ state, common to all peroxy radicals. For a broad, featureless UV-Vis absorption spectrum, it is reasonable to assume that the upper state is repulsive, and the reactive intermediate formed traverses the potential energy surface, leading to bond cleavage; either direct photolysis or isomerisation and subsequent decomposition. Calculating the rate of the photolysis of these species in the atmosphere is important, as currently it is not included as a loss process of HP radicals in models, and could be a significant sink for RO_2 in the atmosphere, as well as a source of other reactive trace intermediates in the atmosphere. Calculating total photolysis rates requires both the absorption cross-sections of the molecule, as well as the total solar flux at a certain time and place. The Tropospheric Ultraviolet and Visible (TUV) model[77] (discussed in section 1.2.4) calculates solar flux as a function of wavelength at a particular time and location. For this application the solar flux was calculated at intervals of 1 nm, giving actinic flux / (quanta s^{-1} cm^{-2} nm^{-1}) vs wavelength / (nm). The data generated by the TRUVAS instrument generates absorbance profiles at wavelength intervals of 0.57 nm, and as such does not align with the output from TUV. For absorption spectra to be used in conjunction with TUV to calculate photolysis rates, a function describing their magnitude as a function of wavelength must be used to fit to the data, and extract y values ($\sigma_{RO2(\lambda)}$) at each x value (λ) generated by TUV. A modified Gaussian model, based on a Gram–Charlier A series[215] (GCAS - E 4.2) was used to fit absorption

cross-section measurements of the HP radical ensembles to obtain $\sigma_{RO2(\lambda)}$ – absorption cross-section as a function of wavelength.

$$\sigma = \frac{A}{w\sqrt{2\pi}}e^{-\frac{z^2}{2}}\left(1 + \frac{a_3}{3!}(z^3 - z) + \frac{a_4}{4!}(z^4 - 6z^3 + 3)\right); z = \frac{\lambda - \lambda_c}{w} \qquad \text{E 4.2}$$

It should be noted that a simple Gaussian function was unsuitable for fitting the absorption spectra, likely due to the fact that the spectra are in fact ensemble HP radical spectra, i.e. they are spectra comprising more than one different absorbing species, which likely have different spectra, necessitating the use of a more flexible Gaussian function.

Table 4.4: Parameters for the Gram–Charlier A series (GCAS) fits to each HP radical ensemble spectra. The parameters can be used to simulate the absorption spectra of each of the HP radical ensembles for wavelengths >280 nm.

Parameter	isoprene	DMBD	BD
A	2.58×10^{-16}	2.85×10^{-16}	2.83×10^{-16}
w	32.0	34.9	31.6
λ_c	250.9	247.4	248.3
a_3	0.546	0.636	0.449
a_4	0.204	0.170	0.241

 To calculate $J_{\lambda,\text{total}}$: the total photolysis frequency at a particular wavelength, the absorption cross-section is multiplied by the radiant (actinic) flux ($S_{e,\lambda}$) at wavelength λ (E 4.3), assuming a total quantum yield of photolysis of unity. Figure 4.13 shows $J_{\lambda,\text{total}}$ as a function of λ for each HP radical; it can be seen by inspection that the photolysis rates for the 3 HP radicals increases at all wavelengths in the order DMBD HP > isoprene HP > BD HP. To quantify the total photolysis rate in the atmosphere, J must be calculated (E 4.4) by integrating the J_λ vs λ function, to find the total area underneath the plot.

$$\sigma_\lambda \cdot S_{e,\lambda} = J_{\lambda,total} \qquad \text{E 4.3}$$

$$J_{total} = \Sigma(\sigma_\lambda \cdot S_{e,\lambda}) \qquad \text{E 4.4}$$
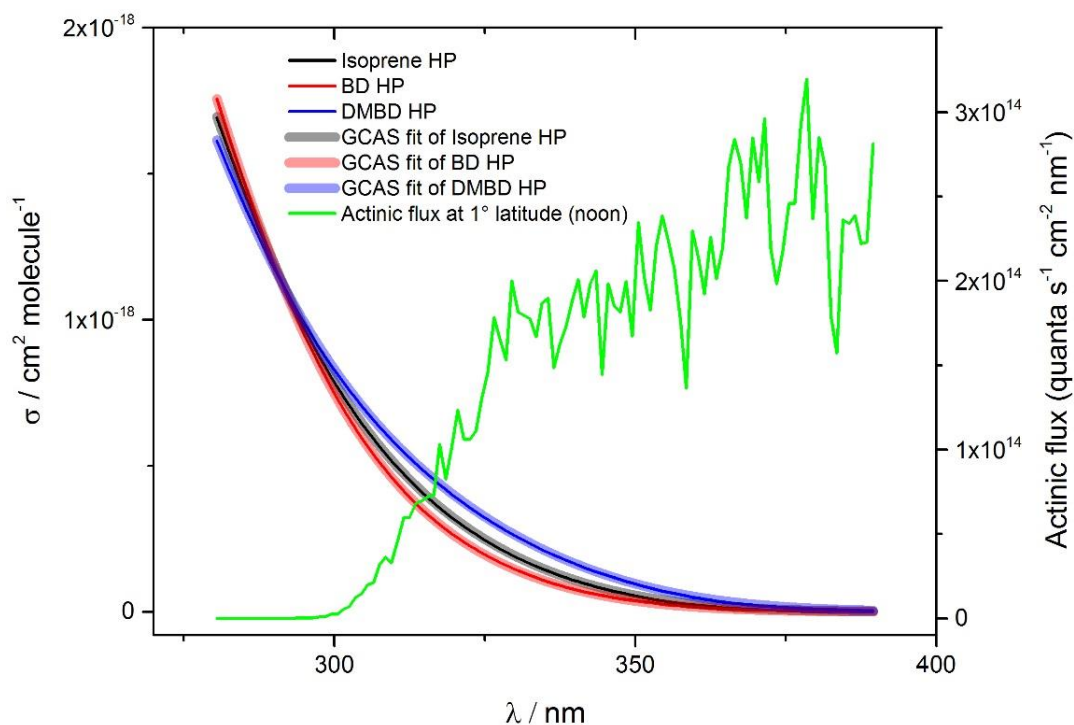
Figure 4.12: GCAS fits to the experimental data, necessary for calculating photolysis rates (Left Y axis). Actinic flux at 1° latitude (corresponding to Borneo) at 12 noon on 30th June, calculated by TUV is shown in green (right Y axis).
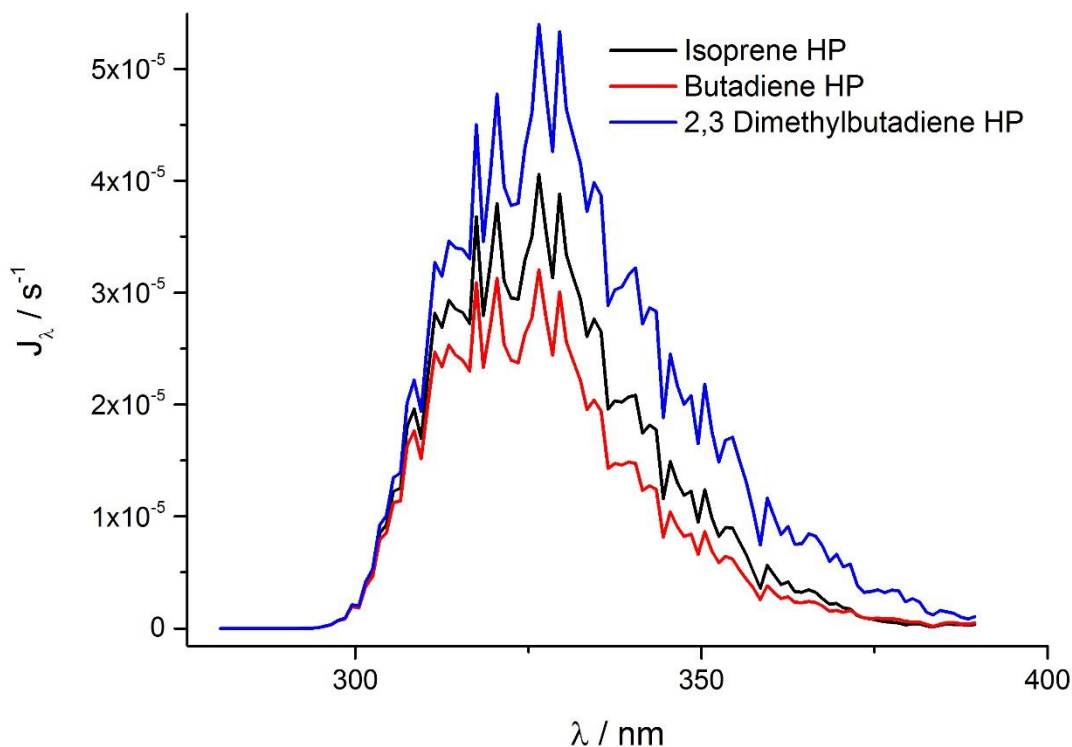
Figure 4.13: J_λ values for the isoprene, DMBD and BD HP radical ensembles calculated from the actinic flux at noon and 1° latitude on the 30th of June, calculated by ACOM TUV. The total photolysis rates (J) of these HP radicals are calculated by integrating each function. 1° latitude is used in this example to calculate the photolysis rates of these HP radicals in the Borneo rainforest, studied in the OP3 campaign, in which OH$_{measured}$ exceeded OH$_{modelled}$ by up to an order of magnitude.

Total photolysis rates for each of the isoprene, DMBD and BD HP radical ensembles are calculated at noon and 1° latitude on the 30th of June are presented in Figure 4.13. The DMBD HP radical ensemble has the fastest rate of photolysis in the atmosphere, with a rate of 1.81×10^{-3} s^{-1}, followed by the isoprene HP radical ensemble with a rate of 1.27×10^{-3} s^{-1} and BD HP radical ensemble with a rate of 1.01×10^{-3} s^{-1}. Actinic flux at 1° latitude is used in this example as it corresponds to the latitude of Borneo in Southeast Asia's Malay Archipelago, which was subject to an extensive field campaign Oxidant and Particle Photochemical Processes above a Southeast Asian tropical rainforest (OP3).[119, 123, 124] Large amounts of biogenic VOCs are emitted by plants in rainforest environments, the primary sink of which is *via.* reaction with OH. Unsaturated compounds undergo OH addition, and subsequently O_2 addition in the atmosphere (for example the reactions R 3.2-R 3.7) to form HP radicals. The most dominant removal processes for these HP radicals is currently *via.* reaction with NO (R 4.11) and HO_2 (R 4.12).

$$HO\text{-}Isop\text{-}OO + NO \rightarrow HO\text{-}Isop\text{-}O + NO_2 \qquad \text{R 4.11}$$

$$HO\text{-}Isop\text{-}OO + HO_2 \rightarrow HO\text{-}Isop\text{-}OOH \qquad \text{R 4.12}$$

$$HO\text{-}DMBD\text{-}OO + NO \rightarrow HO\text{-}DMBD\text{-}O + NO_2 \qquad \text{R 4.13}$$

$$HO\text{-}DMBD\text{-}OO + HO_2 \rightarrow HO\text{-}DMBD\text{-}OOH \qquad \text{R 4.14}$$

$$HO\text{-}BD\text{-}OO + NO \rightarrow HO\text{-}BD\text{-}O + NO_2 \qquad \text{R 4.15}$$

$$HO\text{-}BD\text{-}OO + HO_2 \rightarrow HO\text{-}BD\text{-}OOH \qquad \text{R 4.16}$$
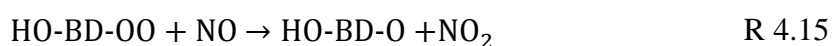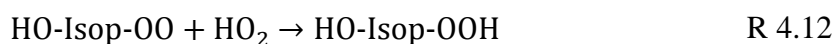
The rate coefficients of these reactions are included in the MCM, and at 300 K are equal to; $k_{11} = 9.04 \times 10^{-12}$ cm^3 molecule^{-1} s^{-1} and $k_{12} = 1.61 \times 10^{-11}$ cm^3 molecule^{-1} s^{-1}. The rate coefficients of the reaction of the BD HP radicals are included in the MCM; $k_{15} = 9.04 \times 10^{-12}$ cm^3 molecule^{-1} s^{-1} and $k_{16} = 1.43 \times 10^{-11}$ cm^3 molecule^{-1} s^{-1}. Rates of reaction of the DMBD HP radicals with NO and HO_2 are not included in the MCM, values are taken from Jenkin *et al.*; $k_{16} = 1.43 \times 10^{-11}$ cm^3 molecule^{-1} s^{-1}.[61] Example NO and HO_2 concentrations of 1.0×10^9 and 2.2×10^8 molecule cm^{-3} were used, as these values are typical noon concentrations as measured in the OP3 campaign.[29, 123]

Removal of isoprene HP by photolysis has a rate of 1.27×10^{-3} s^{-1} which is equivalent to roughly 14 % of the rate of removal *via.* reaction with NO and 45% of the rate of

removal *via.* reaction with HO_2 at noon in Borneo; a significant removal process, and one which should be included when considering the fate of the isoprene HP radical in remote, forested locations.

Table 4.5: Rates of removal of the the isoprene, DMBD and BD HP radical ensembles by reaction with NO ([NO]= 1.0×10^9 molecule cm^{-3}), HO_2 ([HO_2] = 2.2×10^8 molecule cm^{-3}) and by photolysis due to actinic flux at $1°$ latitude at 12 noon on the 30th of June, estimated by TUV, consistent with the OP3 field campaign.[77] Values for [NO], [HO_2] are based on average noon values measured during the OP3 campaign in Borneo.[2, 29, 120, 123, 124]

	Isoprene HP	DMBD HP	BD HP
k_{NO} /10^{-12} s^{-1}	9.04	9.04	9.04
k_{HO2} /10^{-11} s^{-1}	1.61	1.73	1.43
$Rate_{RO2+NO}$ / 10^{-3} s^{-1}	9.04	9.04	9.04
$Rate_{RO2+HO2}$ / 10^{-3} s^{-1}	3.54	3.81	3.15
J_{total} / 10^{-3} s^{-1}	1.27	1.81	1.01
J_{total} / $k_{NO} \times 100\%$	14	20	11
J_{total} / $k_{HO2} \times 100\%$	45	45	45
J_{total} / (J_{total} + k_{NO} + k_{HO2}) $\times 100\%$	9.2 %	12 %	7.7 %

If the rate of photolysis of the isoprene HP radicals are important, it is therefore important for the budget of isoprene HP radicals that the products of the photolysis should be considered. The principal aim of this investigation, in conjunction with the work carried out by Dr Hansen into the absorption cross-sections of HP radicals, was to test the propensity of these radicals to photolyse to OH, in an attempt to reconcile measured and modelled OH concentrations in remote, low NOx, high VOC environments, such as the Borneo rainforest studied in the OP3 campaign. [119, 123, 124] Whilst the instrument in this work is effective for measuring absorption cross-sections, it is unable to determine products of the HP radical photolysis, and as such measures the total absorption cross-section. Alongside the work carried out with the TRUVAS instrument, a 3-laser photolysis experiment was employed by Dr. Robert Hansen to measure the absorption cross-section for OH production of various peroxy radicals, including the isoprene HP radicals between 310 and 362.5 nm (Figure 4.14).

In short, a radical precursor is photolysed within a LIF cell at 248 nm, to yield radicals; in the case of the isoprene HP radical, hydrogen peroxide is photolysed to yield 2 OH radicals, as per R 3.1. OH radicals react with isoprene *via.* R 3.2 and subsequently with O_2 *via.* R 4.5 to form an ensemble of isoprene HP radical isomers, with relative abundances of each isomer given in

Figure 4.1. The reaction mixture is then photolysed a second time using a high energy, tuneable YAG pumped dye laser to photolyse the isoprene HP radicals, followed by a 308 nm OH probe laser, at a delay of typically 1-2 µs. OH is detected *via.* LIF at 308 nm before and after the tuneable photolysis laser, with the increase in OH observed immediately prior to the 248 nm photolysis assigned as OH from RO_2 photolysis. The OH absorption cross-section for the isoprene HP radical ensemble ($\sigma_{HOisopreneO_2,OH}$) is equal to the total absorption cross-section ($\sigma_{HOisopreneO_2,\lambda}$) multiplied by the quantum yield for OH production ($\phi_{HOisopreneO_2,\lambda}$). The OH absorption cross-section at a particular wavelength in the experiments by Dr Hansen, is dependent on the absorption cross-section of the radical precursor at that wavelength, as illustrated in E 3.5 and E 3.6.

$$\frac{OH_{HOisopreneO_2}}{OH_{H_2O_2}} = \frac{[HOisopreneO_2]_0 \times [h\nu]_\lambda \sigma_{HOisopreneO_2,\lambda} \phi_{HOisopreneO_2,\lambda}}{[H_2O_2] \times [h\nu]_\lambda \sigma_{H_2O_2,\lambda} \phi_{H_2O_2,\lambda}}$$

$$= \frac{[h\nu]_{248\,nm}[H_2O_2]\sigma_{H_2O_2,248\,nm}\phi_{H_2O_2,248\,nm} \times [h\nu]_\lambda \sigma_{HOisopreneO_2,\lambda} \phi_{HOisoprene\ell}}{[H_2O_2] \times [h\nu]_\lambda \sigma_{H_2O_2,\lambda} \phi_{H_2O_2,\lambda}} \quad \text{E 4.5}$$

$$= \frac{[h\nu]_{248\,nm}\sigma_{H_2O_2,248\,nm}\sigma_{HOisopreneO_2,\lambda}\phi_{HOisopreneO_2,\lambda}}{\sigma_{H_2O_2,\lambda}}$$

$$\sigma_{HOisopreneO_2,\lambda}\phi_{HOisopreneO_2,\lambda} = \frac{\sigma_{H_2O_2,\lambda}}{[h\nu]_{248\,nm}\sigma_{H_2O_2,248\,nm}} \quad \text{E 4.6}$$

where $OH_{HOisopreneO_2,\lambda}$ and $OH_{H_2O_2}$ represent the OH generated from 248 nm photolysis of isoprene HP radicals and hydrogen peroxide respectively; $[HOisopreneO_2,\lambda]_0$ is the concentration of isoprene HP radicals at t_0; $[h\nu]_\lambda$ is the number of photons of wavelength λ; $\sigma_{HOisopreneO_2,\lambda}$ and $\phi_{HOisopreneO_2,\lambda}$ are the absorption cross-sections and OH quantum yields of the peroxy radical at wavelength λ; $[H_2O_2], \sigma_{H_2O_2,\lambda}$ and $\phi_{H_2O_2,\lambda}$ are the concentration,

absorption cross-section and OH quantum yield for hydrogen peroxide at wavelength λ respectively.
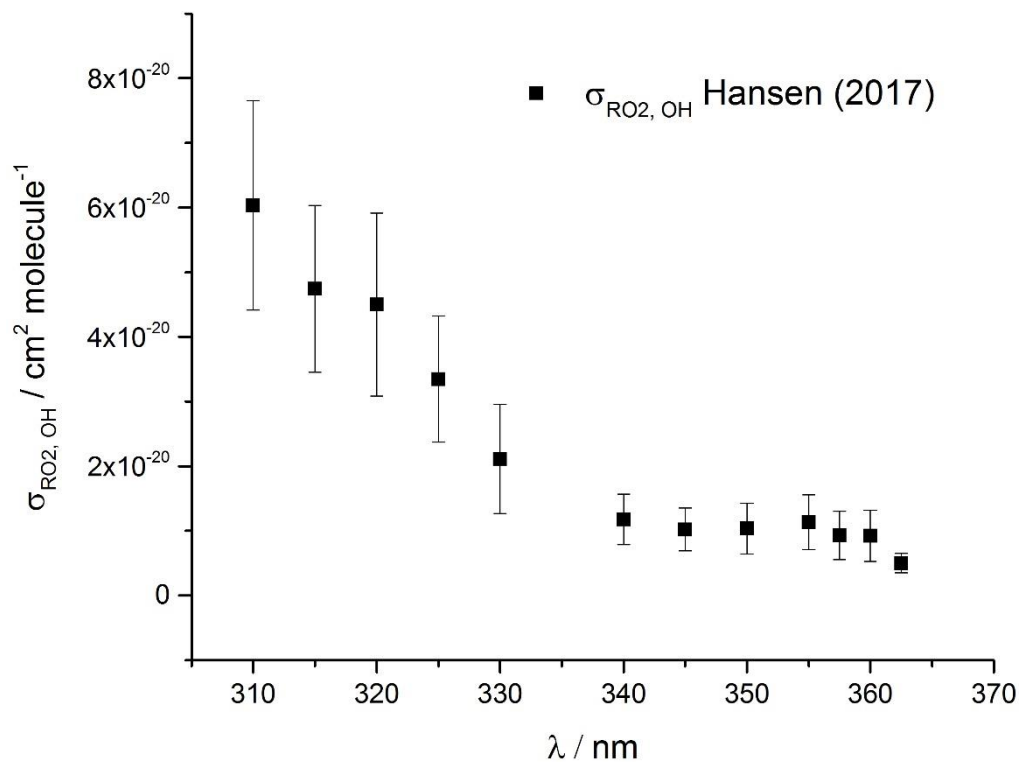
Figure 4.14: The absorption cross-sections for OH production of the isoprene HP radical ensemble as measured by Dr. Robert Hansen using the 3 laser experiment. Values are given as averages of a number of runs, and errors are propagated from the standard deviation of the results. More details can be found in Hansen *et al*. (2017).[194]
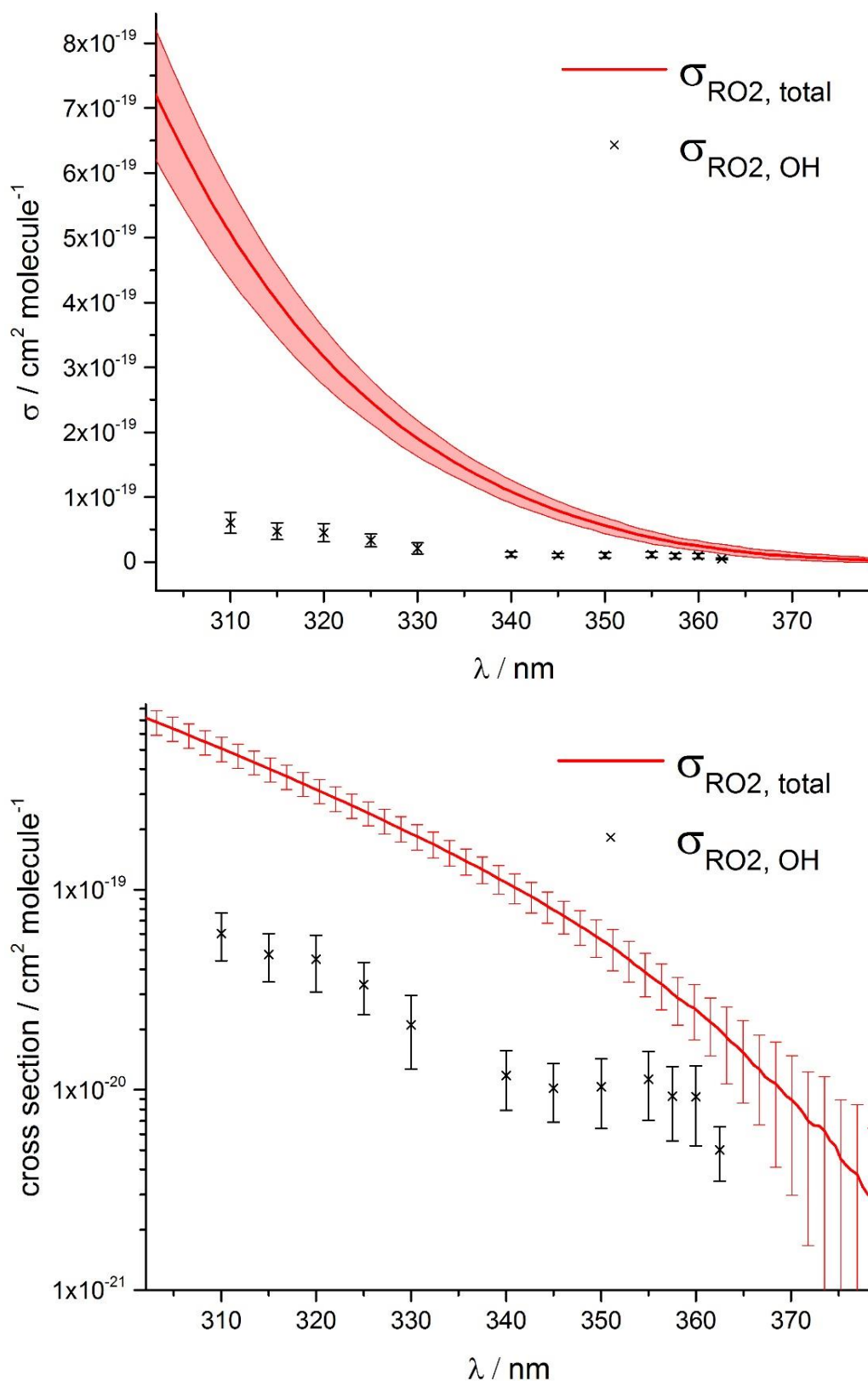
Figure 4.15: The total absorption cross-sections of the isoprene HP radical ensemble as measured by the TRUVAS instrument, with 1σ confidence limits (red) on linear (top) and logarithmic (bottom) y axes. The absorption cross-sections for OH generation are shown (black crosses) with confidence limits. As shown in Figure 4.10, the smallest reliable absorption cross-sections measured by the TRUVAS instrument for the isoprene HP radical are around 373 nm.
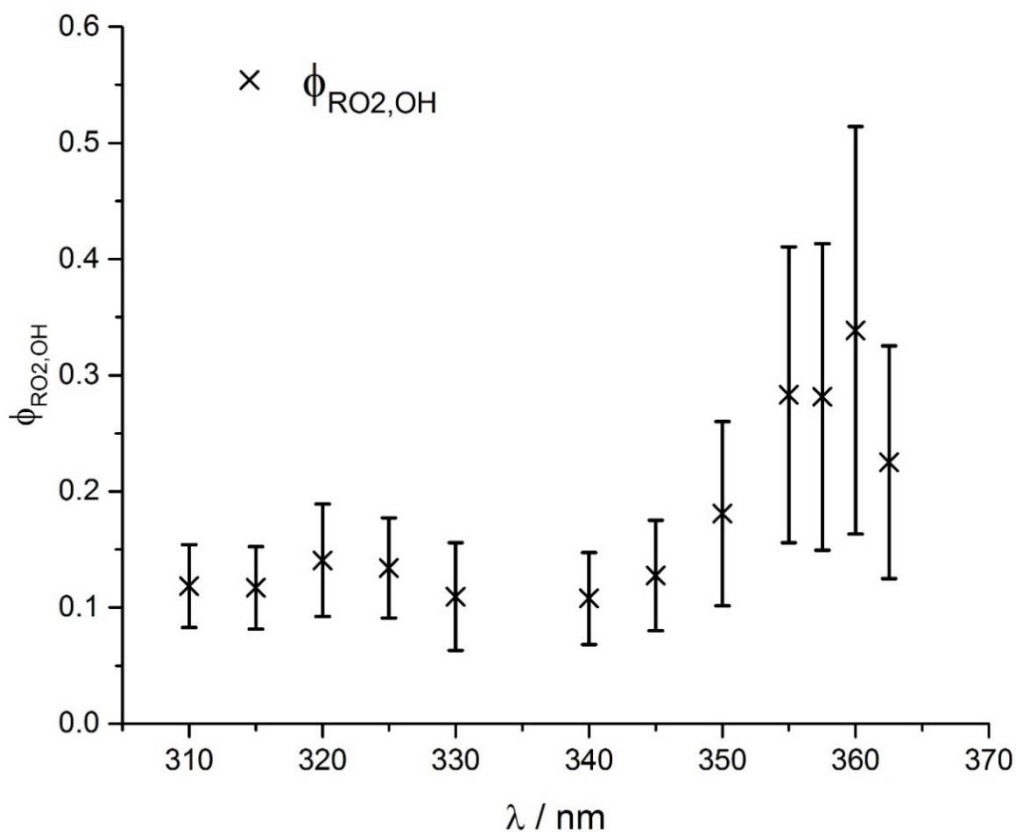
Figure 4.16: The OH quantum yield ($\phi_{OH,RO2}$) for the isoprene HP radical ensemble, from the ratio of $\sigma_{OH,\lambda}/ \sigma_{total,\lambda}$ between 310 – 362.5 nm. An increase in $\phi_{OH,RO2}$ is observed towards longer wavelengths. Note $\phi_{OH,RO2}$ values presented here differ slightly from those published in PCCP.[194] The isoprene HP radical ensemble total absorption cross-sections were re-measured subsequent to the submission of the paper to PCCP, however the values are not significantly different when error bars are taken into consideration. The error bars become increasingly large at longer wavelengths due to the decrease in signal to noise of both experiments as the absorption cross-sections become smaller at longer wavelengths.

4.6   Discussion

The measurements of the 3 HP radical total absorption cross-sections outlined here show a clear trend; the greater the proportion of more substituted carbon centred peroxy radicals, the more red-shifted the ensemble absorption cross-section into the actinic window becomes. The total absorption cross-sections presented in this chapter are ensemble absorption cross-sections, which, as previously described, means that the observed absorption cross-section is a summation of the absorption cross-sections of individual HP radical isomers formed from OH addition to various sites of each diene, multiplied by the branching ratio leading to the corresponding isomer. To highlight the role that the degree of substitution, or more specifically electron density pushing substituents bonded directly to the peroxy radical carbon centre, symmetrical HP radicals with only 1 isomer were investigated. These results,

shown in the previous chapter of this work, show a clear red-shifting, broadening effect on the UV absorption spectrum of the HP radicals. The spectra presented in this chapter show a similar trend, in that the ensemble HP radical total absorption cross-sections appear red shifted as the percentage of tertiary and secondary HP radicals increases. Although the extent of the enhanced absorption cross-sections in the actinic window appear small, actinic flux rises sharply beyond 280 nm, amplifying the increase in the photolysis rates disproportionately. This effect is shown in Figure 4.13, whereby the overall photolysis rate (at typical noon solar flux in the Borneo rainforest) of the predominantly tertiary DMBD HP radical ensemble $(1.81 \times 10^{-3} \text{ s}^{-1})$ is 40% larger than the isoprene HP radical ensemble $(1.27 \times 10^{-3} \text{ s}^{-1})$, which is in turn 26% larger than that of the BD HP radical ensemble $(1.01 \times 10^{-3} \text{ s}^{-1})$. Whilst the isoprene HP radical ensemble is the most atmospherically relevant of the 3 HP radical ensembles outlined in this chapter, the comparison between their absorption spectra is important when considering structure activity relationships. Previous studies have shown that electron withdrawing groups attached to the peroxy radical carbon centre have the propensity to shift the absorption spectra towards shorter wavelengths.[66, 67] In this study, it has been demonstrated that alkyl groups attached to the peroxy radical centre has the opposite effect; red-shifting absorption spectra to extend to longer wavelengths, dramatically increasing the photolysis rates of HP radicals in the atmosphere.

The observed red shifting and broadening of the $\tilde{B} - \tilde{X}$ absorption band observed for the 3 diene HP radical ensembles is consistent with the observed red shifting and broadening of the ethylene, but-2-ene and TME HP radical absorption spectra shown is section 3.3. The electronic ground and excited states of all HP radicals discussed here are assumed to be analogous to those of methyl peroxy (CH_3O_2), which is the most well characterised peroxy radical.[61, 62, 70-72, 198, 202] Miller *et al*. describe a shift in the position (λ_{max}) of the near IR $\tilde{A} - \tilde{X}$ electronic absorption band of alkyl peroxy radicals, observing red shifting as the number of carbons in the alkyl chain increases. Miller *et al*. attribute the red shifting of the IR absorption band to the destabilisation of the ground electronic $\tilde{X}$ state due to inductive effects from the additional alkyl groups attached to the α peroxy carbon centre. Destabilisation of the ground electronic state of the peroxy radical is thought to coincide with an increase in energy the electronically excited states, and so for a change in the transition energy to be

observed, the destabilisation of the ground state must exceed that of the excited state giving rise to the transition. The alkyl groups effectively donate electron density toward the electronegative O atom bonded directly to the α carbon, which serves to decrease the polarisation, and therefore electrostatic restoring force of the O-O bond.

Figure 4.17: Suggested explanation for the broadening observed due to inductive effects from alkyl substitution of the α peroxy carbon. The blue potential curve represents the O-O bond adjacent to the least substituted (primary) α carbon, and has the narrowest and deepest potential energy well. The green curve represents the secondary peroxy radical, and the red curve represents the tertiary potential energy well. Note this diagram is both speculative and qualitative.

Figure 3.19 shows a qualitative illustration of the proposed effect of the induction of electron density from alkyl groups toward the peroxy moiety; increased substitution destabilises the O-O bond stretch for the ground state, resulting in a broader, shallower well. Miller *et al.*[72] calculated an increase in the energy of the ground state for the alkyl peroxy series methyl , ethyl, propyl and butyl peroxy. A destabilisation of ~10 kJ mol^{-1} per additional carbon in the alkyl chain attached to the peroxy radical carbon centre was observed between methyl and ethyl peroxy, with the effect diminishing with increasing total chain length to ~3 kJ mol^{-1} for the change in the

ground state energy between n-propyl and n-butyl peroxy radicals. A broader and shallower well would be expected to have more population in higher vibrational states, facilitating excitation to the upper state at longer wavelengths.

Figure 4.18: Energy and correlation diagram for the electronic excitation of methyl peroxy, and the products of excited methyl peroxy: Products of C-O bond cleavage are shown on the left, and products from O-O bond cleavage are shown on the right. Reproduced from Hartmann *et al*.[71]

The electronically excited states of the methyl peroxy radical have been calculated by Jafri *et al*., who provides potential energy surface information with respect to the O-O and C-O bond stretch. Dissociation about the C-O bond would give rise to an alkyl radical and molecular oxygen (R 3.12-R 3.14).

Table 4.6: Potential reaction pathways resulting from electronic excitation of ground state CH₃O₂ ($\widetilde{X}^2 A''$). ΔH_R **/kJ mol⁻¹ represents the change in potential energy between the ground state CH₃O₂ and the corresponding intermediate or product. Threshold wavelength is the longest λ able to excite ground state CH₃O₂ to its corresponding state in a 1-photon absorption process. Symmetries are taken from Hartmann *et al*..[71]**

Reaction	ΔH_R /kJ mol⁻¹	Threshold Wavelength / nm	
$CH_3O_2(\widetilde{X}^2A'') + h\nu \rightarrow CH_3O_2(\widetilde{B}^2A'')$	-	-	R 4.17
$\rightarrow CH_3(\widetilde{X}^2A_2'') + O_2(X^3\Sigma_g)$	129.0	927	R 4.18
$\rightarrow CH_3(\widetilde{X}^2A_2'') + O_2(a^1\Delta_g)$	223	836	R 4.19
$\rightarrow CH_3(\widetilde{X}^2A_2'') + O_2(b^1\Sigma_g)$	286	418	R 4.20
$\rightarrow CH_3O(\widetilde{X}^2E) + O(^1D)$	438	273	R 4.21
$\rightarrow CH_3O(\widetilde{X}^2E) + O(^3P)$	248	482	R 4.22
$\rightarrow CH_2OOH(^2\widetilde{A}'')$	293	408	R 4.23
$CH_2OOH(^2\widetilde{A}'') \rightarrow OH(A^2\Sigma^+) + CH_2O(\widetilde{X}^1A_1)$	299	400	R 4.24
$\rightarrow OH(X^2\Pi) + CH_2O(\widetilde{X}^1A_1)$	-88	-	R 4.25
$\rightarrow OH(X^2\Pi) + CH_2O(\widetilde{A}^1A'')$	243	493	R 4.26

Hartmann *et al*. propose a mechanism for OH formation from electronic excitation of CH₃O₂ *via.* a non-adiabatic process (i.e. one which involves a crossing between 2 excited state potential energy surfaces -) involving isomerisation of excited $CH_3O_2(\widetilde{B}^2A'')$ to excited CH₂OOH $(^2\widetilde{A}'')$ and then subsequent dissociation to CH₂O$(\widetilde{X}^1A_1)$ plus rotationally hot OH$(A^2\Sigma^+)$.[71] Hartmann *et al*. also note that excitation of CH₃O₂ at 248 nm could produce O(¹D), which would react rapidly to form the observed OH$(A^2\Sigma^+)$, however the experiments carried out by Dr Hansen at the University of Leeds show OH production from the excitation of CH₃O₂ at wavelengths longer than the threshold wavelength for O(¹D) (273 nm - Table 3.5). Isoprene HP photolysis experiments were carried out in a Helium-H₂ buffer mixture by Dr Hansen in order to confirm or deny the production of O(¹D) by detection of OH$(A^2\Sigma^+)$, which would be formed *via.* reaction R 4.27. Indeed no OH$(A^2\Sigma^+)$ was detected, suggesting the route to OH formation from isoprene HP radical photolysis

is not occurring *via.* O(^{1}D), but *via.* the isomerisation route similar to that suggested by Hartmann *et al*. for CH$_3$O$_2$.

$$O(^1D) + H_2 \rightarrow OH(X^2\Pi) + H \qquad\qquad \text{R 4.27}$$

Zhu *et al*. have more recently calculated the possible fates of excited CH$_3$O$_2$, proposing a concerted H-migration/OH-elimination mechanism from the excited CH$_2$OOH($^2\tilde{A}''$) transition state, which lies 288 kJ mol^{-1} above the $OH(X^2\Pi)$ + $CH_2O(\tilde{X}^1A_1)$ products.[75] The transition state CH$_2$OOH($^2\tilde{A}''$) lies 293 kJ mol^{-1} above the $CH_3O_2(\tilde{X}^2A'')$ ground state, corresponding to a threshold frequency of 408 nm. Upon excitation to the electronically excited state, the reaction proceeds *via.* the repulsive $\tilde{B}$ state, before either continuing along the O-O bond stretch to yield the alkoxy radical and O(^{3}P) or crossing *via.* the $^2\tilde{A}''$ transition state resulting in concerted H-migration/OH-elimination. A similar reaction pathway from the excited $\tilde{B}$ state of isoprene HP radicals is the most likely route to the formation of OH observed by Dr Hansen.[194]

4.7   Summary

In summary, the novel TRUVAS instrument has been employed to calculate total absorption cross-sections of HP radical ensembles resulting from the addition of OH and subsequently O$_2$ to 3 dienes: Isoprene, BD and DMBD. A red shifting and broadening effect has been observed, increasing in the series BD HP > isoprene HP > DMBD HP, in agreement with the observation of a similar trend for the ethylene > but-2-ene > TME HP radicals. The extent of the red shifting is quantified here by observing the change in wavelength of the point where the absorption cross section for each molecule is equal to 1×10^{-19} cm^2 molecule, which is 335.8 , 341.1 and 349.3 for the BD HP, isoprene HP, DMBD HP radical ensembles respectively. The broadening and red shifting effect is attributed here to the change in the ground state potential energy surface; specifically the O-O peroxy bond, which is weakened by inductive effects (shown by Miller *et al*.[72]), facilitating electronic excitation from higher rovibrational levels of the ground $\tilde{X}^2A''$ state to the upper $\tilde{B}^2A''$ state. OH absorption cross-sections for the isoprene HP radical ensemble were measured by Dr Hansen at the University of Leeds, and were used in conjunction with the total

absorption cross-sections measured by the TRUVAS instrument to calculate $\phi_{OH,RO2}$ - the quantum yield for OH formation upon excitation of the HP radicals to the upper $\tilde{B}$ state. $\phi_{OH,RO2}$ remains relatively constant at around 11% until ~350 nm, at which point an increase to around 30% is observed. A possible explanation for such an effect could be the promotion of the H-migration/OH-elimination channel at lower excitation energies, which requires a tight 4 membered ring transition state. Another explanation of the uptick in $\phi_{OH,RO2}$ could be the "switching off" of other product channels at lower excitation energies due to the inaccessibility of these channels from the excited $\tilde{B}$ state at lower excitation energies.

5 Alkyl peroxy radical absorption spectra – Methyl, tertiary-butyl and cyclohexyl peroxy radicals

5.1 Introduction

The methyl peroxy radical is the most important atmospheric peroxy radical, chiefly due to its role as an intermediate in the oxidation of methane in the atmosphere.[67, 196, 216] Methane is emitted in large quantities globally (~500-600 Tg yr^{-1}), 90% of which is removed *via.* reaction with the OH radical.[53, 217, 218] The reaction of OH with methane[219, 220] ($k_1 \sim 6.5 \times 10^{-15}$ cm^3 molecule^{-1} s^{-1}) yields the methyl radical(R 5.1), which rapidly reacts with molecular oxygen to form the methyl peroxy radical (R 5.2 – M = bath gas, N$_2$ or O$_2$).

$$CH_4 + OH \rightarrow CH_3 + H_2O \qquad\qquad \text{R 5.1}$$

$$CH_3 + O_2 \xrightarrow{M} CH_3O_2 \qquad\qquad \text{R 5.2}$$

In polluted, high NO environments (>100 ppt), methyl peroxy radical removal is dominated by reaction with NO to form NO$_2$ and an alkoxy radical (R 5.3). NO$_2$ photolyses readily due to absorption of solar UV radiation to yield O^{3}P atoms (R 5.4), which react with O$_2$ to form ozone (R 5.5). This process accounts for ~25% of tropospheric ozone production globally, (the remaining ~75% coming from HO$_2$ and other RO$_2$ species forming NO$_2$ from NO)[88, 89].

$$CH_3O_2 + NO \rightarrow CH_3O + NO_2 \qquad\qquad \text{R 5.3}$$

$$NO_2 + h\nu \rightarrow NO + O^3P \qquad\qquad \text{R 5.4}$$

$$O^3P + O_2 \xrightarrow{M} O_3 \qquad\qquad \text{R 5.5}$$

In pristine environments such as Cape Verde, a tropical island off the west coast of Africa, very low NO concentrations are observed (~2 ppt), limiting the removal of methyl peroxy radicals by NO. In low NO environments, the reaction of the methyl peroxy radical with HO$_2$, OH and RO$_2$ species become competitive with NO.[161]

Methyl peroxy radical concentrations, whilst not measured in the atmosphere directly, can be estimated using a box model such as the Master Chemical Mechanism (MCM).[86, 104, 123, 161, 221] Methyl peroxy radical concentrations in pristine environments such as the Borneo rainforest[29] (~2 $\times$ 10^8 molecule cm^{-3}) and Cape

Verde[162, 221] ($\sim 9 \times 10^8$ molecule cm^{-3}) are estimated to be significantly higher than polluted urban environments such as London[222] ($\sim 5 \times 10^7$ molecule cm^{-3}), chiefly due to their enhanced removal *via.* reaction with NO.

The methyl peroxy radical is commonly detected by probing the broad, featureless $\tilde{B} - \tilde{X}$ transition common to all peroxy radicals, with λ_{max} at around 240 nm.[62, 67, 198, 223, 224] Other methods for investigating the methyl peroxy radical include the use of cavity enhanced techniques to study the weak ($<10^{-21}$ cm^2 molecule^{-1}) $\tilde{A} - \tilde{X}$ absorption band in the near IR, which enjoys much greater selectivity due to the bound $\tilde{A}$ state giving rise to structured absorption bands .[72, 73, 202]

Hartmann *et al.* describe a method for detecting methyl peroxy radicals *via.* laser flash photolysis – laser induced fluorescence (LFP – LIF), involving laser excitation of the methyl peroxy radical at 248 nm to yield various fragments, including OH, which can be detected sensitively using LIF.[71, 225]

The bulk of this chapter involves the investigation of the absolute absorption cross-sections of the methyl peroxy radical using the novel TRUVAS system, with a view to further understanding the photochemistry of these radicals in the troposphere. Total absorption cross-sections are used to calculate the total photolysis rate (J value) of methyl peroxy radicals in the atmosphere (assuming 100% photolysis), to determine whether photolysis is competitive with the removal reactions outlined above. Total absorption cross-sections will be combined with absorption cross-sections to form OH measured by Dr Hansen at the University of Leeds to provide OH quantum yields as a function of wavelength.

The absorption spectra of cyclohexyl peroxy and tertiary butyl (*t*-butyl) peroxy radicals have been measured using the TRUVAS instrument. Cyclohexane is a minor constituent of petrol in the UK, Europe and the USA, comprising $\sim$0.1-1 % by weight.[226] As with all alkanes, the oxidation of cyclohexane proceeds *via.* the alkyl peroxy radical, which for cyclohexane is the cyclohexyl peroxy radical. Cyclohexyl peroxy radicals are formed in the atmosphere by H abstraction from cyclohexane[227] ($k_6 = 2.9 \times 10^{-12}$ cm^3 molecule^{-1} s^{-1}) primarily by the OH radical (R 5.6) to form the cyclohexyl radical, which reacts with O$_2$, forming the cyclohexyl peroxy radical (R 5.7).

$$C_6H_{12} + OH \rightarrow C_6H_{11} + H_2O \qquad\qquad R\ 5.6$$

$$C_6H_{11} + O_2 \xrightarrow{M} C_6H_{11}O_2 \qquad\qquad R\ 5.7$$

The absorption spectrum of the cyclohexane peroxy radical was measured, in part, to aid comparison of the results obtained by the TRUVAS instrument, to those measured previously by Rowley *et al.*[63] in order to further probe the accuracy of absorption cross-sections measured by the TRUVAS instrument. The cyclohexyl peroxy radical was chosen specifically, as it only forms a single isomer, and reacts relatively quickly with OH compared to other alkanes.

Isobutane is a common alkane, used for a variety of applications, such as propellants, refrigerants and combustion fuels. Ter*t*-butyl (*t*-butyl) peroxy radicals are formed in the atmosphere *via.* H abstraction from the tertiary carbon of isobutene by the OH radical[228-230] (R 5.8, $k_8 \sim 3 \times 10^{-12}$ cm^3 molecule^{-1} s^{-1}), to form the *t*-butyl radical, which adds O_2 to form the *t*-butyl peroxy radical.

$$(CH_3)_3CH + OH \rightarrow (CH_3)_3C + H_2O \qquad\qquad R\ 5.8$$

$$(CH_3)_3C + O_2 \xrightarrow{M} (CH_3)_3CO_2 \qquad\qquad R\ 5.9$$
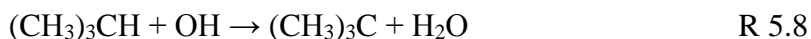
5.2   Experimental

Technical details of the standard experimental procedure and the experimental setup are described in detail in section 2.2 of this work. Specific details pertaining to the nature and mixing ratios of reagents, key reactions, and data analysis are presented in the following section.

Generation of methyl peroxy radicals

The absorption cross-section of the methyl peroxy radical was measured using the TRUVAS absorption system. Methyl peroxy radicals were generated *via.* photolysis of *t*-butyl hydroperoxide at 248 nm, to yield OH and hot (rotationally or vibrationally excited) *t*-butoxy radicals with a quantum yield of unity (R 5.10).[231] Hot *t*-butoxy rapidly decomposes to form acetone and methyl radicals (R 5.11), which combine with O_2 to form the methyl peroxy radical (R 5.12)[232].

$$(CH_3)_3COOH + h\nu \rightarrow (CH_3)_3CO + OH \qquad\qquad R\ 5.10$$

$$(CH_3)_3CO \rightarrow (CH_3)_2CO + CH_3 \qquad\qquad \text{R 5.11}$$

$$CH_3 + O_2 \xrightarrow{M} CH_3O_2 \qquad\qquad \text{R 5.12}$$

OH formed from the 248 nm photolysis of t-butyl hydroperoxide (R 5.10) is intercepted by ethanol (R 5.13), to prevent formation of t-butyl peroxy radicals (R 5.14). OH abstracts primarily from the α carbon at room temperature (92 $\pm$ 8 % at 298 K) yielding the hydroxyethyl radical (R 5.13, $k_{13} = 3.2 \times 10^{-12}$ cm^3 molecule^1 s^{-1}), which combines with O_2 to form the unstable 1-hydroxyethylperoxy radical (R 5.15).[233] The 1-hydroxyethylperoxy radical rapidly falls apart to yield acetaldehyde and HO_2 (R 5.16).

$$CH_3CH_2OH + OH \rightarrow CH_3CHOH + H_2O \qquad\qquad \text{R 5.13}$$

$$(CH_3)_3COOH + OH \rightarrow (CH_3)_3COO + H_2O \qquad\qquad \text{R 5.14}$$

$$CH_3CHOH + O_2 \xrightarrow{M} CH_3CHOH(O_2) \qquad\qquad \text{R 5.15}$$

$$CH_3CHOH(O_2) \rightarrow CH_3CHO + HO_2 \qquad\qquad \text{R 5.16}$$

T-butyl hydroperoxide (70% in water – Sigma Aldrich), was introduced into the buffer/reagent mixture from a bubbler. The concentration of the t-butyl hydroperoxide was measured in situ using the TRUVAS instrument. Ethanol was introduced into the system from a bubbler which sits in-line, after the mixing manifold, in order to introduce high concentrations of the ethanol into the reaction mixture. It was essential to add sufficient ethanol to the reaction mixture to intercept the OH generated, in order to prevent interference in the absorption cross-section measurements from the t-butyl peroxy.

$$k_{14}[tbutyl\ peroxide] = \frac{1}{50} \times k_{13}[Ethanol] \qquad\qquad \text{E 5.1}$$

$$\frac{[Ethanol]}{[tbutyl\ peroxide]} = \frac{k_{14} \times 50}{k_{13}} = \frac{3.56 \times 10^{-12} \times 50}{3.2 \times 10^{-12}} = 56 \qquad\qquad \text{E 5.2}$$

$$[Ethanol] = [tbutyl\ peroxide] \times 56 \qquad\qquad \text{E 5.3}$$

E 5.1-E 5.3 give the conditions necessary for 98% of OH generated from t-butyl hydroperoxide photolysis to be intercepted *via.* reaction with ethanol. Ethanol concentrations must exceed t-butyl peroxide concentrations by a factor of 56 to achieve a conversion rate of 98%, a value deemed acceptable in this study, and not a major source of error. Ethanol concentrations were estimated based on the increase

in pressure upon opening the ethanol bubbler to the system, typically $30 - 40$ Torr corresponding to a concentration of around 1.15×10^{18} molecule cm^{-3}. To prevent evaporative heat loss (and therefore inconsistent and diminished ethanol concentrations) due to ethanol evaporation, the bubbler was submerged in a temperature controlled water bath, set to $23°$ C. T-butoxy radical density at t_0 was calculated by measuring the excimer energy per pulse, which was converted to 248 nm flux (E 5.4,E 5.5). A detailed description of this procedure is given in section 2.2.

$$E_{pulse} = \frac{hc}{\lambda} \times n_{photons} \qquad \text{E 5.4}$$

$$n_{photons} = \frac{\lambda \times E_{pulse}}{hc} \qquad \text{E 5.5}$$

248 nm flux was then multiplied by the concentration of t-butyl peroxy, and the t-butyl peroxy absorption cross-section at 248 nm, to give the t-butoxy radical density, which rapidly converts to acetone and methyl (and therefore methyl peroxy) with a quantum yield of unity.[232]

$$[CH_3O_2]_0 = n_{photons} \times \sigma_{tbhp\ 248\ nm} \times [tbutyl\ hydroperoxide] \qquad \text{E 5.6}$$

Generation of *T*-butyl peroxy radicals

Experiments were carried out to determine the absorption spectrum of the t-butyl peroxy radical. Experiments were carried out in the manner prescribed for the methyl peroxy radical experiments, differing only in that the OH scavenger – Ethanol, was not added. OH formed from 248 nm photolysis of t-butyl peroxide then abstracts H from the peroxide group preferentially, to form the t-butyl peroxy radical (R 5.14).[231]

Generation of cyclohexyl peroxy radicals

Cyclohexyl peroxy radicals were generated by photolysing hydrogen peroxide at 248 nm (R 3.1) using a KrF excimer laser, in the presence of cyclohexane and O$_2$. OH abstracts an H atom from cyclohexane (R 5.18), producing a cyclohexyl radical, which rapidly combines with O$_2$ to form the cyclohexyl peroxy radical (R 5.19).

$$HOOH \xrightarrow{248\ nm} 2OH \qquad \text{R 5.17}$$

$$C_6H_{12} + OH \rightarrow C_6H_{11} + H_2O \qquad \text{R 5.18}$$

$$C_6H_{11} + O_2 \xrightarrow{M} C_6H_{11}O_2 \qquad \text{R 5.19}$$
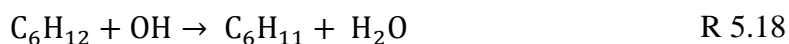
Hydrogen peroxide concentrations were measured in situ using the TRUVAS instrument (details on this procedure are given in section 2.2.4), and 248 nm flux was calculated by measuring the excimer energy (details on this procedure are given in section 2.2.7) and using equation E 5.5. The RO_2 concentration at t_0 (where t_0 is the ms within which the excimer is fired) was calculated using equation E 5.7, assuming a conversion rate of OH to cyclohexyl peroxy radicals of 100%.

$$[C_6H_{11}O_2]_0 = n_{photons} \times \sigma_{H2O2\ 248\ nm} \times [\text{hydrogen peroxide}] \qquad \text{E 5.7}$$

Cyclohexane does not absorb light in the region probed by the TRUVAS instrument[234], allowing high concentrations (up to 6×10^{18} molecule cm^{-3}) to be added, to ensure >99% conversion of OH to RO_2 (as opposed to reaction with H_2O_2).

5.3 Results

Methyl peroxy radical absorption spectrum

The absorption spectrum of the methyl peroxy radical was measured using the TRUVAS instrument, *via.* 248 nm photolysis of *t*-butyl hydroperoxide in the presence of ethanol and O_2. t_n represents a 1 ms time interval, beginning n ms after the excimer pulse. 5 runs were carried out at a range of pressures between 95.5 – 301.5 Torr N_2/O_2 ($[O_2]/[N_2]$ ~0.1). No pressure dependence was observed over the range studied.

Table 5.1: Experimental conditions for the methyl peroxy radical experiments. The results of these runs are shown in Figure 5.1.

Run	Total P / Torr	[peroxide] / 10^{16} molecule cm^{-3}	Excimer energy / mJ	[radical] / 10^{14} molecule cm^{-3}
CH_3O_2 run 1	185	2.58	71.8	4.62
CH_3O_2 run 2	301.5	1.48	71.8	2.65
CH_3O_2 run 3	142.5	2.1	71.8	3.76
CH_3O_2 run 4	142.5	0.961	71.8	1.72
CH_3O_2 run 5	95.5	1.81	71.8	3.24
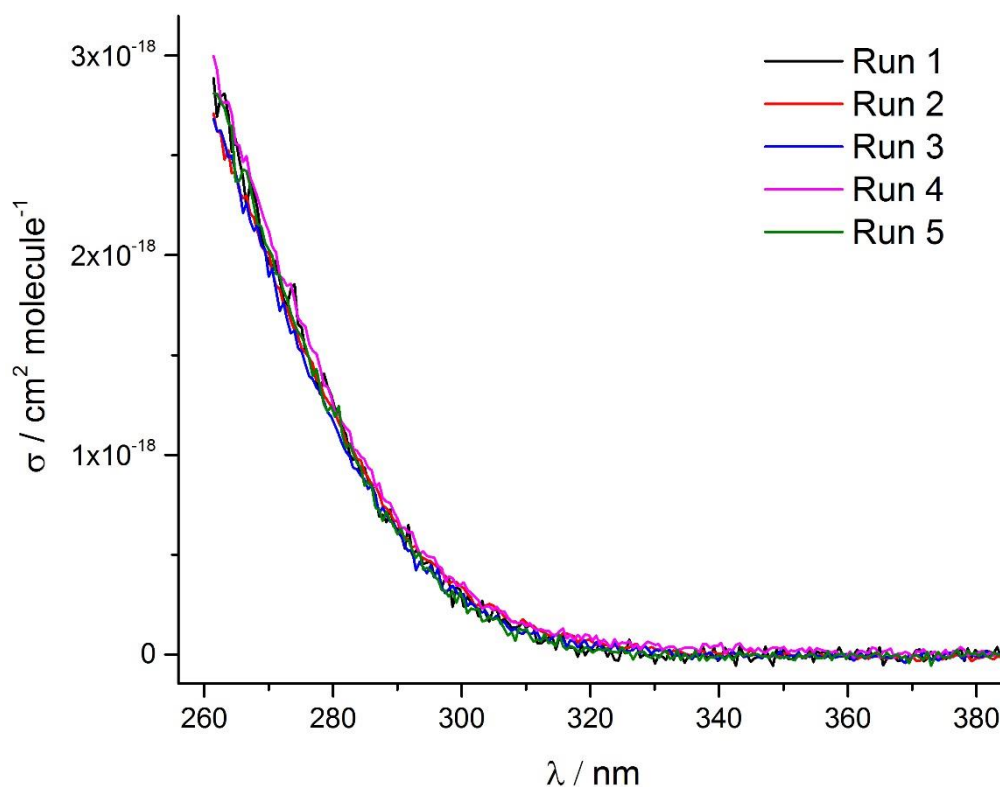
Figure 5.1: Runs 1-5 of the methyl peroxy radical absorption spectrum (1 – black, 2 – red, 3 – blue, 4 – pink, 5 - green. Conditions given in Table 5.1). Transient absorption profiles between 250-650 nm were recorded at .57 nm intervals (resolution 1.5 nm) following the pulsed excimer photolysis of *t*-butyl peroxide-ethanol-O$_2$-N$_2$ mixtures at 248 nm.

A Savitzky-Golay smoothing filter[182] was applied to each of the 5 runs shown in Figure 5.1 to filter out noise from the recorded spectra; The average values were calculated at each wavelength and 1σ error bars were constructed from the sum of the standard deviation across all 5 runs at each wavelength and a 5% overall error from the uncertainty in the path length. Formation of the methyl peroxy radical *via.* *t*-butyl peroxide photolysis in the presence of ethanol leads to the production of acetone, HO$_2$ and acetaldehyde in stoichiometric amounts, such that every methyl peroxy radical generated, 1 acetone, acetaldehyde and HO$_2$ molecule are formed. Although the absorption cross-sections of these species are small ($<10^{-19}$ cm^2 molecule^{-1}), they overlap with the methyl peroxy radical spectrum, and must be accounted for by subtracting the absorption cross-sections of these species from the methyl peroxy radical spectrum recorded by the TRUVAS instrument.
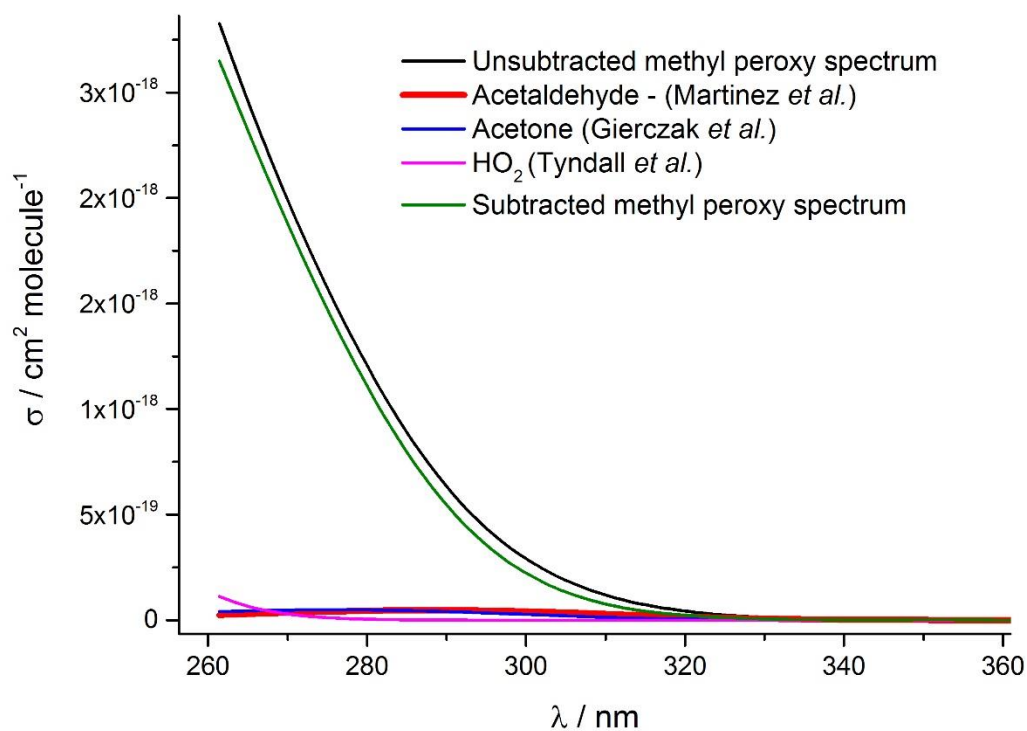
Figure 5.2: The methyl peroxy radical absorption spectrum prior to the subtraction of the spectra of acetaldehyde, acetone and HO₂ is shown in black. Modified Gaussian functions (discussed in more detail in section 4.5) were fit to experimentally determined absorption cross-sections (red: Acetaldehyde – Martinez *et al.*[235], blue: Acetone – Gierczak *et al.*[236]), or extrapolated from experimentally determined absorption cross-sections (magenta: HO₂ - Tyndall *et al.*[196]). The absorption cross-sections of the 3 contaminant species were subtracted from the average value of the experimental results to yield the pure methyl peroxy radical spectrum, shown in green.
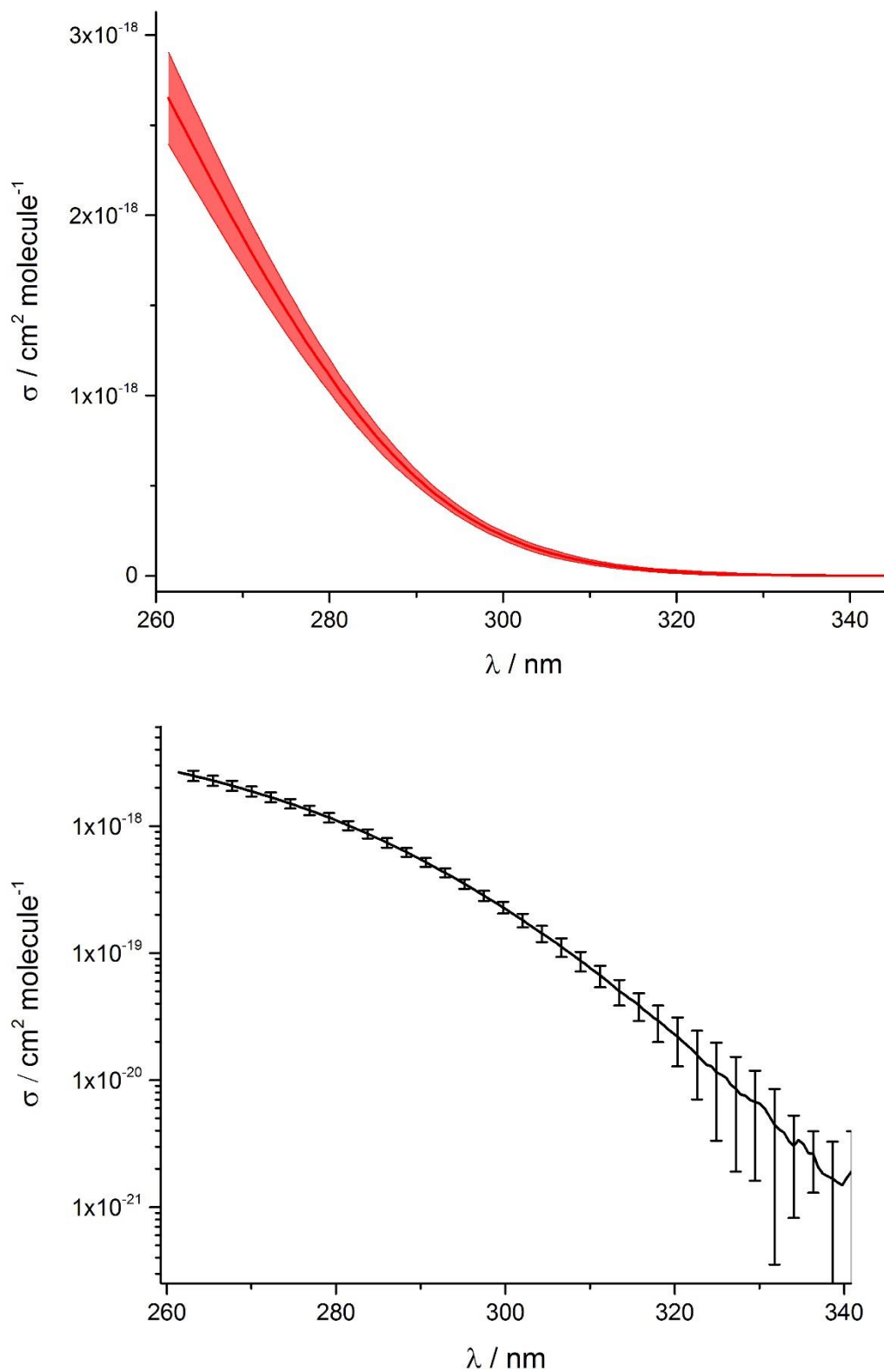
Figure 5.3: The methyl peroxy radical absorption spectrum measured by the TRUVAS instrument. 1σ error bars are shown, constructed by adding together the spread of results and the 5% error in path length (see section 2.2.7). The spectrum is shown on both linear (top) and logarithmic (bottom) scales.
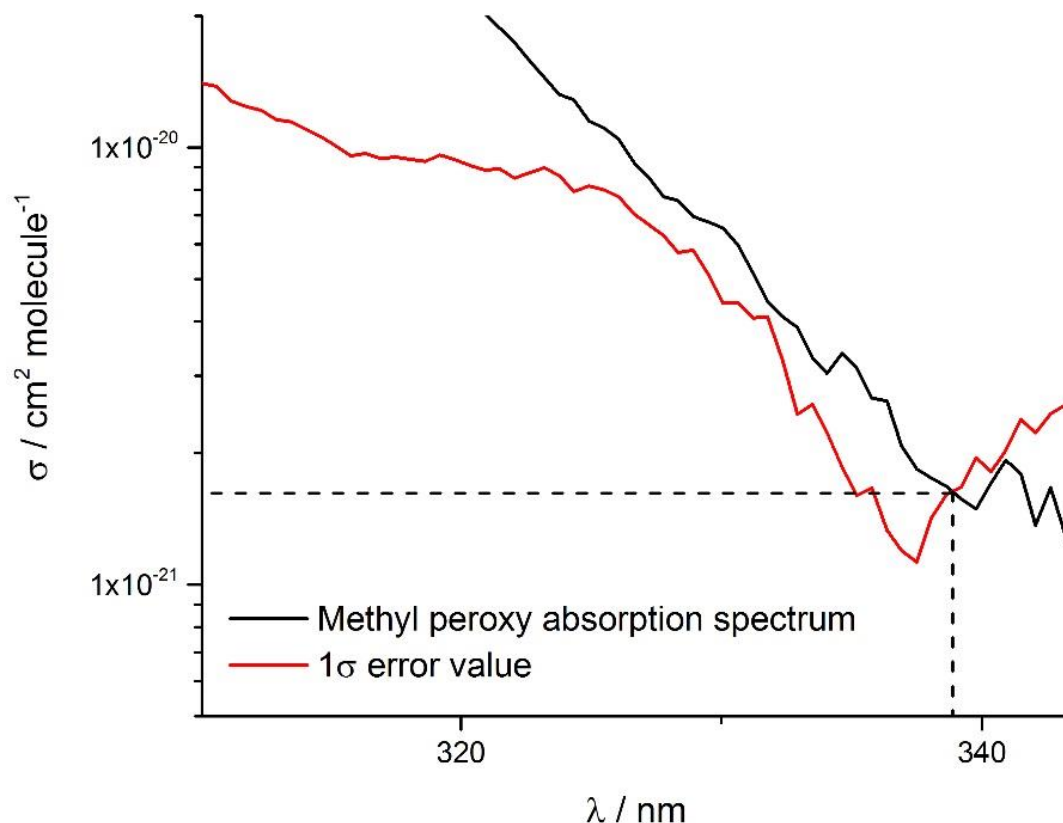
Figure 5.4: A blown up part of the absorption cross-section (black line) shown in Figure 5.3 and the 1σ error value (red line) for the absorption cross-section measurements of the methyl peroxy radical measured using the TRUVAS instrument. The point at which the 2 values are equivalent represents the smallest reliable absorption cross-section for the methyl peroxy radical measured by the TRUVAS system, calculated to be 1.38×10^{-21} cm^2 molecule^{-1} at 338.6 nm.

T-butyl peroxy radical absorption spectrum

The absorption spectrum of the *t*-butyl peroxy radical was measured using the TRUVAS instrument. *T*-butyl hydroperoxide was photolysed using a 248 nm excimer laser in the presence of O_2 ([O_2] 0.6-1.4 $\times$ 10^{18} molecule cm^{-3}) in an N_2 buffer, to yield methyl peroxy and *t*-butyl peroxy radicals (R 5.10-R 5.12).

Table 5.2: Experimental conditions for the *t*-butyl peroxy radical experiments. The results of these runs are shown in Figure 5.5. Note [radical] is given as the concentration of the *t*-butyl peroxy radical, rather than the sum of the *t*-butyl and methyl peroxy radicals

Run	Total P / Torr	[peroxide] / 10^{16} molecule cm^{-3}	Excimer energy / mJ	[radical] / 10^{14} molecule cm^{-3}
T-butyl peroxy run 1	63	2.1	71.8	3.85
T-butyl Peroxy run 2	63	1.44	71.8	2.58
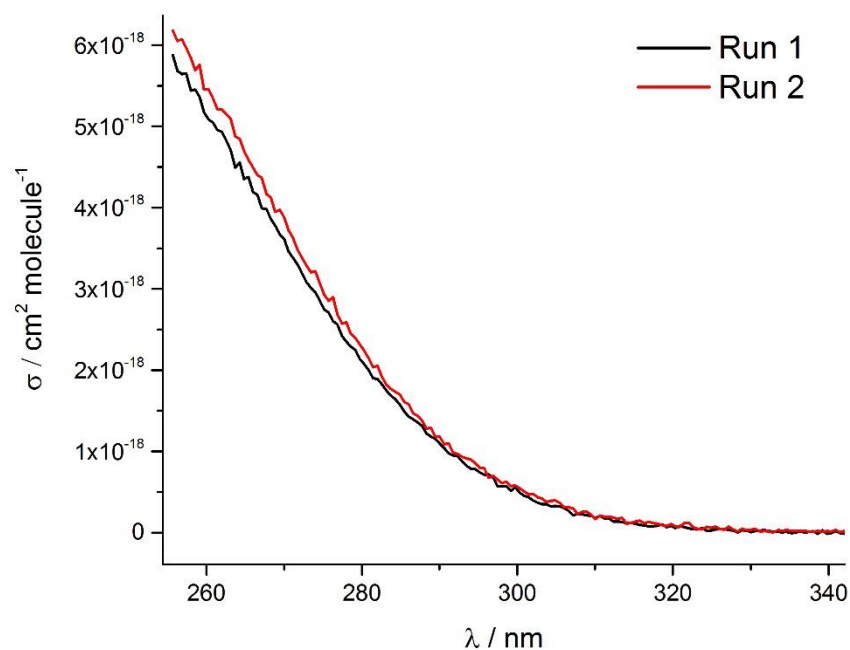
Figure 5.5: Compound spectra (i.e. spectra comprising the sum of both the methyl and *t*-butyl peroxy radical absorption spectra) of the products of *t*-butyl peroxide photolysis at 248 nm (conditions given in Table 5.2). The spectrum shown comprises the sum of the methyl peroxy and the *t*-butyl peroxy radical spectra, since both were present in equal amounts in the reaction mixture. Transient absorption profiles were recorded at .57 nm intervals (resolution 1.5 nm) between 250-650 nm.
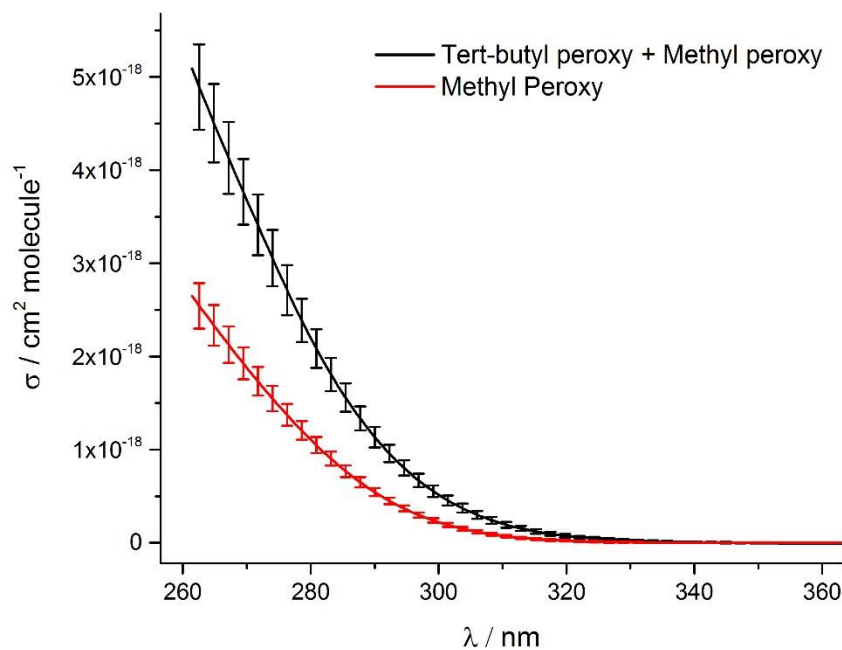
Figure 5.6: Average compound spectra (i.e. spectra comprising the sum of both the methyl and *t*-butyl peroxy radical absorption spectra) from runs 1 and 2 shown in Figure 5.5 (black). 1σ error bars are shown, constructed from the sum of the spread of results and the 5% error in path length. The methyl peroxy radical spectrum is shown in red, to illustrate the difference between the spectrum recorded with and without ethanol present; the difference between the 2 spectra represents the absorption spectrum of the *t*-butoxy radical.
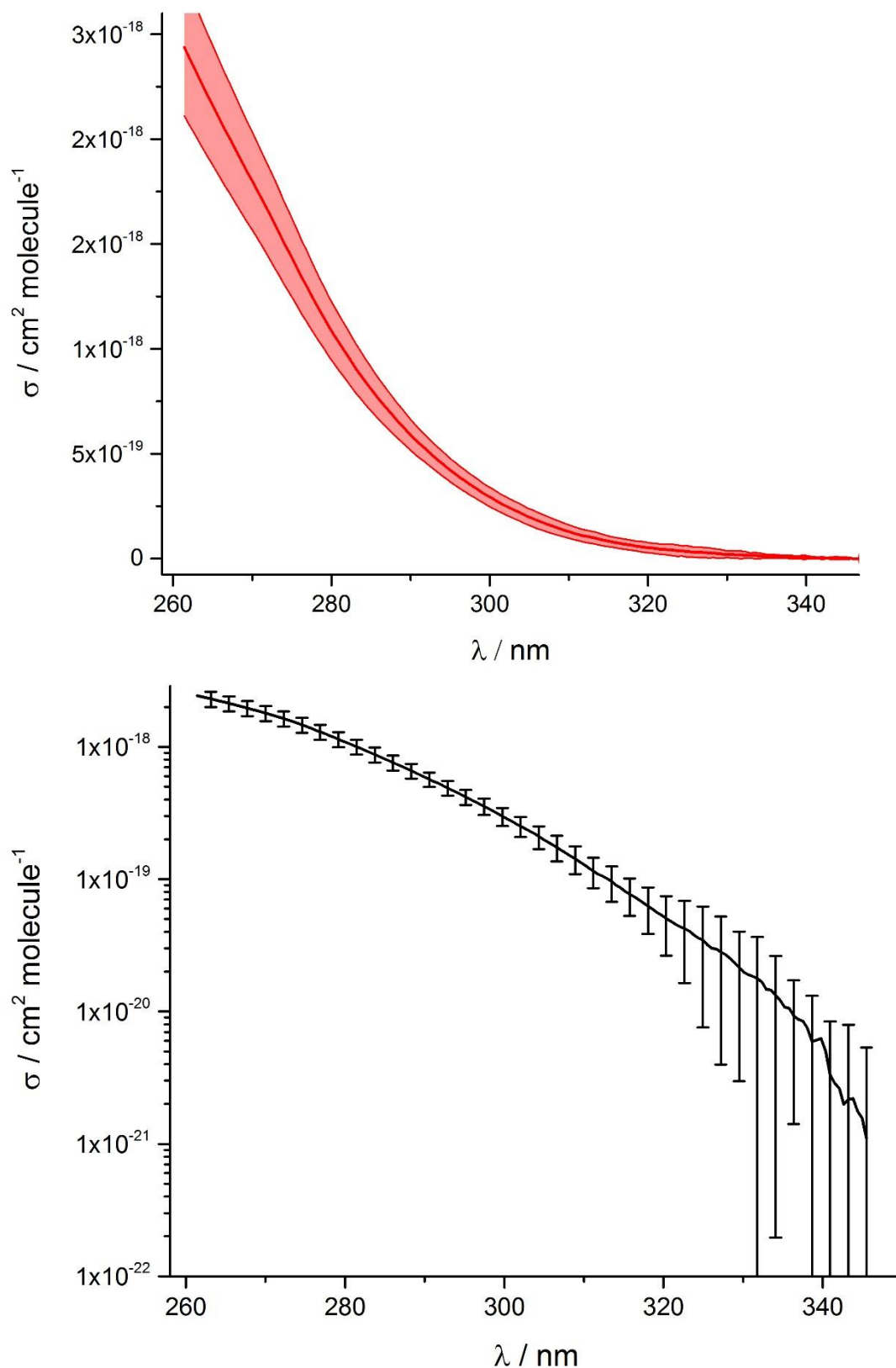
Figure 5.7: The *t*-butyl peroxy radical absorption spectrum measured by the TRUVAS instrument. 1σ error bars are shown, propagated from the errors in both the methyl peroxy radical absorption spectrum, and the compound spectrum shown in Figure 5.5. The spectrum is shown on both linear (top) and logarithmic (bottom) scales.
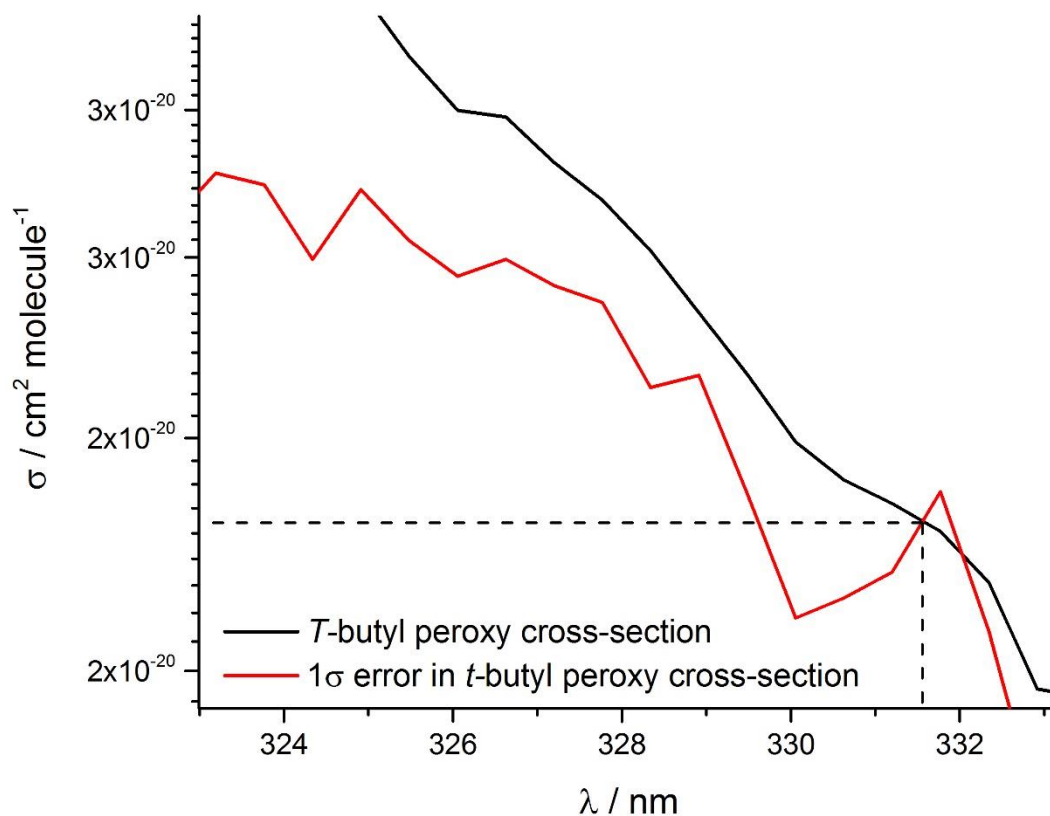
Figure 5.8: The absorption cross-section (black line) and the 1σ error value (red line) for the absorption cross-section measurements of the *t*-butyl peroxy radical measured using the TRUVAS instrument. The point at which the 2 values are equivalent represents the smallest reliable absorption cross-section for the *t*-butyl peroxy radical measured by the TRUVAS system, calculated to be 1.80×10^{-20} cm^2 molecule^{-1} at 331.6 nm.

Cyclohexyl peroxy radical absorption spectrum

The absorption spectrum of the cyclohexyl peroxy radical was measured using the TRUVAS system. Cyclohexyl peroxy radicals were generated *via.* reaction of cyclohexane with OH, from the 248 nm photolysis of H_2O_2, in the presence of O_2. 3 runs were carried out, the results of which are presented in Figure 5.9 (experimental conditions given in Table 5.3).
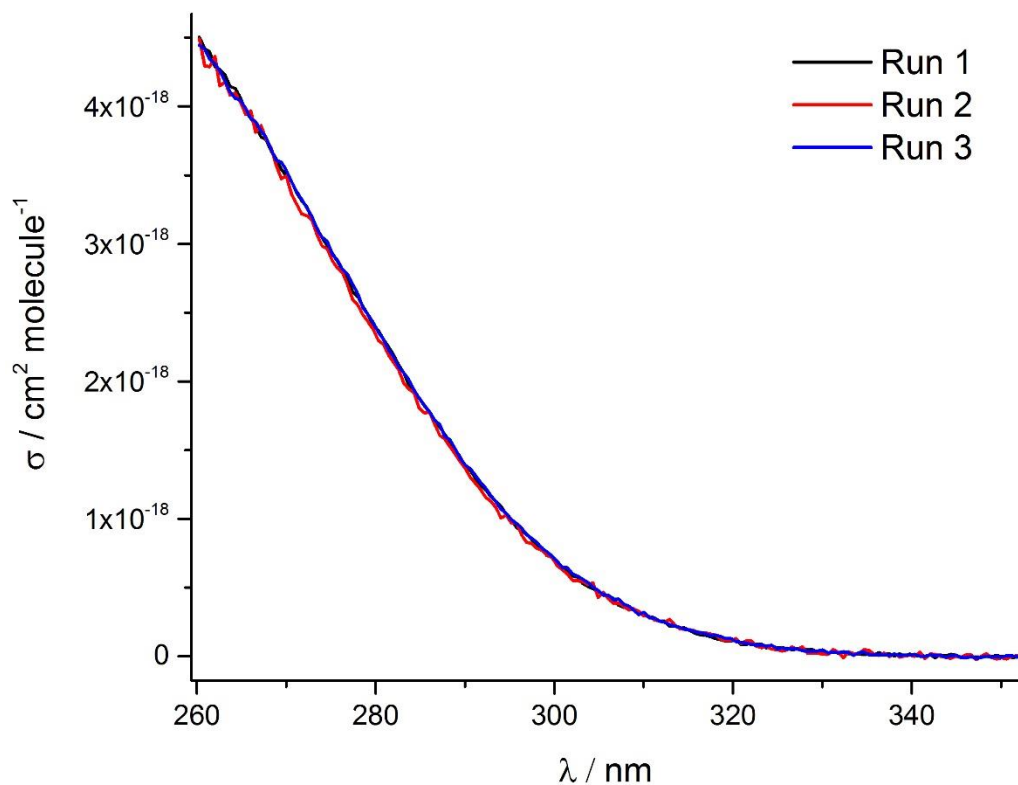
Figure 5.9: Runs 1-3 of the cyclohexyl peroxy radical absorption spectrum (1 – black, 2 – red, 3 – blue. Conditions given in Table 5.3). Transient absorption profiles were recorded at .57 nm intervals (resolution 1.5 nm) following the pulsed excimer photolysis of H_2O_2-cyclohexane-O_2-N_2 mixtures at 248 nm. Note the spread of results for these experiments is very small, and the spectra presented here overlap.

Table 5.3: Experimental conditions for the cyclohexyl peroxy radical experiments. The results of these runs are shown in Figure 5.9.

Run	Total P / Torr	[peroxide] / $\times 10^{15}$ molecule cm^{-3}	Excimer energy / mJ	[radical] / 10^{13} molecule cm^{-3}
Cyclohexyl Peroxy run 1	173	5.20	77.6	9.16
Cyclohexyl Peroxy run 2	176.5	2.35	77.6	4.14
Cyclohexyl Peroxy run 3	260.5	6.50	77.6	11.5
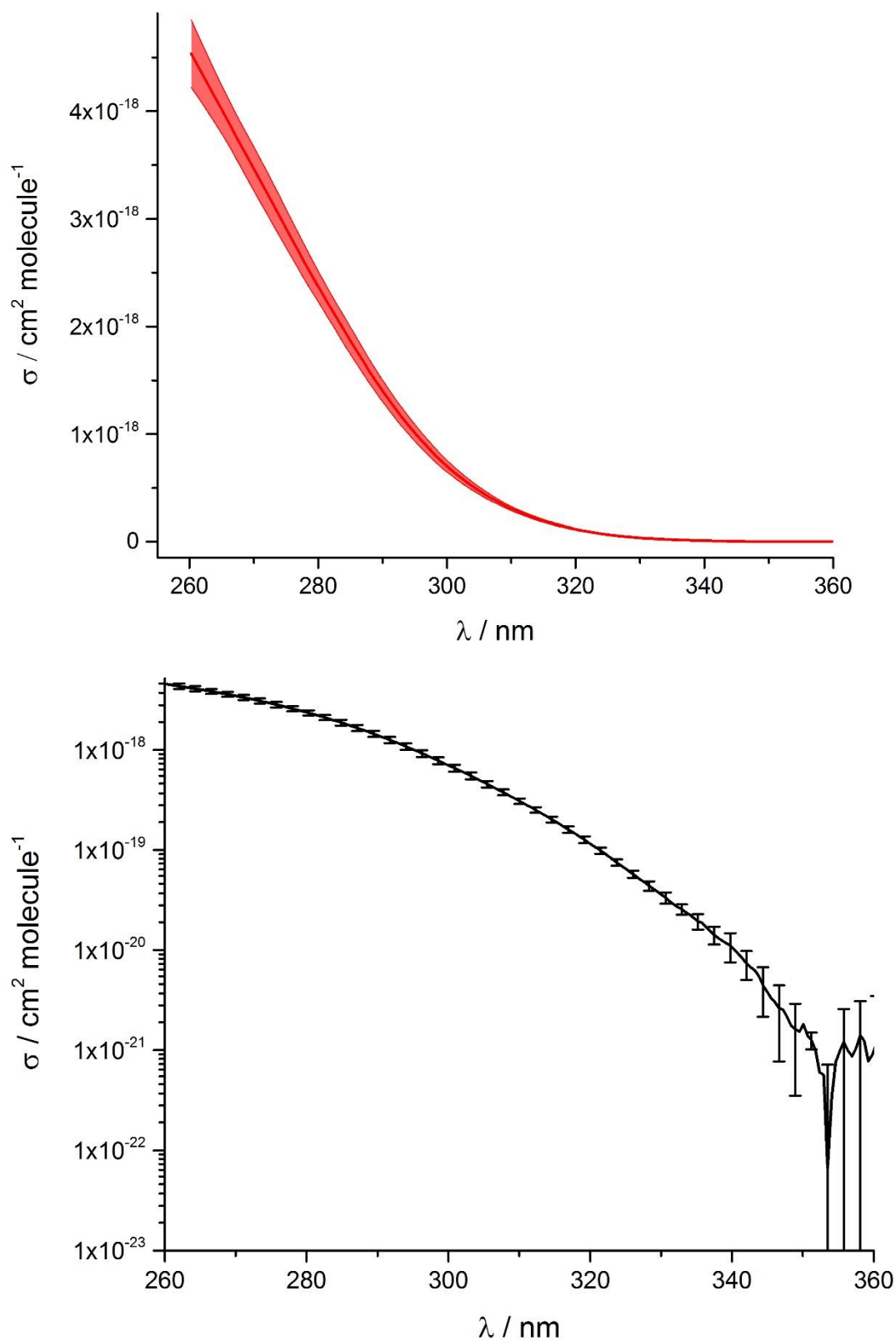
Figure 5.10: The cyclohexyl peroxy radical absorption spectrum measured by the TRUVAS instrument. 1σ error bars are shown, constructed from the sum of the spread of results and the 5% error in path length. The spectrum is shown on both linear (top) and logarithmic (bottom) scales.
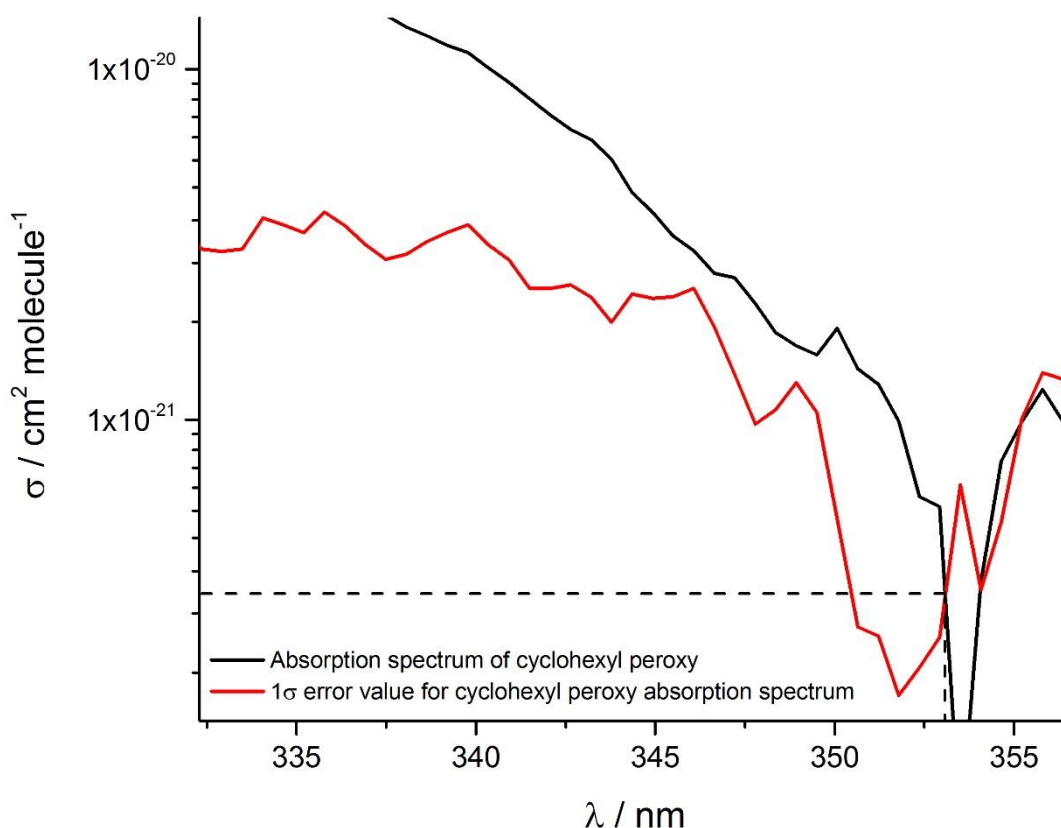
Figure 5.11: The absorption cross-section (black line) and the 1σ error value (red line) for the absorption cross-section measurements of the cyclohexyl peroxy radical measured using the TRUVAS instrument. The point at which the 2 values are equivalent represents the smallest reliable absorption cross-section for the cyclohexyl peroxy radical measured by the TRUVAS system, calculated to be 3.21×10^{-22} cm^2 molecule^{-1} at 353.1 nm.

5.4 Previous studies

The absorption spectra of methyl, *t*-butyl and cyclohexyl peroxy radicals have been measured using the TRUVAS instrument. The following section will discuss the results, and compare these results with those previously obtained in the literature.

Methyl peroxy radical

The methyl peroxy radical absorption spectrum has been studied numerous times over the past 40 years, initially by Parkes *et al*. who observed a weak, broad, smooth absorption band between 200-300 nm.[65-67, 198, 223, 224, 237-248] A comprehensive review of the methyl peroxy radical absorption spectra measured prior to 1992 by Lightfoot *et al*. was published in Atmospheric Environment.[67] Results obtained between 1973 and 1985 were subject to significant disagreement, differing up to a factor of 2

between Kan *et al.* [241] and Adachi *et al.*[223] both of whom employed the same technique (flash photolysis of azomethane), with no clear explanation as to the source of this disagreement given by Lightfoot *et al.*. Tyndall *et al.* published a second broad review of peroxy radical spectra and chemistry in 2001[196], attributing the discrepancies in the Kan measurements (in addition to other pre – 1990 measurements) to incomplete conversion of methyl radicals to methyl peroxy. Tyndall *et al.* also note the overestimation of absorption cross-sections measured by McAdam *et al.* and Moortgat *et al.* are most likely due to the use of NOCl as an actinometer.

The spread of results of the pre – 1985 experiments was improved upon significantly between 1987-1991 resulting in a recommendation by Lightfoot based on values measured by Jenkin *et al.* [198], Moortgat[244], Veyret and Lesclaux[243], Simon[248], Schneider and Moortgat[64], Dagaut and Kurylo[239], and Lightfoot and Jemi-Alade[66].

Fahr *et al.* [224] (1997) and Roehl *et al.* [249] (1996) have measured the methyl peroxy radical absorption spectrum, in good agreement with the recommendations by Lightfoot *et al.* in terms of the peak height and width of the $\tilde{B} - \tilde{X}$ absorption band, however disagreement exists with respect to the shape and intensity of the absorption spectrum at wavelengths > 280 nm as shown in Figure 5.12.
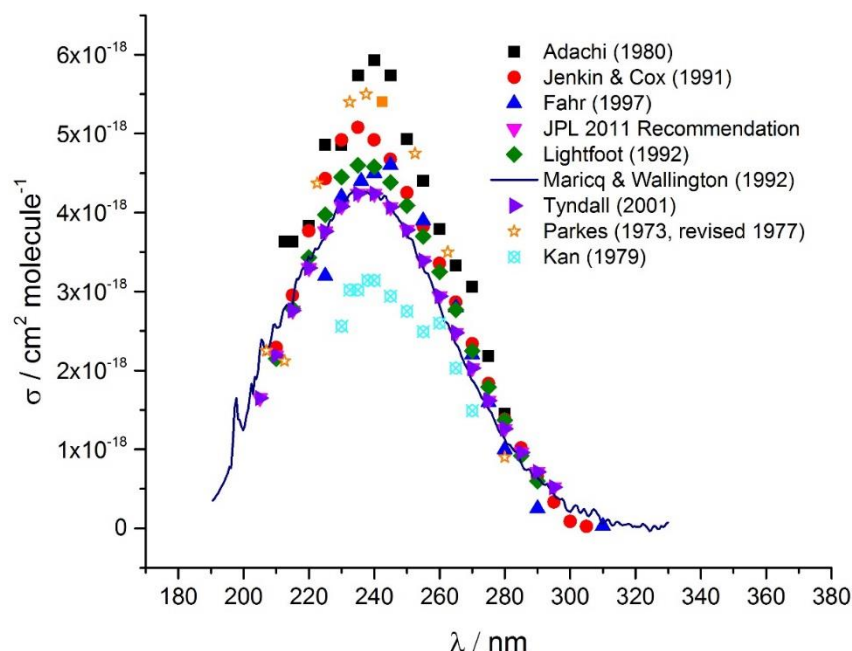
Figure 5.12: A selection of previous measured methyl peroxy radical absorption spectra. Adachi *et al.* [223] (black squares), Jenkin & Cox [198] (red circles), Fahr *et al.* [224] (blue triangles), JPL 2011 recommendation (Pink triangles) = Tyndall [196] (Purple triangles), Lightfoot recommendation (green diamonds), Maricq & Wallington (navy line), Parkes *et al.* (orange stars) and Kan *et al.* (cyan crossed circles).

Tyndall *et al.* also produce a recommended absorption spectrum based on McAdam *et al.* [243] , Moortgat *et al.* [244] (only data > 205 nm), Simon *et al.* [64], Lightfoot and Jemi-Alade [66] , Jenkin and Cox [198] (shape only), and Maricq and Wallington [62] (two experiments), which is the current accepted recommendation by JPL (shown in Figure 5.12).[250]

Table 5.4: Various methyl peroxy radical absorption cross-sections experiments and experimental details. Note this list is not exhaustive and is intended to highlight the various techniques employed prior to this study.

Ref.	Method	Technique
Adachi 1980[223]	Flash photolysis of azomethane in the presence of O_2 using pulsed Xe lamp (λ > 280 nm)	Flash Photolysis
Jenkin Cox 1991[198]	254 nm photolysis of CH_3I in the presence of O_2	Molecular Modulation Spectroscopy
Fahr 1997[224]	193 nm photolysis of acetone in the presence of O_2	Laser flash photolysis
Lightfoot 1990[68]	193 nm photolysis of O_2 in the presence of methane	Flash photolysis
Maricq 1991[62]	193 nm photolysis of methyl chloride in methane and O_2	Laser flash photolysis
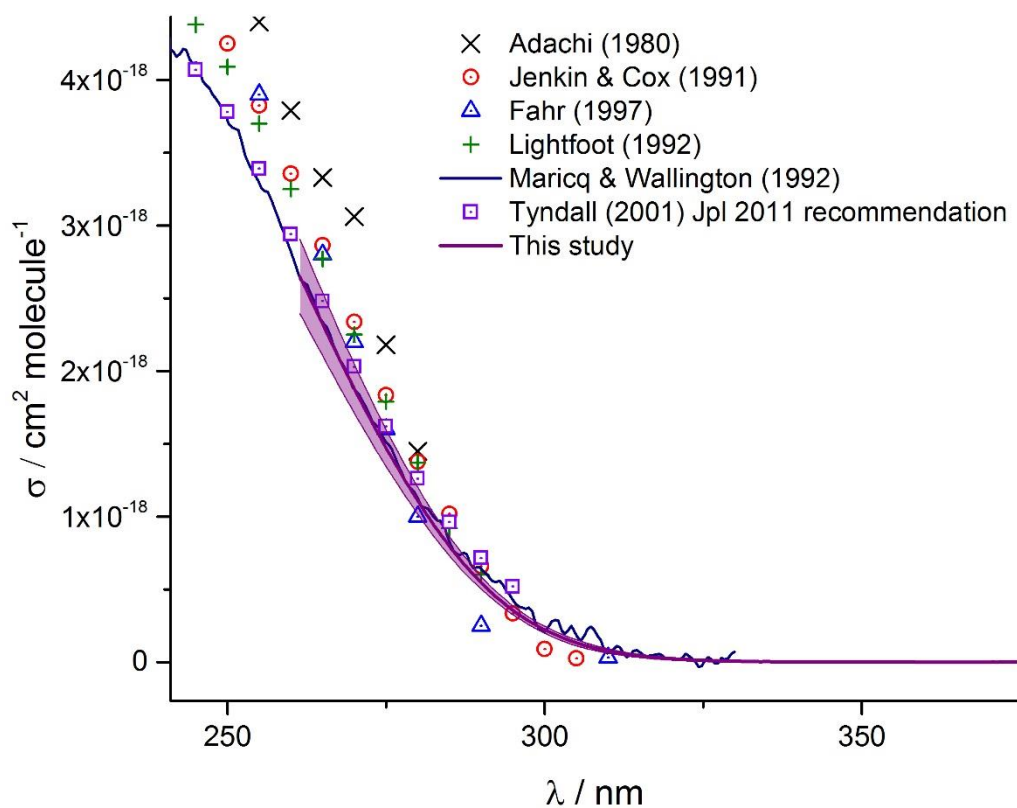
Figure 5.13: Absorption cross-sections for the methyl peroxy radical measured by various groups, alongside recommendations by Lightfoot (green crosses) and Tyndall (purple squares). The absorption cross-sections measured in this study > 260 nm are shown (purple line) with 1σ error bars.

The absorption spectrum between 260 – 338 nm is shown alongside previous studies and recommendations in Figure 5.13. It can be seen that the magnitude of the absorption in the region is in good agreement with the 2001 recommendation by Tyndall *et al.,* more so than the 1992 Lightfoot recommendation, however the shape of the absorption measured by the TRUVAS instrument agrees more closely with the spectrum measured by Maricq and Wallington[62]. Since most studies which probe the $\tilde{B} - \tilde{X}$ absorption band are concerned primarily with following the concentration of methyl peroxy radicals to measure the rates of reactions, less emphasis has been placed on defining the shape of the absorption band in the actinic region (>270 nm), in favour of defining the overall shape and peak intensity for spectroscopic kinetic measurements. If the smallest reliable literature absorption cross-section is taken as the smallest of those recommended by Tyndall *et al.*: 5.2×10^{-19} cm^2 molecule^{-1} at 295 nm, the smallest reliable absorption cross-section measured by the TRUVAS instrument: 1.38×10^{-21} cm^2 molecule^{-1} at 338.6 nm represents an increase in sensitivity of more than 2 orders of magnitude.

T-butyl peroxy radical

The *t*-butyl peroxy radical has been studied previously by Kirsch and Parkes [251], Anastasi *et al*. [237], Tomas *et al*. [252] and Wallington *et al.*[65], all of which are in reasonably good agreement, as shown in Figure 5.14.

Table 5.5: Previous studies of the *t*-butyl peroxy radical, alongside a brief description of the methodology used to generate the *t*-butyl peroxy radical species.

Ref.	Method	Technique
Anastasi *et al*. [237]	OH (generated from H$_2$O photolysis) + *t*-butyl peroxide	Flash Photolysis
Kirsch and Parkes [251]	Photolysis of azo-tert-butane	Molecular Modulation Spectroscopy
Lightfoot [68]	> 280 nm photolysis of Cl$_2$ + isopropane	Flash photolysis
Tomas [252]	Photolysis of Br$_2$ in the presence of *t*-butyl aldehyde	Flash photolysis
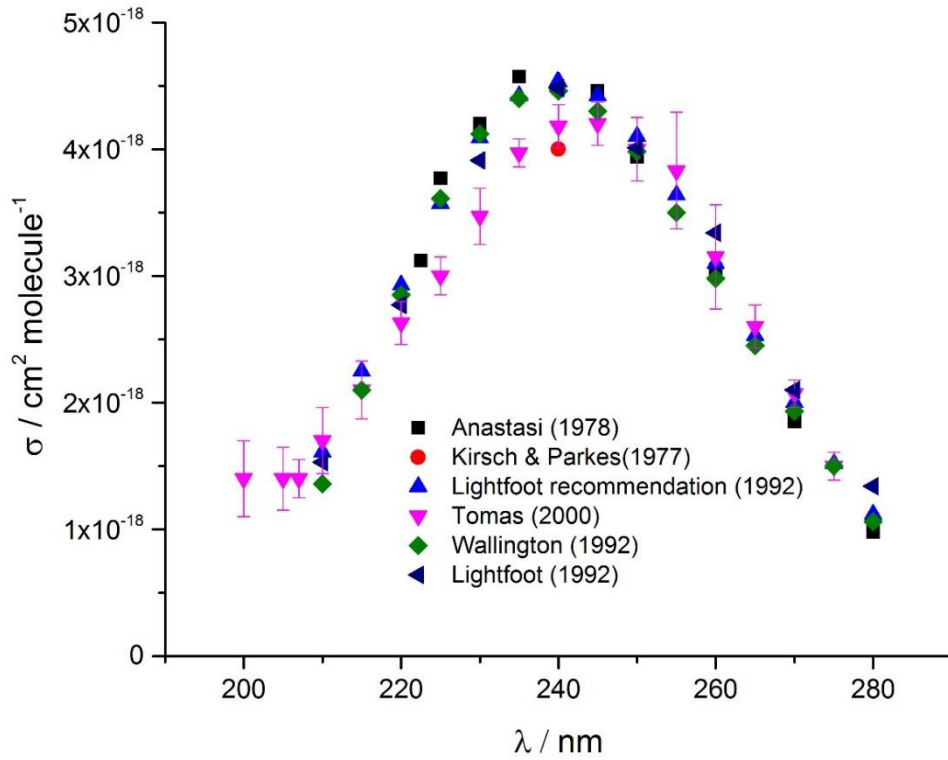
Figure 5.14: *T*-butyl peroxy radical absorption spectra measured by Anastasi *et al*. [237] (black squares), Kirsch and Parkes [251] (red circle), Lightfoot recommendation [67] (blue triangle), Tomas [252] (pink triangles), Wallington [65] (green diamonds) and Lightfoot [68] (navy triangles).
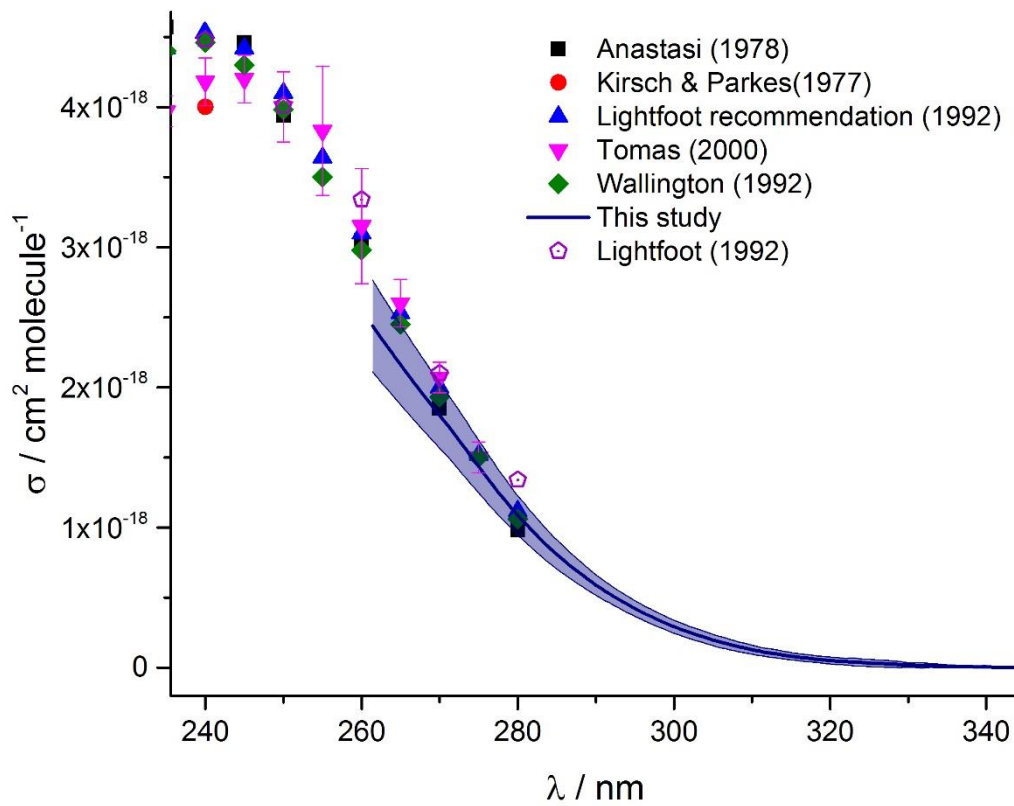
Figure 5.15: The *t*-butyl peroxy radical spectrum measured by the TRUVAS system is shown (navy line) with 1σ error bars alongside previous measurements (details given in Figure 5.14 and

Table 5.5).

The absorption spectrum measured by the TRUVAS instrument agrees well with previous studies at around 280 nm, with the agreement worsening at shorter wavelengths, as shown in Figure 5.15. Possible explanations for this could lie in the experimental methods used previously to generate the t-butyl peroxy radical. In the study by Anastasi *et al*., Xe flash lamps were used to generate OH *via.* H_2O photolysis, however at the wavelengths required to photolyse H_2O, t-butyl hydroperoxide has significant absorption cross-sections as shown in Figure 5.16, and would presumably photolyse to OH and hot t-butoxy as per reaction R 5.10, leading to an overestimation of the absorption cross-sections for the t-butyl peroxy radical.
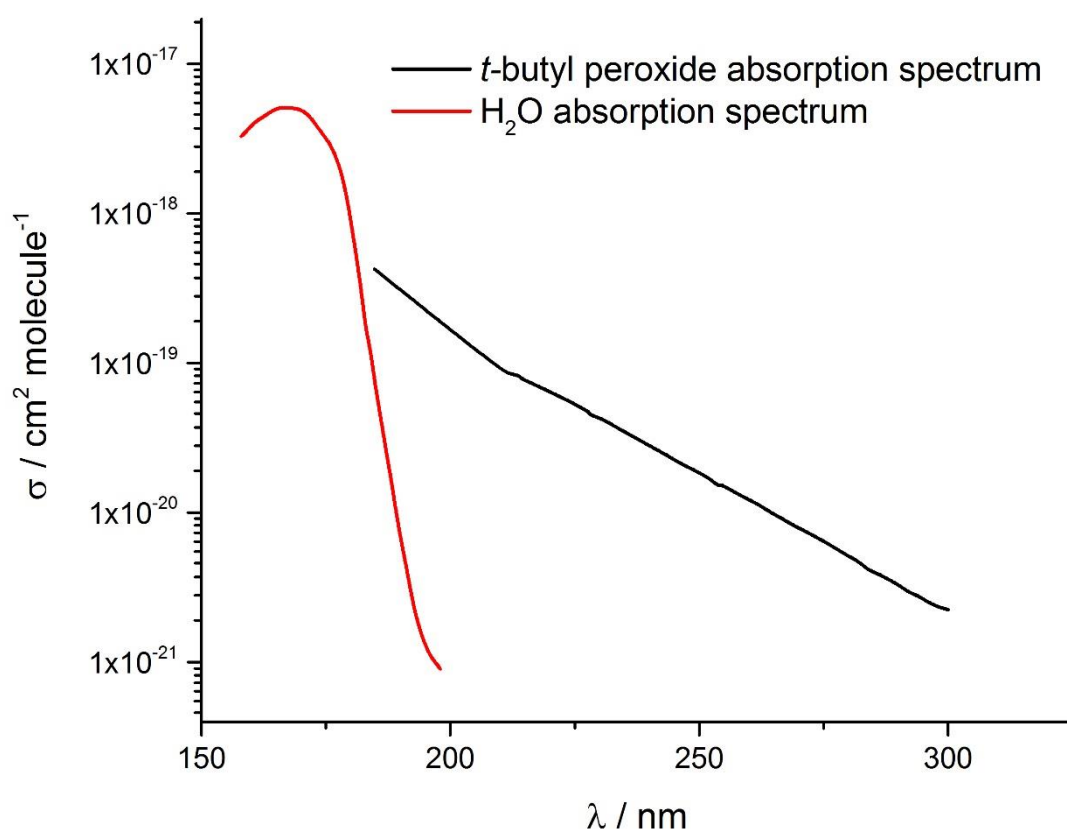
Figure 5.16: The absorption spectra of *t*-butyl peroxide (black line - Baasandorj[231]) and water vapour (red line – JPL recommendation[250]).

The rotationally hot t-butoxy formed *via.* reaction R 5.10 will decompose to acetone and methyl *via.* reaction R 5.11 with methyl radicals combining with O_2 to form methyl peroxy radicals *via.* reaction R 5.12. In fact Anastasi *et al*. comment that they observe residual signal, which they cannot account for in their analysis.[237] Reasons for inconsistencies surrounding the absorption spectrum of the t-butyl peroxy radical

measured by other groups are unclear, however the chemical schemes used to generate the radical were significantly more complex than the methodology outlined here, and could be subject to numerous errors, such as side reactions and unwanted photolysis products (for example HO_2) unaccounted for in their respective analyses. Indeed there are numerous cases in the literature where photolysis quantum yields of a precursor have been found to be in error, subsequent to the study in which they are used.[67] Incomplete conversion of OH to *t*-butyl peroxy radicals in the experiments carried out in this study could lead to an underestimation of the *t*-butyl peroxy radical absorption cross-sections, and reconcile the differences between previous measurements and the measurements by the TRUVAS instrument presented here.

Absorption spectrum of the cyclohexyl peroxy radical

Previous experimentally determined absorption cross-sections of the cyclohexyl peroxy radical are shown in Figure 5.17. The UV absorption spectrum of the cyclohexyl peroxy radical has previously been studied by Rowley *et al*. *via.* Cl_2 photolysis at wavelengths >300 nm in the presence of cyclohexane.[63] Cl formed from Cl_2 photolysis reacts rapidly ($k = 3\text{-}4 \times 10^{-10}$ cm^3 molecule^{-1} s^{-1})[69, 253] with cyclohexane to yield the cyclohexyl radical, which combines with O_2 to form the cyclohexyl peroxy radical.

A more recent study by Platz *et al*. employs pulsed radiolysis of SF_6 to generate F atoms, which abstract H from cyclohexane to yield the cyclohexyl radical, combining with O_2 to yield cyclohexyl peroxy radicals.[226]

In addition to the single absorption cross-section value for the maximum of the cyclohexyl peroxy radical absorption spectrum presented in Figure 5.17, Platz *et al*. present an absorption spectrum which is broader, more intense and slightly red-shifted (~10 nm) compared to the spectrum measured by Rowley *et al*..[63] The reason for this slight disagreement between the 2 methods is unclear, however the spectrum measured in this study resembles the spectrum measured by Rowley *et al*. remarkably well, over and above both the Platz *et al*. measurements and the Lightfoot recommendation as shown in Figure 5.18.
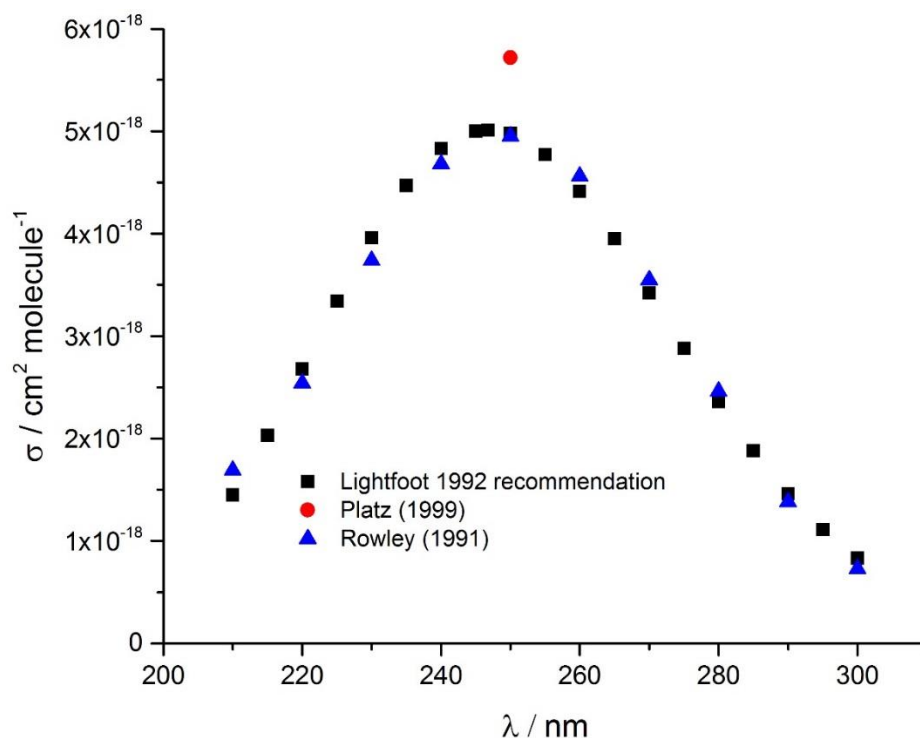
Figure 5.17: Previous measurements of cyclohexyl peroxy radical absorption cross-sections by Rowley *et al*. (blue triangles) [63] **and Platz *et al*. (red circles)** [226]**. The Lightfoot recommendations for the cyclohexyl peroxy radical absorption cross-sections are given (black squares).**[67]
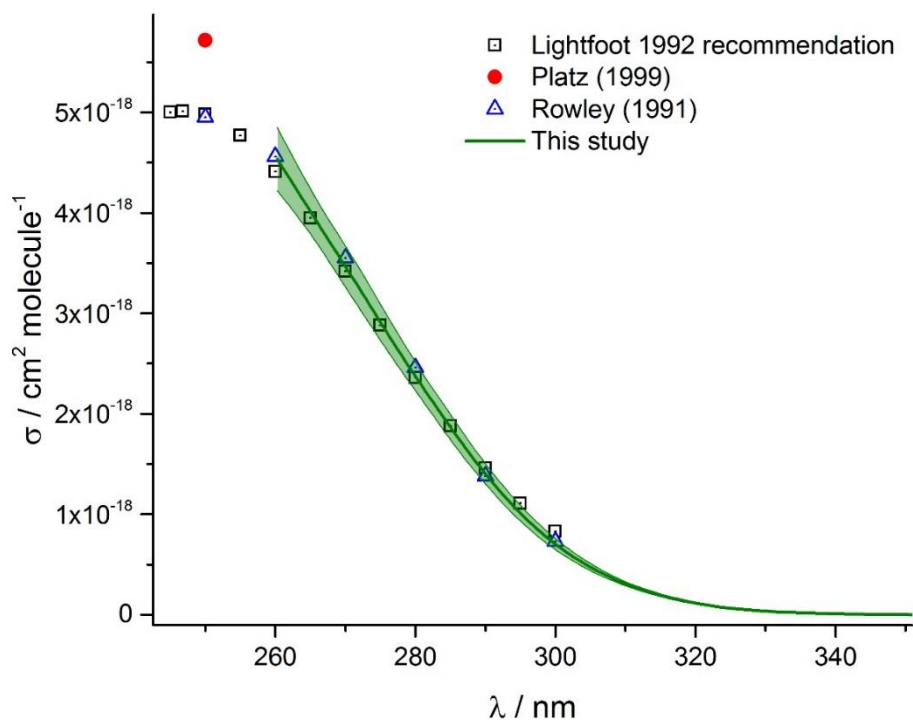
Figure 5.18: Cyclohexyl peroxy radical absorption spectrum measured by the TRUVAS system (green line) with 1σ error bars. Previous measurements of cyclohexyl peroxy radical absorption cross-sections by Rowley *et al*. (Blue triangles – original data, Pink triangles – rescaled to 4.58 × 10^{-18} cm² molecule^{-1} at 240 nm) [63] **and Platz *et al*. (red circle)** [226]**. The Lightfoot recommendations for the cyclohexyl peroxy radical absorption cross-sections are given (black squares).**[67]

The absorption spectrum for the cyclohexyl peroxy radical measured by the TRUVAS instrument is presented down to absorption cross-sections as small as 3.21×10^{-22} cm^2 molecule^{-1} at 353.1 nm, representing the smallest reliable absorption cross-sections measured by the instrument, and the smallest UV absorption cross-section of any transient peroxy radical species in the literature to date. The high degree of precision observed for the cyclohexyl peroxy radical in particular, is likely due to the slow self-reaction rate and therefore removal of the species (2.42×10^{-14} cm^3 molecule^{-1} s^{-1}).[63] Uncertainties in the extrapolation procedure could be a contributing factor toward the variation in spread in results between systems: if significant removal of the target species occurs within the first millisecond, the extrapolated A_0 will be more sensitive to the parameters used to perform the extrapolation, than if only a small fraction of the absorbing species is lost in this time.

5.5 Atmospheric photolysis rates of methyl peroxy radical

The absorption cross-section of the methyl peroxy radical has been measured from 260-338 nm using the TRUVAS instrument. The broad, featureless $\tilde{B} - \tilde{X}$ transition involves excitation to the repulsive $\tilde{B}$ state, common to all peroxy radicals.[63-69] In the following section, the potential impact of methyl peroxy radical photolysis on the tropical marine boundary layer will be discussed, including total photolysis rates and the potential for OH formation from the dissociation of the excited $\tilde{B}$ state, based on experiments carried out by Dr Robert Hansen at the University of Leeds.

A Gaussian function (E 5.8) was used to fit to the experimental data, as shown in Figure 5.19 with parameters given in Table 5.9.

$$y = \frac{a}{w\sqrt{\pi/2}} e^{-2\left(\frac{x-x_c}{w}\right)^2} \qquad \text{E 5.8}$$

Table 5.6: Parameters from Gaussian function shown in Figure 5.19, where x_c is the wavelength at which the Gaussian function is at a maximum, w is the Gaussian width at one tenth the height of the maximum and a is the height of the curve's peak.

x_c	242.3 nm
w	49.3 nm
a	2.20×10^{-16}
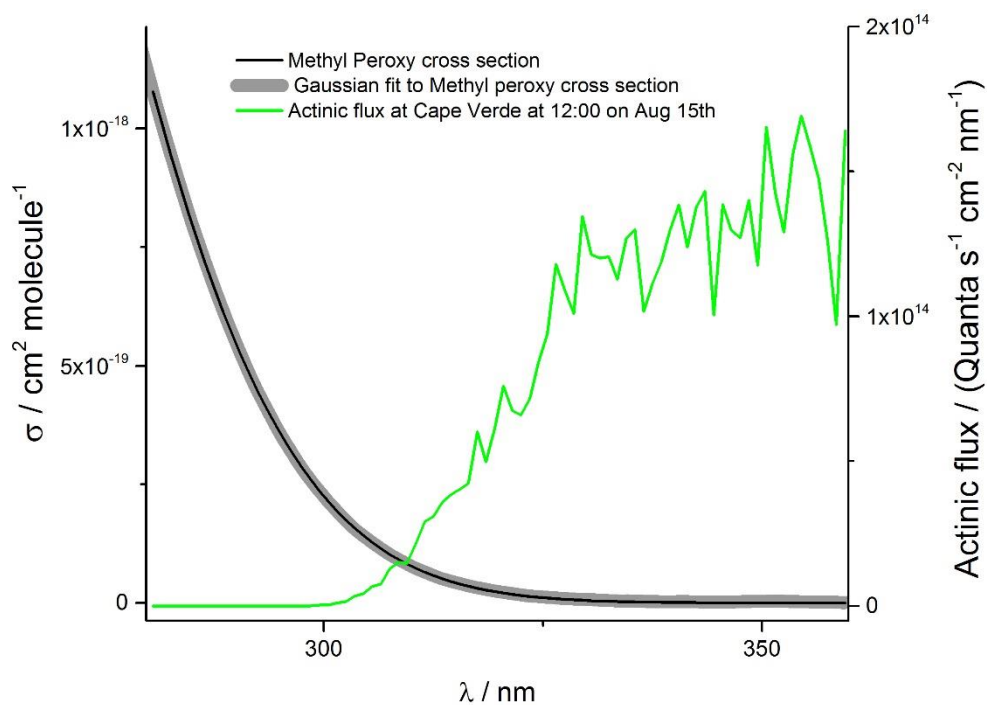
Figure 5.19: The methyl peroxy radical absorption cross-section measured by the TRUVAS instrument (black line) alongside a gaussian fit to the data (grey line), the parameters of which are given in Table 3.2. The actinic flux as a function of wavelength is shown in green, calculated for the 15th of august at 12:00 noon local time (15° North, 23.5° West – corresponding to Cape Verde) using the ACOM TUV model.[77]

To calculate $J_{\lambda,\text{total}}$ the total photolysis frequency at a particular wavelength, the absorption cross-section is multiplied by the radiant (actinic) flux ($S_{e,\lambda}$) at wavelength λ (E 4.3). Figure 5.20 shows $J_{\lambda,\text{total}}$ as a function of λ for the methyl peroxy radical. Due to the fact that the UV absorption band observed is due to excitation to the repulsive $\tilde{B}$ state, and that the absorption band is broad and featureless, the quantum yield for dissociation from the excited state ($\phi_{\text{dissociation}}$) is assumed to be 1. To quantify the total photolysis rate in the atmosphere, J_{total} must be calculated (E 4.4) by integrating the $J_{\lambda,\text{total}}$ vs λ function, to find the total area underneath the plot as shown in Figure 5.20, which for the methyl peroxy radical was calculated to be 4.12×10^{-5} s^{-1} at noon in the tropics (15° North, 23.5° West) on the 15th of August.

$$\sigma_\lambda \cdot S_{e,\lambda} = J_{\lambda,total} \qquad \text{E 5.9}$$

$$J_{total} = \Sigma(\sigma_\lambda \cdot S_{e,\lambda}) \qquad \text{E 5.10}$$
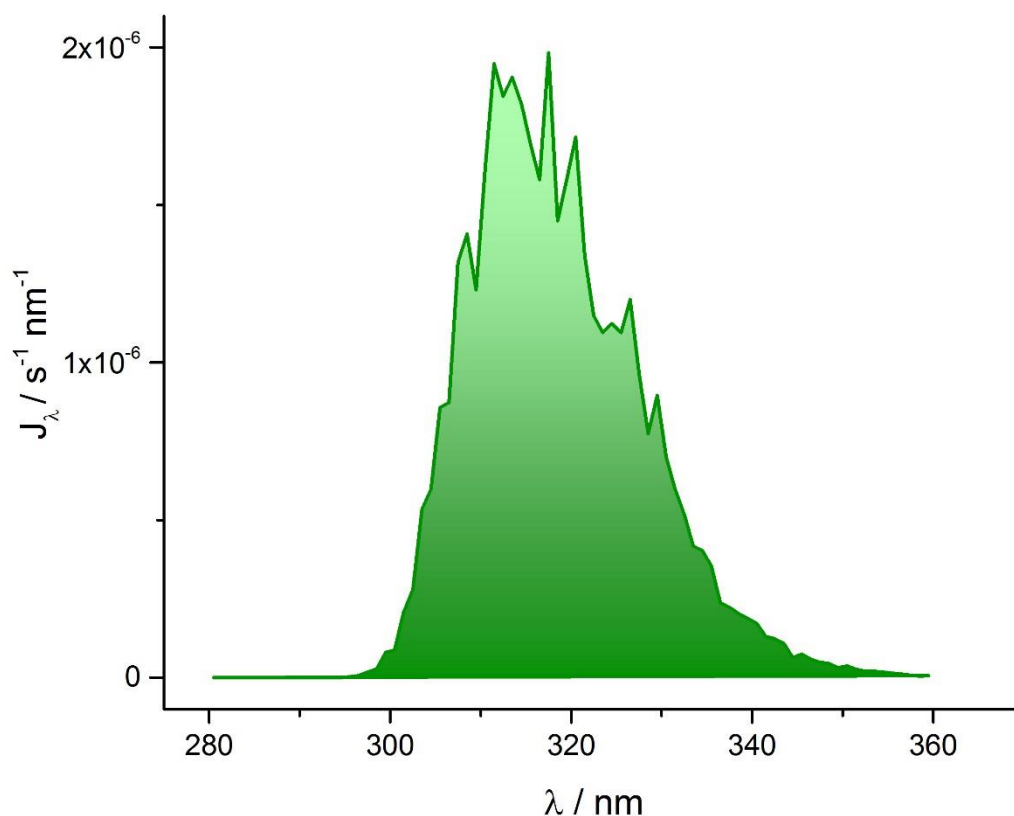
Figure 5.20: $J_{\lambda,total}$ **values for the photolysis of methyl peroxy radicals due to actinic flux as a function of wavelength is shown in green, calculated for the 15th of August at 12:00 noon local time (15° North, 23.5° West – corresponding to Cape Verde) using the ACOM TUV model, discussed in section 1.2.4. The J_{total} value is calculated by integrating the function to give the area, calculated to be 4.12×10^{-5} s^{-1}.**

Table 5.7 and Figure 5.21 show the main sinks for methyl peroxy radicals at Cape Verde. Removal rates given in Table 5.7 are calculated by multiplying the bimolecular rate coefficient by the typical concentration of the co-reactant, the references for which are given within the table. Removal *via.* photolysis accounts for around 1% of the total removal rate of methyl peroxy radicals under these conditions, and has a minor influence on the removal of methyl peroxy radicals in this environment. With a removal rate of 4.17×10^{-5} s^{-1}, the lifetime of methyl peroxy radicals with respect to removal *via.* photolysis is ~6.7 hours, which far exceeds the lifetime with respect to the removal of methyl peroxy radicals *via.* the two most dominant removal processes: reaction with HO_2 (12 minutes) and OH (20 minutes) and the total lifetime of the methyl peroxy radical (4 minutes).

Table 5.7: Removal rates of methyl peroxy radicals at noon in Cape Verde *via.* reaction with HO₂, OH, NO, NO₂ and RO₂ as well as for the removal *via.* photolysis, as shown in Figure 5.20. References for each value are given next to each value. RO₂ includes all alkyl peroxy radical species.

Removal *via.*	Typical noon concentration of species at Cape Verde / cm⁻³	Ref	$k_{species + methyl\ peroxy}$ / 10^{-12} cm³ molecule⁻¹ s⁻¹	Ref	CH_3O_2 removal rate at noon / 10^{-4} s⁻¹	% of total removal rate	τ_{CH3O2} / minutes
HO₂	2.70×10^8	[221]	5.21	[254]	14.1	35.3	12
OH	5.00×10^6	[221]	160	[162]	8	20.1	21
NO	2.10×10^7	[161]	7.70	[86]	1.62	4.06	103
NO₂	3.08×10^8	[161]	4.00	[86]	12.3	30.9	14
RO₂	1.00×10^9	[161]	0.34	[254]	3.4	8.55	49
*J*total					0.412	1.04	405
Total					39.8		4

Figure 5.21: Removal rates of methyl peroxy radicals *via.* reaction with HO₂ (dark blue – 35.3 %), OH (red – 20.1 %), NO (green – 4.06 %), NO₂ (purple – 30.9 %) and RO₂ (light blue – 8.55 %) compared to removal *via.* photolysis (orange – 1.04 %) at Cape Verde.

The OH absorption cross-sections of the methyl peroxy radical were measured in a similar manner to those of ethylene, TME and Isoprene HP radicals presented in sections 3.3 and 4.3 respectively. In short, a radical precursor is photolysed within a LIF cell at 248 nm, to yield radicals; in the case of the methyl peroxy radical, *t*-butyl peroxide is photolysed to yield hot *t*-butoxy and OH. Ethanol is added to scavenge

OH (R 5.13) and hot *t*-butoxy rapidly decomposes to form acetone and methyl radicals (R 5.11), which combine with O_2 to form the methyl peroxy radical (R 5.12). The reaction mixture is then photolysed a second time using a high energy, tuneable YAG pumped dye laser to photolyse the methyl peroxy radical, followed by a 308 nm OH probe laser, at a delay of typically 1-2 µs. OH is detected *via.* LIF at 308 nm before and after the tuneable photolysis laser, with the increase in OH observed immediately prior to the 248 nm photolysis assigned as OH from RO_2 photolysis.
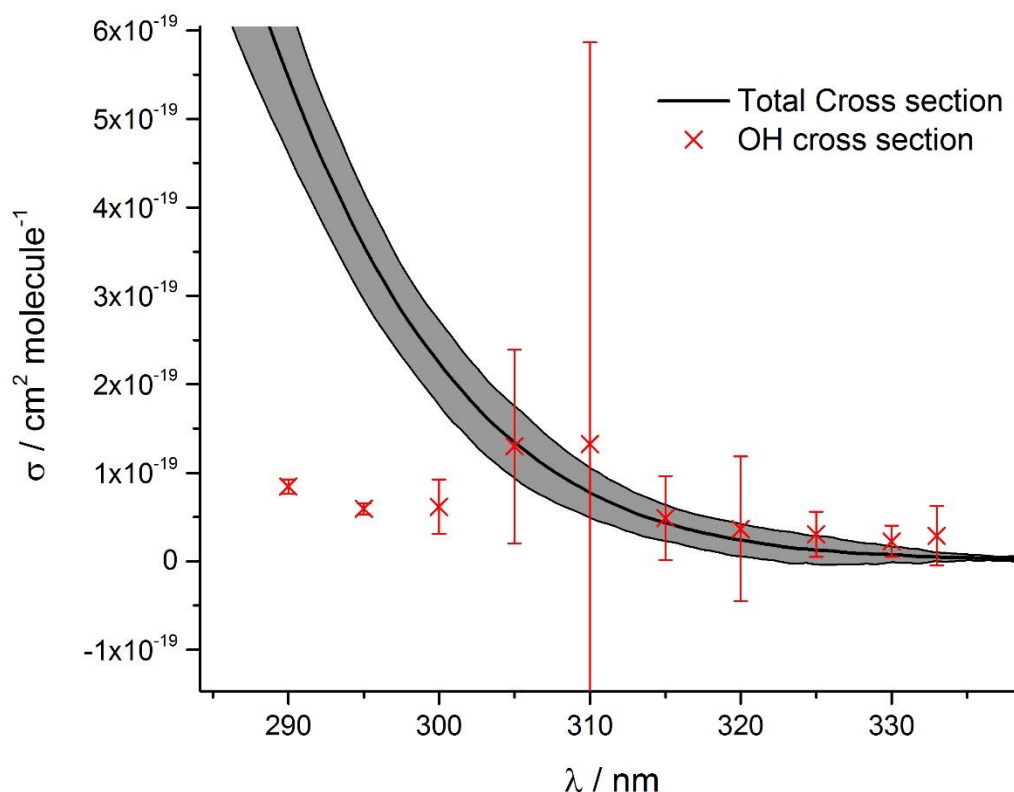
Figure 5.22: Total methyl peroxy radical absorption cross-sections with 1σ error bars are shown in black. Red crosses represent the absorption cross-sections for OH production from the methyl peroxy radical as measured by Dr Hansen, with 2σ errors. Note the large error bars >300 nm are due to significant spread in experimental results, as well as uncertainties in the *t*-butyl peroxide absorption cross-section at these wavelengths.

The OH absorption cross-section for methyl peroxy radical ($\sigma_{CH_3O_2,OH}$) is equal to the total absorption cross-section ($\sigma_{CH_3O_2,\lambda}$) multiplied by the quantum yield for OH production ($\phi_{CH_3O_2,\lambda}$). The OH absorption cross-section at a particular wavelength in the experiments by Dr Hansen, is dependent on the absorption cross-section of the radical precursor at that wavelength, as illustrated in E 5.11 and E 5.12.

$$\frac{OH_{CH_3O_2}}{OH_{tbuOOH}} = \frac{[CH_3O_2]_0 \times [h\nu]_\lambda \sigma_{CH_3O_2,\lambda} \phi_{CH_3O_2,\lambda}}{[tbuOOH] \times [h\nu]_\lambda \sigma_{tbuOOH,\lambda} \phi_{tbuOOH,\lambda}}$$

$$= \frac{[h\nu]_{248\,nm}[tbuOOH]\sigma_{tbuOOH,248\,nm}\phi_{tbuOOH,248\,nm} \times [h\nu]_\lambda \sigma_{CH_3O_2,\lambda}\phi_{CH_3O_2,\lambda}}{[tbuOOH] \times [h\nu]_\lambda \sigma_{tbuOOH,\lambda}\phi_{tbuOOH,\lambda}} \quad \text{E 5.11}$$

$$= \frac{[h\nu]_{248\,nm}\sigma_{tbuOOH,248\,nm}\sigma_{CH_3O_2,\lambda}\phi_{CH_3O_2,\lambda}}{\sigma_{tbuOOH,\lambda}}$$

$$\sigma_{CH_3O_2,\lambda}\phi_{CH_3O_2,\lambda} = \frac{\sigma_{tbuOOH,\lambda}}{[h\nu]_{248\,nm}\sigma_{tbuOOH,248\,nm}} \quad \text{E 5.12}$$

Where $OH_{CH_3O_2}$ and OH_{tbuOOH} represent the OH generated from 248 nm photolysis of methyl peroxy radicals and t-butyl peroxide respectively; $[CH_3O_2]_0$ is the concentration of methyl peroxy radicals at t_0; $[h\nu]_\lambda$ is the number of photons of wavelength λ; $\sigma_{CH_3O_2,\lambda}$ and $\phi_{CH_3O_2,\lambda}$ are the absorption cross-sections and OH quantum yields of the peroxy radical at wavelength λ; $[tbuOOH]$, $\sigma_{tbuOOH,\lambda}$ and $\phi_{tbuOOH,\lambda}$ are the concentration, absorption cross-section and OH quantum yield for t-butyl peroxide at wavelength λ respectively.

The absorption spectrum of t-butyl peroxide in the literature currently only extends to 300 nm. Absorption cross-sections at wavelengths >300 nm are inferred from the absorbance measured by the TRUVAS instrument, scaled to the literature value at 300 nm, providing the "shape" of the tail of the t-butyl peroxy radical UV absorption band. Any inaccuracies in this process due to, for example, short term lamp drift, whereby artefacts in the absorbance arise due to fluctuations in the lamp output between the measurement of I and I_0 would have a directly proportional effect on $\sigma_{CH_3O_2,OH}$ measured by Dr Hansen, and could explain why $\sigma_{CH_3O_2,OH}$ appears to exceed $\sigma_{CH_3O_2,\lambda}$ (the total methyl peroxy radical absorption cross-section) at wavelengths longer than 300 nm. Another explanation for the measured OH absorption cross-sections exceeding total absorption cross-sections, could be contamination of the OH yield by contributions from t-butyl peroxy radicals. Any OH which is not scavenged by ethanol (R 5.13) will react with the t-butyl peroxide precursor to yield t-butyl peroxy radicals (R 5.14), which would likely photolyse to OH *via.* a similar concerted H-migration/OH-elimination of the excited $\tilde{B}$ state proposed by Zhu *et al.* for the formation of OH from the methyl peroxy radical.[75] Additional OH formed from t-butyl peroxy radical photolysis could explain the discrepancy between the 2 results, however the 2σ error margins on the presented values by Dr Hansen are inclusive of the total absorption cross-section measurements

by the TRUVAS instrument, and do not present a significant problem. Since the absorption cross-sections measured by the TRUVAS instrument are subject to fewer sources of inaccuracy, and are based on a more well-known method of measuring absorption cross-sections, OH absorption cross-sections above 300 nm are interpolated from the total absorption cross-sections, and a quantum yield of unity is assumed as shown in Figure 5.23.
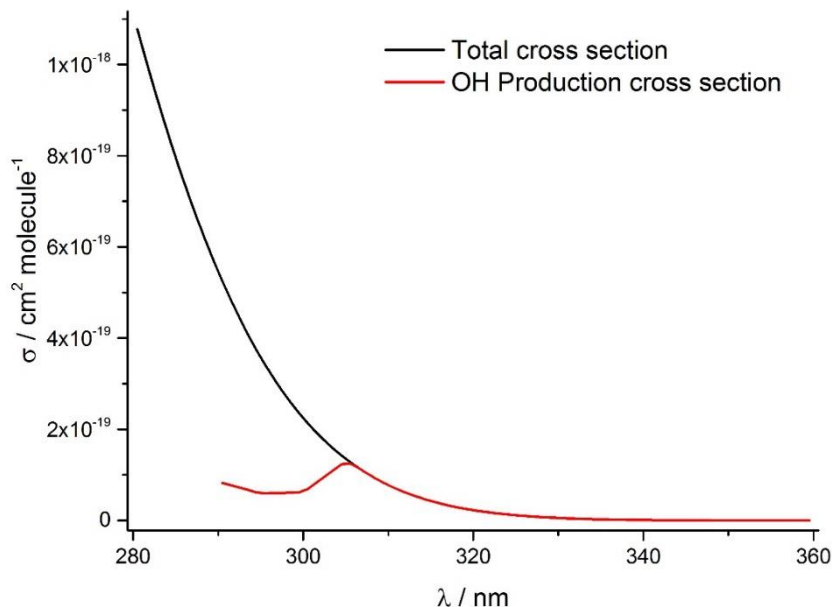
Figure 5.23: OH absorption cross-sections from experiments by Dr Hansen <305nm are concatenated with the Gaussian fit to the total absorption cross-sections (black line) measured by the TRUVAS instrument between 305 – 360 nm, to generate the absorption spectrum for photolysis of methyl peroxy radicals to OH (red line).
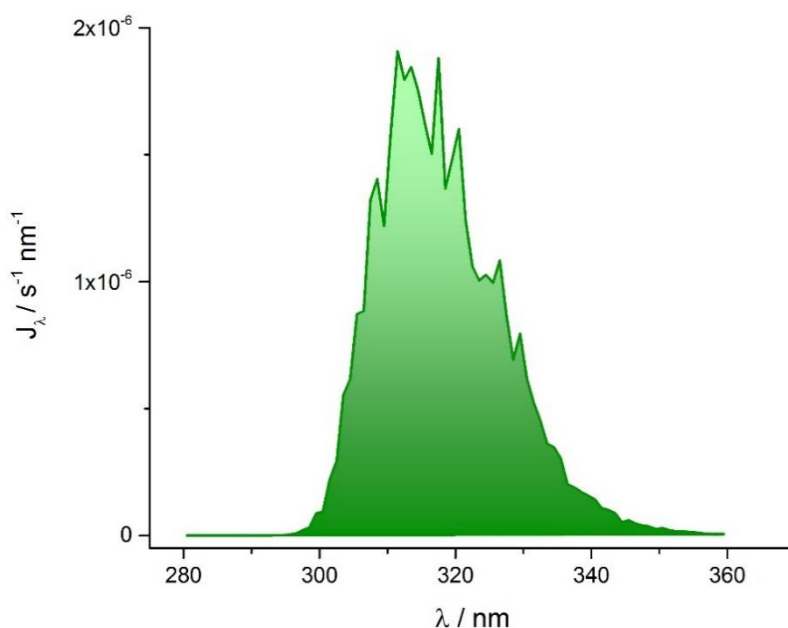
Figure 5.24: The interpolated OH absorption cross-sections shown in Figure 5.23 are used to calculate the photolysis rate of methyl peroxy radicals to OH in the atmosphere due to actinic flux at noon in Cape Verde on the 15th of August, calculated using the ACOM TUV model.[77]

Figure 5.24 shows J(OH) for the methyl peroxy radical at noon around Cape Verde, with avalue of 3.89×10^{-5} s^{-1}. The rate of methyl peroxy radical photolysis to OH is ~94% as fast as the total methyl peroxy radical photolysis rate, i.e. the overall quantum yield of photolysis to OH: $\phi_{CH_3O_2,OH} = 0.94$ in the atmosphere. Typically J(O^{1}D) in the tropical boundary layer is ~3×10^{-5} s^{-1}; a comparable value to the J(OH) value for the methyl peroxy radical calculated here. O(^{1}D) is formed *via.* ozone photolysis by solar radiation at $\lambda < 320$ (R 5.20).

$$O_3 + h\nu \rightarrow O(^1D) + O_2 \qquad\qquad R\ 5.20$$

O(^{1}D) can react with H$_2$O in the atmosphere to make 2 OH radicals (R 5.21), or undergo collisional stabilisation by molecular oxygen (R 5.22) or nitrogen (R 5.23) to O^{3}P, with reactions R 5.21-R 5.23 representing the dominant sinks for O(^{1}D) in the atmosphere.

$$O(^1D) + H_2O \rightarrow 2OH \qquad\qquad R\ 5.21$$

$$O(^1D) + O_2 \rightarrow O^3P + O_2 \qquad\qquad R\ 5.22$$

$$O(^1D) + N_2 \rightarrow O^3P + N_2 \qquad\qquad R\ 5.23$$

Table 5.8: Rates of the 3 main O(^{1}D) removal processes, with branching ratios. R 5.21 depends on [H$_2$O], which is calculated for 70% relative humidity here. Values are taken from the MCM.[86]

Reaction	Rate at 298 K, 760 Torr / s^{-1}	Branching ratio
R 5.21	1.03×10^8	0.112
R 5.22	2.32×10^8	0.217
R 5.23	6.19×10^8	0.671

At 70% relative humidity, 11.2 % of O(^{1}D) formed reacts with H$_2$O, with each reaction forming 2 OH, the rate of formation of OH from O(^{1}D) is $3 \times 10^{-5} \times 0.224 = 6.72 \times 10^{-6}$ s^{-1}.

To estimate the total OH flux from both ozone and methyl peroxy radical photolysis, the J_{total} value for each process is multiplied by the concentration of each species (E 5.13).

$$\frac{d[OH]_x}{dt} = J(x) \times [x] \qquad\qquad \text{E 5.13}$$

Typical methyl peroxy radical and ozone concentrations in Cape Verde are around 1 $\times$ 10^9 (40 ppt) and 1 $\times$ 10^{12} (40 ppb) molecule cm^{-3} respectively, yielding OH formation rates of 3.89 $\times$ 10^4 and 6.48 $\times$ 10^6 molecule cm^{-3} s^{-1} from methyl peroxy radicals and ozone photolysis respectively.[162, 255] The additional OH formation from methyl peroxy radicals contributes ~0.6 % to the total OH formation in Cape Verde, and is therefore almost negligible when modelling the atmospheric chemistry of this climate, and similar climates (pristine tropical marine boundary layer).

5.6 Discussion

OH formation from methyl peroxy radical photolysis has previously been observed by Hartmann *et al*., who propose a mechanism for OH formation from electronic excitation of CH$_3$O$_2$ *via*. a non-adiabatic process (i.e. one which involves a crossing between 2 excited state potential energy surfaces) involving isomerisation of excited $CH_3O_2(\tilde{B}^2A'')$ to excited CH$_2$OOH$(^2\tilde{A}'')$ and then subsequent dissociation to CH$_2$O$(\tilde{X}^1A_1)$ plus rotationally hot OH$(A^2\Sigma^+)$.[71] Hartmann *et al*. also note that excitation of CH$_3$O$_2$ at 248 nm could produce O(^{1}D), which would react rapidly with any hydrocarbon present to form OH. The experiments carried out by Dr Hansen at the University of Leeds show OH production from the excitation of CH$_3$O$_2$ at wavelengths longer than the threshold wavelength for photolytic O(^{1}D) formation (273 nm - Table 3.5), implying unimolecular OH formation. The energies of possible states resulting from electronic excitation of the ground state methyl peroxy radical $(\tilde{X}^2A'')$ to the excited $\tilde{B}^2A''$ state, and its subsequent reaction are shown in Figure 1.7.

Table 5.9: Potential reaction pathways resulting from electronic excitation of ground state CH$_3$O$_2$ ($\tilde{X}^2A''$). ΔH_R /kJ mol^{-1} represents the change in potential energy between the ground state CH$_3$O$_2$ and the corresponding intermediate or product. Threshold wavelength is the longest λ able to excite ground state CH$_3$O$_2$ to its corresponding state in a 1-photon absorption process. Symmetries are taken from Hartmann *et al.*.[71]

Reaction	ΔH_R /kJ mol^{-1}	Threshold Wavelength / nm	
$CH_3O_2(\tilde{X}^2A'') + h\nu \rightarrow CH_3O_2(\tilde{B}^2A'')$	-	-	R 5.24
$\rightarrow CH_3(\tilde{X}^2A_2'') + O_2(X^3\Sigma_g)$	129.0	927	R 5.25
$\rightarrow CH_3(\tilde{X}^2A_2'') + O_2(a^1\Delta_g)$	223	836	R 5.26
$\rightarrow CH_3(\tilde{X}^2A_2'') + O_2(b^1\Sigma_g)$	286	418	R 5.27
$\rightarrow CH_3O(\tilde{X}^2E) + O(^1D)$	438	273	R 5.28
$\rightarrow CH_3O(\tilde{X}^2E) + O(^3P)$	248	482	R 5.29
$\rightarrow CH_2OOH(^2\tilde{A}'')$	293	408	R 5.30
$CH_2OOH(^2\tilde{A}'') \rightarrow OH(A^2\Sigma^+) + CH_2O(\tilde{X}^1A_1)$	299	400	R 5.31
$\rightarrow OH(X^2\Pi) + CH_2O(\tilde{X}^1A_1)$	-88	-	R 5.32
$\rightarrow OH(X^2\Pi) + CH_2O(\tilde{A}^1A'')$	243	493	R 5.33

Zhu *et al.* have more recently calculated the possible fates of excited CH$_3$O$_2$, proposing a concerted H-migration/OH-elimination mechanism from the excited CH$_2$OOH($^2\tilde{A}''$) transition state, which lies 288 kJ mol^{-1} above the OH($X^2\Pi$) + CH$_2$O($\tilde{X}^1A_1$) products.[75] The transition state CH$_2$OOH($^2\tilde{A}''$) lies 293 kJ mol^{-1} above the CH$_3$O$_2\left(\tilde{X}^2A''\right)$ ground state, corresponding to a threshold frequency of 408 nm. Upon excitation to the electronically excited state, the reaction proceeds *via.* the repulsive $\tilde{B}$ state, before either continuing along the O-O bond stretch to yield the alkoxy radical and O(^3P) or crossing *via.* the $^2\tilde{A}''$ transition state resulting in concerted H-migration/OH-elimination to yield the OH($X^2\Pi$) + CH$_2$O($\tilde{X}^1A_1$) products.
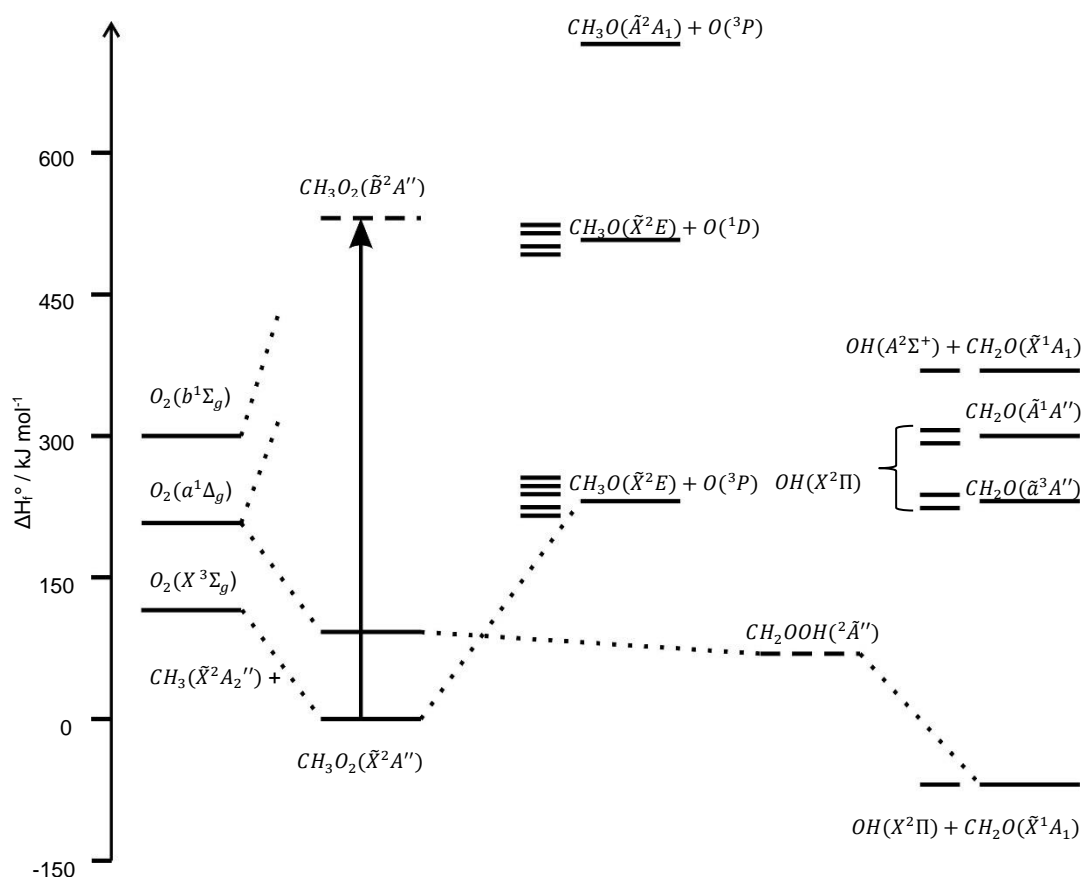
Figure 5.25: Energy and correlation diagram for the electronic excitation of the methyl peroxy radical, and the products of excited methyl peroxy radicals: Products of C-O bond cleavage are shown on the left, and products from O-O bond cleavage are shown on the right. Reproduced from Hartmann *et al*.[71]

In the OH absorption cross-section experiments conducted by Dr Hansen, OH is detected as $OH(X^2\Pi)$ *via.* the $A^2\Sigma^+ \leftarrow X^2\Pi$ transition at 308 nm, under the assumption that any vibrationally hot $OH(X^2\Pi)$ formed from methyl peroxy radical photolysis, will have relaxed down to the $X^2\Pi$ state. Based on estimated [H$_2$O] in the cell, excited $OH(X^2\Pi)$ has a lifetime of around 6-7 µs; H$_2$O is an efficient quencher of excited OH, with a rate coefficient of 1.3×10^{-11} cm^3 molecule^{-1} s^{-1}. To test this assumption, the delay between the photolysis and probe lasers was varied between 1-10 µs, resulting in no change in the measured $\sigma_{CH_3O_2,OH}$ value over this range, implying that the $OH(X^2\Pi)$ measured is representative of the total OH generated from methyl peroxy radical photolysis.

5.7 Summary

In summary, the absorption spectra of methyl, *t*-butyl and cyclohexyl peroxy radicals have been measured using the novel TRUVAS instrument beyond 260 nm. The absorption spectrum of the methyl peroxy radical measured here agrees well with previous recorded spectra between 260-280 nm, and offers some clarification regarding the shape of the spectrum beyond this range, down to a absorption cross-section of 1.38×10^{-21} cm^2 molecule^{-1} at 338.6 nm. The current smallest absorption cross-section in the most recently accepted recommendation by Tyndall *et al.*is 5.2 $\times 10^{-19}$ cm^2 molecule^{-1} at 295 nm, and so the absorption cross-sections measured by the TRUVAS instrument offer an increase in sensitivity of more than 2 orders of magnitude. The importance of atmospheric photolysis of methyl peroxy radicals was assessed, showing a modest enhancement of the total removal rate of methyl peroxy radicals *via.* photolysis of ~1% at noon in Cape Verde in the tropics. The contribution to the rate of OH formation from methyl peroxy radical photolysis by solar radiation at noon in Cape Verde was estimated to be around 0.6 % of the rate of formation *via.* reaction of O(^{1}D) with water vapour.

The absorption spectrum of the *t*-butyl peroxy radical was measured *via.* photolysis of *t*-butyl peroxide at 248 nm, yielding equal amounts of *t*-butyl and methyl peroxy radicals, resulting in the measurement of a compound spectrum of methyl peroxy and *t*-butyl peroxy radicals. The absorption spectrum of the methyl peroxy radical measured by the TRUVAS instrument was then subtracted from the compound spectrum measured from the photolysis of *t*-butyl peroxide to calculate the *t*-butyl peroxy radical absorption spectrum. Agreement between previously reported literature values and the values measured by the TRUVAS instrument is good between 270 – 280 nm, worsening at shorter wavelengths. The most likely explanation for this is lack of sensitivity of the TRUVAS instrument at these wavelengths due to lack of signal at shorter wavelengths (detailed explanation given in the experimental section of this work), an effect compounded by the subtraction of 2 spectra. The *t*-butyl peroxy radical absorption spectrum was measured down to 1.80×10^{-20} cm^2 molecule^{-1} at 331.6 nm, which represents an increase in sensitivity of over 2 orders of magnitude compared to the smallest literature absorption cross-sections at 1×10^{-18} cm^2 molecule^{-1} at 280 nm.

The absorption spectrum of the cyclohexyl peroxy radical was measured *via.* photolysis of hydrogen peroxide at 248 nm in the presence of O_2 and cyclohexane. The spectrum measured by the TRUVAS instrument agrees very well with the spectrum measured by Rowley *et al*., measured down to 7.3×10^{-19} cm^2 molecule^{-1} at 300 nm. The smallest reliable absorption cross-section for the cyclohexyl peroxy radical measured by the TRUVAS system is calculated to be 3.21×10^{-22} cm^2 molecule^{-1} at 353.1 nm, representing an increase in sensitivity of more than 3 orders of magnitude above previous measurements. The absorption spectrum of the cyclohexyl peroxy radical is a good example of the sensitivity of the TRUVAS system, particularly in the actinic region where absorption cross-sections of peroxy radicals are small.

6   Synopsis

6.1   Background

The background of the research leading to this project is centred around the problem of discrepancies between measured and modelled OH levels in remote, near-pristine environments, particularly those which experience high levels of the BVOC isoprene. In these remote low NO_x, high isoprene environments, the rapid reaction of OH with isoprene is currently essentially a sink for OH, i.e. reaction of OH with isoprene results in a net loss of OH and the formation of a suite of peroxy radicals. In urban environments, NO_x levels are sufficient to recycle peroxy radicals *via.* R 6.1-R 6.5.

$$OH + R\text{-}H \rightarrow R + H_2O \qquad\qquad \text{R 6.1}$$

$$R + O_2 + M \rightarrow RO_2 + M \qquad\qquad \text{R 6.2}$$

$$RO_2 + NO \rightarrow RO + NO_2 \qquad\qquad \text{R 6.3}$$

$$R\text{-}O + O_2 \rightarrow HO_2 + R{=}O \qquad\qquad \text{R 6.4}$$

$$HO_2 + NO \rightarrow OH + NO_2 \qquad\qquad \text{R 6.5}$$
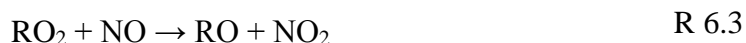
In remote environments, where $[NO_x]$ is low, R 6.2 and R 6.5 are too slow to efficiently recycle OH. Under these conditions [OH] measured exceeds [OH] predicted by models up to a factor of 10.

Various mechanisms have been proposed to attempt to find an OH recycling route from the isoprene peroxy radical, including various intramolecular H-shifting reactions. A 1,6-H shift mechanism was proposed by Peeters *et al.*[127] which results in photolabile HPALD molecules, which would readily photolyse in the atmosphere to OH. HPALD formation rates measured in chamber studies[115] convincingly contradict the extent of OH recycling proposed by Peeters *via* this mechanism, leading Peeters to reassess the rates of the 1,6-H shift in a following publication[134].

The Peroxy Radical Photolysis and its Impact on Atmospheric Chemistry (PRiPIAC) projects aim was to investigate the possibility of direct photolysis of isoprene derived peroxy radicals to OH as a viable OH recycling mechanism in remote, near-pristine

environments, which could reconcile discrepancies between measured and modelled [OH].

OH production from peroxy radical photolysis has been observed numerous times in previous studies, particularly the study by Hartmann *et al.*[71] in which excited OH radical formation was observed when photolysing the methyl peroxy radical at 248 nm.

Peroxy radicals ubiquitously exhibit a broad-featureless UV absorption band, typically 30-50 nm wide, centred around 220-260 nm. This absorption band arises from the $\tilde{B}^2A'' \leftarrow \tilde{X}^2A''$ transition, from the ground $\tilde{X}^2A''$ state, to the excited, unbound $\tilde{B}^2A''$ state. Numerous fates of the unbound $\tilde{B}^2A''$ states are possible, including the concerted H-migration/OH-elimination pathway, which represents a photolytic source of OH from the electronic excitation of peroxy radicals.

Absorption cross-sections of peroxy radicals have been measured in the past by various groups, however historically the $\tilde{B}^2A'' \leftarrow \tilde{X}^2A''$ absorption band has been used as a diagnostic tool for measuring the concentrations and therefore rates of reactions of peroxy radicals in kinetic experiments, and are usually measured down to around 1×10^{-19} cm^2 molecule. The focus of this project is on the photolability of peroxy radicals in the actinic region, above 280 nm. In this region, the absorption cross sections of peroxy radicals tend to be small ($<10^{-19}$ cm^2 molecule^{-1}) and so a sensitive method of detection is required for this purpose.

6.2   Implications

The total absorption cross-section measurements outlined in this thesis were used in conjunction with cross-sections for OH formation measured as part of the PRiPIAC project to determine OH quantum yields and overall photolysis rates of isoprene derived peroxy radicals in remote tropical locations, resulting in a publication in PCCP[194]. Whilst isoprene derived peroxy radical photolysis to OH does contribute to lessening the [OH] measured to modelled discrepancy, it falls short of contributing significantly to modelled [OH] concentrations, increasing [OH] above the base case by around 1% in the case of the Borneo rainforest, as shown in Figure 6.1.
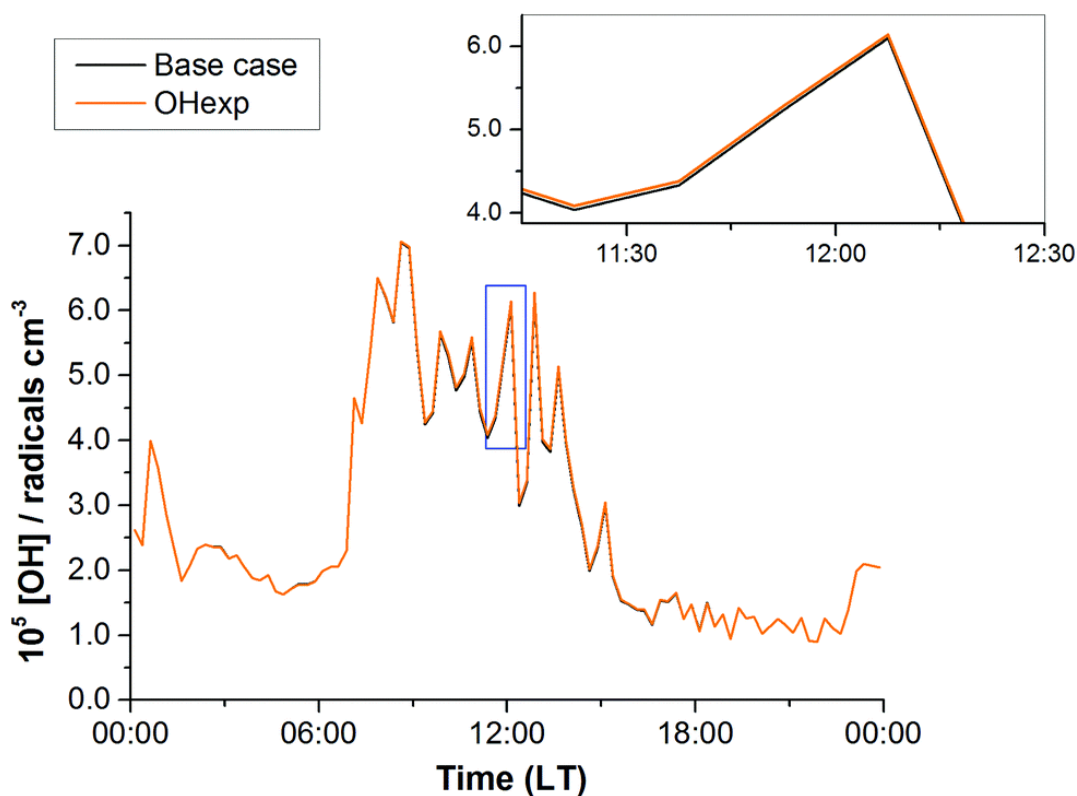
Figure 6.1: Modeled diurnal average OH concentrations for the base (black) and OHexp (orange) cases, calculated at 15 minute intervals. The inset shows, for clarity, an expanded view of the area contained within the blue box from 11:15–12:30 LT. Taken from Hansen et al.[194].

Total photolysis rates of the various atmospherically relevant peroxy radicals were calculated at noon in Borneo, based on the total absorption cross-sections measured using the TRUVAS instrument, and were found to be minor removal processes for these molecules in the atmosphere. Of the peroxy radicals studied in this thesis, the isoprene and ethylene HP and methyl peroxy radicals are of the most atmospheric relevance. Removal of the isoprene and ethylene HP radicals *via* photolysis at noon in Borneo represents around 9.6 and 4.9 % of their removal (respectively) by reaction with NO_x and HO_2 combined: their most dominant removal processes in Borneo. These total removal rates are not insignificant, and should be incorporated into models which calculate the concentrations of these species in the complex Borneo rainforest atmospheric chemistry.

Whilst the methyl peroxy radical was shown to have a near unity quantum yield for photolysis to OH in the actinic region, the absorption cross-sections of the species in the actinic region is insufficient to significantly impact either OH formation or

methyl peroxy removal in the marine boundary layer, increasing the rates of these processes by around 1 and 0.6 % respectively at noon in Cape Verde.

One of the initial reactions studied by the TRUVAS instrument was that of the Criegee intermediate formaldehyde oxide with water vapour, specifically water dimer, which forms at high partial pressures of water vapour. Previous studies into the reaction of water dimer with water were carried out at low water concentrations, and found the rate of reaction of formaldehyde oxide with water to be slow (k_{H2O} = 4×10^{-15} cm^3 molecule^{-1} s^{-1}), and not a dominant sink for the species in the atmosphere. Due to the ability of the TRUVAS instrument to operate at a wide range of pressures, significant concentrations of water vapour (similar to those in the atmosphere) could be introduced to the reaction mixture, increasing the concentration of water dimer to around 1.2×10^{14} molecule cm^{-3}. The rate of reaction of formaldehyde oxide with water dimer was found to be $4.0 \pm 1.2 \times 10^{12}$ cm^3 molecule^1 s^{-1}, corresponding to a removal rate in the atmosphere of around 1000-2000 s^{-1} and representing the dominant sink of the simplest Criegee intermediate in the atmosphere. This result has significant atmospheric implications, as it represents a paradigm shift in the reactions of formaldehyde oxide, which it was thought may contribute significantly to particle formation and air quality *via* reactions with SO$_2$ and NO$_2$ respectively.

6.3   Future Work

In this thesis it has been demonstrated that local constituent groups effect the width and position of the UV absorption band of peroxy radical species. Modest increases in the absorption cross sections of peroxy radicals can increase their photolability in the atmosphere, as shown for the ethylene – but-2-ene – TME HP radical absorption spectra, whereby a factor of 3 increase is observed in the atmospheric photolysis rate between the primary ethylene HP radical and the tertiary TME HP radical. Absorption cross-sections of peroxy radicals with particularly electron-rich groups bonded directly to the peroxy radical carbon centre could exhibit significant red-shifting and therefore significant increases in the rate of their photolysis in the atmosphere. For this reason, it is important that absorption spectra of other peroxy radicals, for example those derived from aromatic compounds, are measured in order to investigate their potential to photolyse in the atmosphere.

Whilst the reaction of the simplest Criegee intermediate with water dimer is able to be studied using the TRUVAS instrument, it was found that the removal rate of the higher Criegee intermediates precluded the investigation of their reactions. Better time-resolution would facilitate the study of more reactive Criegee intermediates, particularly to investigate whether the same rapid rate of reaction of the higher Criegee intermediates with water dimer occurs. To achieve faster time-resolution from the TRUVAS instrument, as well as solving problems of stray light contamination, alternative spectrograph/CCD systems should be considered.

References

1.   R. Dlugi, M. Berger, M. Zelger, A. Hofzumahaus, M. Siese, F. Holland, A. Wisthaler, W. Grabmer, A. Hansel, R. Koppmann, G. Kramm, M. Mollmann-Coers and A. Knaps, 'Turbulent exchange and segregation of HO_x radicals and volatile organic compounds above a deciduous forest', *Atmos Chem Phys*, 2010, **10**, 6215-6235.

2.   L. Whalley, D. Stone and D. Heard, 'New Insights into the Tropospheric Oxidation of Isoprene: Combining Field Measurements, Laboratory Studies, Chemical Modelling and Quantum Theory', in *Atmospheric and Aerosol Chemistry*, eds. V.F. McNeill and P.A. Ariya, Springer Berlin Heidelberg, 2014, vol. 339, Chapter 359, 55-95.

3.   T.R. Lewis, M.A. Blitz, D.E. Heard and P.W. Seakins, 'Direct evidence for a substantive reaction between the Criegee intermediate, CH_2OO , and the water vapour dimer', *Physical Chemistry Chemical Physics*, 2015, **17**, 4859-4863.

4.   F.L. Eisele, G.H. Mount, F.C. Fehsenfeld, J. Harder, E. Marovich, D.D. Parrish, J. Roberts, M. Trainer and D. Tanner, 'Intercomparison of Tropospheric Oh and Ancillary Trace Gas Measurements at Fritz-Peak-Observatory, Colorado', *Journal of Geophysical Research-Atmospheres*, 1994, **99**, 18605-18626.

5.   G.H. Mount and F.L. Eisele, 'An Intercomparison of Tropospheric Oh Measurements at Fritz-Peak-Observatory, Colorado', *Science*, 1992, **256**, 1187-1190.

6.   C.A. Cantrell, R.E. Shetter, J.G. Calvert, F.L. Eisele, E. Williams, K. Baumann, W.H. Brune, P.S. Stevens and J.H. Mather, 'Peroxy radicals from photostationary state deviations and steady state calculations during the Tropospheric OH Photochemistry Experiment at Idaho Hill, Colorado, 1993', *Journal of Geophysical Research-Atmospheres*, 1997, **102**, 6369-6378.

7.   P.S. Stevens, J.H. Mather, W.H. Brune, F. Eisele, D. Tanner, A. Jefferson, C. Cantrell, R. Shetter, S. Sewall, A. Fried, B. Henry, E. Williams, K. Baumann, P. Goldan and W. Kuster, 'HO_2/OH and RO_2/HO_2 ratios during the Tropospheric OH Photochemistry Experiment: Measurement and theory', *Journal of Geophysical Research-Atmospheres*, 1997, **102**, 6379-6391.

8.   S.A. McKeen, G. Mount, F. Eisele, E. Williams, J. Harder, P. Goldan, W. Kuster, S.C. Liu, K. Baumann, D. Tanner, A. Fried, S. Sewell, C. Cantrell and R. Shetter, 'Photochemical modeling of hydroxyl and its relationship to

other species during the Tropospheric OH Photochemistry Experiment', *Journal of Geophysical Research-Atmospheres*, 1997, **102**, 6467-6493.

9. D.J. Creasey, D.E. Heard and J.D. Lee, 'OH and HO_2 measurements in a forested region of north-western Greece', *Atmospheric environment*, 2001, **35**, 4713-4724.

10. N. Carslaw, D.J. Creasey, D. Harrison, D.E. Heard, M.C. Hunter, P.J. Jacobs, M.E. Jenkin, J.D. Lee, A.C. Lewis, M.J. Pilling, S.M. Saunders and P.W. Seakins, 'OH and HO_2 radical chemistry in a forested region of north-western Greece', *Atmospheric environment*, 2001, **35**, 4725-4737.

11. D. Tan, I. Faloona, J.B. Simpas, W. Brune, P.B. Shepson, T.L. Couch, A.L. Sumner, M.A. Carroll, T. Thornberry, E. Apel, D. Riemer and W. Stockwell, 'HOx budgets in a deciduous forest: Results from the PROPHET summer 1998 campaign', *Journal of Geophysical Research-Atmospheres*, 2001, **106**, 24407-24427.

12. I. Faloona, D. Tan, W. Brune, J. Hurst, D. Barket, T.L. Couch, P. Shepson, E. Apel, D. Riemer, T. Thornberry, M.A. Carroll, S. Sillman, G.J. Keeler, J. Sagady, D. Hooper and K. Paterson, 'Nighttime observations of anomalously high levels of hydroxyl radicals above a deciduous forest canopy', *Journal of Geophysical Research-Atmospheres*, 2001, **106**, 24315-24333.

13. X. Ren, J.R. Olson, J. Crawford, W.H. Brune, J. Mao, R.B. Long, Z. Chen, G. Chen, M.A. Avery, G.W. Sachse, J.D. Barrick, G.S. Diskin, G. Huey, A. Fried, R.C. Cohen, B. Heikes, P.O. Wennberg, H.B. Singh, D. Blake and R. Shetter, 'HO_x chemistry during INTEX-A 2004: Observations, model calculation and comparison with previous studies', *Journal of Geophysical Research-Atmospheres*, 2008, **113**, D05310.

14. W. Chao, J.-T. Hsieh, C.-H. Chang and J.J.-M. Lin, 'Direct kinetic measurement of the reaction of the simplest Criegee intermediate with water vapor', *Science*, 2015, **347**, 751-754.

15. Y. Kanaya, A. Hofzumahaus, H.-P. Dorn, T. Brauers, H. Fuchs, F. Holland, F. Rohrer, B. Bohn, R. Tillmann, R. Wegener, A. Wahner, Y. Kajii, K. Miyamoto, S. Nishida, K. Watanabe, A. Yoshino, D. Kubistin, M. Martinez, M. Rudolf, H. Harder, H. Berresheim, T. Elste, C. Plass-Dulmer, G. Stange, J. Kleffmann, Y. Elshorbany and U. Schurath, 'Comparison of observed and modeled OH and HO_2 concentrations during the ambient measurement period of the HO_xComp field campaign', *Atmos Chem Phys Discuss*, 2011, **11**, 28851-28894.

16. J. Lelieveld, T.M. Butler, J.N. Crowley, T.J. Dillon, H. Fischer, L. Ganzeveld, H. Harder, M.G. Lawrence, M. Martinez, D. Taraborrelli and J.

Williams, 'Atmospheric oxidation capacity sustained by a tropical forest', *Nature*, 2008, **452**, 737-740.

17. T.M. Butler, D. Taraborrelli, C.B.H. Fischer, H. Harder, M. Martinez, J. Williams, M.G. Lawrence and J. Lelieveld, 'Improved simulation of isoprene oxidation chemistry with the ECHAM5/MESSy chemistry-climate model: lessons from the GABRIEL airborne field campaign', *Atmospheric Chemistry and Physics*, 2008, **8**, 4529-4546.

18. M. Martinez, H. Harder, D. Kubistin, M. Rudolf, H. Bozem, G. Eerdekens, H. Fischer, T. Klupfel, C. Gurk, R. Konigstedt, U. Parchatka, C.L. Schiller, A. Stickler, J. Williams and J. Lelieveld, 'Hydroxyl radicals in the tropical troposphere over the Suriname rainforest: airborne measurements', *Atmospheric Chemistry and Physics*, 2010, **10**, 3759-3773.

19. D. Kubistin, H. Harder, M. Martinez, M. Rudolf, R. Sander, H. Bozem, G. Eerdekens, H. Fischer, C. Gurk, T. Klupfel, R. Konigstedt, U. Parchatka, C.L. Schiller, A. Stickler, D. Taraborrelli, J. Williams and J. Lelieveld, 'Hydroxyl radicals in the tropical troposphere over the Suriname rainforest: comparison of measurements with the box model MECCA', *Atmospheric Chemistry and Physics*, 2010, **10**, 9705-9728.

20. A. Hofzumahaus, F. Rohrer, K. Lu, B. Bohn, T. Brauers, C.C. Chang, H. Fuchs, F. Holland, K. Kita, Y. Kondo, X. Li, S. Lou, M. Shao, L. Zeng, A. Wahner and Y. Zhang, 'Amplified Trace Gas Removal in the Troposphere', *Science*, 2009, **324**, 1702-1704.

21. S. Lou, F. Holland, F. Rohrer, K. Lu, B. Bohn, T. Brauers, C.C. Chang, H. Fuchs, R. Haeseler, K. Kita, Y. Kondo, X. Li, M. Shao, L. Zeng, A. Wahner, Y. Zhang, W. Wang and A. Hofzumahaus, 'Atmospheric OH reactivities in the Pearl River Delta - China in summer 2006: measurement and model results', *Atmospheric Chemistry and Physics*, 2010, **10**, 11243-11260.

22. K. Lu, F. Rohrer, F. Holland, H. Fuchs, B. Bohn, T. Brauers, C.C. Chang, R. Haeseler, M. Hu, K. Kita, Y. Kondo, X. Li, S. Lou, S. Nehr, M. Shao, L. Zeng, A. Wahner, Y. Zhang and A. Hofzumahaus, 'Observations and modelling of OH and HO_2 concentrations in the Pearl River Delta 2006: a missing OH source in a VOC rich atmosphere', *Atmos Chem Phys*, 2012, **12**, 1541-1569.

23. R. Commane, C.F.A. Floquet, T. Ingham, D. Stone, M.J. Evans and D.E. Heard, 'Observations of OH and HO_2 radicals over West Africa', *Atmospheric Chemistry and Physics*, 2010, **10**, 8783-8801.

24. D. Stone, M.J. Evans, R. Commane, T. Ingham, C.F.A. Floquet, J.B. McQuaid, D.M. Brookes, P.S. Monks, R. Purvis, J.F. Hamilton, J. Hopkins, J. Lee, A.C. Lewis, D. Stewart, J.G. Murphy, G. Mills, D. Oram, C.E.

Reeves and D.E. Heard, ′HO$_x$ observations over West Africa during AMMA: impact of isoprene and NO$_x$′, *Atmospheric Chemistry and Physics*, 2010, **10**, 9415-9429.

25.   P. Di Carlo, W.H. Brune, M. Martinez, H. Harder, R. Lesher, X.R. Ren, T. Thornberry, M.A. Carroll, V. Young, P.B. Shepson, D. Riemer, E. Apel and C. Campbell, ′Missing OH reactivity in a forest: Evidence for unknown reactive biogenic VOCs′, *Science*, 2004, **304**, 722-725.

26.   X. Ren, W.H. Brune, A. Oliger, A.R. Metcalf, J.B. Simpas, T. Shirley, J.J. Schwab, C. Bai, U. Roychowdhury, Y. Li, C. Cai, K.L. Demerjian, Y. He, X. Zhou, H. Gao and J. Hou, ′OH, HO2, and OH reactivity during the PMTACS-NY Whiteface Mountain 2002 campaign: Observations and model comparison′, *Journal of Geophysical Research-Atmospheres*, 2006, **111**.

27.   G.M. Wolfe, J.A. Thornton, N.C. Bouvier-Brown, A.H. Goldstein, J.H. Park, M. McKay, D.M. Matross, J. Mao, W.H. Brune, B.W. LaFranchi, E.C. Browne, K.E. Min, P.J. Wooldridge, R.C. Cohen, J.D. Crounse, I.C. Faloona, J.B. Gilman, W.C. Kuster, J.A. de Gouw, A. Huisman and F.N. Keutsch, ′The Chemistry of Atmosphere-Forest Exchange (CAFE) Model - Part 2: Application to BEARPEX-2007 observations′, *Atmospheric Chemistry and Physics*, 2011, **11**, 1269-1294.

28.   T.A.M. Pugh, A.R. MacKenzie, C.N. Hewitt, B. Langford, P.M. Edwards, K.L. Furneaux, D.E. Heard, J.R. Hopkins, C.E. Jones, A. Karunaharan, J. Lee, G. Mills, P. Misztal, S. Moller, P.S. Monks and L.K. Whalley, ′Simulating atmospheric composition over a South-East Asian tropical rainforest: performance of a chemistry box model′, *Atmospheric Chemistry and Physics*, 2010, **10**, 279-298.

29.   L.K. Whalley, P.M. Edwards, K.L. Furneaux, A. Goddard, T. Ingham, M.J. Evans, D. Stone, J.R. Hopkins, C.E. Jones, A. Karunaharan, J.D. Lee, A.C. Lewis, P.S. Monks, S. Moller and D.E. Heard, ′Quantifying the magnitude of a missing hydroxyl radical source in a tropical rainforest′, *Atmospheric Chemistry and Physics Discussions*, 2011, **11**, 5785-5809.

30.   D. Stone, M.J. Evans, P.M. Edwards, R. Commane, T. Ingham, A.R. Rickard, D.M. Brookes, J. Hopkins, R.J. Leigh, A.C. Lewis, P.S. Monks, D. Oram, C.E. Reeves, D. Stewart and D.E. Heard, ′Isoprene oxidation mechanisms: measurements and modelling of OH and HO(2) over a South-East Asian tropical rainforest during the OP3 field campaign′, *Atmospheric Chemistry and Physics*, 2011, **11**, 6749-6771.

31.   A.T. Archibald, J.G. Levine, N.L. Abraham, M.C. Cooke, P.M. Edwards, D.E. Heard, M.E. Jenkin, A. Karunaharan, R.C. Pike, P.S. Monks, D.E. Shallcross, P.J. Telford, L.K. Whalley and J.A. Pyle, ′Impacts of HO$_x$ regeneration and recycling in the oxidation of isoprene: Consequences for

the composition of past, present and future atmospheres*', *Geophysical Research Letters*, 2011, **38**.

32.   J. Mao, X. Ren, W. Brune, D.M. Van Duin, R.C. Cohen, J.H. Park, A. Goldstein, F. Paulot, M.R. Beaver, J.D. Crounse, P.O. Wennberg, J.P. DiGangi, S.B. Henry, F.N. Keutsch, C. Park, G.W. Schade, G.M. Wolfe and J.A. Thornton, *'*Insights into hydroxyl measurements and atmospheric oxidation in a California forest*', *Atmos Chem Phys Discuss*, 2012, **12**, 6715-6744.

33.   T.F. Stocker, D.P. Qin, G.-K., M.S. Tignor, K. Allen, J. Boschung, A. Nauels, Y. Xia, V. Bex and P.M. Midgley, *IPCC, 2013: Summary for Policymakers*, 2013.

34.   S. Rahmstorf, *'*A new view on sea level rise*', *Nature reports climate change*, 2010, 44-45.

35.   S.C. Doney, V.J. Fabry, R.A. Feely and J.A. Kleypas, *'*Ocean acidification: the other CO_2 problem*', *Marine Science*, 2009, **1**.

36.   J.M. Lyman, S.A. Good, V.V. Gouretski, M. Ishii, G.C. Johnson, M.D. Palmer, D.M. Smith and J.K. Willis, *'*Robust warming of the global upper ocean*', *Nature*, 2010, **465**, 334-337.

37.   M.R. Kaplan, J.M. Schaefer, G.H. Denton, D.J. Barrell, T.J. Chinn, A.E. Putnam, B.G. Andersen, R.C. Finkel, R. Schwartz and A.M. Doughty, *'*Glacier retreat in New Zealand during the Younger Dryas stadial*', *Nature*, 2010, **467**, 194-197.

38.   E. Rignot, I. Velicogna, M. Van den Broeke, A. Monaghan and J. Lenaerts, *'*Acceleration of the contribution of the Greenland and Antarctic ice sheets to sea level rise*', *Geophysical Research Letters*, 2011, **38**.

39.   M. Wang and J.E. Overland, *'*A sea ice free summer Arctic within 30 years?*', *Geophysical Research Letters*, 2009, **36**, L07502.

40.   B.D. Santer, J.F. Painter, C. Bonfils, C.A. Mears, S. Solomon, T.M. Wigley, P.J. Gleckler, G.A. Schmidt, C. Doutriaux and N.P. Gillett, *'*Human and natural influences on the changing thermal structure of the atmosphere*', *Proceedings of the National Academy of Sciences*, 2013, **110**, 17235-17240.

41.   A. Dai, *'*Drought under global warming: a review*', *Wiley Interdisciplinary Reviews: Climate Change*, 2011, **2**, 45-65.

42.   A. Dai, *'*Increasing drought under global warming in observations and models*', *Nature climate change*, 2012, **3**, 52-58.

43. O.L. Phillips, L.E. Aragão, S.L. Lewis, J.B. Fisher, J. Lloyd, G. López-González, Y. Malhi, A. Monteagudo, J. Peacock and C.A. Quesada, *'*Drought sensitivity of the Amazon rainforest*'*, *Science*, 2009, **323**, 1344-1347.

44. Y. Hirabayashi, S. Kanae, S. Emori, T. Oki and M. Kimoto, *'*Global projections of changing risks of floods and droughts in a changing climate*'*, *Hydrological Sciences Journal*, 2008, **53**, 754-772.

45. C.B. Field, V. Barros, T.F. Stocker and Q. Dahe, *Managing the Risks of Extreme Events and Disasters to Advance Climate Change Adaptation: Special Report of the Intergovernmental Panel on Climate Change*, Cambridge University Press, 2012.

46. R. Mendelsohn, K. Emanuel, S. Chonabayashi and L. Bakkensen, *'*The impact of climate change on global tropical cyclone damage*'*, *Nature climate change*, 2012, **2**, 205-209.

47. A.J. Colbert, B.J. Soden, G.A. Vecchi and B.P. Kirtman, *'*The impact of anthropogenic climate change on North Atlantic tropical cyclone tracks*'*, *Journal of Climate*, 2013.

48. C.D. Allen, A.K. Macalady, H. Chenchouni, D. Bachelet, N. McDowell, M. Vennetier, T. Kitzberger, A. Rigling, D.D. Breshears and E. Hogg, *'*A global overview of drought and heat-induced tree mortality reveals emerging climate change risks for forests*'*, *Forest Ecology and Management*, 2010, **259**, 660-684.

49. D.O. Åström, B. Forsberg, K.L. Ebi and J. Rocklöv, *'*Attributing mortality from extreme temperatures to climate change in Stockholm, Sweden*'*, *Nature climate change*, 2013.

50. D. Malakoff, *'*Scientists Assess Damage From Sandy's Deadly Punch*'*, *Science*, 2012, **338**, 728-729.

51. M. Marshall, *One of strongest typhoons in history hits Philippines* [online],2013. Available from: http://www.newscientist.com/article/dn24549-one-of-strongest-typhoons-in-history-hits-philippines.html#.UoOYXBq-3To

52. H.E. Tonnang, R.Y. Kangalawe and P.Z. Yanda, *'*Review Predicting and mapping malaria under climate change scenarios: the potential redistribution of malaria vectors in Africa*'*, *Malaria journal*, 2010, **9**, 1-10.

53. S. Kirschke, P. Bousquet, P. Ciais, M. Saunois, J.G. Canadell, E.J. Dlugokencky, P. Bergamaschi, D. Bergmann, D.R. Blake and L. Bruhwiler,

'Three decades of global methane sources and sinks', *Nature Geoscience*, 2013, **6**, 813-823.

54.   M. Jerrett, R.T. Burnett, C.A. Pope, K. Ito, G. Thurston, D. Krewski, Y. Shi, E. Calle and M. Thun, 'Long-Term Ozone Exposure and Mortality', *New England Journal of Medicine*, 2009, **360**, 1085-1095.

55.   D. Krewski, M. Jerrett, R. Burnett, R. Ma, E. Hughes, Y. Shi, M. Turner, C. Pope 3rd, G. Thurston and E. Calle, 'Extended follow-up and spatial analysis of the American Cancer Society study linking particulate air pollution and mortality', *Research report (Health Effects Institute)*, 2009, 5-114; discussion 115-136.

56.   M. Kampa and E. Castanas, 'Human health effects of air pollution', *Environmental pollution*, 2008, **151**, 362-367.

57.   P.L. Kinney, 'Climate change, air quality, and human health', *American journal of preventive medicine*, 2008, **35**, 459-467.

58.   A.H. Wolfe and J.A. Patz, 'Reactive nitrogen and human health: acute and long-term implications', *Ambio: A journal of the human environment*, 2002, **31**, 120-125.

59.   A. Beer, 'Bestimmung der absorption des rothen lichts in farbigen flussigkeiten', *Ann. Physik*, 1852, **162**, 78-88.

60.   J.H. Lambert, *Photometria sive de mensura et gradibus luminis, colorum et umbrae*, Klett, 1760.

61.   M.E. Jenkin, A.A. Boyd and R. Lesclaux, 'Peroxy Radical Kinetics Resulting from the OH-Initiated Oxidation of 1,3-Butadiene, 2,3-Dimethyl-1,3-Butadiene and Isoprene', *Journal of Atmospheric Chemistry*, 1998, **29**, 267-298.

62.   M.M. Maricq and T.J. Wallington, 'Absolute UV cross sections of methyl and ethyl peroxy radicals', *The Journal of Physical Chemistry*, 1992, **96**, 986-992.

63.   D.M. Rowley, P.D. Lightfoot, R. Lesclaux and T.J. Wallington, 'UV absorption spectrum and self-reaction of cyclohexylperoxy radicals', *Journal of the Chemical Society, Faraday Transactions*, 1991, **87**, 3221-3226.

64.   F.G. Simon, W. Schneider and G.K. Moortgat, 'UV-Absorption spectrum of the methylperoxy radical and the kinetics of its disproportionation reaction at 300 K', *International Journal of Chemical Kinetics*, 1990, **22**, 791-813.

65.   T. Wallington, P. Dagaut and M. Kurylo, 'UV absorption cross sections and reaction kinetics and mechanisms for peroxy radicals in the gas phase', *Chemical Reviews*, 1992, **92**, 667-710.

66.   A.A. Jemi-Alade, P.D. Lightfoot and R. Lesclaux, 'Measurements of the UV absorption cross sections of $CF_3CCl_2O_2$, CF_3CHFO_2, $CFCl_2CH_2O_2$ and $CF_2ClCH_2O_2$ in the gas phase', *Chemical Physics Letters*, 1991, **179**, 119-124.

67.   P.D. Lightfoot, R.A. Cox, J.N. Crowley, M. Destriau, G.D. Hayman, M.E. Jenkin, G.K. Moortgat and F. Zabel, 'Organic peroxy radicals: Kinetics, spectroscopy and tropospheric chemistry', *Atmospheric Environment. Part A. General Topics*, 1992, **26**, 1805-1961.

68.   P.D. Lightfoot, P. Roussel, B. Veyret and R. Lesclaux, 'Flash photolysis study of the spectra and self-reactions of neopentylperoxy and t-butylperoxy radicals', *J. Chem. Soc., Faraday Trans.*, 1990, **86**, 2927-2936.

69.   D.M. Rowley, R. Lesclaux, P.D. Lightfoot, B. Noziere, T.J. Wallington and M.D. Hurley, 'Kinetic and mechanistic studies of the reactions of cyclopentylperoxy and cyclohexylperoxy radicals with hydroperoxy radical', *The Journal of Physical Chemistry*, 1992, **96**, 4889-4894.

70.   J.A. Jafri and D.H. Phillips, 'Ground and lower excited states of methylperoxy radical, CH_3O_2: a computational investigation', *Journal of the American Chemical Society*, 1990, **112**, 2586-2590.

71.   D. Hartmann, J. Karthaeuser and R. Zellner, 'The 248-nm photofragmentation of the peroxymethyl radical', *The Journal of Physical Chemistry*, 1990, **94**, 2963-2966.

72.   E.N. Sharp, P. Rupper and T.A. Miller, 'The structure and spectra of organic peroxy radicals', *Physical Chemistry Chemical Physics*, 2008, **10**, 3955-3981.

73.   M.B. Pushkarsky, S.J. Zalyubovsky and T.A. Miller, 'Detection and characterization of alkyl peroxy radicals using cavity ringdown spectroscopy', *Journal of Chemical Physics*, 2000, **112**, 10695-10698.

74.   G.J. Frost, G.B. Ellison and V. Vaida, 'Organic peroxyl radical photolysis in the near-infrared: Effects on tropospheric chemistry', *The Journal of Physical Chemistry A*, 1999, **103**, 10169-10178.

75.   R. Zhu, C.-C. Hsu and M.C. Lin, 'Ab initio study of the $CH3+O_2$ reaction: Kinetics, mechanism and product branching probabilities', *The Journal of Chemical Physics*, 2001, **115**, 195-203.

76.   D.E. Heard and M.J. Pilling, *'Measurement of OH and HO₂ in the troposphere'*, *Chemical Reviews*, 2003, **103**, 5163-5198.

77.   *Tropospheric Ultraviolet and Visible (TUV) Radiation Model* [online], 2017. Available from: https://www2.acom.ucar.edu/modeling/tropospheric-ultraviolet-and-visible-tuv-radiation-model

78.   J. Beckers, *'The profiles of Fraunhofer lines in the presence of Zeeman splitting'*, *Solar Physics*, 1969, **9**, 372-386.

79.   E.A. Gurtovenko and R.I. Kostyk, *'Fraunhofer spectrum and a system of solar oscillator strengths'*, *Kiev Izdatel Naukova Dumka*, 1989.

80.   C.E. Sioris and W.F. Evans, *'Filling in of Fraunhofer and gas-absorption lines in sky spectra as caused by rotational Raman scattering'*, *Applied Optics*, 1999, **38**, 2706-2713.

81.   R. Wildey, E. Burbidge, A. Sandage and G. Burbidge, *'On the Effect of Fraunhofer Lines on u, b, V Measurements'*, *The Astrophysical Journal*, 1962, **135**, 94.

82.   A.C. Vandaele, P.C. Simon, J.M. Guilmot, M. Carleer and R. Colin, *'SO_2 absorption cross section measurement in the UV using a Fourier transform spectrometer'*, *Journal of Geophysical Research: Atmospheres*, 1994, **99**, 25599-25605.

83.   A.C. Vandaele, C. Hermans, S. Fally, M. Carleer, R. Colin, M.F. Merienne, A. Jenouvrier and B. Coquart, *'High-resolution Fourier transform measurement of the NO_2 visible and near-infrared absorption cross sections: Temperature and pressure effects'*, *Journal of Geophysical Research: Atmospheres*, 2002, **107**.

84.   K. Bogumil, J. Orphal, T. Homann, S. Voigt, P. Spietz, O. Fleischmann, A. Vogel, M. Hartmann, H. Kromminga and H. Bovensmann, *'Measurements of molecular absorption spectra with the SCIAMACHY pre-flight model: instrument characterization and reference data for atmospheric remote-sensing in the 230–2380 nm region'*, *Journal of Photochemistry and Photobiology A: Chemistry*, 2003, **157**, 167-184.

85.   F.J. Dentener and P.J. Crutzen, *'Reaction of N_2O_5 on tropospheric aerosols: Impact on the global distributions of NO_x, O_3, and OH'*, *Journal of Geophysical Research: Atmospheres*, 1993, **98**, 7149-7163.

86.   S.M. Saunders, M.E. Jenkin, R.G. Derwent and M.J. Pilling, *'Protocol for the development of the Master Chemical Mechanism, MCM v3 (Part A): tropospheric degradation of non-aromatic volatile organic compounds'*, *Atmos. Chem. Phys.*, 2003, **3**, 161-180.

87.   G.P. Brasseur, J.J. Orlando, G.S. Tyndall and N.C.f.A. Research, *Atmospheric Chemistry and Global Change*, Oxford University Press, 1999.

88.   G. Zeng, J.A. Pyle and P.J. Young, 'Impact of climate change on tropospheric ozone and its global budgets', *Atmos. Chem. Phys.*, 2008, **8**, 369-387.

89.   J.A. Logan, M.J. Prather, S.C. Wofsy and M.B. McElroy, 'Tropospheric chemistry: A global perspective', *Journal of Geophysical Research: Oceans*, 1981, **86**, 7210-7254.

90.   B.J. Finlayson-Pitts and J.N. Pitts, 'Atmospheric Chemistry of Tropospheric Ozone Formation: Scientific and Regulatory Implications', *Air & Waste*, 1993, **43**, 1091-1100.

91.   S. Liu, C. Wang, S. Zhang, J. Liang, F. Chen and K. Zhao, 'Formation and distribution of polycyclic aromatic hydrocarbons (PAHs) derived from coal seam combustion: A case study of the Ulanqab lignite from Inner Mongolia, northern China', *International Journal of Coal Geology*, 2012, **90**, 126-134.

92.   K.F. Souza, L.R. Carvalho, A.G. Allen and A.A. Cardoso, 'Diurnal and Nocturnal Measurements of PAH, Nitro-PAH, and Oxy-PAH Compounds in Atmospheric Particulate Matter of a Sugar Cane Burning Region', *Atmospheric environment*, 2013.

93.   G. St. Helen, M.L. Goniewicz, D. Dempsey, M. Wilson, P. Jacob III and N.L. Benowitz, 'Exposure and kinetics of polycyclic aromatic hydrocarbons (PAHs) in cigarette smokers', *Chemical research in toxicology*, 2012, **25**, 952-964.

94.   P. Jones and P. Leber, 'Polynuclear aromatic hydrocarbons: third international symposium on chemistry and biology, carcinogenesis and mutagenesis', 1979.

95.   S. Baek, R. Field, M. Goldstone, P. Kirk, J. Lester and R. Perry, 'A review of atmospheric polycyclic aromatic hydrocarbons: Sources, fate and behavior', *Water, Air, & Soil Pollution*, 1991, **60**, 279-300.

96.   J.L. Mumford, X. Lee, J. Lewtas, T.L. Young and R.M. Santella, 'DNA Adducts As Biomarkers for Assessing Exposure to Polycyclic Aromatic Hydrocarbons in Tissues from Xuan Wei Women with High Exposure to Coal Combustion Emissions and High Lung Cancer Mortality', *Environmental Health Perspectives*, 1993, 83-87.

97.   S.T. Holgate, "Every breath we take: the lifelong impact of air pollution'–a call for action', *Clinical Medicine*, 2017, **17**, 8-12.

98. K.A. Kourtidis, P. Fabian, C. Zerefos and B. RappenglÜCk, *'*Peroxyacetyl nitrate (PAN), peroxypropionyl nitrate (PPN) and PAN/ozone ratio measurements at three sites in Germany*'*, *Tellus B*, 1993, **45**, 442-457.

99. H.W. Barker, G.L. Stephens, P.T. Partain, J.W. Bergman, B. Bonnel, K. Campana, E.E. Clothiaux, S. Clough, S. Cusack, J. Delamere, J. Edwards, K.F. Evans, Y. Fouquart, S. Freidenreich, V. Galin, Y. Hou, S. Kato, J. Li, E. Mlawer, J.J. Morcrette, W. O'Hirok, P. Räisänen, V. Ramaswamy, B. Ritter, E. Rozanov, M. Schlesinger, K. Shibata, P. Sporyshev, Z. Sun, M. Wendisch, N. Wood and F. Yang, *'*Assessing 1D Atmospheric Solar Radiative Transfer Models: Interpretation and Handling of Unresolved Clouds*'*, *Journal of Climate*, 2003, **16**, 2676-2699.

100. V.E. Larson, R. Wood, P.R. Field, J.-C. Golaz, T.H.V. Haar and W.R. Cotton, *'*Small-Scale and Mesoscale Variability of Scalars in Cloudy Boundary Layers: One-Dimensional Probability Density Functions*'*, *Journal of the Atmospheric Sciences*, 2001, **58**, 1978-1994.

101. J.A. Logan, M. Prather, S. Wofsy and M. McElroy, *'*Atmospheric chemistry: Response to human influence*'*, *Philosophical Transactions of the Royal Society of London A: Mathematical, Physical and Engineering Sciences*, 1978, **290**, 187-234.

102. E.L. Fleming, S. Chandra, C.H. Jackman, D.B. Considine and A.R. Douglass, *'*The middle atmospheric response to short and long term solar UV variations: analysis of observations and 2D model results*'*, *Journal of Atmospheric and Terrestrial Physics*, 1995, **57**, 333-365.

103. J.S. Fuglestvedt, T.K. Berntsen, I.S.A. Isaksen, H. Mao, X.-Z. Liang and W.-C. Wang, *'*Climatic forcing of nitrogen oxides through changes in tropospheric ozone and methane; global 3D model studies*'*, *Atmospheric environment*, 1999, **33**, 961-977.

104. S. Saunders, M. Jenkin, R. Derwent and M. Pilling, *'*World Wide Web site of a Master Chemical Mechanism (MCM) for use in tropospheric chemistry models*'*, *Atmospheric environment*, 1997, **31**, 1249.

105. I. Galbally and C. Roy, *'*Destruction of ozone at the earth's surface*'*, *Quarterly Journal of the Royal Meteorological Society*, 1980, **106**, 599-620.

106. P.I. Palmer, D.J. Jacob, A.M. Fiore, R.V. Martin, K. Chance and T.P. Kurosu, *'*Mapping isoprene emissions over North America using formaldehyde column observations from space*'*, *Journal of Geophysical Research: Atmospheres*, 2003, **108**, 4180.

107. G. Sonnemann and M. Grygalashvyly, *'*Global annual methane emission rate derived from its current atmospheric mixing ratio and estimated lifetime*'*, in, Copernicus GmbH, 2014, 277-283.

108. D.E. Heard, *Analytical Techniques for Atmospheric Measurement*, Blackwell Publishing, 2006.

109. D.E. Heard, 'Atmospheric Field Measurements of the Hydroxyl Radical Using Laser-Induced Fluorescence Spectroscopy', *Annual Review of Physical Chemistry*, 2006, **57**, 191-216.

110. T. Brauers, U. Aschmutat, U. Brandenburger, H.P. Dorn, M. Hausmann, M. Heßling, A. Hofzumahaus, F. Holland, C. Plass-Dülmer and D.H. Ehhalt, 'Intercomparison of tropospheric OH radical measurements by multiple folded long-path laser absorption and laser induced fluorescence', *Geophysical Research Letters*, 1996, **23**, 2545-2548.

111. T.M. Hard, R.J. O'Brien, C.Y. Chan and A.A. Mehrabzadeh, 'Tropospheric free radical determination by fluorescence assay with gas expansion', *Environmental Science & Technology*, 1984, **18**, 768-777.

112. J. Mao, X. Ren, W. Brune, D.M. Van Duin, R.C. Cohen, J.H. Park, A. Goldstein, F. Paulot, M.R. Beaver, J.D. Crounse, P.O. Wennberg, J.P. DiGangi, S.B. Henry, F.N. Keutsch, C. Park, G.W. Schade, G.M. Wolfe and J.A. Thornton, 'Insights into hydroxyl measurements and atmospheric oxidation in a California forest', *Atmospheric Chemistry and Physics*, 2012, **12**, 8009-8020.

113. X. Ren, W.H. Brune, A. Oliger, A.R. Metcalf, J.B. Simpas, T. Shirley, J.J. Schwab, C. Bai, U. Roychowdhury, Y. Li, C. Cai, K.L. Demerjian, Y. He, X. Zhou, H. Gao and J. Hou, 'OH, HO_2, and OH reactivity during the PMTACS–NY Whiteface Mountain 2002 campaign: Observations and model comparison', *Journal of Geophysical Research: Atmospheres*, 2006, **111**.

114. D. Tan, I. Faloona, J.B. Simpas, W. Brune, P.B. Shepson, T.L. Couch, A.L. Sumner, M.A. Carroll, T. Thornberry, E. Apel, D. Riemer and W. Stockwell, 'HO x budgets in a deciduous forest: Results from the PROPHET summer 1998 campaign', *Journal of Geophysical Research: Atmospheres*, 2001, **106**, 24407-24427.

115. H. Fuchs, A. Hofzumahaus, F. Rohrer, B. Bohn, T. Brauers, H. Dorn, R. Häseler, F. Holland, M. Kaminski and X. Li, 'Experimental evidence for efficient hydroxyl radical regeneration in isoprene oxidation', *Nature Geoscience*, 2013.

116. A. Guenther, T. Karl, P. Harley, C. Wiedinmyer, P.I. Palmer and C. Geron, 'Estimates of global terrestrial isoprene emissions using MEGAN (Model of Emissions of Gases and Aerosols from Nature)', *Atmos. Chem. Phys.*, 2006, **6**, 3181-3210.

117. K.R. Gurney, R.M. Law, A.S. Denning, P.J. Rayner, D. Baker, P. Bousquet, L. Bruhwiler, Y.-H. Chen, P. Ciais and S. Fan, 'Towards robust regional estimates of CO_2 sources and sinks using atmospheric transport models', *Nature*, 2002, **415**, 626-630.

118. J. Mao, X. Ren, L. Zhang, D.M. Van Duin, R.C. Cohen, J.H. Park, A.H. Goldstein, F. Paulot, M.R. Beaver, J.D. Crounse, P.O. Wennberg, J.P. DiGangi, S.B. Henry, F.N. Keutsch, C. Park, G.W. Schade, G.M. Wolfe, J.A. Thornton and W.H. Brune, 'Insights into hydroxyl measurements and atmospheric oxidation in a California forest', *Atmos. Chem. Phys.*, 2012, **12**, 8009-8020.

119. D. Stone, M.J. Evans, P.M. Edwards, R. Commane, T. Ingham, A.R. Rickard, D.M. Brookes, J. Hopkins, R.J. Leigh, A.C. Lewis, P.S. Monks, D. Oram, C.E. Reeves, D. Stewart and D.E. Heard, 'Isoprene oxidation mechanisms: measurements and modelling of OH and HO_2 over a South-East Asian tropical rainforest during the OP3 field campaign', *Atmospheric Chemistry and Physics*, 2011, **11**, 6749-6771.

120. D. Stone, L.K. Whalley and D.E. Heard, 'Tropospheric OH and HO_2 radicals: field measurements and model comparisons', *Chemical Society Reviews*, 2012, **41**, 6348-6404.

121. F.L. Eisele, G.H. Mount, F.C. Fehsenfeld, J. Harder, E. Marovich, D.D. Parrish, J. Roberts, M. Trainer and D. Tanner, 'Intercomparison of tropospheric OH and ancillary trace gas measurements at Fritz Peak Observatory, Colorado', *Journal of Geophysical Research: Atmospheres*, 1994, **99**, 18605-18626.

122. T.M. Butler, D. Taraborrelli, C.B.H. Fischer, H. Harder, M. Martinez, J. Williams, M.G. Lawrence and J. Lelieveld, 'Improved simulation of isoprene oxidation chemistry with the ECHAM5/MESSy chemistry-climate model: lessons from the GABRIEL airborne field campaign', *Atmos. Chem. Phys*, 2008, **8**, 4529-4546.

123. C.N. Hewitt, J.D. Lee, A.R. MacKenzie, M.P. Barkley, N. Carslaw, G.D. Carver, N.A. Chappell, H. Coe, C. Collier, R. Commane, F. Davies, B. Davison, P. DiCarlo, C.F. Di Marco, J.R. Dorsey, P.M. Edwards, M.J. Evans, D. Fowler, K.L. Furneaux, M. Gallagher, A. Guenther, D.E. Heard, C. Helfter, J. Hopkins, T. Ingham, M. Irwin, C. Jones, A. Karunaharan, B. Langford, A.C. Lewis, S.F. Lim, S.M. MacDonald, A.S. Mahajan, S. Malpass, G. McFiggans, G. Mills, P. Misztal, S. Moller, P.S. Monks, E. Nemitz, V. Nicolas-Perea, H. Oetjen, D.E. Oram, P.I. Palmer, G.J. Phillips, R. Pike, J.M.C. Plane, T. Pugh, J.A. Pyle, C.E. Reeves, N.H. Robinson, D. Stewart, D. Stone, L.K. Whalley and X. Yin, 'Overview: Oxidant and particle photochemical processes above a south-east Asian tropical rainforest (the OP3 project): introduction, rationale, location characteristics and tools', *Atmos. Chem. Phys.*, 2010, **10**, 169-199.

124. P.M. Edwards, M.J. Evans, K.L. Furneaux, J. Hopkins, T. Ingham, C. Jones, J.D. Lee, A.C. Lewis, S.J. Moller, D. Stone, L.K. Whalley and D.E. Heard, *'*OH reactivity in a South East Asian tropical rainforest during the Oxidant and Particle Photochemical Processes (OP3) project*'*, *Atmos. Chem. Phys.*, 2013, **13**, 9497-9514.

125. J. Vilà-Guerau de Arellano, E.G. Patton, T. Karl, K. van den Dries, M.C. Barth and J.J. Orlando, *'*The role of boundary layer dynamics on the diurnal evolution of isoprene and the hydroxyl radical over tropical forests*'*, *Journal of Geophysical Research: Atmospheres*, 2011, **116**, D07304.

126. F. Paulot, J.D. Crounse, H.G. Kjaergaard, A. Kürten, J.M.S. Clair, J.H. Seinfeld and P.O. Wennberg, *'*Unexpected epoxide formation in the gas-phase photooxidation of isoprene*'*, *Science*, 2009, **325**, 730-733.

127. J. Peeters, T.L. Nguyen and L. Vereecken, *'*HO_x radical regeneration in the oxidation of isoprene*'*, *Physical Chemistry Chemical Physics*, 2009, **11**, 5935-5939.

128. T.A.M. Pugh, A.R. MacKenzie, B. Langford, E. Nemitz, P.K. Misztal and C.N. Hewitt, *'*The influence of small-scale variations in isoprene concentrations on atmospheric chemistry over a tropical rainforest*'*, *Atmos. Chem. Phys.*, 2011, **11**, 4121-4134.

129. G.M. Wolfe, J.D. Crounse, J.D. Parrish, J.M.S. Clair, M.R. Beaver, F. Paulot, T.P. Yoon, P.O. Wennberg and F.N. Keutsch, *'*Photolysis, OH reactivity and ozone reactivity of a proxy for isoprene-derived hydroperoxyenals (HPALDs)*'*, *Physical Chemistry Chemical Physics*, 2012, **14**, 7276-7286.

130. J. Peeters and J.-F. Müller, *'*HO_x radical regeneration in isoprene oxidation via peroxy radical isomerisations. II: experimental evidence and global impact*'*, *Physical Chemistry Chemical Physics*, 2010, **12**, 14227-14235.

131. G.d. Silva, C. Graham and Z.-F. Wang, *'*Unimolecular β-Hydroxyperoxy Radical Decomposition with OH Recycling in the Photochemical Oxidation of Isoprene*'*, *Environmental Science & Technology*, 2009, **44**, 250-256.

132. A.A. Boyd, P.-M. Flaud, N. Daugey and R. Lesclaux, *'*Rate constants for RO_2+ HO_2 reactions measured under a large excess of HO_2*'*, *The Journal of Physical Chemistry A*, 2003, **107**, 818-821.

133. A. Hofzumahaus, F. Rohrer, K. Lu, B. Bohn, T. Brauers, C.-C. Chang, H. Fuchs, F. Holland, K. Kita, Y. Kondo, X. Li, S. Lou, M. Shao, L. Zeng, A. Wahner and Y. Zhang, *'*Amplified Trace Gas Removal in the Troposphere*'*, *Science*, 2009, **324**, 1702-1704.

134. J. Peeters, J.-F.o. Müller, T. Stavrakou and V.S. Nguyen, 'Hydroxyl radical recycling in isoprene oxidation driven by hydrogen bonding and hydrogen tunneling: The upgraded LIM1 mechanism', *The Journal of Physical Chemistry A*, 2014, **118**, 8625-8643.

135. H. Fuchs, B. Bohn, A. Hofzumahaus, F. Holland, K. Lu, S. Nehr, F. Rohrer and A. Wahner, 'Detection of HO_2 by laser-induced fluorescence: calibration and interferences from RO_2 radicals', *Atmospheric Measurement Techniques Discussions*, 2011, **4**, 1255-1302.

136. S.M. MacDonald, H. Oetjen, A.S. Mahajan, L.K. Whalley, P.M. Edwards, D.E. Heard, C.E. Jones and J.M.C. Plane, 'DOAS measurements of formaldehyde and glyoxal above a south-east Asian tropical rainforest', *Atmos. Chem. Phys.*, 2012, **12**, 5949-5962.

137. D. Johnson, S. Raoult, R. Lesclaux and L.N. Krasnoperov, 'UV absorption spectra of methyl-substituted hydroxy-cyclohexadienyl radicals in the gas phase', *Journal of Photochemistry and Photobiology A: Chemistry*, 2005, **176**, 98-106.

138. R. Talukdar, J. Burkholder, M. Gilles and J. Roberts, 'Atmospheric fate of several alkyl nitrates Part 2UV absorption cross-sections and photodissociation quantum yields', *Journal of the Chemical Society, Faraday Transactions*, 1997, **93**, 2797-2805.

139. D.K. Papanastasiou, V.C. Papadimitriou, D.W. Fahey and J.B. Burkholder, 'UV absorption spectrum of the ClO dimer (Cl_2O_2) between 200 and 420 nm', *The Journal of Physical Chemistry A*, 2009, **113**, 13711-13726.

140. C. Robert, 'Simple, stable, and compact multiple-reflection optical cell for very long optical paths', *Applied Optics*, 2007, **46**, 5408-5418.

141. J.U. White, 'Long optical paths of large aperture', *Journal of the Optical Society of America (1917-1983)*, 1942, **32**, 285.

142. F. Wicktor, A. Donati, H. Herrmann and R. Zellner, 'Laser based spectroscopic and kinetic investigations of reactions of the Cl atom with oxygenated hydrocarbons in aqueous solution', *Physical Chemistry Chemical Physics*, 2003, **5**, 2562-2572.

143. S. Himmelmann, J. Orphal, H. Bovensmann, A. Richter, A. Ladstätter-Weissenmayer and J.P. Burrows, 'First observation of the OIO molecule by time-resolved flash photolysis absorption spectroscopy', *Chemical Physics Letters*, 1996, **251**, 330-334.

144. D.R. Herriott and H.J. Schulte, 'Folded Optical Delay Lines', *Applied Optics*, 1965, **4**, 883-889.

145.   J. Altmann, R. Baumgart and C. Weitkamp, 'Two-mirror multipass absorption cell', *Applied Optics*, 1981, **20**, 995-999.

146.   B. Wert, A. Fried, S. Rauenbuehler, J. Walega and B. Henry, 'Design and performance of a tunable diode laser absorption spectrometer for airborne formaldehyde measurements', *Journal of Geophysical Research: Atmospheres (1984–2012)*, 2003, **108**.

147.   C.V. Horii, M.S. Zahniser, D.D. Nelson Jr, J.B. McManus and S.C. Wofsy, 'Nitric acid and nitrogen dioxide flux measurements: a new application of tunable diode laser absorption spectroscopy', in, International Society for Optics and Photonics, 1999, 152-161.

148.   J.S. Pilgrim, R.T. Jennings and C.A. Taatjes, 'Temperature controlled multiple pass absorption cell for gas phase chemical kinetics studies', *Review of Scientific Instruments*, 1997, **68**, 1875-1878.

149.   J.B. McManus, M.S. Zahniser, D.D. Nelson, L.R. Williams and C.E. Kolb, 'Infrared laser spectrometer with balanced absorption for measurement of isotopic ratios of carbon gases', *Spectrochimica Acta Part A: Molecular and Biomolecular Spectroscopy*, 2002, **58**, 2465-2479.

150.   J. McManus, P. Kebabian and M. Zahniser, 'Astigmatic mirror multipass absorption cells for long-path-length spectroscopy', *Applied Optics*, 1995, **34**, 3336-3348.

151.   M.S. Zahniser, D.D. Nelson, J.B. McManus, P.L. Kebabian and D. Lloyd, 'Measurement of trace gas fluxes using tunable diode laser spectroscopy', *Philosophical Transactions: Physical Sciences and Engineering*, 1995, 371-382.

152.   J.B. McManus, 'Paraxial matrix description of astigmatic and cylindrical mirror resonators with twisted axes for laser spectroscopy', *Applied Optics*, 2007, **46**, 472-482.

153.   J.B. McManus, M.S. Zahniser, D.D. Nelson, J.H. Shorter, S. Herndon, E. Wood and R. Wehr, 'Application of quantum cascade lasers to high-precision atmospheric trace gas measurements', *Optical Engineering*, 2010, **49**.

154.   J.B. McManus, M.S. Zahniser and D.D. Nelson, 'Dual quantum cascade laser trace gas instrument with astigmatic Herriott cell at high pass number', *Applied Optics*, 2011, **50**, A74-A85.

155.   D.B. Atkinson, 'Solving chemical problems of environmental importance using cavity ring-down spectroscopy', *Analyst*, 2003, **128**, 117-125.

156. D.B. Atkinson and J.L. Spillman, 'Alkyl peroxy radical kinetics measured using near-infrared CW-cavity ring-down spectroscopy', *The Journal of Physical Chemistry A*, 2002, **106**, 8891-8902.

157. S. Wu, P. Dupre and T.A. Miller, 'High-resolution IR cavity ring-down spectroscopy of jet-cooled free radicals and other species', *Physical Chemistry Chemical Physics*, 2006, **8**, 1682-1689.

158. D. Amedro, A.E. Parker, C. Schoemaecker and C. Fittschen, 'Direct observation of OH radicals after 565 nm multi-photon excitation of NO_2 in the presence of H_2O', *Chemical Physics Letters*, 2011, **513**, 12-16.

159. E.P. Faragó, B. Viskolcz, C. Schoemaecker and C. Fittschen, 'Absorption Spectrum and Absolute Absorption Cross Sections of CH_3O_2 Radicals and CH_3I Molecules in the Wavelength Range 7473–7497 cm^{-1}', *The Journal of Physical Chemistry A*, 2013, **117**, 12802-12811.

160. M. Blocquet, C. Schoemaecker, D. Amedro, O. Herbinet, F. Battin-Leclerc and C. Fittschen, 'Quantification of OH and HO_2 radicals during the low-temperature oxidation of hydrocarbons by Fluorescence Assay by Gas Expansion technique', *Proceedings of the National Academy of Sciences*, 2013, **110**, 20014-20017.

161. C. Fittschen, L.K. Whalley and D.E. Heard, 'The Reaction of CH_3O_2 Radicals with OH Radicals: A Neglected Sink for CH_3O_2 in the Remote Atmosphere', *Environmental Science & Technology*, 2014, **48**, 7700-7701.

162. E. Assaf, L. Sheps, L. Whalley, D. Heard, A. Tomas, C. Schoemaecker and C. Fittschen, 'The Reaction between CH_3O_2 and OH Radicals: Product Yields and Atmospheric Implications', *Environmental Science & Technology*, 2017, **51**, 2170-2177.

163. T.A. Miller, 'Chemistry and Chemical Intermediates in Supersonic Free Jet Expansions', *Science*, 1984, **223**, 545-553.

164. C.C. Carter, S. Gopalakrishnan, J.R. Atwell and T.A. Miller, 'Laser Excitation Spectra of Large Alkoxy Radicals Containing 5−12 Carbon Atoms', *The Journal of Physical Chemistry A*, 2001, **105**, 2925-2928.

165. S.J. Zalyubovsky, B.G. Glover and T.A. Miller, 'Cavity Ringdown Spectroscopy of the Ã-X̃ Electronic Transition of the $CH_3C(O)O_2$ Radical', *The Journal of Physical Chemistry A*, 2003, **107**, 7704-7712.

166. A.E. Parker, C. Jain, C. Schoemaecker, P. Szriftgiser, O. Votava and C. Fittschen, 'Simultaneous, time-resolved measurements of OH and HO_2 radicals by coupling of high repetition rate LIF and cw-CRDS techniques to

a laser photolysis reactor and its application to the photolysis of H2O2′, *Applied Physics B*, 2011, **103**, 725-733.

167. S.E. Fiedler, A. Hese and A.A. Ruth, ′Incoherent broad-band cavity-enhanced absorption spectroscopy′, *Chemical Physics Letters*, 2003, **371**, 284-294.

168. L. Sheps and D.W. Chandler, *Time-resolved broadband cavity-enhanced absorption spectroscopy for chemical kinetics*, Sandia National Laboratories (SNL-CA), Livermore, CA (United States), 2013.

169. J. Langridge, T. Laurila, R. Watt, R. Jones, C. Kaminski and J. Hult, ′Cavity enhanced absorption spectroscopy of multiple trace gas species using a supercontinuum radiation source′, *Optics Express*, 2008, **16**, 10178-10188.

170. S.-S. Kiwanuka, T. Laurila and C.F. Kaminski, ′Sensitive Method for the Kinetic Measurement of Trace Species in Liquids Using Cavity Enhanced Absorption Spectroscopy with Broad Bandwidth Supercontinuum Radiation′, *Analytical Chemistry*, 2010, **82**, 7498-7501.

171. D.M. Rowley, M.H. Harwood, R.A. Freshwater and R.L. Jones, ′A novel flash photolysis/UV absorption system employing charge-coupled device (CCD) detection: A study of the BrO+ BrO reaction at 298 K′, *The Journal of Physical Chemistry*, 1996, **100**, 3020-3029.

172. P. Spietz, J.C.G. Martín and J.P. Burrows, ′Spectroscopic studies of the I$_2$/O$_3$ photochemistry: Part 2. Improved spectra of iodine oxides and analysis of the IO absorption spectrum′, *Journal of Photochemistry and Photobiology A: Chemistry*, 2005, **176**, 50-67.

173. E. Jiménez, B. Lanza, A. Garzón, B. Ballesteros and J. Albaladejo, ′Atmospheric Degradation of 2-Butanol, 2-Methyl-2-butanol, and 2,3-Dimethyl-2-butanol: OH Kinetics and UV Absorption Cross Sections′, *The Journal of Physical Chemistry A*, 2005, **109**, 10903-10909.

174. J.C. Gómez Martín, P. Spietz, J. Orphal and J.P. Burrows, ′Principal and independent components analysis of overlapping spectra in the context of multichannel time-resolved absorption spectroscopy′, *Spectrochimica Acta Part A: Molecular and Biomolecular Spectroscopy*, 2004, **60**, 2673-2693.

175. W.J. Bloss, D.M. Rowley, R.A. Cox and R.L. Jones, ′Rate coefficient for the BrO+ HO 2 reaction at 298 K′, *Physical Chemistry Chemical Physics*, 2002, **4**, 3639-3647.

176. G. Stresing, [online], 2017. Available from: http://www.stresing.de/

177. L.T. Molina and M.J. Molina, *'*UV absorption cross sections of HO_2NO_2 vapor*'*, *Journal of Photochemistry*, 1981, **15**, 97-108.

178. C. Hochanadel, J. Ghormley and P.J. Ogren, *'*Absorption spectrum and reaction kinetics of the HO_2 radical in the gas phase*'*, *The Journal of Chemical Physics*, 1972, **56**, 4426-4432.

179. C. Lin, N. Rohatgi and W. DeMore, *'*Ultraviolet absorption cross sections of hydrogen peroxide*'*, *Geophysical Research Letters*, 1978, **5**, 113-115.

180. J. Nicovich and P. Wine, *'*Temperature-dependent absorption cross sections for hydrogen peroxide vapor*'*, *Journal of Geophysical Research: Atmospheres*, 1988, **93**, 2417-2421.

181. R. Hansen, M. Blitz, D. Heard, T. Ingham, P. Seakins and L. Whalley, *'*Investigation of Organic Peroxy Radical Photolysis as a Source of OH*'*, in, 2015.

182. A. Savitzky and M.J.E. Golay, *'*Smoothing and Differentiation of Data by Simplified Least Squares Procedures*'*, *Analytical Chemistry*, 1964, **36**, 1627-1639.

183. B. Ouyang, M.W. McLeod, R.L. Jones and W.J. Bloss, *'*NO_3 radical production from the reaction between the Criegee intermediate CH_2OO and NO_2*'*, *Physical Chemistry Chemical Physics*, 2013, **15**, 17070-17075.

184. A.S. Hasson, G. Orzechowska and S.E. Paulson, *'*Production of stabilized Criegee intermediates and peroxides in the gas phase ozonolysis of alkenes: 1. Ethene, trans-2-butene, and 2, 3-dimethyl-2-butene*'*, *Journal of Geophysical Research: Atmospheres*, 2001, **106**, 34131-34142.

185. W.R. Wadt and W.A. Goddard III, *'*Electronic structure of the Criegee intermediate. Ramifications for the mechanism of ozonolysis*'*, *Journal of the American Chemical Society*, 1975, **97**, 3004-3021.

186. J. Rudolph, *'*Biogenic sources of atmospheric alkenes and acetylene*'*, *Biogenic Volatile Organic Compounds in the Atmosphere–Summary of Present Knowledge, SPB Academic Publishers, Amsterdam, The Netherlands*, 1997, 53-65.

187. O. Welz, J.D. Savee, D.L. Osborn, S.S. Vasu, C.J. Percival, D.E. Shallcross and C.A. Taatjes, *'*Direct kinetic measurements of Criegee intermediate (CH_2OO) formed by reaction of CH_2I with O_2*'*, *Science*, 2012, **335**, 204-207.

188.	Y. Scribano, N. Goldman, R. Saykally and C. Leforestier, *'*Water dimers in the atmosphere III: equilibrium constant from a flexible potential*'*, *The Journal of Physical Chemistry A*, 2006, **110**, 5411-5419.

189.	Y.-T. Su, H.-Y. Lin, R. Putikam, H. Matsui, M.C. Lin and Y.-P. Lee, *'*Extremely rapid self-reaction of the simplest Criegee intermediate CH_2OO and its implications in atmospheric chemistry*'*, *Nat Chem*, 2014, **6**, 477-483.

190.	W.-L. Ting, C.-H. Chang, Y.-F. Lee, H. Matsui, Y.-P. Lee and J.J.-M. Lin, *'*Detailed mechanism of the $CH_2I + O_2$ reaction: Yield and self-reaction of the simplest Criegee intermediate CH_2OO *'*, *The Journal of Chemical Physics*, 2014, **141**, 104308.

191.	Y. Liu, K.D. Bayes and S.P. Sander, *'*Measuring Rate Constants for Reactions of the Simplest Criegee Intermediate (CH_2OO) by Monitoring the OH Radical*'*, *The Journal of Physical Chemistry A*, 2014, **118**, 741-747.

192.	A. Novelli, L. Vereecken, J. Lelieveld and H. Harder, *'*Direct observation of OH formation from stabilised Criegee intermediates*'*, *Physical Chemistry Chemical Physics*, 2014, **16**, 19941-19951.

193.	C.A. Taatjes, *'*Criegee Intermediates: What Direct Production and Detection Can Teach Us About Reactions of Carbonyl Oxides*'*, *Annual Review of Physical Chemistry*, 2017, **68**, 183-207.

194.	R.F. Hansen, T.R. Lewis, L. Graham, L.K. Whalley, P.W. Seakins, D.E. Heard and M.A. Blitz, *'*OH production from the photolysis of isoprene-derived peroxy radicals: cross-sections, quantum yields and atmospheric implications*'*, *Physical Chemistry Chemical Physics*, 2017.

195.	S. Sawada and T. Totsuka, *'*Natural and anthropogenic sources and fate of atmospheric ethylene*'*, *Atmospheric Environment (1967)*, 1986, **20**, 821-832.

196.	G. Tyndall, R. Cox, C. Granier, R. Lesclaux, G. Moortgat, M. Pilling, A. Ravishankara and T. Wallington, *'*Atmospheric chemistry of small organic peroxy radicals*'*, *Journal of Geophysical Research: Atmospheres*, 2001, **106**, 12157-12182.

197.	A.P. Teng, J.D. Crounse and P.O. Wennberg, *'*Isoprene Peroxy Radical Dynamics*'*, *Journal of the American Chemical Society*, 2017, **139**, 5367-5377.

198.	M.E. Jenkin and R.A. Cox, *'*Kinetics of reactions of methylperoxy and 2-hydroxyethylperoxy radicals produced by the photolysis of iodomethane and 2-iodoethanol*'*, *The Journal of Physical Chemistry*, 1991, **95**, 3229-3237.

199. T.P. Murrells, M.E. Jenkin, S.J. Shalliker and G.D. Hayman, 'Laser flash photolysis study of the UV spectrum and kinetics of reactions of $HOCH_2CH_2O_2$ radicals', *Journal of the Chemical Society, Faraday Transactions*, 1991, **87**, 2351-2360.

200. C. Anastasi, D. Muir, V. Simpson and P.B. Pagsberg, 'Spectrum and mutual kinetics of $HOCH_2CH_2O_2$ radicals', 1991.

201. M.E. Jenkin and G.D. Hayman, 'Kinetics of reactions of primary, secondary and tertiary β-hydroxy peroxyl radicals', *J. Chem. Soc., Faraday Trans.*, 1995, **91**, 1911-1922.

202. G.M.P. Just, 'High Resolution Cavity Ringdown Spectroscopy of the A - X Electronic Transition of Alkyl Peroxy Radicals', *The Ohio State University*, 2009.

203. J. Zádor, R.X. Fernandes, Y. Georgievskii, G. Meloni, C.A. Taatjes and J.A. Miller, 'The reaction of hydroxyethyl radicals with O_2: A theoretical analysis and experimental product study', *Proceedings of the Combustion Institute*, 2009, **32**, 271-277.

204. A. Guenther, C.N. Hewitt, D. Erickson, R. Fall, C. Geron, T. Graedel, P. Harley, L. Klinger, M. Lerdau and W. McKay, 'A global model of natural volatile organic compound emissions', *Journal of Geophysical Research: Atmospheres*, 1995, **100**, 8873-8892.

205. T. Pugh, A. MacKenzie, B. Langford, E. Nemitz, P. Misztal and C. Hewitt, 'The influence of small-scale variations in isoprene concentrations on atmospheric chemistry over a tropical rainforest', *Atmospheric Chemistry and Physics*, 2011, **11**, 4121-4134.

206. R. Atkinson, 'Kinetics and mechanisms of the gas-phase reactions of the hydroxyl radical with organic compounds under atmospheric conditions', *Chemical Reviews*, 1986, **86**, 69-201.

207. M.E. Jenkin, T.P. Murrells, S.J. Shalliker and G.D. Hayman, 'Kinetics and product study of the self-reactions of allyl and allyl peroxy radicals at 296 K', *Journal of the Chemical Society, Faraday Transactions*, 1993, **89**, 433-446.

208. M.E. Jenkin and G.D. Hayman, 'Kinetics of reactions of primary, secondary and tertiary β-hydroxy peroxyl radicals', *Journal of the Chemical Society, Faraday Transactions*, 1995, **91**, 1911-1922.

209. R. Atkinson, D.L. Baulch, R.A. Cox, R.F. Hampson, J.A. Kerr and J. Troe, 'Evaluated kinetic and photochemical data for atmospheric chemistry:

Supplement III', *International Journal of Chemical Kinetics*, 1989, **21**, 115-150.

210.   G. Martins, A. Ferreira-Rodrigues, F. Rodrigues, G. De Souza, N. Mason, S. Eden, D. Duflot, J.-P. Flament, S.V. Hoffmann and J. Delwiche, 'Valence shell electronic spectroscopy of isoprene studied by theoretical calculations and by electron scattering, photoelectron, and absolute photoabsorption measurements', *Physical Chemistry Chemical Physics*, 2009, **11**, 11219-11231.

211.   A.A. Boyd, B. Nozière and R. Lesclaux, 'Kinetic studies of the allylperoxyl radical self-reaction and reaction with HO$_2$', *Journal of the Chemical Society, Faraday Transactions*, 1996, **92**, 201-206.

212.   A.A. Boyd, R. Lesclaux, M.E. Jenkin and T.J. Wallington, 'A spectroscopic, kinetic, and product study of the $(CH_3)_2C(OH)CH_2O_2$ radical self reaction and reaction with HO$_2$', *The Journal of Physical Chemistry*, 1996, **100**, 6594-6603.

213.   M.M. Maricq and J.J. Szente, 'A kinetic study of the reaction between ethylperoxy radicals and HO$_2$', *The Journal of Physical Chemistry*, 1994, **98**, 2078-2082.

214.   S.P. Sander, M. Peterson, R.T. Watson and R. Patrick, 'Kinetics studies of the hydrogen dioxide+ hydrogen dioxide and deuterium dioxide+ deuterium dioxide reactions at 298 K', *The Journal of Physical Chemistry*, 1982, **86**, 1236-1240.

215.   V.B. Di Marco and G.G. Bombi, 'Mathematical functions for the representation of chromatographic peaks', *Journal of Chromatography A*, 2001, **931**, 1-30.

216.   J.J. Orlando and G.S. Tyndall, 'Laboratory studies of organic peroxy radical chemistry: an overview with emphasis on recent issues of atmospheric significance', *Chemical Society Reviews*, 2012, **41**, 6294-6317.

217.   P. Bousquet, B. Ringeval, I. Pison, E.J. Dlugokencky, E.G. Brunke, C. Carouge, F. Chevallier, A. Fortems-Cheiney, C. Frankenberg, D.A. Hauglustaine, P.B. Krummel, R.L. Langenfelds, M. Ramonet, M. Schmidt, L.P. Steele, S. Szopa, C. Yver, N. Viovy and P. Ciais, 'Source attribution of the changes in atmospheric methane for 2006–2008', *Atmos. Chem. Phys.*, 2011, **11**, 3689-3700.

218.   A. Turner, D.J. Jacob, K. Wecht, J. Maasakkers, E. Lundgren, A. Andrews, S. Biraud, H. Boesch, K. Bowman and N.M. Deutscher, 'Estimating global and North American methane emissions with high spatial resolution using GOSAT satellite data', *Atmos. Chem. Phys*, 2015, **15**, 7049-7069.

219. N. Srinivasan, M.-C. Su, J. Sutherland and J. Michael, 'Reflected shock tube studies of high-temperature rate constants for OH+ CH$_4$→ CH$_3$+ H$_2$O and CH$_3$+ NO$_2$→ CH$_3$O+ NO', *The Journal of Physical Chemistry A*, 2005, **109**, 1857-1863.

220. A. Bonard, V. Daële, J.-L. Delfau and C. Vovelle, 'Kinetics of OH Radical Reactions with Methane in the Temperature Range 295− 660 K and with Dimethyl Ether and Methyl-tert-butyl Ether in the Temperature Range 295− 618 K', *The Journal of Physical Chemistry A*, 2002, **106**, 4384-4389.

221. L. Whalley, K. Furneaux, A. Goddard, J.D. Lee, A. Mahajan, H. Oetjen, K.A. Read, N. Kaaden, L.J. Carpenter and A. Lewis, 'The chemistry of OH and HO 2 radicals in the boundary layer over the tropical Atlantic Ocean', *Atmospheric Chemistry and Physics*, 2010, **10**, 1555-1576.

222. L. Whalley, D. Stone, B. Bandy, R. Dunmore, J.F. Hamilton, J. Hopkins, J.D. Lee, A.C. Lewis and D.E. Heard, 'Atmospheric OH reactivity in central London: observations, model predictions and estimates of in situ ozone production', *Atmospheric Chemistry and Physics*, 2016, **16**, 2109-2122.

223. H. Adachi, N. Basco and D. James, 'Mutual interactions of the methyl and methylperoxy radicals studied by flash photolysis and kinetic spectroscopy', *International Journal of Chemical Kinetics*, 1980, **12**, 949-977.

224. A. Fahr, A.H. Laufer, M. Krauss and R. Osman, 'Gas phase absorption spectrum and cross sections of vinylperoxy (C$_2$H$_3$O$_2$) radical', *The Journal of Physical Chemistry A*, 1997, **101**, 4879-4886.

225. D. Hartmann and R. Zellner, 'Laser Photofragment Emission: A Novel Technique for the Study of Gas Phase Reactions of the CH$_3$O$_2$ Radical', in *Physico-Chemical Behaviour of Atmospheric Pollutants*, Springer, 1990, 352-358.

226. J. Platz, J. Sehested, O. Nielsen and T. Wallington, 'Atmospheric Chemistry of Cyclohexane: UV Spectra of c-C6H11• and (c-C6H11) O2• Radicals, Kinetics of the Reactions of (c-C6H11) O2• Radicals with NO and NO$_2$, and the Fate of the Alkoxy Radical (c-C6H11) O•', *The Journal of Physical Chemistry A*, 1999, **103**, 2688-2695.

227. R. Atkinson, 'Kinetics of the gas-phase reactions of OH radicals with alkanes and cycloalkanes', *Atmospheric Chemistry and Physics*, 2003, **3**, 2233-2307.

228. R. Gorse and D. Volman, 'Photochemistry of the gaseous hydrogen peroxide-carbon monoxide system: rate constants for hydroxyl radical reactions with hydrogen peroxide and isobutane by competitive kinetics', *Journal of Photochemistry*, 1972, **1**, 1-10.

229.   R. Baker, R. Baldwin and R. Walker, 'The use of the $H_2 + O_2$ reaction in determining the velocity constants of elementary reaction in hydrocarbon oxidation', in, Elsevier, 1971, 291-299.

230.   N. Greiner, 'Hydroxyl Radical Kinetics by Kinetic Spectroscopy. VII. The Reaction with Ethylene in the Range 300–500° K', *The Journal of Chemical Physics*, 1970, **53**, 1284-1285.

231.   M. Baasandorj, D.K. Papanastasiou, R.K. Talukdar, A.S. Hasson and J.B. Burkholder, '$(CH_3)_3COOH$ (tert-butyl hydroperoxide): OH reaction rate coefficients between 206 and 375 K and the OH photolysis quantum yield at 248 nm', *Physical Chemistry Chemical Physics*, 2010, **12**, 12101-12111.

232.   M. Blitz, M. Pilling, S. Robertson and P. Seakins, 'Direct studies on the decomposition of the tert-butoxy radical and its reaction with NO', *Physical Chemistry Chemical Physics (Incorporating Faraday Transactions)*, 1999, **1**, 73-80.

233.   S.A. Carr, M.A. Blitz and P.W. Seakins, 'Site-Specific Rate Coefficients for Reaction of OH with Ethanol from 298 to 900 K', *The Journal of Physical Chemistry A*, 2011, **115**, 3335-3345.

234.   L.W. Pickett, M. Muntz and E. McPherson, 'Vacuum Ultraviolet Absorption Spectra of Cyclic Compounds. I. Cyclohexane, Cyclohexene, Cyclopentane, Cyclopentene and Benzene1', *Journal of the American Chemical Society*, 1951, **73**, 4862-4865.

235.   R.D. Martinez, A.A. Buitrago, N.W. Howell, C.H. Hearn and J.A. Joens, 'The near UV absorption spectra of several aliphatic aldehydes and ketones at 300 K', *Atmospheric Environment. Part A. General Topics*, 1992, **26**, 785-792.

236.   T. Gierczak, J.B. Burkholder, S. Bauerle and A. Ravishankara, 'Photochemistry of acetone under tropospheric conditions', *Chemical Physics*, 1998, **231**, 229-244.

237.   C. Anastasi, I.W. Smith and D.A. Parkes, 'Flash photolysis study of the spectra of CH_3O_2 and $C(CH_3)_3O_2$ radicals and the kinetics of their mutual reactions and with NO', *Journal of the Chemical Society, Faraday Transactions 1: Physical Chemistry in Condensed Phases*, 1978, **74**, 1693-1701.

238.   R. Cox and G. Tyndall, 'Rate constants for reactions of CH_3O_2 in the gas phase', *Chemical Physics Letters*, 1979, **65**, 357-360.

239. P. Dagaut and M.J. Kurylo, 'The gas phase UV absorption spectrum of CH$_3$O$_2$ radicals: A reinvestigation', *Journal of Photochemistry and Photobiology A: Chemistry*, 1990, **51**, 133-140.

240. C.J. Hochanadel, J.A. Ghormley, J.W. Boyle and P.J. Ogren, 'Absorption spectrum and rates of formation and decay of the methyldioxy radical', *The Journal of Physical Chemistry*, 1977, **81**, 3-7.

241. C.S. Kan, R.D. McQuigg, M.R. Whitbeck and J.G. Calvert, 'Kinetic flash spectroscopic study of the CH$_3$O$_2$ + CH$_3$O$_2$ and CH$_3$O$_2$ + SO$_2$ reactions', *International Journal of Chemical Kinetics*, 1979, **11**, 921-933.

242. M.J. Kurylo, T.J. Wallington and P.A. Ouellette, 'Measurements of the UV absorption cross-sections for HO 2 and CH 3 O 2 in the gas phase', *Journal of Photochemistry*, 1987, **39**, 201-215.

243. K. McAdam, B. Veyret and R. Lesclaux, 'UV absorption spectra of HO$_2$ and CH$_3$O$_2$ radicals and the kinetics of their mutual reactions at 298 K', *Chemical Physics Letters*, 1987, **133**, 39-44.

244. G. Moortgat, B. Veyret and R. Lesclaux, 'Absorption spectrum and kinetics of reactions of the acetylperoxy radical', *The Journal of Physical Chemistry*, 1989, **93**, 2362-2368.

245. D.A. Parkes, D.M. Paul, C.P. Quinn and R.C. Robson, 'The ultraviolet absorption by alkylperoxy radicals and their mutual reactions', *Chemical Physics Letters*, 1973, **23**, 425-429.

246. M.J. Pilling and M.J. Smith, 'A laser flash photolysis study of the reaction methyl+ molecular oxygen. fwdarw. methylperoxy (CH$_3$O$_2$) at 298 K', *The Journal of Physical Chemistry*, 1985, **89**, 4713-4720.

247. S.P. Sander and R.T. Watson, 'Temperature dependence of the self-reaction of methyldioxy radicals', *The Journal of Physical Chemistry*, 1981, **85**, 2960-2964.

248. F.-G. Simon, 'Spektrum und Kinetik der Selbstreaktion des Methylperoxy-Radikals CH$_3$O$_2$ [CHO] und seiner Reaktion mit ClO', 1989.

249. C.M. Roehl, D. Bauer and G.K. Moortgat, 'Absorption spectrum and kinetics of the acetylperoxy radical', *The Journal of Physical Chemistry*, 1996, **100**, 4038-4047.

250. S. Sander, R. Friedl, J. Barker, D. Golden, M. Kurylo, P. Wine, J. Abbatt, J. Burkholder, C. Kolb and G. Moortgat, *Chemical kinetics and photochemical data for use in Atmospheric Studies Evaluation Number 16: supplement to Evaluation 15: update of key reactions*, Pasadena, CA: Jet

Propulsion Laboratory, National Aeronautics and Space Administration, 2009, 2009.

251. L.J.P. Kirsch, A, 'Absorption cross sections of the 1,1,1-dimethylethylperoxy radical (tert-butylperoxy radical) t-$C_4H_9O_2$,' in, Manchester, Royal Society of Chemistry, 1997, 37.

252. A. Tomas, E. Villenave and R. Lesclaux, 'Kinetics of the $(CH_3)_2CHCO$ and $(CH_3)_3CCO$ radical decomposition: temperature and pressure dependences', *Physical Chemistry Chemical Physics*, 2000, **2**, 1165-1174.

253. R.S. Anderson, L. Huang, R. Iannone and J. Rudolph, 'Measurements of the $^{12}C/^{13}C$ kinetic isotope effects in the gas-phase reactions of light alkanes with chlorine atoms', *The Journal of Physical Chemistry A*, 2007, **111**, 495-504.

254. R. Atkinson, D. Baulch, R. Cox, J. Crowley, R. Hampson Jr, J. Kerr, M. Rossi and J. Troe, 'Summary of evaluated kinetic and photochemical data for atmospheric chemistry', 2001, 1-56.

255. J.D. Lee, G. McFiggans, J.D. Allan, A.R. Baker, S.M. Ball, A.K. Benton, L.J. Carpenter, R. Commane, B.D. Finley, M. Evans, E. Fuentes, K. Furneaux, A. Goddard, N. Good, J.F. Hamilton, D.E. Heard, H. Herrmann, A. Hollingsworth, J.R. Hopkins, T. Ingham, M. Irwin, C.E. Jones, R.L. Jones, W.C. Keene, M.J. Lawler, S. Lehmann, A.C. Lewis, M.S. Long, A. Mahajan, J. Methven, S.J. Moller, K. Müller, T. Müller, N. Niedermeier, S. O'Doherty, H. Oetjen, J.M.C. Plane, A.A.P. Pszenny, K.A. Read, A. Saiz-Lopez, E.S. Saltzman, R. Sander, R. von Glasow, L. Whalley, A. Wiedensohler and D. Young, 'Reactive Halogens in the Marine Boundary Layer (RHaMBLe): the tropical North Atlantic experiments', *Atmos. Chem. Phys.*, 2010, **10**, 1031-1055.